A Study of $e^+e^- \to \mu^+\mu^-(\gamma)$ events at BaBar

Zinkoo Yun

April 27, 2005

A Study of $e^+e^- \rightarrow \mu^+\mu^-(\gamma)$ events at BaBar

by

Zinkoo Yun

B.Sc., Inha University, Korea, 1999.

A Thesis Submitted in Partial Fulfilment of the
Requirements for the Degree of

MASTER OF SCIENCE

in the Department of Physics and Astronomy.

We accept this thesis as conforming
to the required standard.

Supervisors: Dr. M. Roney

ABSTRACT

This thesis evaluates the validity of a Monte Carlo simulation of the process $e^+e^- \rightarrow \mu^+\mu^-(\gamma)$ using data collected using the BaBar detector at the PEP-II e^+e^- collider. Because the same Monte Carlo program simulates both $e^+e^- \rightarrow \mu^+\mu^-(\gamma)$ and $e^+e^- \rightarrow \tau^+\tau^-(\gamma)$, these studies also test the Monte Carlo description of $e^+e^- \rightarrow \tau^+\tau^-(\gamma)$. In particular, we quantify the validity of the implementation of quantum electrodynamics (QED) in the KK2f Monte Carlo generator. To do that, $e^+e^- \rightarrow \mu^+\mu^-(\gamma)$ events in 0.99 fb^{-1} of data from BaBar and 4.5 million KK2f $e^+e^- \rightarrow \mu^+\mu^-(\gamma)$ Monte Carlo events are compared. This study provides a measure of the uncertainty on the average τ lepton momentum predicted by the Monte Carlo, an uncertainty that is required in a precision τ lifetime measurement. It is also used in systematic studies of the detector response required in a search for $\tau \rightarrow \mu\gamma$ events and to verify the ability of the Monte Carlo to describe the $\tau \rightarrow \mu\gamma$ signal and lepton pair background in that search.

Contents

ABSTRACT ii

1 INTRODUCTION 1

2 THEORY 3

2.1 $e^+e^- \to \mu^+\mu^-(\gamma)$ process in the Standard Model 3

2.2 $e^+e^- \to \tau^+\tau^-\gamma$ process in the Standard Model 5

2.3 $e^+e^- \to \tau^+\tau^-\gamma$ process in new physics 9

2.4 Detecting direct $\tau^- \to \mu^-\gamma$ decays 9

2.5 τ lifetime measurement 11

2.6 KK2f and KORALB 13

3 APPARATUS:BABAR & PEP-II 15

3.1 The BaBar experiment 15

3.2 Slac linear accelerator 16

3.3 PEP-II 16

3.4 Detector 18

3.4.1 SVT(Silicon Vertex Tracker) 19

3.4.2 DCH(Drift Chamber) 21

3.4.3 DIRC(Detection of Internally Reflected Cerenkov Light) 25

3.4.4 EMC(Electromagnetic Calorimeter) 29

3.4.5 IFR(Instrumented flux return) 38
3.4.6 Trigger 41
3.4.7 Online computing 49

4 DATA SELECTION **51**

4.1 Preselection 52
4.2 Acoplanarity and Acolinearity in center of momentum 53
4.3 Rm versus Remc plane, Geometrical cut 55
4.4 Improving $\mu\mu(\gamma)$ events selection 1 - Extended cut 60
4.5 Improving $\mu\mu(\gamma)$ events selection 2 - Final cut 72
4.6 Photon energy cut 98

5 ANALYSIS **107**

5.1 Modelling of the detector response 107
5.2 KK2f modelling of QED 109
5.2.1 Angular distributions 109
5.2.2 $P_{\mu^{\pm},CM}/P^{max}_{\mu,CM}$ study 109
5.3 Systematic study of ΔE and $M_{EC,\mu\gamma}$ 128

6 CONCLUSION **146**

List of Tables

3.1 Principal physics processes at 10.58GeV 42

3.2 Trigger primitives for the DCT and EMT 44

3.3 L3 trigger efficiency 46

3.4 L3 output rates 47

5.1 Muon Efficiency, purity, bias error of $P_{\mu,cm}/P_{\mu,cm}^{max}$ before and after correction for KK2f 122

5.2 Bias error of $P_{\mu,cm}/P_{\mu,cm}^{max}$ for KK2f. 123

5.3 Bias error of $P_{\mu,cm}/P_{\mu,cm}^{max}$ for KK2f. 124

5.4 Bias error of $P_{\mu,cm}/P_{\mu,cm}^{max}$ for KORALB. 125

5.5 Bias error of $P_{\mu,cm}/P_{\mu,cm}^{max}$ for KORALB. 126

List of Figures

2.1 The Standard Model 3

2.2 $e^+e^- \rightarrow \tau^+\tau^-\gamma$ in the Standard Model 5

2.3 Standard Model processes 7

2.4 "New physics" process 9

2.5 Standard model events and new physics events 10

2.6 Standard model + new physics 11

2.7 τ decay in the CM 12

2.8 Comparing two MC 14

3.1 SLAC linear accelerator and PEP-II rings[7] 17

3.2 Cross section of BaBar detector 18

3.3 SVT strips 19

3.4 Cross section of silicon vertex tracker 20

3.5 Structure of SVT 20

3.6 Drift chamber schematic 22

3.7 Measurement of dE/dX versus momentum of charged particles 24

3.8 Longitudinal cross section of DCH 25

3.10 DIRC Components 26

3.9 Generation of Cerenkov light by a charged particle 26

3.11 DIRC Operation 27

3.12 Particle identification in DIRC 28
3.13 Array of Thallium doped Cesium iodide(CsI(Tl)) crystals 29
3.14 Schematic of electromagnetic and Hadronic shower 31
3.15 Diagram of CsI(Tl) crystal module 35
3.16 EMC barrel support structure with detail of module 36
3.17 A longitudinal cross section(in mm) of EMC with 56 crystal rings. 37
3.18 IFR structure 38
3.19 Cross section of a planar RPC 39
3.20 Muon efficiency and pion misidentification probability 40
3.21 Simplified flowchart of L1 algorithm 42
3.22 Schematic diagram of data acquisition 43
3.23 Front-End Electronics(FEE) 43
3.24 Event display 47
3.25 Schematic draw of BaBar online system 48

4.1 Final state radiation(FSR) 53
4.2 Initial state radiation(ISR) 54
4.3 Signal MC($\mu\mu$ MC) after preselection 54
4.4 Rm vs Remc 57
4.5 Remc after geometrical cut 58
4.6 Rm after geometrical cut 59
4.7 Acolinearitycm between μ^+ and μ^- in CM after geometrical cut 60
4.8 Dividing into sub-regions for mu MC 60
4.9 Acolinearitycm 62
4.10 Acolinearitycm 63
4.11 Sub region(0.2<Rm<0.3) 64
4.12 $E_{\gamma 1,CM}$ 66

4.13 $E_{\gamma 1,CM}$ 67

4.14 Profile of acolinearitycm vs Rm after extended cut 68

4.15 $P_{\mu^+,CM}/P^{max}_{\mu,CM}$ after extended cut 69

4.16 $P_{\mu^-,CM}/P^{max}_{\mu,CM}$ after extended cut 70

4.17 $P_{\mu^\pm,CM}/P^{max}_{\mu,CM}$ after extended cut 71

4.18 Remc after extended cut 73

4.19 Rm after extended cut 74

4.20 $E_{\gamma 1,CM}$ and $\Sigma E_{\gamma,CM}$ 75

4.21 $E_{\mu^+ onEMC}$ vs $P_{\mu^+,CM}$ and $E_{\mu^- onEMC}$ vs $P_{\mu^-,CM}$ After extended cut 76

4.22 $< E_{\mu^+ onEMC} >$ vs $P_{\mu^+,CM}$ and $< E_{\mu^- onEMC} >$ vs $P_{\mu^-,CM}$ After extended cut 77

4.23 Only extra events 81

4.24 $E_{\mu^+,CMonEMC} + E_{\mu^-,CMonEMC}$ and Remc 82

4.25 $E_{\gamma 1,CM}$ and $E_{\gamma 2,CM}$ 83

4.26 $\Sigma E_{\gamma,CM}$ and $E_{\gamma 1,CM}$ 84

4.27 $E_{\gamma 1,lab}$ and $—P_{\mu^+,CM} - P_{\mu^-,CM}—$ 85

4.28 θ between μ^+ and $\gamma 1, CM$ and θ between μ^- and $\gamma 1, CM$ 86

4.29 Only extra events 87

4.30 Only extra events 88

4.31 Rm vs Remc and $E_{\mu^- onEMC}$ vs $P_{\mu^-,CM}$ 89

4.32 Minimum of $E_{\mu^+,LABonEMC}$ and $E_{\mu^-,LABonEMC}$ and $dE/dX_{\mu^+} inDCH$ . . 90

4.33 Minimum of $E_{\mu^+,CMonEMC}$ and $E_{\mu^-,CMonEMC}$ and $dE/dX_{\mu^-} inDCH$ . . . 91

4.34 cos(θ,CM, μ^+) and cos(θ,CM, μ^-) 92

4.35 $E_{\mu^+,CMonEMC} + E_{\mu^-,CMonEMC}$ 93

4.36 Only $E_{\mu^+,CMonEMC} + E_{\mu^-,CMonEMC} > 2$ GeV events 94

4.37 cos(θ,CM, μ^+) and cos(θ,CM, μ^-) 95

4.38 Final cut (excluding extra events) 96

4.39 $E_{\gamma 1,lab}$ for number of photon=1 97
4.40 No photon energy cut 100
4.41 Energy of most energetic photon in CM($E_{\gamma 1,CM}$) 101
4.42 $E_{\gamma,lab}$ >80MeV 102
4.43 $E_{\gamma 1,CM}$ 103
4.44 Total energy of photons in CM($\Sigma E_{\gamma,CM}$) 104
4.45 $\theta_{\mu\gamma,CM}$ 105
4.46 $E_{\gamma 1,lab}$ for number of photon=1 106

5.1 Minimum of $E_{\mu^+,LABonEMC}$ and $E_{\mu^-,LABonEMC}$ 110
5.2 cos(θ,CM, μ) 111
5.3 $\phi_{CM,\mu}$ 112
5.4 acoplanaritycm(in radian) between $\mu^+\mu^-$ 113
5.5 acolinearitycm(in radian) between $\mu^+\mu^-$ 114
5.6 $\phi_{\gamma,CM}$ of 1st energy photon 115
5.7 No-radiation cut 116
5.8 $\pi - \theta_{CM,\mu^+} - \theta_{CM,\mu^-}$ 117
5.9 $P_{transverse,\mu}/sin(\theta_\mu)$ 118
5.10 Profile of acolinearitycm vs $\Sigma E_{\gamma,CM}$ 119
5.11 $P_{\mu^+,CM}/P^{max}_{\mu,CM}$ 129
5.12 $P_{\mu^-,CM}/P^{max}_{\mu,CM}$ 130
5.13 $P_{\mu^\pm,CM}/P^{max}_{\mu,CM}$ 131
5.14 $P_{\mu,CM}/P^{max}_{\mu,CM}$ 132
5.15 $P_{\mu^+,CM}/P^{max}_{\mu,CM}$ and $P_{\mu^-,CM}/P^{max}_{\mu,CM}$ 133
5.16 $P_{\mu^+,CM,corr}/P^{max}_{\mu,CM}$ and $P_{\mu^-,CM,corr}/P^{max}_{\mu,CM}$ 134
5.17 $P_{\mu,CM,corr}/P^{max}_{\mu,CM}$ 135
5.18 $P_{\mu^+,CM,corr}/P^{max}_{\mu,CM}$ 136

5.19 $P_{\mu^-,CM,corr}/P^{max}_{\mu,CM}$ 137

5.20 $P_{\mu^\pm,CM,corr}/P^{max}_{\mu,CM}$ 138

5.21 M_{EC} of $\mu^+\gamma$, and M_{EC} of $\mu^-\gamma$ 142

5.22 $\Delta E(=E_{CM}/2 - E^{CM}_{\mu\gamma})$ of $\mu^+\gamma$ 143

5.23 $\Delta E(=E_{CM}/2 - E^{CM}_{\mu\gamma})$ 144

5.24 $M^2_{EC} - M^2_{recoil}$ 145

Chapter 1

INTRODUCTION

The Standard Model is the current theory describing the fundamental particles and how they interact. This model tells us that six quarks(up, down, charm, strange, bottom and top) and six leptons(electron, muon, tau lepton and their associated neutrinos) and their anti-particles comprise the universe of sub-atomic physics and that they interact via four mediator particles(gluon, photon, W$\pm$, Z^0). This theory includes three known interactions and excludes gravity. The strength of the gravitational interaction is small compared to other interactions, so it is neglected in describing the experiments. The strong interaction arises from the color charge of quarks and gluons described in terms of the exchanging of gluons. The electromagnetic and weak interaction are combined into the electroweak theory and are described by the exchange of photons, W$\pm$ and Z^0 bosons.

Until recently, the Standard Model has been very successful in explaining almost all particle physics experiments. In the Standard Model, the electron, muon and tau lepton are said to have different flavors which do not mix. For instance $\tau \rightarrow \mu\gamma$ cannot happen in the Standard Model because before the interaction the tau lepton flavor number is 1 and muon lepton flavor number is 0 but after interaction tau lepton flavor number is 0 and muon lepton flavor number is 1. However, recent theory[1] predicts new phenomena which cannot be explained by the Standard Model. One of the predictions is lepton flavor-violating decays such

as $\tau \rightarrow \mu\gamma$ and $\mu \rightarrow e\gamma$. This research is the prerequisite step of searching for $\tau \rightarrow \mu\gamma$ decay.

In Chapter 2, the theory of lepton flavor violation decay and how to detect that process by experiment will be explained. How this study contributes to that research and the τ lifetime measurement study will also be discussed. In Chapter 3, the experimental apparatus employed in this work (The SLAC Linear Accelerator, PEP-II and BaBar detector) will be explained. The BaBar detector will be explained in detail because it is very important to know about the detector operation to understand clearly the experimental results. In Chapter 4 the methods to obtain a sample of $e^+e^- \rightarrow \mu + \mu - (\gamma)$ with high efficiency and purity will be explained with various supporting histograms. In Chapter 5, using these events, some useful features of $e^+e^- \rightarrow \mu + \mu - (\gamma)$ will be presented and using this control sample we will discuss the contribution of this study to the $\tau \rightarrow \mu\gamma$ and τ lifetime measurements.

Chapter 2

THEORY

2.1 $e^+e^- \rightarrow \mu^+\mu^-(\gamma)$ process in the Standard Model

In non-relativistic quantum mechanics we use perturbation theory to get the cross section and transition rate of a process. We can consider the process $e^+e^- \rightarrow \mu^+\mu^-$ as the transition of the e^+e^- state to the $\mu^+\mu^-$ state. In quantum field theory(relativistic quantum mechanics) we calculate the matrix element M to describe a perturbation term. We can calculate the matrix element with the help of a Feynman diagram. Each perturbation term has corresponding Feynman diagrams.

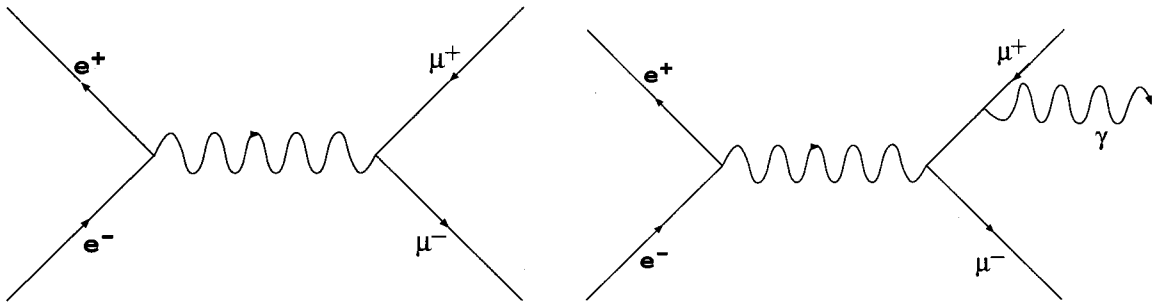

(a) $e^+e^- \rightarrow \mu^+\mu^-$ (b) $e^+e^- \rightarrow \mu^+\mu^-\gamma$

Figure 2.1: (a) First order Feynman diagram and (b) second order Feynman diagram for the Standard Model process: $e^+e^- \rightarrow \mu^+\mu^-(\gamma)$. Figure (b) represents final state radiation. There is also initial state radiation to be considered.

For example, the differential cross section of two body scattering $1 + 2 \rightarrow 3 + 4$ in the center of momentum frame(CM) is

$$\frac{d\sigma}{d\Omega} = \left(\frac{1}{8\pi}\right)^2 \frac{|M|^2}{s} \frac{P_f}{P_i}$$

here $\hbar c \equiv 1$, $\sqrt{s}$ is the total energy in the CM ($\approx$10.58 GeV in BaBar), P_f is the magnitude of either outgoing momentum and P_i is the magnitude of either incoming momentum. If we calculate matrix element M using Feynman diagram, the differential cross section of $e^+e^- \rightarrow \mu^+\mu^-$ process turns out to be [2]

$$\frac{d\sigma}{d\Omega} = \frac{\alpha^2}{4s} \frac{P_f}{P_i} \left(1 + cos^2\theta + \frac{m_e^2 + m_\mu^2}{E^2} + \frac{m_e^2 m_\mu^2}{E^4} cos^2\theta\right)$$

where α is the fine structure constant defined by

$$\alpha \equiv \frac{e^2}{4\pi}$$

with $\hbar c \equiv 1$, θ is the angle between incoming e^- and outgoing μ^- and E is the energy of each particle in CM. In BaBar experiment beam energy is high compared to the mass of the muon and electron. So we can write

$$\frac{d\sigma}{d\Omega} \approx \frac{\alpha^2}{4s}(1 + cos^2\theta)$$

for the production of a muon into the solid angle $d\Omega$. This is the first order perturbation expression.

Figure 2.1 (b) shows one of the next order Feynman diagrams. Accounting for higher order perturbation terms, the experimentally observable energy-weighted differential cross section up to the order of α^3 is [2]

$$\frac{d\Sigma}{d\Omega} = \frac{d\sigma}{d\Omega}\left(1 + \frac{3\alpha}{4\pi}\right) + \frac{3\alpha^3}{16\pi s}(1 - 3cos^2\theta)$$

Here $d\sigma/d\Omega$ is the differential cross section for $e^+e^- \rightarrow \mu^+\mu^-$ process.

KORALB and KK2f[3] are the simulation packages for e^+e^- $\rightarrow$ lepton pair events. KORALB does not contain initial state radiation and final state radiation corrections beyond

order of α^2 although it includes the interference between initial and final state radiation. KK2f attempts to include orders up to α^3. Thus, at least for photon radiation events, KK2f is expected to show better agreement with data than KORALB does. This has been checked in my analysis.

EvtGen is an event generator designed for the simulation of the physics of B decays as well as $u\bar{u}$, $d\bar{d}$, $s\bar{s}$ and $c\bar{c}$ events. It is especially useful in complex sequential decays such as semileptonic decays and CP violating decays. To study the effects of uds and $c\bar{c}$ background contamination, we used EvtGen configured with Jetset for $e^+e^- \to q\bar{q}$[4].

2.2 $e^+e^- \to \tau^+\tau^-\gamma$ process in the Standard Model

The Feynman diagram in figure 2.2 shows one of the possible diagrams for the $e^+e^- \to \tau^+\tau^-\gamma$ process. It is also possible for τ^+ to decay in exactly same way but with opposite charge. The tau lepton can decay in many other ways. $\tau^- \to \nu_\tau\bar{\nu}_\mu\mu^-$ decay probability is about 18% of total possible decay mode of τ^-. The invariant mass of $\nu_\tau\bar{\nu}_\mu\mu^-$ is the rest mass of τ^- particle because the τ^- is an on-shell particle:

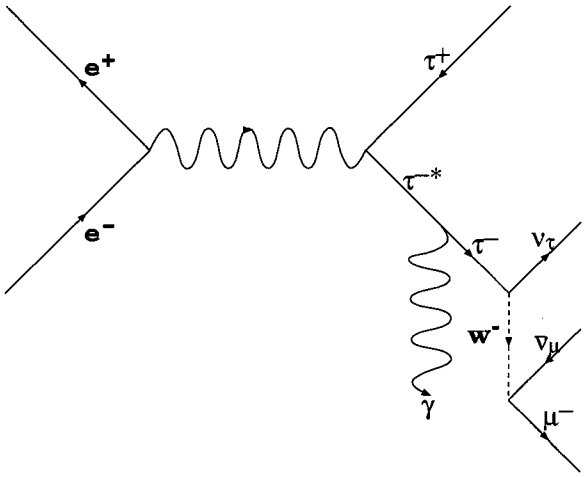

Figure 2.2: $e^+e^- \to \tau^+\tau^-\gamma$ in the Standard Model

$$(E_{\mu^-} + E_{\bar{\nu}_\mu} + E_{\nu_\tau})^2 - (\vec{P}_{\mu^-} + \vec{P}_{\bar{\nu}_\mu} + \vec{P}_{\nu_\tau})^2 = m_{0\tau}^2.$$

The invariant mass of $\nu_\tau\bar{\nu}_\mu\mu^-\gamma$ is different from the rest mass of τ particle, because τ^{-*} is an off-shell particle:

$$(E_{\mu^-} + E_{\bar{\nu}_\mu} + E_{\nu_\tau} + E_\gamma)^2 - (\vec{P}_{\mu^-} + \vec{P}_{\bar{\nu}_\mu} + \vec{P}_{\nu_\tau} + \vec{P}_\gamma)^2 = m_{\tau^*}^2$$

This holds for any reference frame. If a photon is radiated by an initial particle (in this case e^+ or e^-), it is called initial state radiation (ISR). If a photon is radiated by a final

resulting particle (in this case τ^+ or τ^-), it is called final state radiation (FSR). In the $e^+e^- \rightarrow \tau^+\tau^-\gamma$ process, if there is high energy ISR, the energy of each tau lepton would be less than it would be without ISR. The invariant mass of a set of final particles is relatively insensitive to the ISR. In the $e^+e^- \rightarrow \tau^+\tau^-\gamma$ process, if there is a high energy FSR from one of the τ's , then the τ^* particle is an off shell particle which has no particular value of invariant mass(=rest mass). Thus the invariant mass of this photon combined with any other particle would not peak at specific value (for example rest mass of μ, τ,...) and the energy of one τ is not the same as the energy of the other τ. Moreover, the momentum of one tau can be any value from 0 to $E_{cm} - 2m_\tau$. Therefore the invariant mass of the μ and γ ($m_{\mu\gamma}$) in Figure 2.2 mode would not peak at a specific value (such as m_{τ_0}) and $E_{\mu\gamma}$ would not peak any specific value if the energy of FSR is high enough. Even if the energy of FSR is low in Figure 2.2, $m_{\mu^-\gamma}$ would not peak at m_{τ_0} because the minimum energy of two neutrinos is too big to be ignored. If the energy of FSR is low enough, the τ^{-*} will have approximately half of the beam energy:

$$E_{\mu\gamma} + E_{\bar{\nu}_\mu} + E_{\nu_\tau} \simeq E_{beam}/2$$

Because the energy of neutrinos can be arbitrary($> E_{\nu_{min}}$), $E_{\mu\gamma}$ does not peak at a specific value. However if the energy of FSR is low and two neutrinos have the minimum energy, then $E_{\mu\gamma}$ would be just below the half of the beam energy.

To answer the minimum effect of the neutrinos to this study, let's find the minimum energy of two neutrinos in Figure 2.2 mode when the energy of FSR is small:

$$(E_\mu + E_\nu)^2 - (\vec{P}_\mu + \vec{P}_\nu)^2 = m_{\tau_0}^2$$

where ν means $\bar{\nu}_\mu\nu_\tau$.

Because we want minimum value of E_ν satisfying this equation,

$$(E_\mu + E_\nu)^2 - (|\vec{P}_\mu| - |\vec{P}_\nu|)^2 = m_{\tau_0}^2$$

$$(E_\mu + E_\nu)^2 - (P_\mu - E_\nu)^2 = m_{\tau_0}^2$$

$$(E_\mu + E_\nu + P_\mu - E_\nu)(E_\mu + E_\nu - P_\mu + E_\nu) = m_{\tau_0}^2$$
$$(E_\mu + P_\mu)(E_\mu - P_\mu + 2E_\nu) = m_{\tau_0}^2$$
$$E_\mu^2 - P_\mu^2 + 2E_\nu(E_\mu + P_\mu) = m_{\tau_0}^2$$
$$E_{\nu min} = \frac{m_{\tau_0}^2 - m_{\mu_0}^2}{2(E_\mu + P_\mu)}$$

In the center of momentum frame at BaBar the beam energy, E_μ, can be up to 5.28GeV. So if the energy of FSR is small, $E_{\nu min} \simeq 150$MeV.

Therefore, in general, invariant mass of μ and γ in 2.2 does not peak at m_{τ_0} and $E_{\mu\gamma}$ also does not peak at any specific value. $m_{\mu\gamma}, E_{\mu\gamma}$ values are spread over all kinematically possible values.

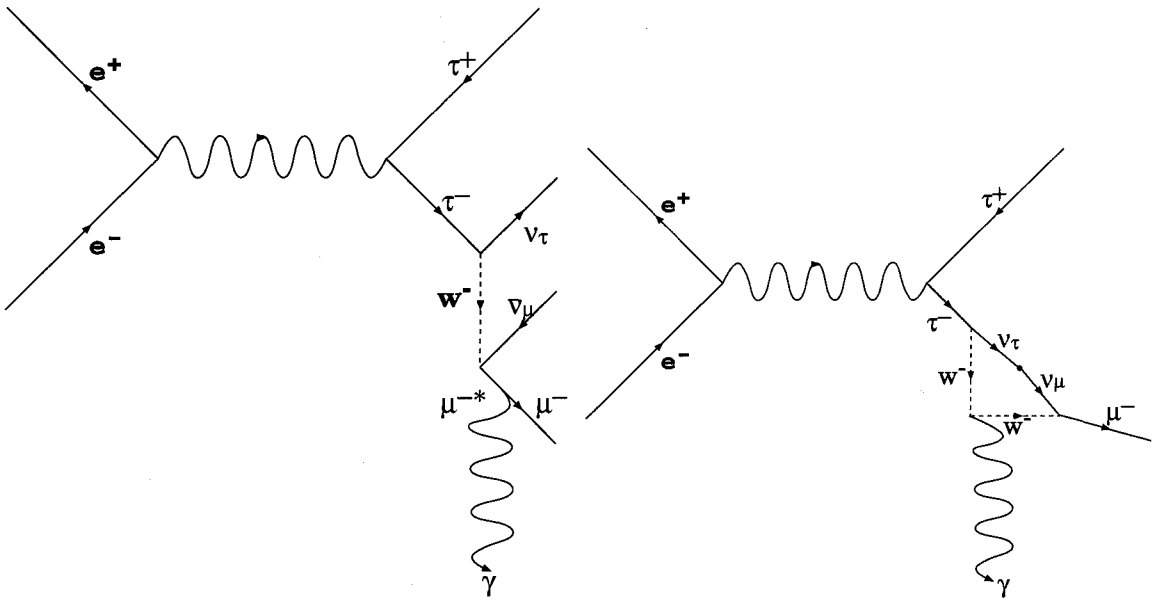

(a) In the Standard Model (b) Neutrino oscillation in the Standard Model

Figure 2.3: Standard Model processes

Figure 2.3 (a) shows another possible decay mode of τ. Here, the τ^- is an on-shell

particle because the photon comes from τ^- decay and so:

$$(E_{\mu^-} + E_{\bar{\nu}_\mu} + E_{\nu_\tau} + E_\gamma)^2 - (\vec{P}_{\mu^-} + \vec{P}_{\bar{\nu}_\mu} + \vec{P}_{\nu_\tau} + \vec{P}_\gamma)^2 = m_{\tau_0}^2$$

$$E_{\mu^-} + E_{\bar{\nu}_\mu} + E_{\nu_\tau} + E_\gamma = \frac{E_{beam}}{2}.$$

Because the energy of neutrino can be arbitrary ($E_\nu > 0$) in 2.3 (a), the $m_{\mu\gamma}$ and $E_{\mu\gamma}$ do not peak at specific values. If the energy of two neutrinos is tiny, then invariant mass of the $\mu\gamma$ system would be the rest mass of the τ and the energy of the $\mu\gamma$ system would be half of the beam energy.

$$\left.\begin{array}{l} m_{\mu\gamma} = m_{\tau_0} \\ E_{\mu\gamma} = \frac{E_{beam}}{2} \end{array}\right\} \text{if } E_{\bar{\nu}_\mu} + E_{\nu_\tau} \to 0$$

Thus, in general in the Standard Model decay of the τ, $m_{\mu\gamma}$ and $E_{\mu\gamma}$ do not peak at specific values. They show a smooth distribution over all kinematically possible values. But even though $m_{\mu\gamma}$ and $E_{\mu\gamma}$ do not peak at specific values, they can have values of m_{τ_0} and $E_{beam}/2$ by chance.

In the Standard Model lepton flavor is always conserved in every decay mode. But recent research indicates that the neutrino has mass and that it can change its lepton flavor. So in addition to $\tau^- \to \nu_\tau \bar{\nu}_\mu \mu^-$ decay, $\tau^- \to \mu^- \gamma$ decay is also possible via flavor change of $\nu_\tau \to \nu_\mu$. But this is a loop mode decay not a tree mode decay, Figure 2.3 (b), and the Standard model predicts that the branching ratio of this loop decay mode is too small to be measured in our sample(the branching ratio is expected at less than 10^{-50}). Thus we can ignore this rare decay mode in our consideration.

2.3 $e^+e^- \rightarrow \tau^+\tau^-\gamma$ process in new physics

The ultimate goal of this research is to discover experimental evidence of direct $\tau^- \rightarrow \mu^-\gamma$ decay, which would indicate the presence of physics beyond the Standard Model. In this process the photon comes from τ decay and so the invariant mass of μ, γ must peak at m_{τ_0} and $E_{\mu\gamma}$ must peak at the half of the beam energy in center of momentum frame. If we compare a "new physics" event(2.4) to a Standard Model event(2.2 2.3 (a)) we know that we measure the same detectable particles (μ, γ) because we cannot directly detect neutrinos by experiment. The problem is to distinguish μ^-, γ Standard Model events(2.2 2.3 (a)) from a "new physics" event(Figure 2.4).

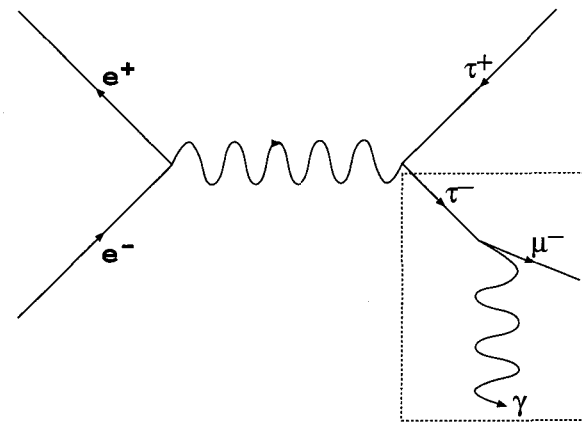

Figure 2.4: "New physics" process. Lepton number is not conserved from tauon lepton number to muon lepton number. Invariant mass of $\mu^-\gamma$ is the the rest mass of τ

2.4 Detecting direct $\tau^- \rightarrow \mu^-\gamma$ decays

In any process containing a $\mu\gamma$ system we can define invariant mass of μ, γ

$$m^2_{\mu\gamma} \equiv (E_\mu + E_\gamma)^2 - (\vec{P}_\mu + \vec{P}_\gamma)^2 = E^2_\mu + E^2_\gamma + 2E_\mu E_\gamma - (\vec{P}^2_\mu + \vec{P}^2_\gamma + 2|\vec{P}_\mu||\vec{P}_\gamma| cos(\theta_{\mu\gamma}))$$

If in the CM system $E^{CM}_\mu \gg m_{\mu_0}$, $E^{CM}_\mu \simeq |\vec{P}^{CM}_\mu|$

then

$$\begin{aligned} m^2_{\mu\gamma} &\approx 2E^{CM}_\mu E^{CM}_\gamma (1 - cos(\theta^{CM}_{\mu\gamma})) \\ &= 2(E^{CM}_{Tot}/2 - E^{CM}_\gamma) E^{CM}_\gamma (1 - cos(\theta^{CM}_{\mu\gamma})) \\ &= (E^{CM}_{Tot} - 2E^{CM}_\gamma) E^{CM}_\gamma (1 - cos(\theta^{CM}_{\mu\gamma})) \end{aligned} \quad (2.1)$$

and is distributed as in Figure 2.5 (b) in the new physics process.

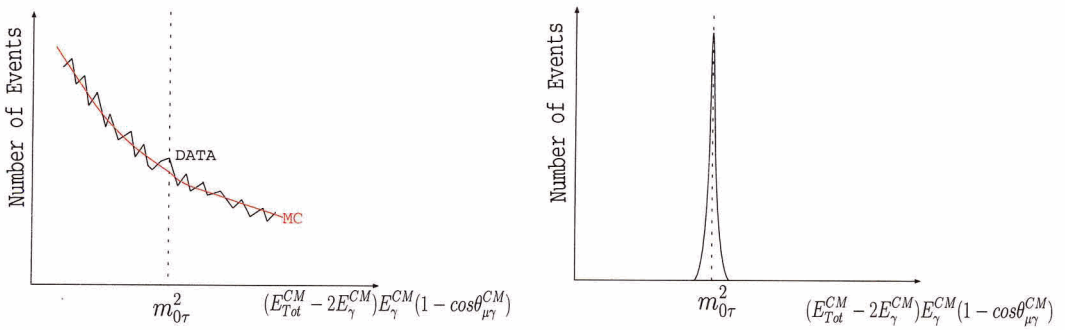

(a) Standard model events

(b) In new physics process(without ISR, Figure 2.4)

Figure 2.5: Standard model events and new physics events. They show different distribution of $(E^{CM}_{Tot} - 2E^{CM}_{\gamma})E^{CM}_{\gamma}(1 - cos(\theta^{CM}_{\mu}\gamma))$

In the Standard Model we can express invariant mass of μ^-, γ by

$$m^2_{\mu\gamma} = E^2_{\mu} + E^2_{\gamma} + 2E_{\mu}E_{\gamma} - (\vec{P}^2_{\mu} + \vec{P}^2_{\gamma} + 2|\vec{P}_{\mu}||\vec{P}_{\gamma}|cos(\theta_{\mu\gamma}))$$

But in the Standard Model events, E^{CM}_{γ} and $\theta^{CM}_{\mu\gamma}$ are not directly related quantities. They are also related to other possible arbitrary quantities such as $E_{\bar{\nu}_{\mu}}, E_{\nu_{\tau}}$. So $(E^{CM}_{Tot} - 2E^{CM}_{\gamma})E^{CM}_{\gamma}(1 - cos(\theta^{CM}_{\mu}\gamma))$ will not give a preferred value as in Figure 2.5 (a). It will show a smooth distribution in the Standard Model events.

If neutrino flavor oscillation processes(Figure 2.3 (b)) happen then the calculation of

$$(E^{CM}_{Tot} - 2E^{CM}_{\gamma})E^{CM}_{\gamma}(1 - cos(\theta^{CM}_{\mu}\gamma)) \tag{2.2}$$

will be $m^2_{\tau_0}$. But this kind of Standard Model events happen very rarely so it will not affect the smooth distribution of Standard Model events.

If the $m^2_{\mu\gamma}$ distribution of data shows a significant enhancement around $m^2_{\tau_0}$ compare to MC as shown in Figure 2.6(a), we can confidently say new physics events are really present along with Standard Model events.

However, if the distribution of data shows a small distortion around $m^2_{\tau_0}$ compared to MC

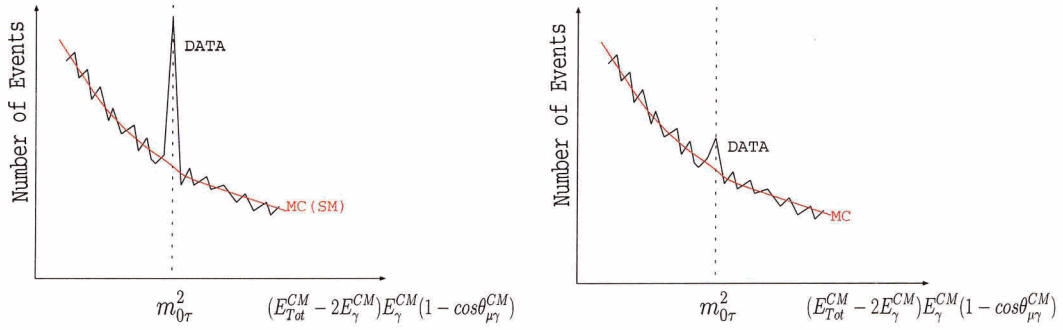

(a) Standard model events + new physics events

(b) Standard model events + ?new physics event?

Figure 2.6: Standard model + new physics. In the case of distribution (b), we can give the upper limit of branching ratio of new physics events.

as shown in Figure 2.6(b), we cannot say confidently new physics events occurred. But we also cannot say new physics events didn't happen. In this case we can give the upper limit of branching ratio of new physics events. Even if we cannot discover clear evidence of new physics events, it is still meaningful to give the upper limit as this rules out some theories that are beyond the Standard Model.

In order to have confidence in the Monte Carlo simulations of the $\tau \rightarrow \mu\gamma$ signal and Standard Model background, we need to ensure that QED is adequately described by the Monte Carlo generator. This work uses $e^+e^- \rightarrow \mu^+\mu^-(\gamma)$ events to do so.

2.5 τ lifetime measurement

This work is also helpful for the τ lifetime measurement being performed[20]. In the $e^+e^- \rightarrow \tau^+\tau^-(\gamma)$ process, usually the τ decays to other particles within detector. If we know average momentum of the τ and we measure its average decay length, we can calculate τ lifetime:

$$< t^{CM}_{\tau \text{ life}} >= \frac{< d^{CM} >}{< v^{CM} >} = \frac{< d^{CM} >}{c\beta^{CM}}$$

$$t^{proper}_{\tau \text{ life}} = \frac{< t^{CM}_{\tau \text{ life}} >}{\gamma} = \frac{< d^{CM} >}{c\gamma\beta^{CM}} = \frac{< d^{CM} > m_{\tau_0}}{< P^{CM} >}$$

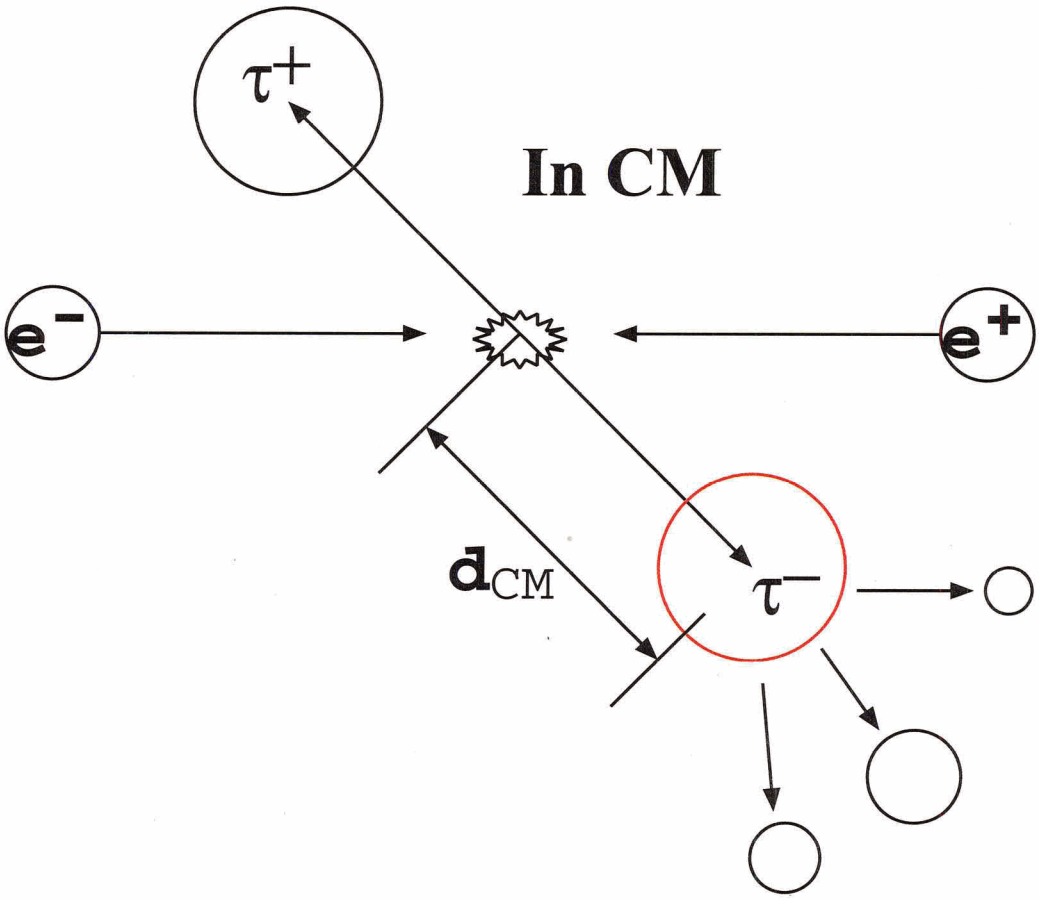

Figure 2.7: τ decay in the CM

The momentum of the τ depends on the radiation, and since we use the Monte Carlo simulator to get the average τ momentum, it is important to know how well the Monte Carlo describes the radiation.

2.6 KK2f and KORALB

Before we compare real data to MC, we have to be able to say confidently that "The Monte Carlo simulation adequately describes the Standard Model(Figure 2.2)." In this research, it means that the Monte Carlo must calculate $E_{\mu}^{CM}, E_{\gamma}^{CM}, \theta_{\mu\gamma}^{CM}$ of Standard Model event (Figure 2.2) to sufficient precision for the requirement of the measurements.

We consider two Monte Carlo generators: KK2f and KORALB. Both can produce $e^+e^- \rightarrow \tau^+\tau^-\gamma$ and $e^+e^- \rightarrow \mu^+\mu^-\gamma$ Standard Model events. We believe that there is no new physics for $e^+e^- \rightarrow \mu^+\mu^-\gamma$ events in our data. We believe that $e^+e^- \rightarrow \mu^+\mu^-\gamma$ events are perfectly described by the Standard Model. So $e^+e^- \rightarrow \mu^+\mu^-\gamma$ events can be a good data sample to determine how well the Monte Carlo software describes the Standard Model. To put it concretely, we can check whether the Monte Carlo software can produce $E_{\mu}^{CM}, E_{\gamma}^{CM}, \theta_{\mu\gamma}^{CM}$ distributions in $e^+e^- \rightarrow \mu^+\mu^-\gamma$ events that reproduce those we have in the data. To do this job we have to compare data and Monte Carlo generated by KK2f and KORALB for $E_{\mu}^{CM}, E_{\gamma}^{CM}, \theta_{\mu\gamma}^{CM}$ of $e^+e^- \rightarrow \mu^+\mu^-\gamma$ events.

In KK2f and KORALB the algorithm to generate $e^+e^- \rightarrow \tau^+\tau^-\gamma$ events is exactly same as the algorithm to generate $e^+e^- \rightarrow \mu^+\mu^-\gamma$ once the mass difference between τ and μ is also taken into account. Thus if we make sure right side of the Figure 2.8 Standard Model QED process(especially about $E_{\mu}^{CM}, E_{\gamma}^{CM}, \theta_{\mu\gamma}^{CM}$) is described perfectly by KK2f, we can also say $e^+e^- \rightarrow \tau^+\tau^-\gamma$ Standard Model QED process (inside red dash line on left side of 2.8) is also well described by KK2f. Then we can say "$E_{\mu\gamma}, m_{\mu\gamma}$ and $(E_{beam}^{CM} - 2E_{\gamma}^{CM})E_{\gamma}^{CM}(1 - cos(\theta_{\mu}^{CM}\gamma))$ calculated from the $E_{\mu}^{CM}, E_{\gamma}^{CM}, \theta_{\mu\gamma}^{CM}$ information in $e^+e^- \rightarrow \tau^+\tau^-\gamma$ Standard Model QED processes are well described by KK2f".

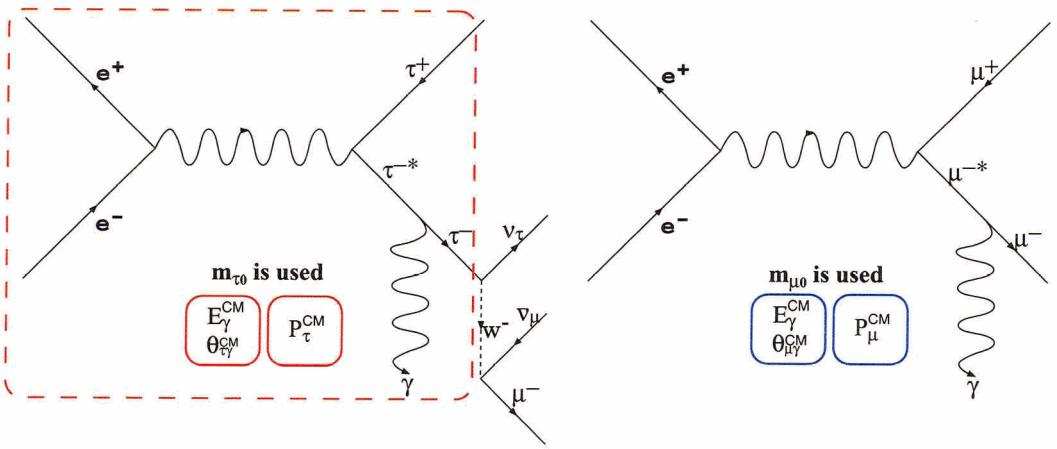

Figure 2.8: Comparing two MC. $e^+e^- \to \tau^+\tau^-\gamma$ process inside the red dashed line follows the same MC algorithm as $e^+e^- \to \mu^+\mu^-\gamma$ process.

Chapter 3

APPARATUS:BABAR & PEP-II

3.1 The BaBar experiment

BaBar is investigating the mystery of why there is more matter than antimatter in the universe. This asymmetry indicates that the laws of physics must be asymmetric too. It means charge conjugation-parity (CP) symmetry relating matter and antimatter must be violated.

In 1964 a small CP violation was observed using K mesons (K^0 meson has $d\bar{s}$ quarks). But CP violation of K mesons does not fully constrain the matter-antimatter asymmetry parameters of the Standard Model. The BaBar experiment gives more constraints to matter-antimatter asymmetry parameters using neutral B mesons (B^0 meson has $d\bar{b}$ quarks). If there is an asymmetry between matter and antimatter, it will reveal subtle differences between B^0 and $\bar{B}^0$ decays as a function of decay time.

In the late 1980s, it was known that the way to get the best source of B mesons for a CP asymmetry study is from e^+e^- collisions at the $\Upsilon(4s)$ resonance energy but with asymmetric energies of the e^+ and e^- beams. If we collide e^+e^- with symmetric beam energies, the resulting B mesons are almost at rest, making it hard to measure decay length of B meson. But if we collide e^+e^- with asymmetric energies we can get B mesons with significant momentum in the laboratory frame. So it is relatively easy to measure decay length of the B meson, which is related to the decay time. Out of all decay modes of B meson, less than

0.01% of them are useful for measuring CP asymmetry. Since the branching ratio is so small($\sim 10^{-5}$) we need more than 10^7 B meson pairs to observe CP asymmetries with error less than 10%.

The BaBar detector was designed and optimized primarily to study CP violation of B meson; In addition to that we can study a number of rare decays of B meson. Since PEP-II also produces large numbers of τ pairs, it is also a good resource to study τ physics. My research will ultimately contribute to one of τ physics studies, lepton flavor violating τ decay. BaBar uses SLAC linear accelerator to get high energy e^+e^- beam. PEP-II B factory is used to force these high energy e^+ and e^- particles to collide with each other.

3.2 Slac linear accelerator

BaBar uses the SLAC linear accelerator(linac) to get high energy e^+e^- beams [6]. It is a 3.2km long accelerator. The linear accelerator accelerates charged particles in a straight line by means of radio frequency oscillating electric fields. The passage of the charged particle is synchronized with the phase of the accelerating field.

3.3 PEP-II

Electrons and positrons from SLAC accelerator are extracted when they reach the correct energy and are then transported in dedicated bypass lines and injected into PEP-II storage rings (PEP stands for Positron Electron Project). The vacuum pipe rings are located one on top of the other. 9GeV electrons go clockwise around the lower ring which is an upgrade of the older PEP storage ring. 3.1GeV positrons go counterclockwise around the newly built upper ring. Electrons and positrons from the SLAC accelerator are extracted when they reach the correct energy and are then transported in dedicated bypass lines and injected into the PEP-II rings.

PEP-II has surpassed its design goals of the instantaneous luminosity($3 \times 10^{33} cm^{-2} s^{-1}$).

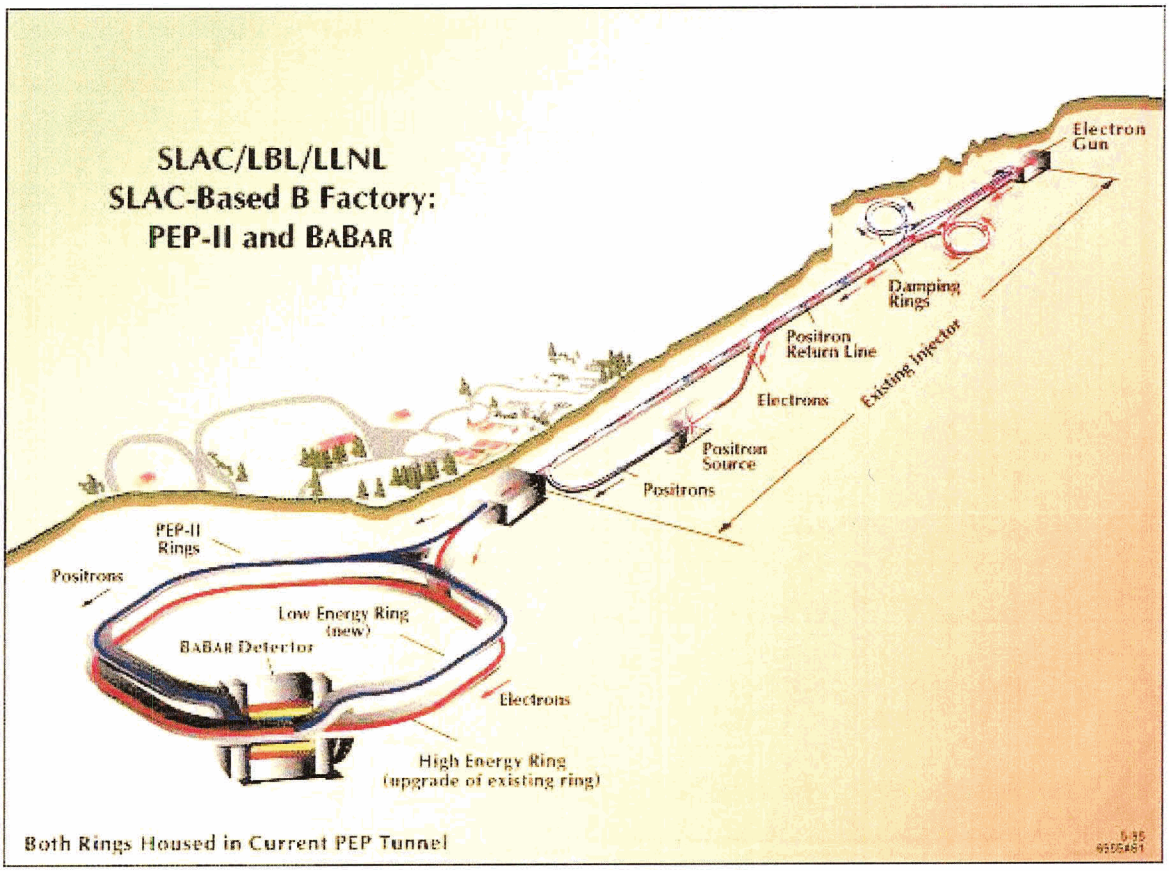

Figure 3.1: SLAC linear accelerator and PEP-II rings[7]

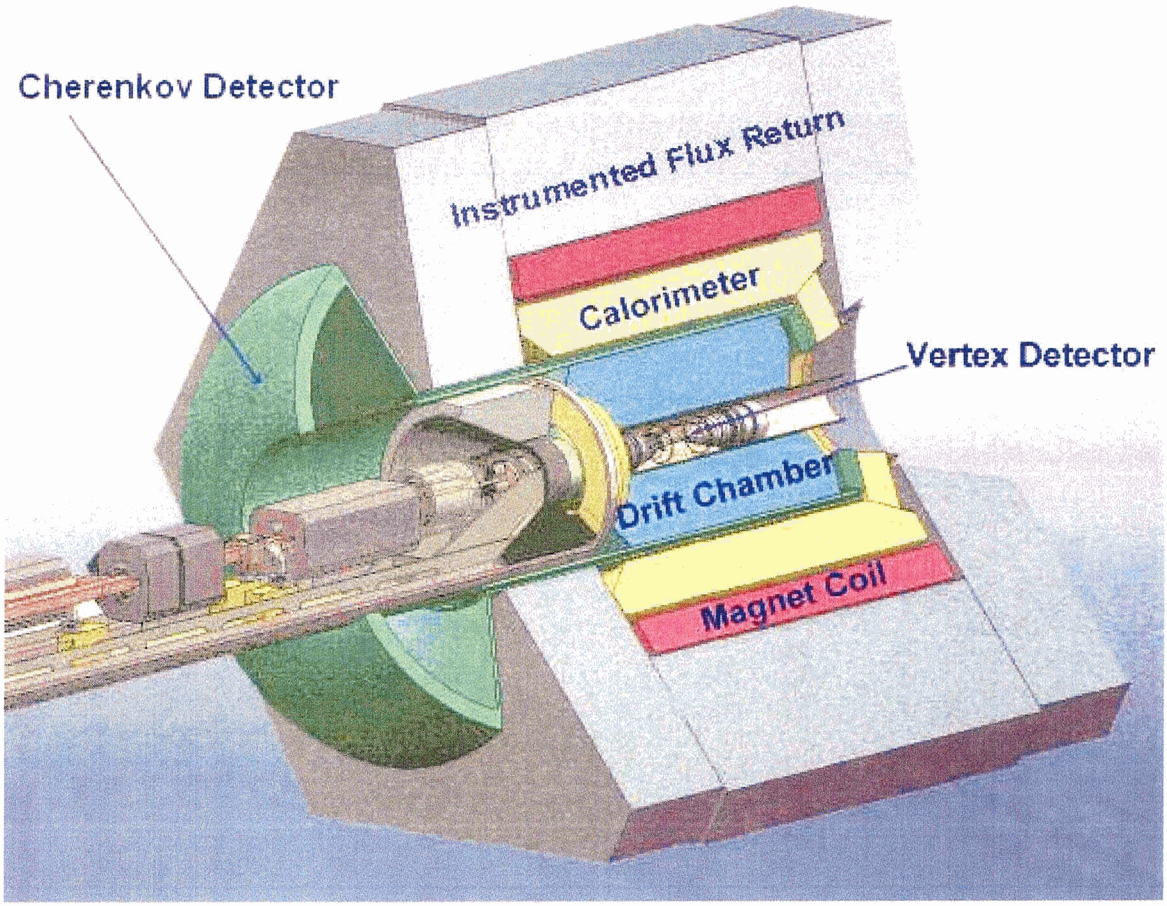

Figure 3.2: Cross section of BaBar detector showing inner components

PEP-II typically operate on a 40∼50 minute fill cycle. Data from BaBar is divided into runs. One run typically corresponds to 30∼60 minutes long. During that time beam and detector conditions are expected to be stable. 12% of data are taken at a center of mass energy 40MeV lower than the energy of the peak of the $\Upsilon(4s)$ resonance. It allows non-resonant background study.

3.4 Detector

Figure 3.2 shows the cross section of BaBar detector. We will describe each component from the inner part. Details of the detector are described in [6]. Figures in this chapter

were obtained from [7].

3.4.1 SVT(Silicon Vertex Tracker)

The Silicon Vertex Tracker (SVT) is designed to measure the trajectory of charged particle and decay vertices just outside the beam pipe. The SVT is made of five layers of double-sided silicon strip detectors. An SVT strip operates as a p-n junction diode.

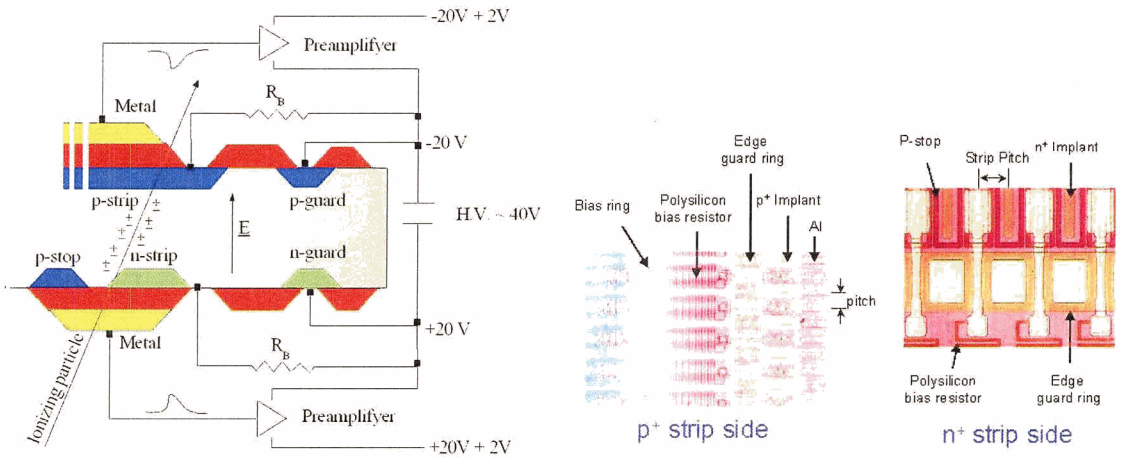

(a) (b)

Figure 3.3: SVT strips. A charged particle passing depletion region between p-type and n-type strips induce drift current.

In the SVT, to create minority carriers, instead of thermal excitation of valence band electrons of silicon, we shoot charged particles though the semiconductor. When a charged particle passes through the depletion region between p-type and n-type strips, it will knock off electrons. This creates about 24,000 electron-holes pairs to generate a drift current. Because of a high reverse bias, the diffusion current is highly suppressed. As a result of drift current, holes are attracted to the p-strip and electrons are attracted to the n-strip. These electrons and holes induce current on the strip. Then we detect this current to check whether a charged particle passed through that strip or not.

Phi strips run parallel to the beam axis. Z strips run circumferentially across the width

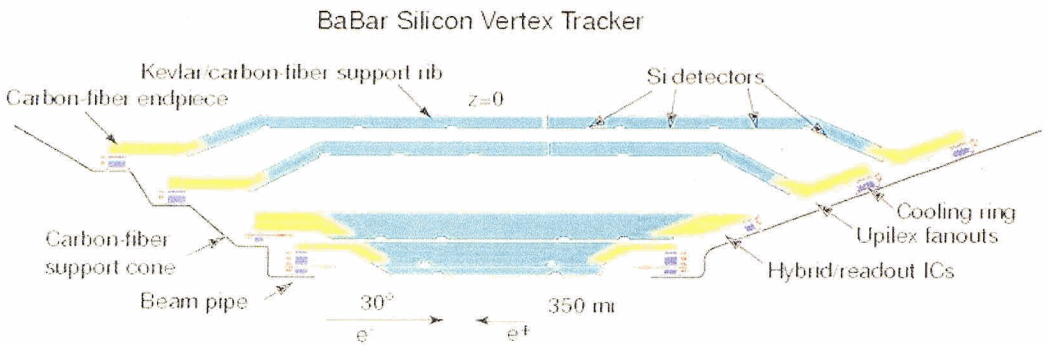

Figure 3.4: Cross section of silicon vertex tracker. Each layer is shown.

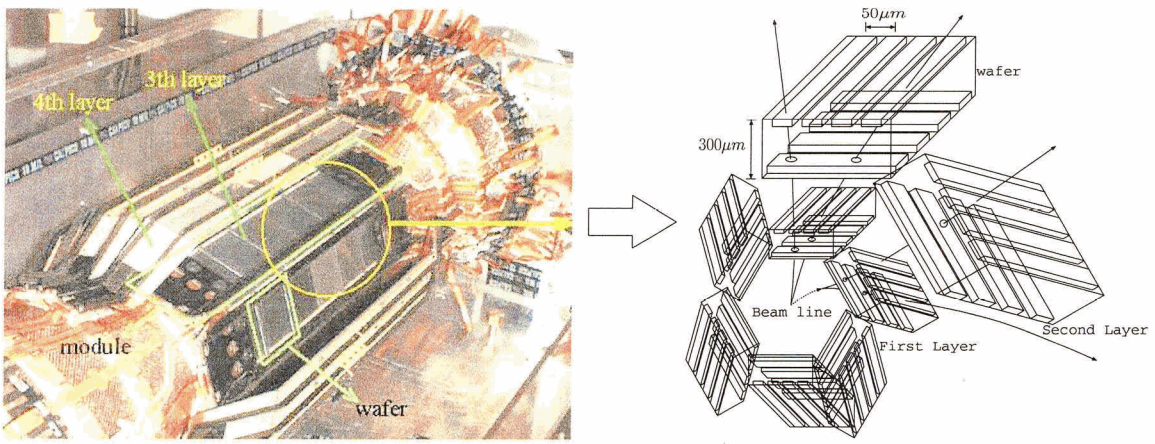

(a) Layers, Modules, Wafers

(b) Wafer(In fact there are much more strips for each wafer)

Figure 3.5: Structure of SVT

of one module. Layer 1, 2, 3 use the n-side of the silicon for phi strip, and p-side for Z strips. Layer 4 and 5 use the p-side of the silicon for phi strips and n-side for Z strips. All five layers can be used to measure the position and angle information of charged particles. Especially, the position and angle information of charged particle by the inner three layers is used to measure the vertex position. We can detect particles passing through the silicon strip by each silicon strip detector. Because the strips on both sides are orthogonal, each other and strips are close together ($50\mu m-100\mu m$ pitch for layers 1, 2 and 3 and $80\mu m-210\mu m$ pitch for layers 4 and 5 for the phi pitch; $100\mu m$ pitch for layers 1, 2 and 3 and $210\mu m$ pitch for layers 4 and 5 for the z pitch) we can measure the position where the charged particle passes very precisely. The resolution is $10\mu m-15\mu m$ for layers 1, 2 and 3 and $30\mu m-40\mu m$ for layers 4 and 5.

By connecting these positions on each layer we can reconstruct the trajectory of the charged particles. We know that charged particles are not often created alone. So when we project them back, then two or more trajectories meet at single point and we can conclude that two or more charged particles are created at that point. This is the vertex point.

If we found the vertex is in the region where two incident electron, positron bunches are overlapped it means the created particles comes directly from the electron-positron collision energy. If we found the vertex is outside of the collision region, it means a very short lived particle was created in collision region and then decayed to charged particles at the vertex point. By this method we can determine whether or not an unstable particle was created. The inner three layers are installed very close to the beam pipe to minimize the effect of multiple scattering in the beam pipe. The outer two layers are near the main support tube to give the trajectory information which is to be linked with drift chamber(DCH) tracks.

3.4.2 DCH(Drift Chamber)

The drift chamber is the device used to measure the trajectory of charged particles(in order to measure the momentum of charged particles) by using gas ionization.

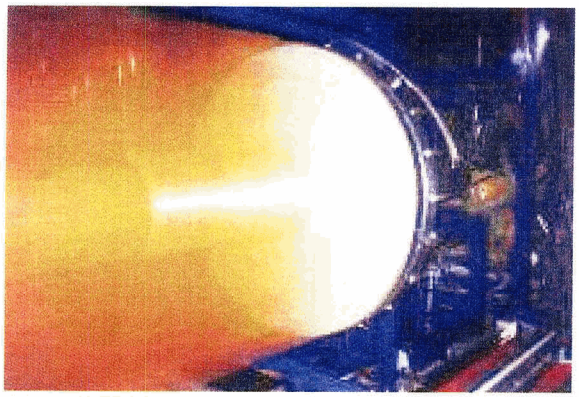

(a) BaBar DCH

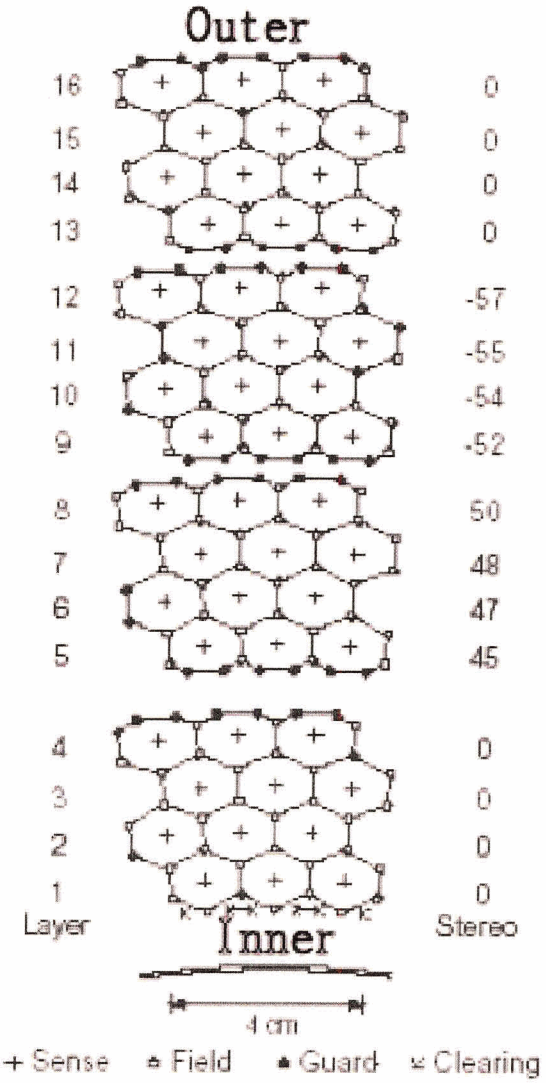

(b) Cross section of DCH showing the geometry of the wires in the xy plane.r_{inner}=261mm, r_{outer}=780mm

Figure 3.6: Drift chamber schematic

It has 40 layers of small hexagonal cells which give the trajectory information of up to 40 points about ionization loss for charged particles having transverse momentum greater than 180 MeV/c. Each cell has one sense wire surrounded by six field wires. We supply the nominal operating voltage of 1960 V to the sense wires. A total of 28,768 wires connect two aluminium plates which have precisely positioned holes through which the wires are passed and fastened. The chamber is filled with helium(He)-isobutane C_4H_{10} gas mixture with 80:20 % ratio. Because we want to minimize the multiple scattering inside the DCH we choose light wires and a helium based gas mixture.

When a charged particle passes through the C_4H_{10} gas, it ionizes the gas. The high voltage sense wire attracts released electrons. On the way to the sense wire, released electrons further ionize the C_4H_{10} gas and generate more electrons. This cascade of electrons is attracted to the sense wire. A large electronic signal is produced mainly as the ions drift away from the wire.

The sense wires in layers are set to connect two aluminium plates at three different angles. Any three sense wires are only nearby at one spot so the set of sense wires responding to electronic signals gives the information of the trajectory of charged particles passing that sense wire. Thus we can get the information about the three dimensional trajectory of charged particles. If the decay happens outside of SVT we can reconstruct the track only by information from DCH. On the boundary inside the layer 1, and on the boundary outside the layer 40, there are two clearing wires for each cell to collect charges created by photon conversions in the walls.

It takes some time for ionized electrons arriving to the nearest sense wire from the place where the charged particle ionizes an atom. By measuring this drift time we can determine the location of the original trajectory much more precisely than the actual spacing between the sense wires. The drift chamber measures particles trajectory with an average 90 μm hit position resolution along the transverse drift direction.

Since particles move in a strong magnetic field of 1.5 T aligned approximately parallel to the beam direction they draw a curved trajectory in the plane transverse to the beam axis. By measuring this curvature we can calculate the transverse momentum of charged particles. To know the total momentum of charged particles we should know the longitudinal momentum, z component of the momentum, too. By arranging some wires to have small angle with the Z-axis, we can determine the longitudinal trajectory of charged particles with a resolution of about 4 mm. Then we can find the angle between longitudinal trajectory and the Z-axis. With this angle information along with the transverse momentum information from the transverse curvature, we can calculate total momentum of the charged particles.

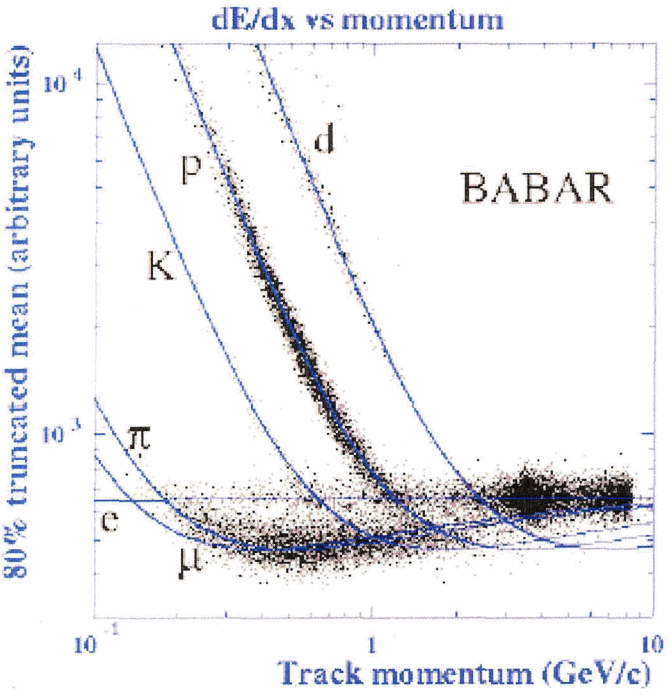

Figure 3.7: Measurement of dE/dX versus momentum of charged particles. Curve lines are the Bethe-Bloch predictions.

If we measure the total charge deposited in each drift cell, we can calculate the specific energy loss, dE/dX, of charged particles. As we can see in the Figure 3.7, we can identify the low momentum particles by measuring ionization loss dE/dX. A resolution of about 7% is enough to distinguish π from K up to 0.7 GeV/c.We can also distinguish π from K in

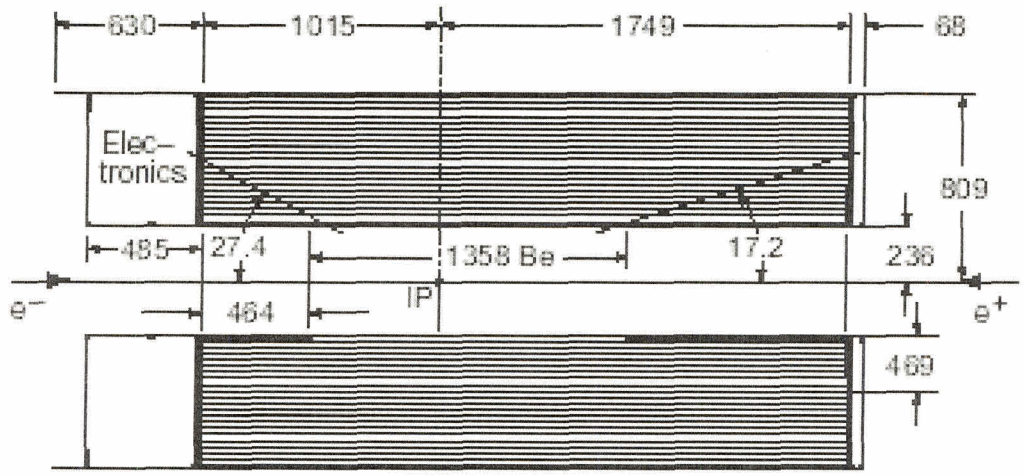

Figure 3.8: Longitudinal cross section of DCH

the DIRC (Detection of Internally Reflected Cerenkov Light). But only if they have large enough momentum. Very low momentum charged particles make a small curvature inside the DCH so they cannot reach the DIRC.

Figure 3.8 shows a longitudinal cross section of DCH. The forward length 1749 mm from the collision point is chosen so that particles emitted at 17.2° pass half of the layers. The backward length 1015 mm is chosen so that particles emitted at 27.4° pass half of the layers. This choice is good enough to detect forward going tracks. The inner cylindrical wall is made thin for easy linking of SVT and DCH tracks, to improve the track resolution for high momentum tracks and to minimize the background from photon conversions and interactions. The outer wall and material in the forward direction is also minimized so as not to degrade the performance of EMC and DIRC.

3.4.3 DIRC(Detection of Internally Reflected Cerenkov Light)

The drift chamber cannot distinguish clearly π from K with momentum greater than 0.7 GeV/c. DIRC is a device designed to measure the velocities of charged particles (e,μ, p,π, K). All other charged particles are too short-lived to reach DIRC without decaying. DIRC

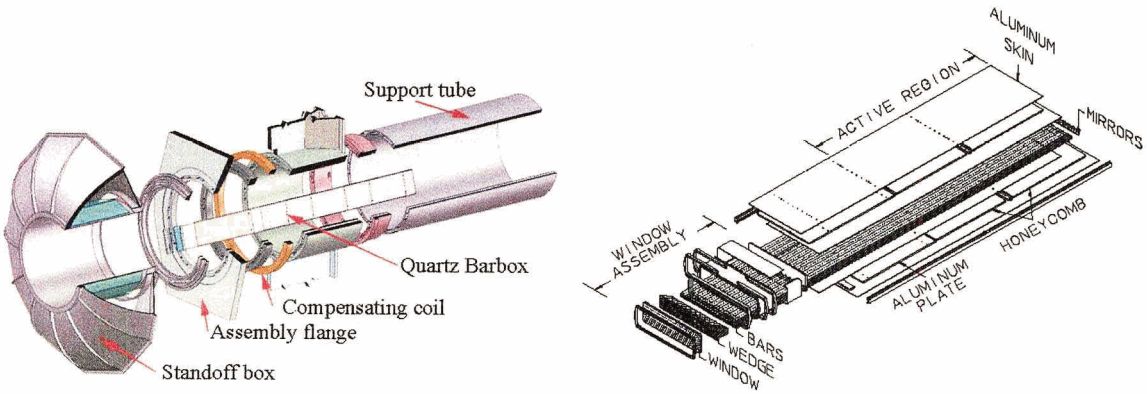

(a) Components of DIRC

(b) Components of Bar box

Figure 3.10: DIRC Components

is useful for measuring particles with momentum from about 0.5 GeV/c to the kinematic limit of 4.5 GeV/C.

If a charged particle travels in a medium faster than the speed of light in that medium, it generates a wave front of Cerenkov light. If we measure the θ in Figure 3.9, we can calculate the velocity of the charged particle. Together with the momentum given by DCH, we can calculate the mass of the charged particle. Therefore we can know what kind of particle we are observing. Figure 3.10 shows the components of the DIRC.

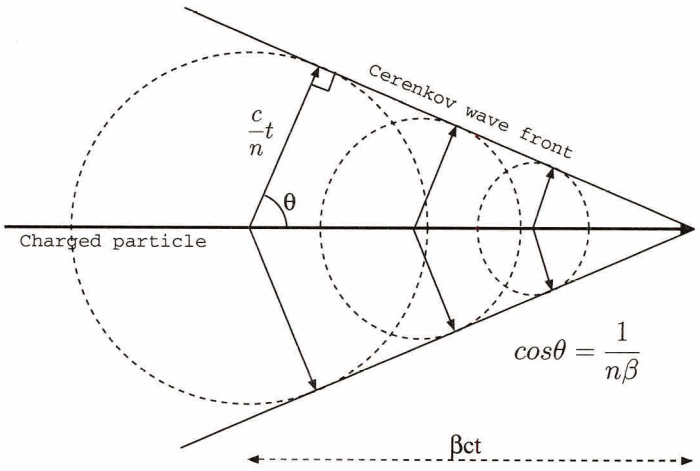

Figure 3.9: Generation of Cerenkov light by a charged particle

A bar box containing 12 quartz bars are shown in Figure 3.10. 12 bar boxes are arranged in 12 sided polygon around the beam line. Figure 3.11 shows how the DIRC works.

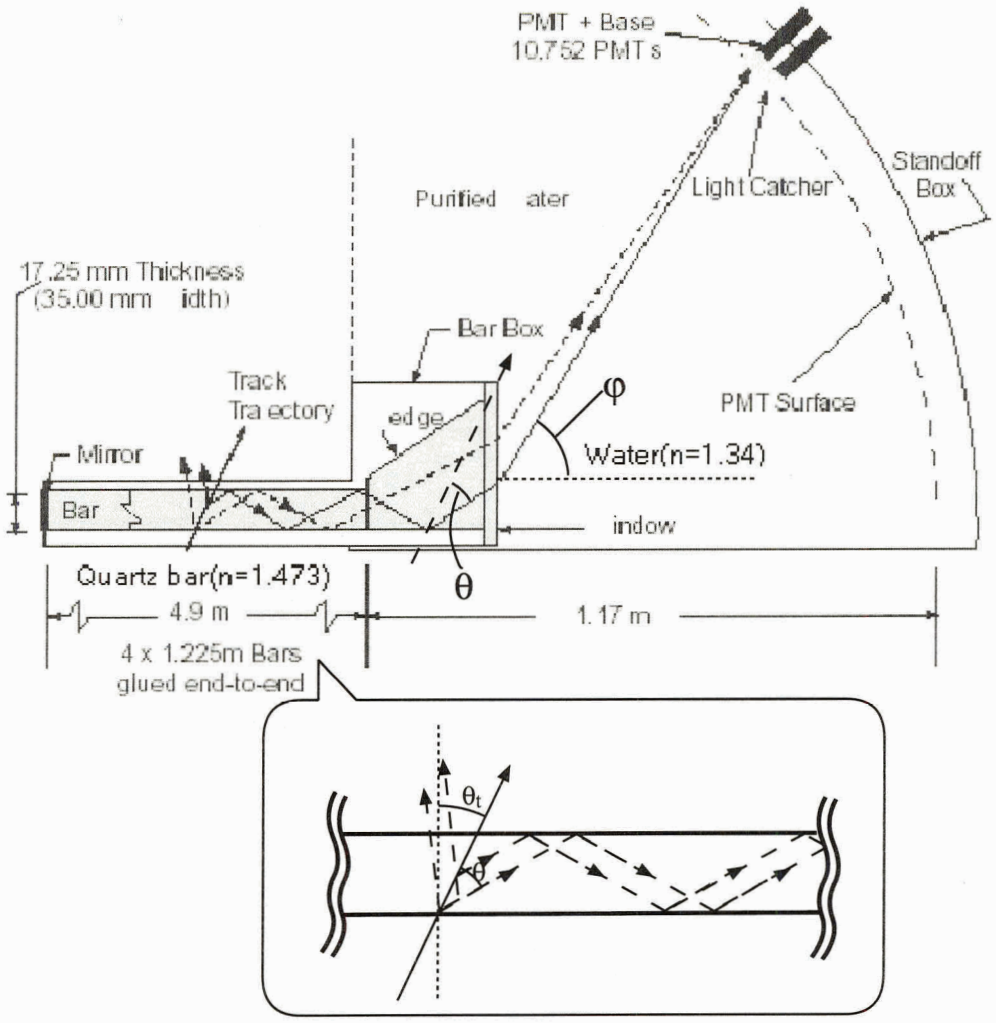

Figure 3.11: DIRC Operation

When a fast charged particle passes through the quartz bar(n=1.473) it generates Cerenkov light. The quartz bar is used to induce the Cerenkov light and transmit the Cerenkov light by total internal reflection in the bar preserving angle θ. The asymmetry of incident beam boosts the scattered particles to the forward direction.

A quartz wedge is glued to the readout end of bar to reflect the downward light to upward direction. The Cerenkov light coming from the wedge experiences little refraction in the water filled expansion region, called the standoff box. The standoff box is surrounded by a steel box to shield the phototubes from magnetic field. We can detect this Cerenkov light using an array of photomultiplier tubes (PMTs). We can measure the angle φ between PMT detecting light and the quartz bar. We can measure the track angle θ_t from the drift chamber. Using these two angles φ and θ_t we can calculate the Cerenkov angle θ. Cerenkov ring images are reconstructed by measuring the position and time of arrival of the signals in PMT. Note for the same track angle particles, faster particles give larger Cerenkov angle θ so the smaller angle φ. We know the momentum of the charged particles from DCH. So we can calculate the rest mass of the charged particles using the relativistic relation

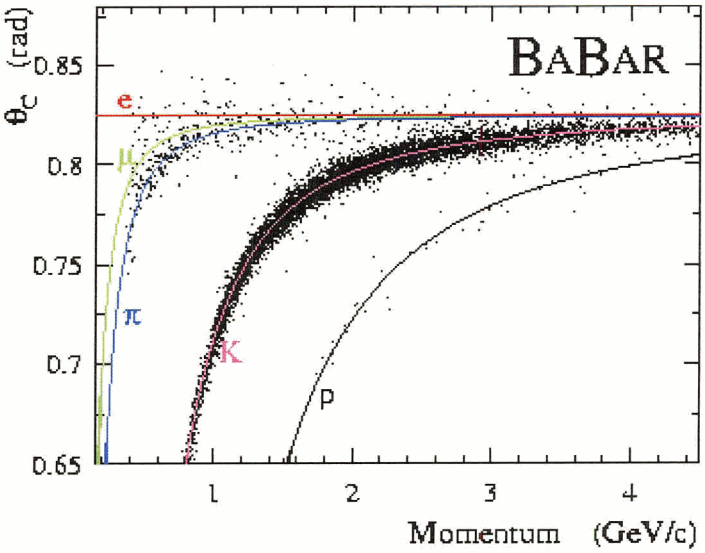

Figure 3.12: Particle identification in DIRC

$$P = \frac{m_0 v}{\sqrt{1-(v/c)^2}}$$

Figure 3.12 shows the relation between momentum of the charged particles and Cerenkov

angle.

3.4.4 EMC(Electromagnetic Calorimeter)

$B^0 \rightarrow \rho^{\pm}\pi^{\pm}$ with $\rho^{\pm} \rightarrow \pi^{\pm}\pi^0$, $B^0 \rightarrow J/\psi K_s^0$ with $J/\psi \rightarrow e^+e^-, \mu^+\mu^-$ decays are important to study CP violation at BaBar.

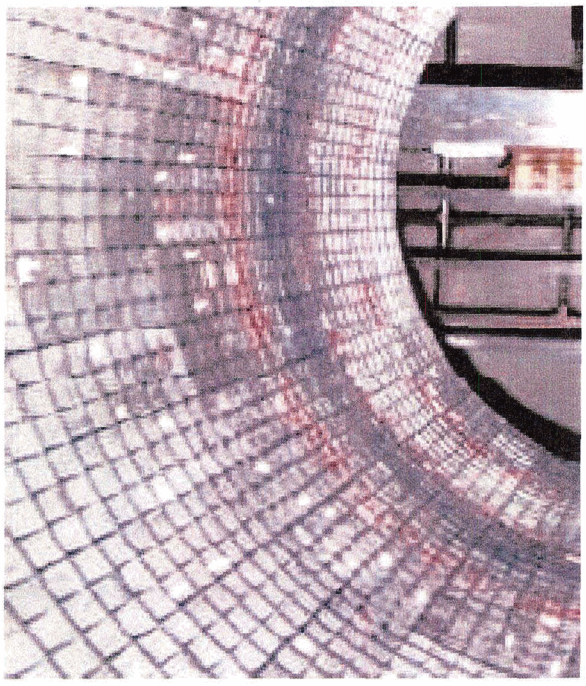

Figure 3.13: Array of Thallium doped Cesium iodide(CsI(Tl)) crystals

A high energy electron or positron creates a pure (not subsequent electromagnetic shower from an hadronic shower) electromagnetic shower (cascade of electron-positron generation) when it passes through the electromagnetic calorimeter. A high energy real photon also generates a pure electromagnetic shower when it passes into the electromagnetic calorimeter. The electromagnetic calorimeter (EMC) is designed to measure the energy and angular position of high energy photon or electron or positron which generates electromagnetic showers from 5 GeV down to 20 MeV. This range of energy corresponds to the low energy photon from π^0, η^0 decay of generic B decays, and the high energy photons and electrons from electromagnetic, weak, radiative processes. For instance, photons of $B^0 \rightarrow \pi^0\pi^0$ may reach energies up to 4.5 GeV.

Figure 3.13 shows the array of Thallium doped Cesium iodide (CsI(Tl)) crystals used in the electromagnetic calorimeter. The electromagnetic shower happens in the CsI region. The individual crystals have two silicon photodiodes to make the electronic signal of a shower event.

When a high energy electron shoot through the cesium diode(CsI(Tl)) crystal, because of its high incident energy, it can approach the charged nucleus very closely. It therefore experiences a very strong electric field produced by the charged nucleus. This causes the emission of high energy real and virtual photons by the deflection of electron trajectory. This real or virtual photon has only some portion of the energy of the incident electron or real photon. But the energy of the photon is enough to create an electron-positron pair. So the electron-positron pair is created from a high energy photon in the presence of a nucleus. [1] Generated electron-positron pairs also have high momenta roughly parallel to the direction of the initial electron. When these generated electrons and positrons pass close to the nucleus of CsI(Tl) crystal, they again feel very strong electric fields, and create secondary high energy real or virtual photons. These secondary high energy virtual or real photons again create secondary electron-positron pairs. In this way a cascade of electron-positron pairs and real photons are increasingly created.

Figure 3.14 (a) shows the typical electromagnetic shower processed by high energy electron. The photons can be real or virtual in this picture. Eventually the high energy incident electron or positron or real photon converts into many lower energy electron-positron pairs and lower energy photons. If the initial high energy electron or positron or photon has more energy, the depth of the shower is increased and the total number of electron-positron pairs and real photons also increases. Finally the number of electron-positron pairs and real photons increase but they have small energy individually. Because they don't have enough energy to create more electron-positron pairs, a generated positron annihilates with atomic electrons and produces two 511 KeV photons. The low energy real photons undergo Compton scattering with atomic electrons. The ejected electron puts atoms in crystal into an excited state and emits ultraviolet and optical radiation when returning to the ground

[1] Because of momentum conservation, isolated real photons cannot produce an electron-positron pair. But a high energy real photon converts to an electron-positron pair when it passes close to nucleus of CsI(Tl) crystal.

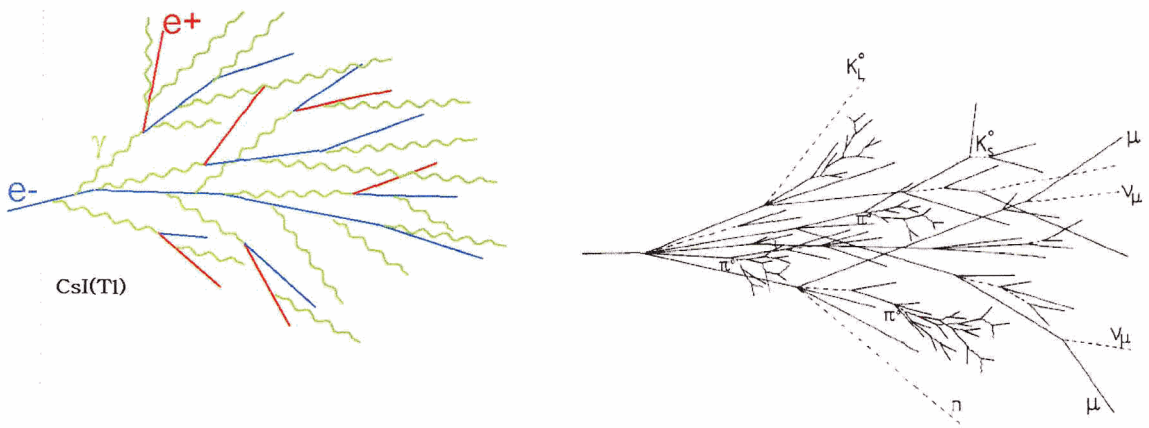

(a) Typical electromagnetic (EM) shower in CsI(Tl)

(b) Hadronic shower has various process involved and is much more complicate than an EM shower.

Figure 3.14: Schematic of electromagnetic and Hadronic shower

state. The photo-diode is efficient for detecting ultraviolet and optical photons. Thus if we measure the number of photoelectrons, we can calculate the energy of incident high energy electron or positron or real photon.

Since hadrons are much heavier than an electron, charged hadrons(especially $K^{\pm}, \pi^{\pm}$ in BaBar) are not much deviated by electric field of nucleus even if they pass close to it. So the electromagnetic shower of charged hadron is not as obvious as electron shower. But when a high energy hadron passes very close to the protons or neutrons of the material of an electromagnetic or hadronic calorimeter because of its high energy, the residual strong interaction between hadron and nucleus creates a gluon. Just as a photon converts to an electron-positron pair, a gluon can converts to a quark anti-quark pair. This quark pair forms a meson which has the roughly the same direction of momentum as the incident

hadron. Produced mesons may decay to other hadrons or leptons or photons by strong, weak or electromagnetic interactions. If decayed particles have high enough energy, the hadron again experiences strong interaction with the nuclei of the calorimeter to produce more gluons or electrons and photons which generate a subsequent electromagnetic shower by electromagnetic interactions with nucleus. In this way a hadron passing through the EM or hadronic calorimeter can generate an hadronic shower as well as a subsequent electromagnetic shower. Eventually all generated particles are absorbed by hadronic calorimeter.

Figure 3.14 (b) shows typical hadronic shower. In BaBar detector CsI(Tl) crystal shows little effect of hadronic showers because we didn't set up a large volume of crystal material to contain the full hadronic shower. Crystal is expensive so generally crystals are not used for hadronic calorimeters because we would need a large volume of crystal to completely absorb the energy of incident particle in strong interaction.

While incident electrons or real photons cannot penetrate the CsI(Tl) crystal, hadrons ($K^{\pm}, \pi^{\pm}$) can. Thus, if we found the electromagnetic shower contained inside CsI(Tl) crystal, it means the initial particle is an electron or positron or real photon. In this case the momentum of the incident particle measured in DCH is almost the same as the energy deposited in the electromagnetic calorimeter($p/E \approx 1$). If it has no track inside SVT or DCH, it is photon. If it has a track inside SVT or DCH, it is electron or positron. We can decide whether it is electron or positron by observing the direction of curvature inside the magnetic field of DCH. If we found the electromagnetic shower is not fully contained inside the CsI(Tl) crystal, it means incident particle is hadron.

Because a muon is not affected by the strong interaction, the incident muon doesn't generate an hadronic shower. Because the muon is heavy it doesn't generate electromagnetic shower either at these energies. Muons are sufficiently massive that their trajectories are

not deviated to create virtual photons. Muon energy loss through ionization process is therefore very small and muons can penetrate the CsI(Tl) crystal without any showering. Because the effective strong field region of a nucleus is much smaller than the effective electromagnetic field region of an nucleus, the probability of an incident hadron experiencing the strong field is much smaller than that of incident electron experiencing the electric field. Thus the hadronic shower is more rare than electromagnetic shower. So the starting point of the hadronic shower is much deeper than the starting point of an electromagnetic shower. Moreover, hadronic showers are usually wider than electromagnetic showers. So by comparing the dept of starting point of shower we can distinguish electromagnetic shower and hadronic shower. This means we can distinguish high energy incident electron or positron or real photon from high energy incident hadrons such as $K^{\pm}, \pi^{\pm}$.

As we have seen before, the mass of a charged particle can be measured by using the information about momentum and velocity of the particle from DCH and DIRC respectively. We can measure the mass of a π^0 by measuring the momentum of two photons from the decay of π^0. If we know the momentum of two photons, we can calculate the invariant mass of them, namely the mass of π^0. Measurement of π^0 mass is dominated by the energy resolution for lower than 2 GeV energy. At high energy the angular resolution is important. The angular resolution should be the order of a few mrad.
Although the decay $B^0 \rightarrow \pi^0\pi^0$ is extremely rare, photons from this decay can be up to 4.5 GeV. So to reconstruct the pion decay event, excellent resolution and efficiency for detecting energy and angular position of photons from π^0 decay are required. The energy resolution of a crystal calorimeter is empirically expressed by

$$\frac{\sigma_E}{E} = \frac{a}{E(GeV)^{1/4}} + b.$$

E :Energy of photon (GeV)
σ_E :RMS error on E

The energy dependent term a primarily comes from the fluctuations in photon statistics. Electronic noise of photon detector and electronics also contribute to it. The a term is dominant at low energies (below 1GeV). For good energy resolution at low energy, the electronic noise should be less than 150 keV of equivalent noise energy(ENE). The constant term b is dominant at high energies(over 1GeV). b comes from non-uniformities in the light yield, leakage, absorption in the material between and in front of the crystals and uncertainties in the calibrations. The goal for the energy resolution is

$$\frac{\sigma_E}{E} = \frac{1\%}{E(GeV)^{1/4}} + 1.2\%$$

for photons at an angle of 90°.

Actually measured resolution is

$$\frac{\sigma_E}{E} = \frac{2.32\pm0.30\%}{E(GeV)^{1/4}} + 1.85\pm0.12\%$$

To study the decay of π^0, η to two photons with almost equal energy we need good angular resolution of electromagnetic calorimeter. The transverse crystal size and distance from the center of detector decide the angular resolution. An angular resolution is also expressed empirically

$$\sigma_\theta = \sigma_\phi = \frac{c}{\sqrt{E(GeV)}} + d.$$

We want to the angular resolution of

$$\sigma_\theta = \frac{3mrad}{\sqrt{E(GeV)}} + 2mrad$$

The measured value is

$$\sigma_\theta = \sigma_\phi = \frac{3.87 \pm 0.07mrad}{\sqrt{E(GeV)}} + 0.00 \pm 0.04mrad$$

This resolution allows a position resolution in a few mm.

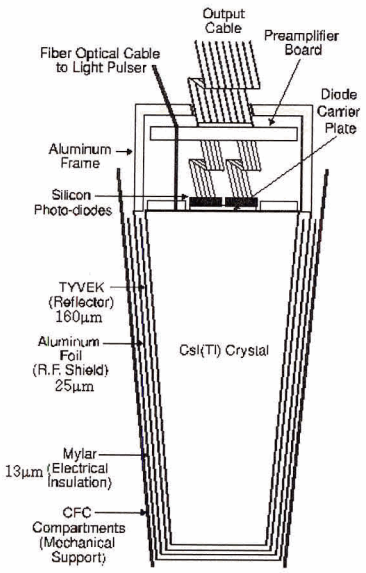

Figure 3.15: The wrapped CsI(Tl) crystal end the front-end readout package mounted on the rear face. Note that CFC compartment is open at the front. This drawing is not to scale.

Parameter	Values
Light Yield	50,000 γ / MeV
Moliere Radius	3.8 cm
Radiation Length	1.85 cm

Figure 3.15 shows the wrapped CsI(Tl) crystal and the readout package on the rear face. There are two photodiodes for the readout. Above table gives the properties of CsI(Tl) crystal used in BaBar detector. The light yield should be high enough and uniform along the length of the crystal to get a high resolution of photon energy. A Moliere Radius is a characteristic constant of a material describing its electromagnetic interaction properties, and related to the radiation length by $R_M = 0.0265 X_0 (Z + 1.2)$ with X_0 the radiation length and Z the atomic number. The Moliere Radius should be small to get an excellent angular resolution. As shown in the table, since the radiation length is short, we can minimize the volume of crystals. The intrinsic efficiency for the detection of photons is almost 100% down to a few MeV. The minimum measurable energy of a photon is about 20 MeV. To detect low energy photons from π^0 decay we need to make the material in front of CsI(Tl) crystal as thin as possible. The electric signal from two photodiodes goes to the preamplifier. Here the signals with two different gains are amplified then the signals from two photodiodes are added. Among gain A, gain B, or average of A, B the most appropriate signal is passed to 10-bit ADC boards at the ends of the detector. Then the signal is sent to the trigger electronics.

Figure 3.16 shows the crystal support structure. Each of the crystals are inserted into

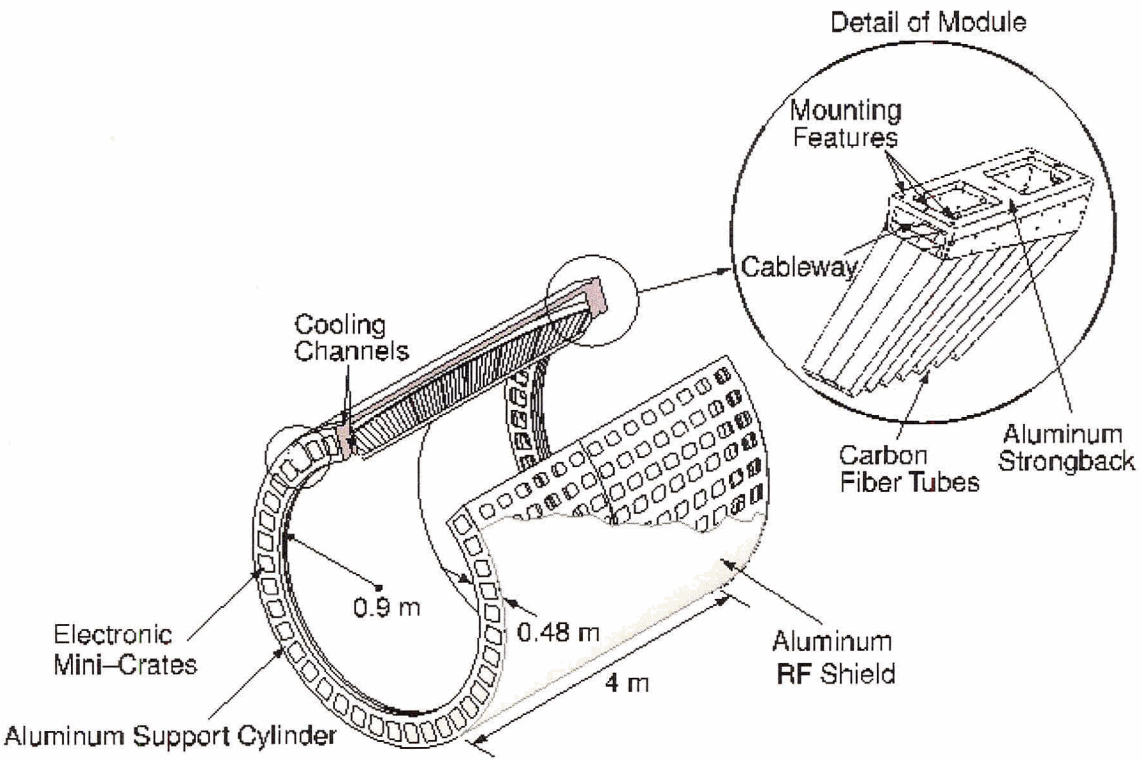

Figure 3.16: EMC barrel support structure with detail of module

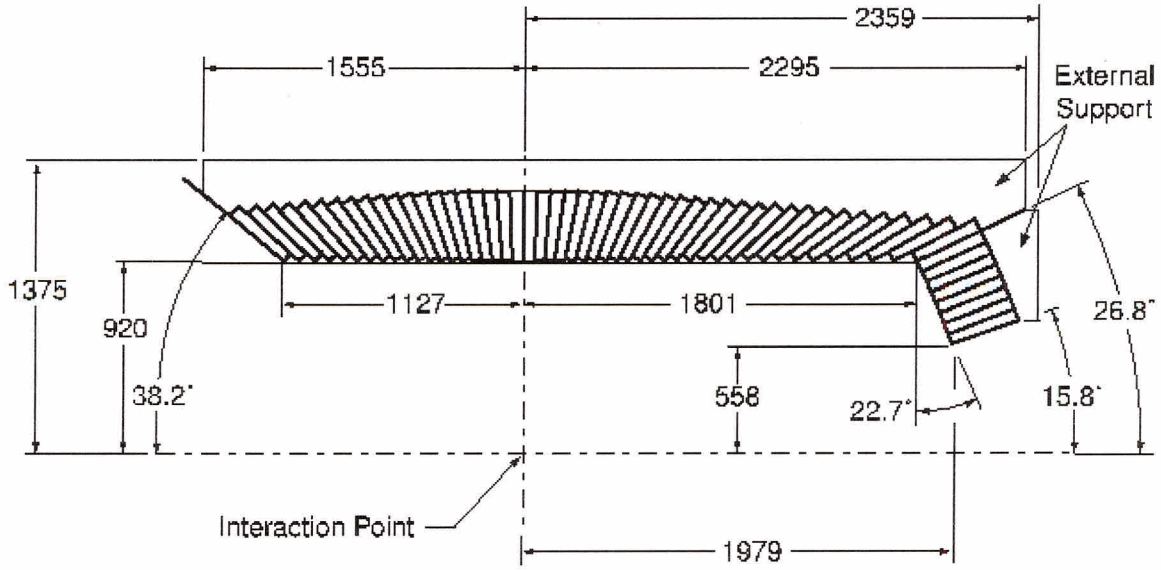

Figure 3.17: A longitudinal cross section(in mm) of EMC with 56 crystal rings.

modules. The modules for the barrel and end cap are made from carbon-fibber epoxy composite(CFC) with 200μm thick walls. The aluminium strong support cylinder called "strong back", fixes the position of each module, so that each module doesn't lean against another. By supporting the modules at the back, we can minimize the material in front of the crystal. To shield the diodes and preamplifiers from external noise the whole calorimeter is covered by two 1mm thick aluminium sheets.

Figure 3.17 shows a longitudinal cross section of the electromagnetic calorimeter. The cylindrical barrel has 48 distinct rings. Each ring has 120 identical crystals. The end cap has 820 crystals in 8 rings. So the total number of crystals used in electromagnetic calorimeter is 6580. The length of the crystals range from 297.6 mm to 325.5 mm. All crystals are pointing toward the interaction point. To keep the symmetry in the ϕ direction, the overlap of neighbouring modules along the ϕ axis is impossible. About 2.5% of photons escape and undetected through these gaps.

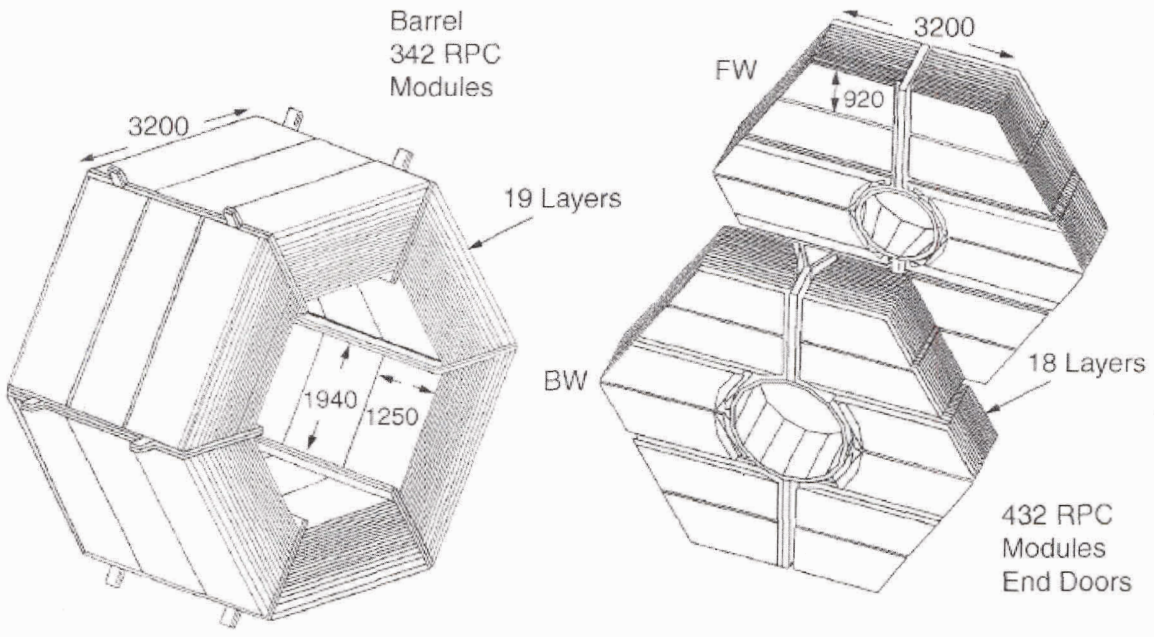

Figure 3.18: Left:barrel sector of IFR Right:forward and backward end doors

The angular coverage in the lab frame is

$$15.8 \leq \theta \leq 141.8$$

$$0.962 \leq cos\theta \leq -0.775$$

This corresponds to the angular coverage in center of momentum frame of

$$0.895 \leq cos\theta \leq -0.916$$

corresponding to 90% solid angle coverage which is approximately symmetric in center of momentum frame.

3.4.5 IFR(Instrumented flux return)

A 1.5 T magnetic field is produced by superconducting solenoid surrounding EMC. Liquid helium cools this solenoid coil. Because this magnetic field is so strong, we observe small radii of charged particle trajectories in DCH for fixed momentum(r=mv/qB). This means

we have a small DCH and outer components.

The primary goals of the IFR are first confining the 1.5 T magnetic field inside the detector, second identification of muons, especially discriminating muons and pions, third detection of neutral hadrons, especially K_L^0 identification when used together with the EMC.

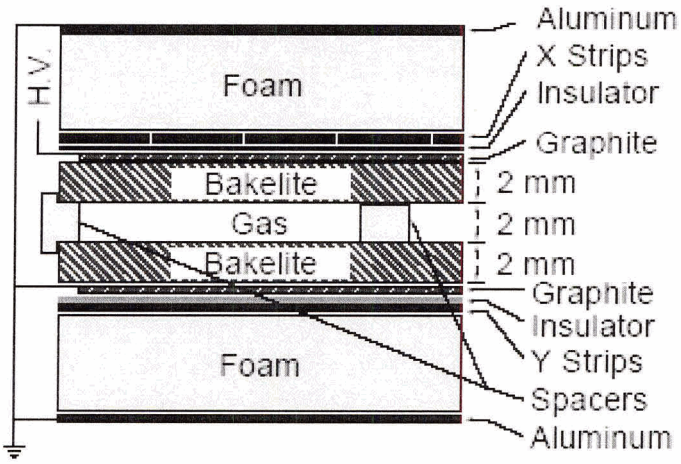

Figure 3.19: Cross section of a planar RPC

Figure 3.18 shows the IFR structure. 65cm thick Barrel and 60cm thick end doors are segmented into 18 plates. The innermost 9 plates are 2cm thick, followed by four of 3cm and three of 5cm and two of 10cm thick outer-most plates. For the end doors, the thickness of the outermost plates are 5cm and 10cm. The gap between 2cm thickness steel plates is 3.5cm and 3.2cm for between the other plates. The Resistive Plate Chambers(RPCs) are inserted in this gap. As a detector for charged tracks, 19 planar RPC layers are inserted in the barrel and 18 in the end doors. In addition there are two layers of cylindrical RPCs just outside the radius of the EMC.

Figure 3.19 is the cross section of a planar RPC inserted in the gaps of segmented steel of the barrel and the end doors. It is 125cm wide and 180cm to 320cm long depending on radial distance from the IP.

If charged or neutral hadrons interact with the steel plate it generates an hadronic shower. An hadronic shower contains many charged and neutral particles. If these charged particles or muons enter RPC they ionize gas inside RPC. Because two graphite surfaces are

connected to high voltage(~8KV) and ground, ionized particles move to either surface and generate electric signals. We can detect this signal using X and Y strips shown in figure 3.19. The strip widths on the RPC are 19.7~38.5mm and X and Y strips are orthogonal each other. Thus we can detect the position of generated electric signal and the coordinate of entering charged particle into RPCs. Since 19 RPC layers are in the radial direction, we can reconstruct the 3-dimensional trajectory of the charged particle. The strips are connected to the readout electronics at one end and terminated with a 2 kΩ register at the other. Even and odd numbered strips are connected to different front-end cards(FECs). A charged particle passing through the RPC usually generates signals in two or more adjacent strips. Thus even if one card fails to detect signal from one strip, the other cards can detect signal from adjacent strips. So, we can minimize the dead area where we fail to detect charged particles passage.

Efficiency of muon identification and rate of misidentification have been tested using a control sample. From Figure 3.20 we can see 90% efficiency is achieved for the momentum range $1.5 < P_{lab} < 3.0$ GeV/c with the rate of fake muon 6~8%.

If neutral or charged hadrons meet the steel of IFR they interact with nuclei in the steel and generate hadronic showers. About 64% of K_L^0 above 1GeV/c produce showers in the cylindrical RPC, or in two or more planar RPC layers according to Monte Carlo simulation. Unassociated clusters with angular sep-

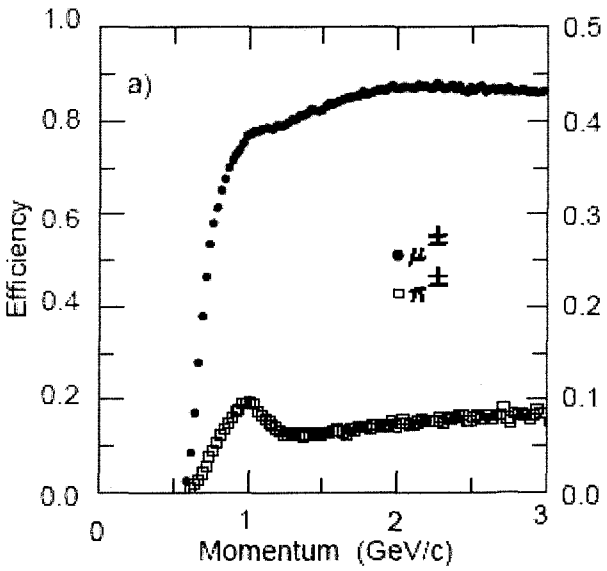

Figure 3.20: Muon efficiency(left scale) and pion misidentification probability(right scale) as a function of lab track momentum. It is obtained with loose selection criteria.

aration less than 0.3 radian are combined into a composite cluster, joining clusters. In contrast to the charged hadronic shower, for neutral hadronic showers on IFR steel we cannot associate this cluster with inside charged tracks. The direction of the neutral hadron is determined from the event vertex and the center of the neutral cluster. We match the cluster angle of hadronic shower in IFR with the cluster angle of hadronic shower in the EMC and in the cylindrical RPC. In this way, neutral showers in the EMC are associated with the neutral hadrons detected in the IFR. For a good match above 1% of χ^2 probability is required.

The graded segmentation of the iron is the result of Monte Carlo studies. The simulation tells us that muon identification at low momentum and K_L^0 detection can be improved using some amount of absorber depending on the incident momentum. Thus we need several thicknesses of iron plates. The fine IFR iron segmentation allows the detection of muons down to 500MeV/c which penetrate just a few cm of iron.

Many RPC modules had problems in efficiency during the first year of operation. One of the reason was the high temperature of the IFR. Because there many RPC layers, it did not affect too much the overall performance. Even after installing cooling water on the steel, there still existed severe problems. Because the IFR is not capable of identifying muons, I did not use IFR in my analysis.

3.4.6 Trigger

In the PEP-II collider, the electron and positron beams cross every 4.2ns. BaBar uses level 1(L1, implemented on hardware) and level 3(L3, software level) triggers to quickly select interesting events ($b\bar{b}$, $c\bar{c}$, uds,$\mu^+\mu^-$,$\tau^+\tau^-$,...) with high (99% for all $B\bar{B}$ events and 90~95% for other interesting events), stable, well-understood efficiency while rejecting background events (beam-induced background, Bhabha, two-photon events). Beam-induced background charged particles are produced in material close to the IP. For one or more tracks in the drift chamber with $P_t > 120MeV/c$ or for at least one EMC cluster with $E >$

Event type	Cross section (nb)	Production rate (Hz)	Level 1 trigger rate(Hz)
$b\bar{b}$	1.1	3.2	3.2
other $q\bar{q}$	3.4	10.2	10.1
e^+e^-	~53	159	156
$\mu^+\mu^-$	1.2	3.5	3.1
$\tau^+\tau^-$	0.9	2.8	2.4

Table 3.1: Principal physics processes at 10.58GeV for a luminosity of $3 \times 10^{33} cm^{-2} s{-}1$. The e^+e^- cross section refers to events with either the e^+, e^-, or both inside the EMC detection volume.

$100 MeV$, beam-induced background rates are usually about 20kHz at design luminosity.

Table 3.1 lists the cross sections, production and trigger rates for the principal physics processes at 10.58GeV for a luminosity of $3 \times 10^{33} cm^{-2} s^{-1}$. Since we are not interested in Bhabha events the total production rate of interesting events is less than 20Hz. Thus it is enough to have a triggering system which extract interesting events at this rate or little more. The trigger is designed to manage

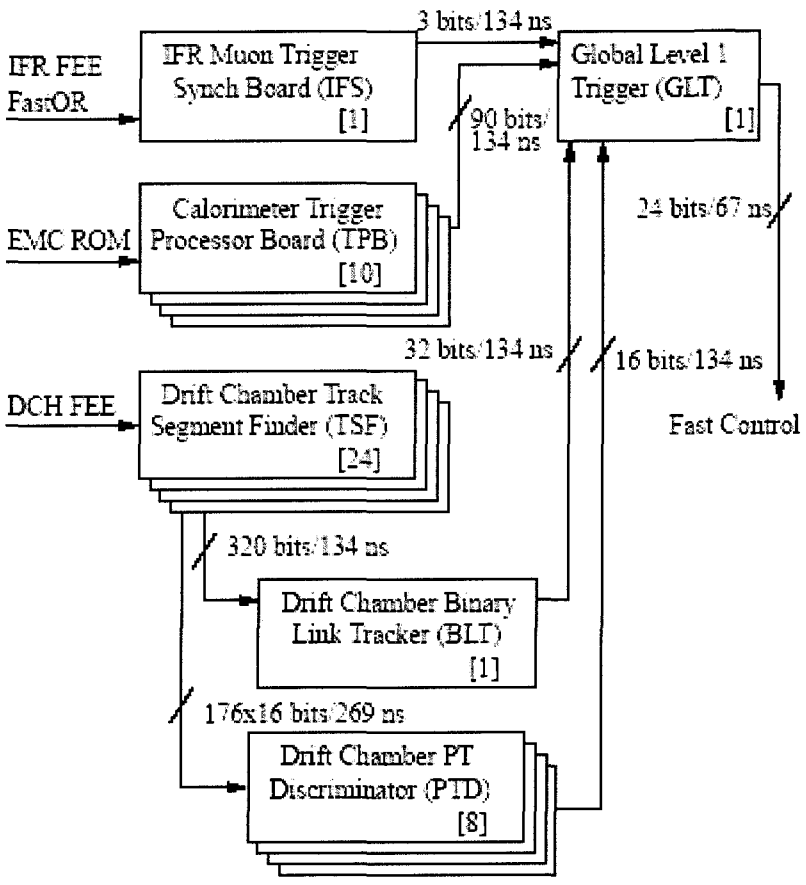

Figure 3.21: Simplified flowchart of L1 algorithm. Numbers in square brackets mean the number of modules

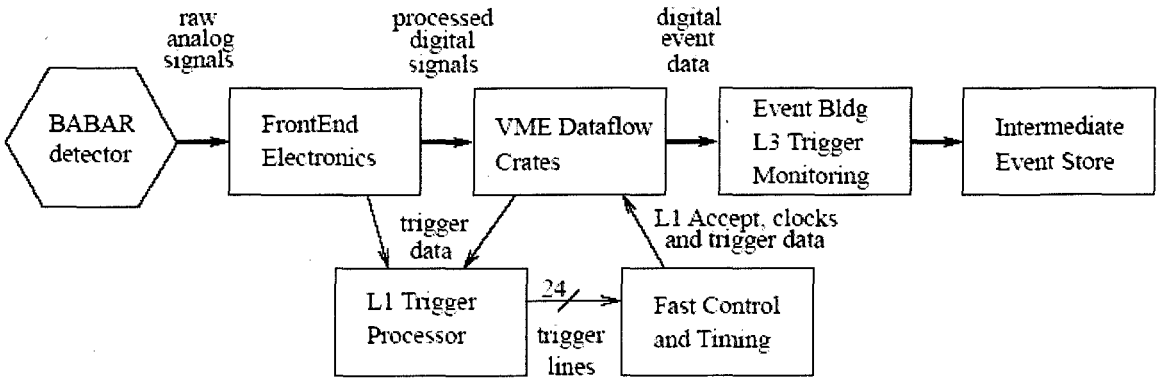

Figure 3.22: Schematic diagram of data acquisition

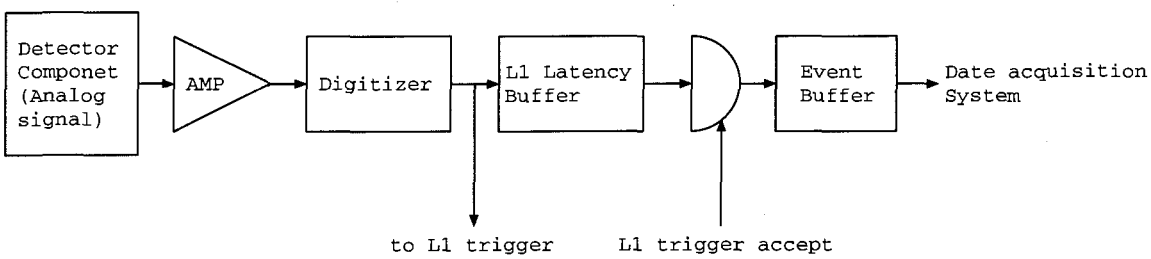

Figure 3.23: Front-End Electronics(FEE)

up to ten times the initially projected PEP-II background rates at design luminosity.

Front-End Electronics(FEE)

Figure 3.22 is the schematic diagram of the data acquisition system and Figure 3.21 is the magnified algorithm of the L1 trigger part. EMC untriggered personality cards(UPCs) send raw data to EMC trigger(EMT) about $2\mu s$ after e^+e^- collision. Event data from DCH and IFR flows through each Front-End Electronics(FEEs) into the IFR muon trigger synch Board(IFS) and the DCH Track Segment Finder(TSF).

Figure 3.23 shows the schematic diagram of the FEE. Each FEE chain consists of an amplifier, a digitizer, a trigger latency buffer and an event buffer. The digitizer converts the analog signals to digital. The L1 latency buffer stores data during the L1 trigger processing. The event buffer stores data between the L1 Accept and subsequent transfer to the

	Decryption	Origin	# of bits	Threshold
B	Short track reaching DCH super layer 5	BLT	16	120MeV/c
A	Long track reaching DCH super layer 10	BLT	16	180MeV/c
A'	High P_t track	PTD	16	800MeV/c
M	All-θ MIP energy	TPB	20	100MeV
G	All-θintermediate energy	TPB	20	250MeV
E	All-θ high energy	TPB	20	700MeV
X	Forward end-cap MIP	TPB	20	100MeV
Y	Backward barrel high energy	TPB	10	1GeV

Table 3.2: Trigger primitives for the DCT and EMT. Most energy thresholds are adjustable. those listed are typical values

data acquisition system. All FEEs are mounted on the detector to optimize performance and to avoid noise pickup. Analog signal processing, digitization and data readout occur continuously and simultaneously.

Level 1 trigger

The role of the L1 trigger is to remove beam-induced background on the basis of event information from DCH, EMC and IFR. The L1 trigger system consists of four subsystems: DCH trigger(DCT), EMC trigger(EMT), IFR trigger(IFT) and global level trigger(GLT). DCT and EMT receive track or neutral information from DCH and EMC and generates trigger primitives which are then sent to GLT every 134ns. A trigger primitive is a kind of cut variable to which threshold momentum or threshold energy is applied. A candidate track or neutral is expected to pass one of trigger primitives. Table 3.2 represents trigger primitives for the DCT and EMT.

Level 3 trigger

The role of L3 trigger software is background filtering while keeping interesting events; event reconstruction; event classification and monitoring. Using both the complete event information and output of L1 trigger, L3 trigger apply a much more rigid background eliminating

cut. L3 triggering is a part of Online Event Processing(OEP) framework. L3 uses a sequence of module codes(scripts) to apply a variety of event selections. A script may execute DCH or EMC algorithms to construct quantities of interest and to use them as selection parameters.

Many beam-induced background events pass the L1 level trigger. L3 uses a DCH-based algorithm(L3DCH) to reduce these backgrounds. Every neutral trigger used in the L3 trigger is based on the EMC information. EMC information is also important to identifying Bhabha events. The L3 EMC-based trigger(L3Emc) identifies energy clusters with enough sensitivity to detect minimum ionizing particles. The EMC typically sends data corresponding about 1400 crystals out of 6580 crystal resources. Most of these are electronic noise and beam-induced background. To exclude these contaminations, L3Emc rejects individual crystal signals below an energy threshold of 20MeV or which lie outside of a 1.3μs time window around event time.

L3 uses DCH information to construct track filter variables and uses EMC information to construct cluster filter variables. 1 track filter requires a transverse momentum of $P_t > 600MeV/c$ and a vertex condition $|d_0^{IP}| < 1.0cm, |z_0^{IP} - z_{IP}| < 7.0cm$. The IP position is a fixed location close to the average beam position over many months. But the IP position is not on the origin. d_0^{IP} means the x-y closest approach distance from the current interaction beam to fixed IP position. z_0^{IP} means corresponding z coordinate. 2 track filter requires $P_t > 250MeV/c$ and $|d_0^{IP}| < 1.5cm, |z_0^{IP} - z_{IP}| < 10.0cm$.
2 cluster filter requires at least two clusters of $E_{cm} > 350MeV$ and event mass(effective mass calculated from the cluster energy sums and the energy weighted centroid positions of all clusters in the event assuming massless particles) greater than 1.5GeV. 4 cluster filter requires at least four clusters and an event mass greater than 1.5GeV. Bhabha events dominate output of both DCH and EMC filter. Using a Bhabha veto filter and E/P we can

L3 Trigger	$B\bar{B}$	$B \to \pi^0\pi^0$	$B \to \tau\nu$	$c\bar{c}$	uds	$\tau\tau$
1 track filter	89.9	69.9	86.5	89.2	88.2	94.1
2 track filter	98.9	84.1	94.5	96.1	93.2	87.6
Combined DCH filters	99.4	89.1	96.6	97.1	95.4	95.5
2 cluster filter	25.8	91.2	14.5	39.2	48.7	34.3
4 cluster filter	93.5	95.2	62.3	87.4	85.5	37.8
Combined EMC filters	93.5	95.7	62.3	87.4	85.6	46.3
DCH or EMC filters	>99.9	99.3	98.1	99.0	97.6	97.3
Combined L1+L3	>99.9	99.1	97.8	98.9	95.8	92.0

Table 3.3: L3 trigger efficiency for various physics processes, derived from MC

reduce them.

Bhabha, radiative Bhabha, $\gamma\gamma$ final state and cosmic ray events are flagged by requiring some criteria for each. We need these events for calibration and offline luminosity measurement. A track based lepton pair selection in L3 with a well know efficiency monitors the luminosity. Since the $B\bar{B}$ production rate is very sensitive to beam energy around the $\Upsilon(4s)$ peak, by counting the number of $B\bar{B}$ for given luminosity we can monitor beam energy too.

Table 3.3 shows the result of L3 trigger efficiency(%) for the events already passing the L1 trigger. The L3 trigger is not expected to reduce significantly the efficiency delivered by L1.

We can see an example of the L3 event display used for online trigger monitoring in Figure 3.24. The left column contains the L1 trigger lines. 1 means on and 0 means off state. L3 trigger lines are also shown on right column.

The L3 event rate at luminosity of $2.6 \times 10^{33} cm^{-2} s^{-1}$ is represented in Table 3.4. After rate reduction for the main physics sources, L3 trigger writes passed events to archival storage to less than 100Hz. The rates of all interesting physics processes amount to only 16Hz of the 100Hz budget at the design luminosity of $3 \times 10^{33} cm^{-2} s^{-1}$.

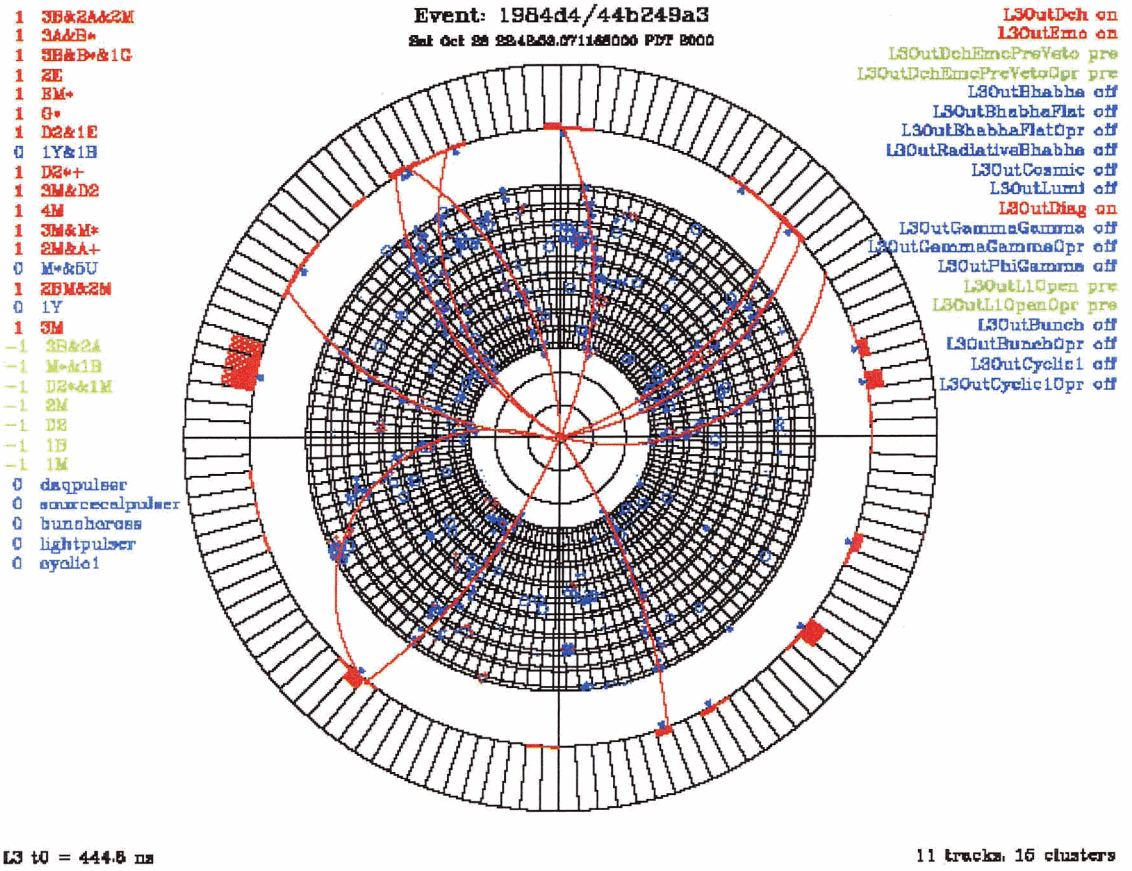

Figure 3.24: Event display. The small circles and small crosses in the DCH volume represent the DCH hits and TSF segment hit wires respectively. The filled EMC crystals represent energy deposit(full crystal depth=2GeV) from Level 3 EMC clusters. The small triangles just inside the EMC indicate the location of the cluster centroid.

Event type	Rate(Hz)
Hadrons,$\tau\tau$,$\mu\mu$	16
Other QED, 2-photon events	13
Unidentified Bhabha backgrounds	18
Beam-induced backgrounds	26
Total physics accept	73
Calibration Bhabhas(e^+e^-)	30
$\gamma\gamma$, Radiative Bhabhas($e^+e^-\gamma$)	10
Random triggers and cosmic rays	2
L1, L3 pass through diagnostics	7
Total calibration/diagnostics	49

Table 3.4: L3 output rates for a luminosity of $2.6 \times 10^{33} cm^{-2} s^{-1}$

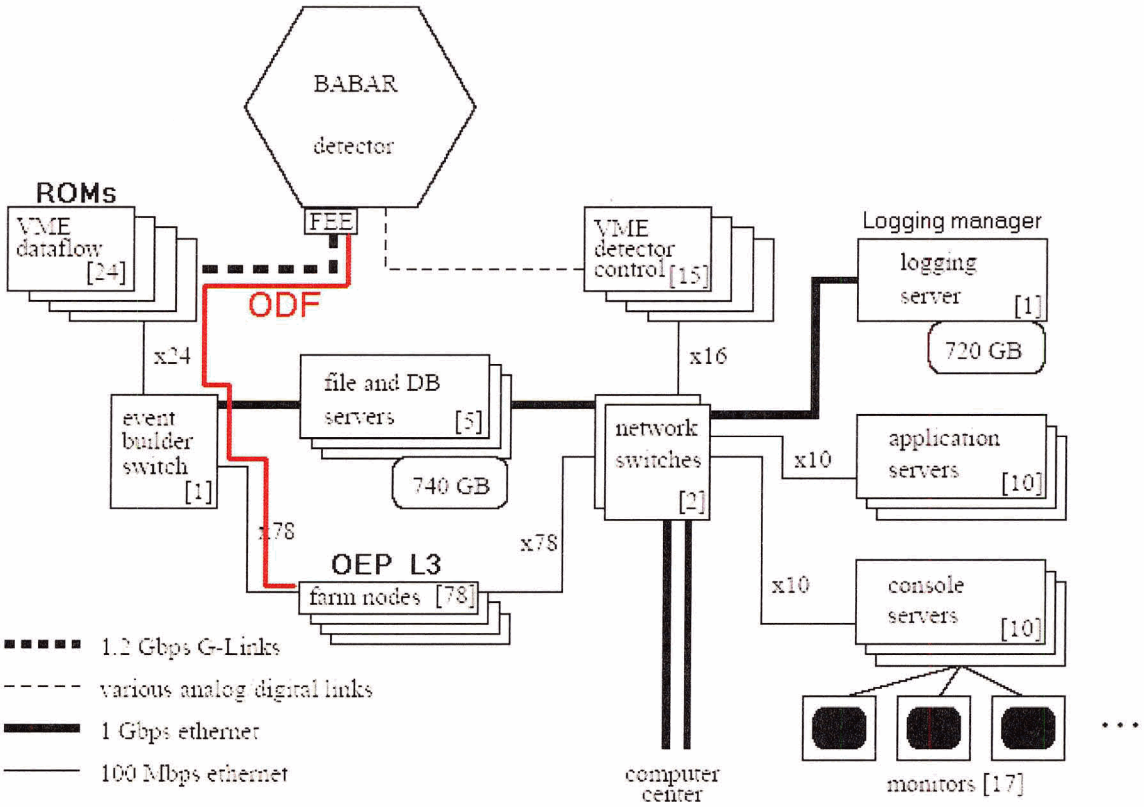

Figure 3.25: Schematic draw of BaBar online system

3.4.7 Online computing

Every detector output comes out to FEEs of each component in the form of analog signals. We need to digitize this analog signal, refine and save it to the disk. The online computing systems do this job. The Trigger is a part of this computing system. The computing system also calibrates and tests the detector output by using triggers and provides for the control and monitoring of the detector and run.

Figure 3.25 shows the physical infrastructure of the BaBar online system. There are 157 ReadOut Modules(ROMs) in 19 physical VME crates divided into 24 logical crates. The ROM provides the standard interface between the specific FEE, the FCTS and event builder.

The event data from the FEEs of each detector systems are sent to 157 ROMS in VME crates that are controlled by the Online Data Flow(ODF) software. ODF is software code responding acquisition and processing the data flow from each FEE to event building. FCTS is a part of ODF. If FCTS sends L1 Accepts to ROMs, ODF makes ROMs send this L1 Accept signal back to FEE. Then ROMs read and process the data from the FEEs, and ODF assemble them into events. ODF delivers this complete event to the online farm for Online Event Processing(OEP). Events sent to a farm machine still busy with a previous event are held in a buffer to await processing. ODF software runs on one of the application servers.

A farm of commercial Unix processors and associated software do OEP. Complete events delivered by ODF are processed in 32 nodes of OEP using the L3 trigger. The events accepted by the L3 trigger are logged to a logging server and written to a disk buffer (intermediate storage) for later reconstruction and ultimate storage. The results of L3 event analysis are stored in this way so the trigger decision and the tracks and calorimeter clusters based on the L3 trigger can be used later for studies of the reconstruction and trigger performance. Data from all 32 nodes are merged into a single file for each data taking run.

Completed data files are copied to the SLAC High Performance Storage System(HPSS) for archiving to tape.

Files and database servers hold the online databases and production software releases. 15 VME crates with embedded processors contain the data acquisition hardware for the detector control subsystem. Online Detector Control(ODC) monitors and controls detector systems and assures the safety of the detector. Online Run Control(ORC) provides graphical user interface(GUI) to control detector operation. Various data quality monitoring and final stage of online calibrations run on farm machines which are not used for data acquisition. The fast monitoring system provides automated comparison of monitoring data with defined references.

Chapter 4

DATA SELECTION

Since we want to compare data and Monte Carlo(MC) for $e^+e^- \rightarrow \mu^+\mu^-(\gamma)$, the selection of μ pair events is a very important aspect of this study. Thus it is critical to select μ pair events with as high an efficiency and low background as possible. Swagato Banerjee developed the utility, TauNtuple package (in analysis-14a software release 12.5.2-physics-1a), selecting $e^+e^- \rightarrow \mu^+\mu^-$ and $e^+e^- \rightarrow \tau^+\tau^-$ events in both data and MC[8]. Using this we selected 24.0% of data, 66.6% of MC $\mu\mu$, and 64.2% of MC $\tau\tau$ events. For my analysis the $\mu\mu$, $\tau\tau$ MC generated by KK2f (release SP5) simulator have been used. The uds MC from EvtGen event generator was also included as a background [4]. A total 996,298/nanobarn of data corresponding February, April, June over 2001, 2002, 2003 have been used. This corresponds to 3,351,137 total events. Here the nanobarn (nb) is the unit of cross section, σ, and corresponds to $10^{-33}cm^2$. The cross section is proportional to the probability that an interaction of an e^+ and e^- will occur. The infinitesimal cross section $d\sigma$ is related to the luminosity L (The number of beam particles per unit time, per unit area) and dN(the number of interactions per unit time) by

$$dN = L \times d\sigma.$$

The MC was produced using monthly snap shots of the detector and beam background conditions for each of these months. A total of 4.5 million $\mu^+\mu^-$ simulated KK2f events were used and 4.5 million $\tau^+\tau^-$ simulated events were used. The cross section for $e^+e^- \rightarrow \mu^+\mu^-$

is 1.16 nb and for $e^+e^- \rightarrow \tau^+\tau^-$ is 0.89 nb. The number of generated events corresponds to 3.88 fb^{-1} for $\mu^+\mu^-$ and 5.06 fb^{-1} for $\tau^+\tau^-$.

4.1 Preselection

The IFR selection of μ was not used. The cut used to select $e^+e^- \rightarrow \mu^+\mu^-(\gamma)$ signal events has been divided into 4 parts. Here Rm means total measured energy in center of momentum frame(CM) divided by beam energy and Remc means total neutral and track energy in the CM measured by EMC divided by beam energy.

$$Rm \equiv E^{total}_{CM,measurable}/E_{beam}$$

$$Remc \equiv (E^{total}_{CM,neutral,byEMC} + E^{total}_{CM,track,byEMC})/E_{beam}$$

We also define the following requirements, on "cuts"

mupaircut[0] Number of tracks=2, each track is prime track, track charges of two tracks are different from each other, mutau preselection[8] which is used in Banerjee's utility (Ntuple generating code)[8].

mupaircut[1] $0.555 < \theta_{track,CM} < 2.5866$ ($|cos(\theta_{track,CM})| < 0.85$)

mupaircut[2] $0 < E_{EMC,track} < 0.4GeV$ for at least one of tracks

A prime track is a track having DocaZ[1] < 10 cm, Doca2DXY of track < 0.2 cm. These cuts select most of the MC primary tracks. Because we already applied the mutau preselection[8] to data(but not to MC) in Banerjee's utility[8], we also have to apply it to MC. To avoid edge effects of the detector, the fiducial angle cut was applied. Sometimes a particle goes between two modules of EMC crystal. In that case we cannot detect it well in EMC and this event is assigned to $E_{EMC,twotracks} = -1$. Thus, all these mupaircuts above are simple but necessary to select $e^+e^- \rightarrow \mu^+\mu^-(\gamma)$ events.

[1]DOCA:Distance Of Closest Approach

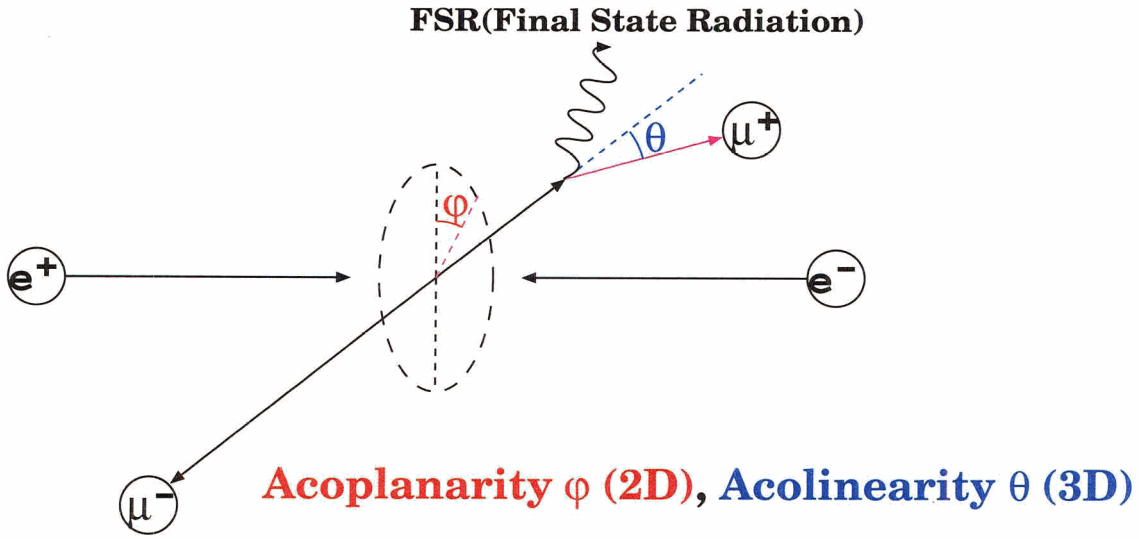

Figure 4.1: Final state radiation(FSR)

4.2 Acoplanarity and Acolinearity in center of momentum

For the $\tau \to \mu\gamma$ study, most photons in the background are from final state radiation(FSR) photons not from initial state radiation(ISR) photons as seen in Figure 2.2. If it is a FSR photon, acoplanaritycm(the angle between two tracks in xy plane in the CM) will increase with photon energy, as does acolinearitycm(the angle between the two tracks in three dimensions in center of momentum frame)(Figure 4.1). On the other hand if it is a ISR photon then acolinearitycm will increase as the photon energy increases but acoplanaritycm will not change. See Figure 4.1 and Figure 4.2. Figure 4.3 shows acoplanaritycm and acolinearitycm of $e^+e^- \to \mu^+\mu^-(\gamma)$ MC events in the Rm versus Remc plane after preselection. The region indicated by the blue line shows low acoplanaritycm and high acolinearitycm so it is a ISR region. The red line region shows high acoplanaritycm and high acolinearitycm, so it is a FSR region.

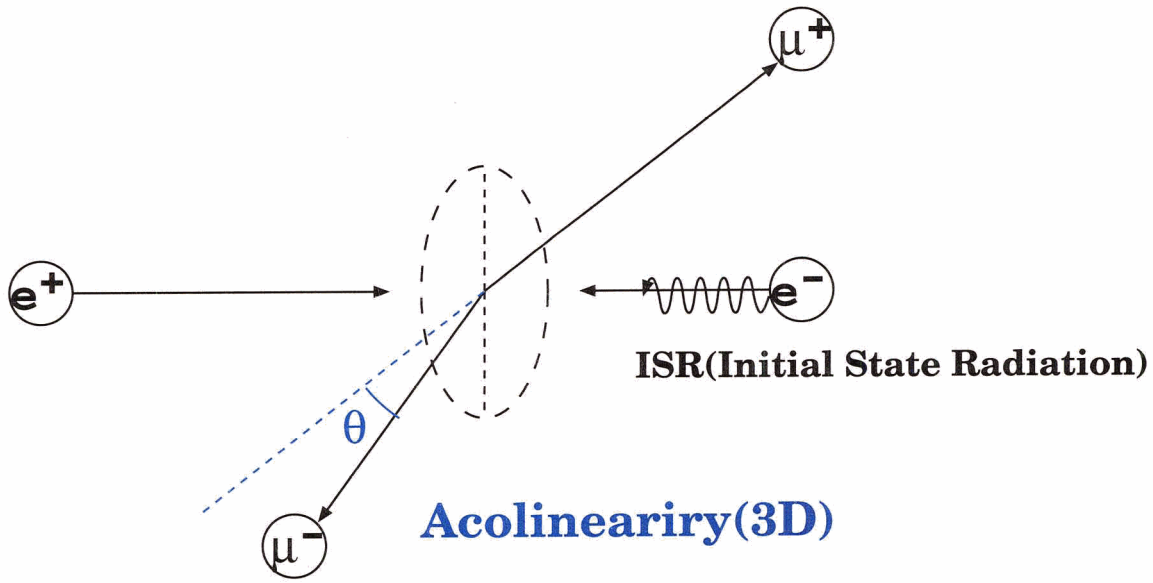

Figure 4.2: Initial state radiation(ISR)

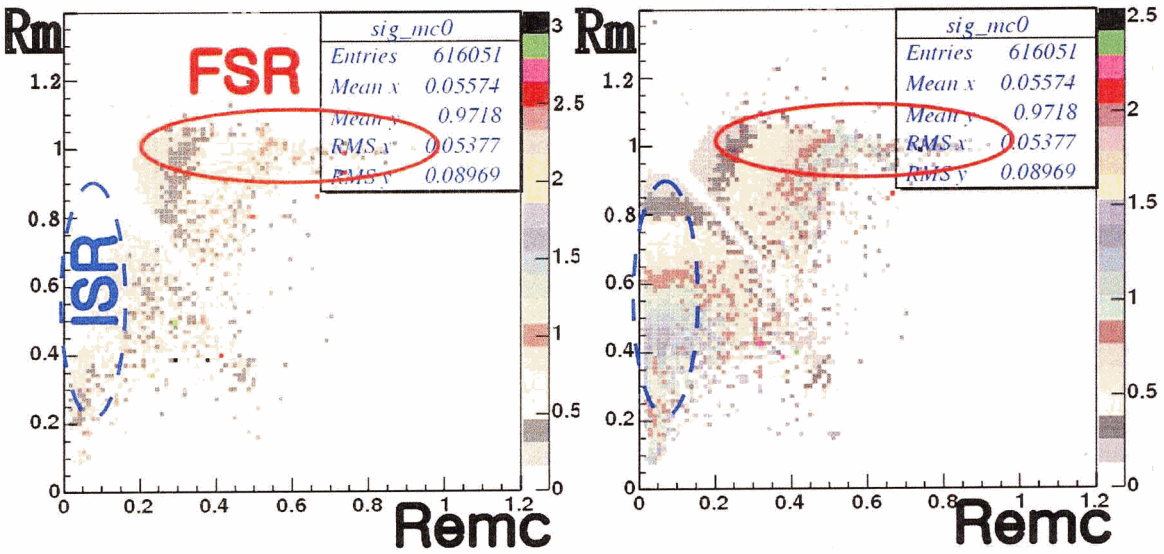

Figure 4.3: Signal MC($\mu\mu$ MC) after preselection Left:—acoplanaritycm—Right:acolinearitycm in Rm vs Remc plane. The color coding indicates the magnitude of the acoplanarity or acolinearity

4.3 Rm versus Remc plane, Geometrical cut

The total energy of $e^+e^- \rightarrow \mu^+\mu^-(\gamma)$ events may all be detectable if there is no initial state radiation(ISR). So these signal events mostly give Rm$\approx$1. Other MC events($\tau\tau$, uds, $c\bar{c}$, $b\bar{b}$) usually miss some energy in the form of generated neutrinos. Neutrinos almost do not interact with any detector components. This means other MC events have some energy which is not detectable. It gives Rm$\leq$1 for other MC events containing neutrinos. Thus if we plot the Rm histogram we can easily distinguish $e^+e^- \rightarrow \mu^+\mu^-(\gamma)$ events(except ISR events) from other MC events. But the total energy of $e^+e^- \rightarrow e^+e^-(\gamma)$ events is also all detectable. To distinguish signal events($e^+e^- \rightarrow \mu^+\mu^-(\gamma)$) from $e^+e^- \rightarrow e^+e^-(\gamma)$ events, other methods are needed. Almost all electrons or positrons lose all energy in the EMC, while μ charged tracks usually leave very small energy in the EMC. So the Remc histogram enables us to distinguish signal events from $e^+e^- \rightarrow e^+e^-(\gamma)$ events. We can understand the reason we draw 2D histograms of Rm versus Remc to extract signal events. Figure 4.4 shows 2D histogram of Rm versus Remc for data, signal($\mu\mu$), background ($\tau\tau$+uds+$c\bar{c}$+$b\bar{b}$) and each of background events respectively. (The histogram of $b\bar{b}$ is not shown because the number of events of $b\bar{b}$ after preselection is about 10% of $c\bar{c}$.). The red dashed line represents the geometrical cut used to distinguish signal from background. Since we want to include the radiation region as much as possible with high purity, the geometrical cut has been applied as shown in Figure 4.4. This geometrical cut has been assigned as mupaircut[3]. After preselection and before the geometrical cut the efficiency of $\mu\mu$ was 53.31% and purity of $\mu\mu$ was 71.96%. After geometrical cut efficiency of $\mu\mu$ is 52.71% and purity of $\mu\mu$ is 91.96%. By the geometrical cut we lose about 0.6% of signal events compared to the number of events in the preselection. At this stage it has been decided to ignore $c\bar{c}$, $b\bar{b}$ events in analysis because their contamination is less than 0.04%.

Figure 4.5 shows Remc distribution of data minus background MC, signal MC and each MC after geometrical cut. The point with error bars represent that data minus the back-

ground. The signal MC ($e^+e^- \rightarrow \mu^+\mu^-(\gamma)$ KK2f) is shown in red, the τ pair background in blue, uds in green and $c\bar{c}$ in grey. The upper plot is on a linear scale and lower one is on a log scale to magnify small parts of the distribution. Bias error means the relative error between data - background MC and signal MC. It is defined by (< signal MC > - < data - background MC >)/< data - background MC > and the bias standard deviation(σ) is the significance of the discrepancy between MC and data. Lots of uds contamination for the high Remc region can be seen. Figure 4.6 shows Rm after geometrical cut. We can see lots of $\tau\tau$ contamination in the ISR region.

Since an ISR photon normally makes a very small angle with the beam pipe, it usually escapes detection. So some energy of ISR events in signal is not detectable giving Rm<1. Therefore we can expect contamination for ISR events in the signal process by other MC events containing neutrinos. It will be explained soon how these contaminations are excluded while conserving $\mu\mu$ events.

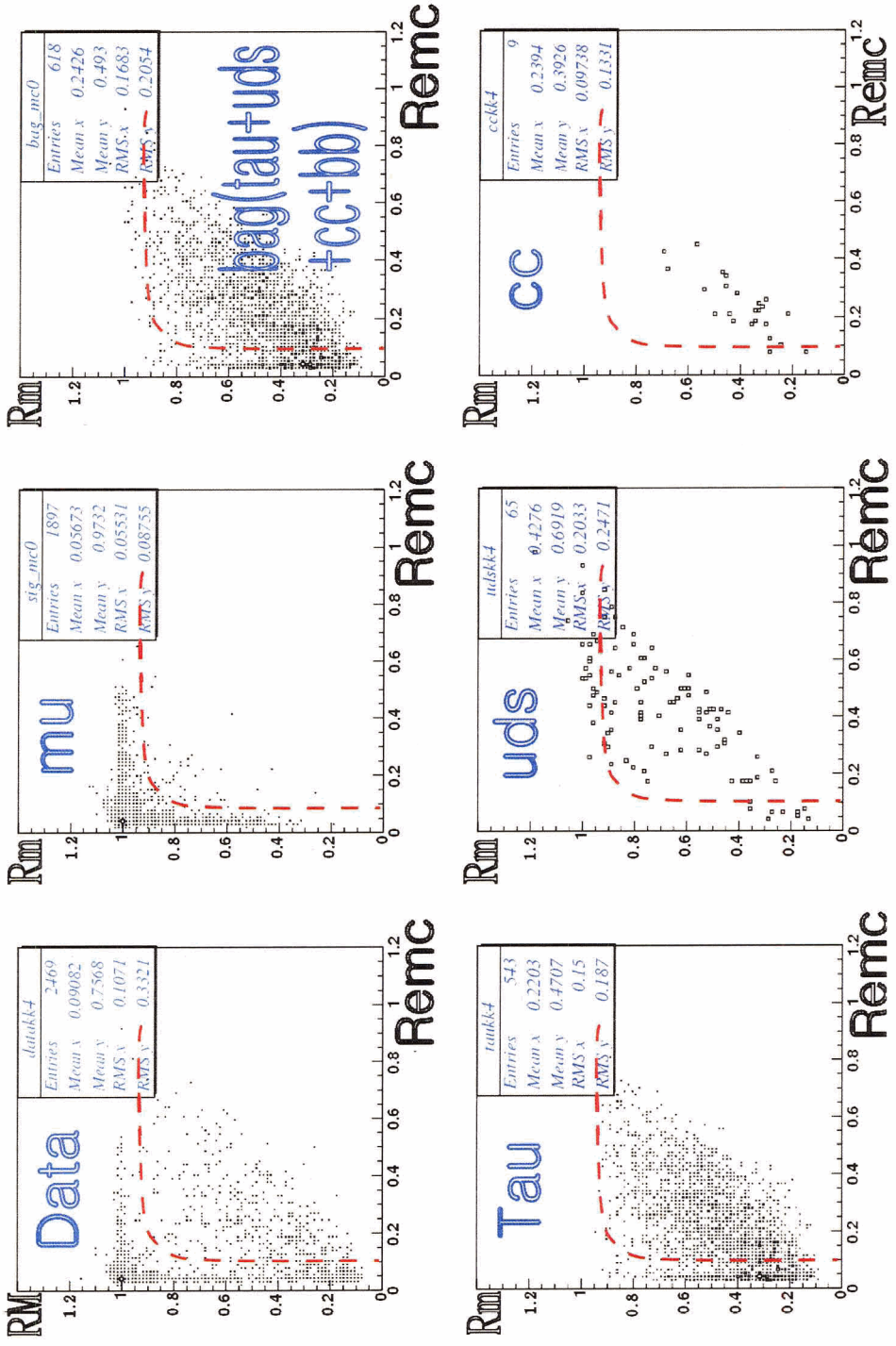

Figure 4.4: Rm vs Remc Upper:For data, MC sig($\mu\mu$), MC background($\tau\tau$+uds+$c\bar{c}$+$b\bar{b}$) Lower:For $\tau\tau$, uds, $c\bar{c}$. Note dashed curve indicates the geometrical cut to select $\mu\mu$ events.

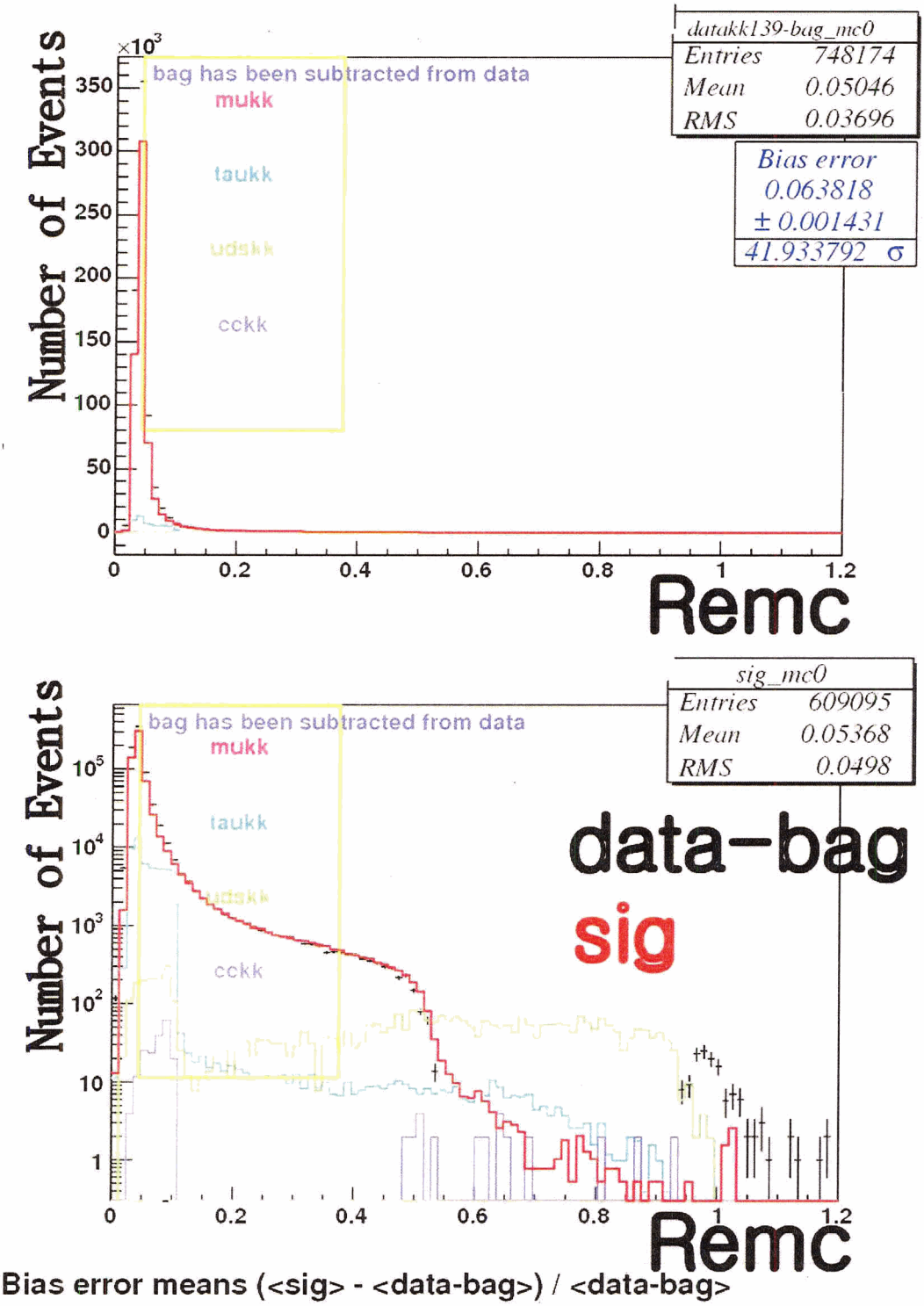

Figure 4.5: Remc after geometrical cut. Note that points with error bars do not represent only data. They represent data minus background. Red line histograms represent KK2f MC for $e^+e^- \to \mu^+\mu^-(\gamma)$

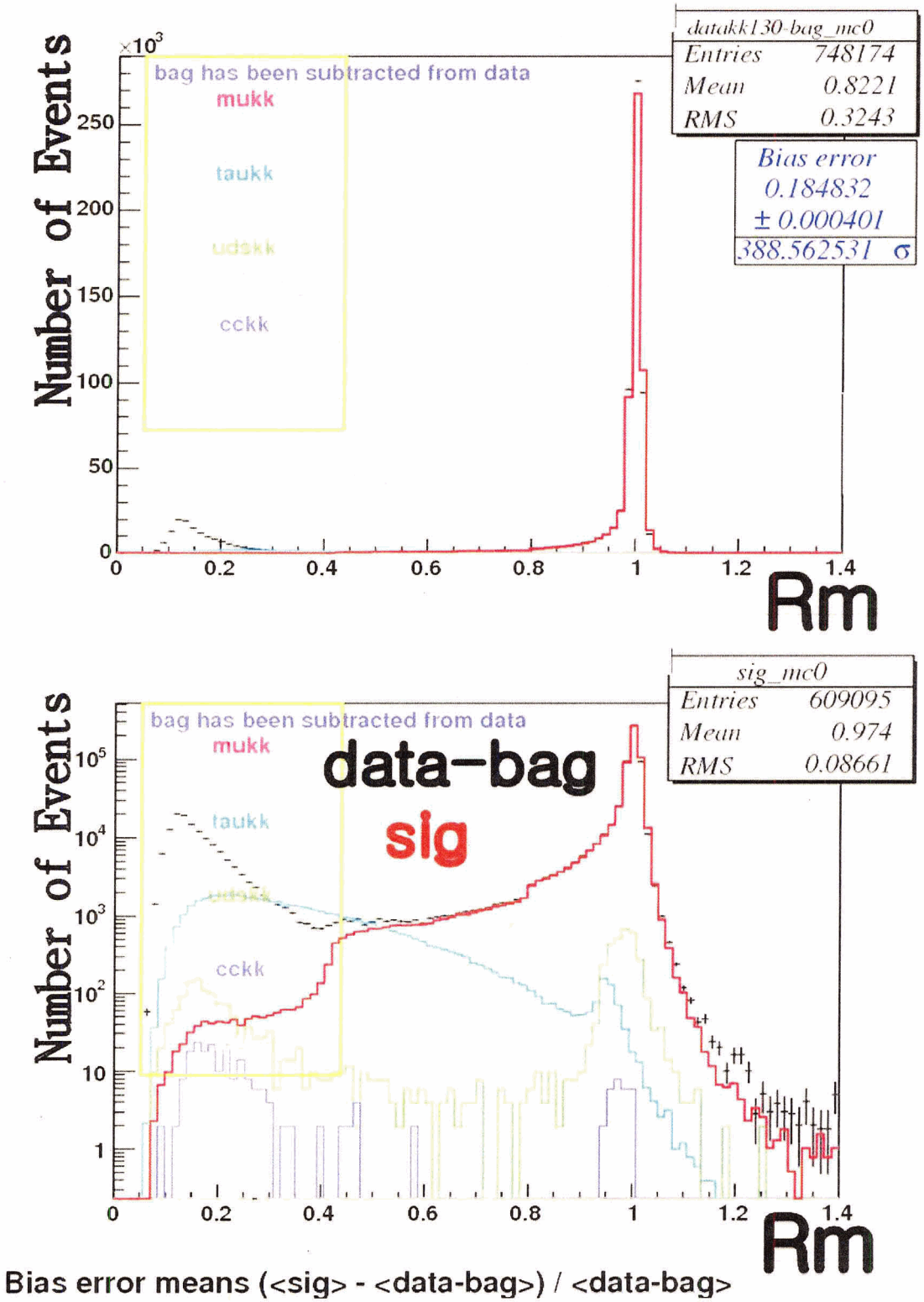

Figure 4.6: Rm after geometrical cut

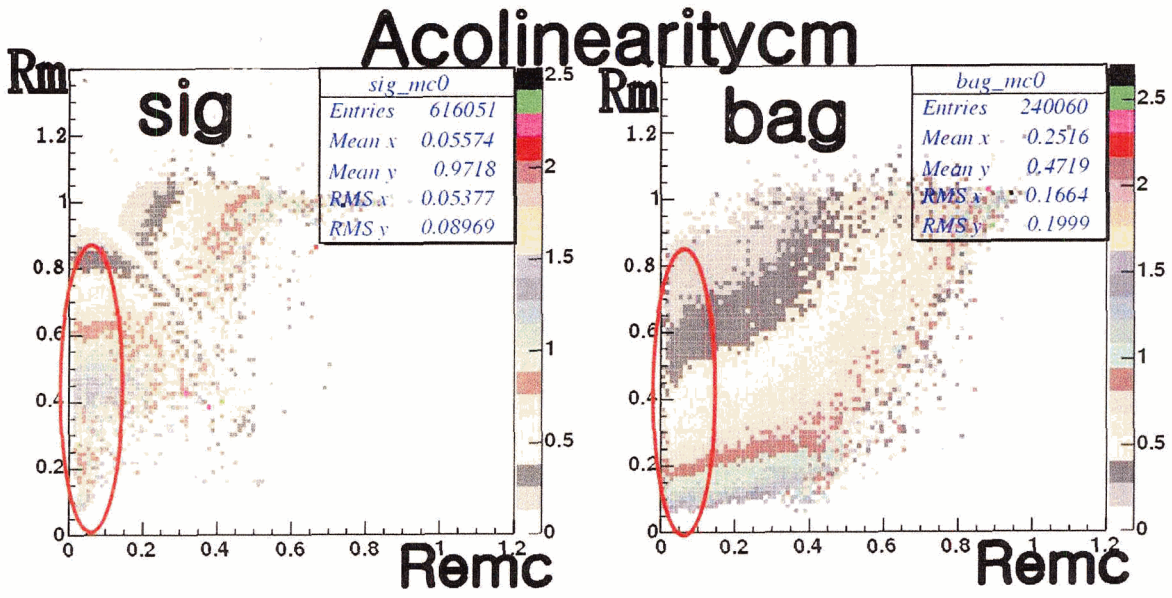

Figure 4.7: Acolinearitycm between μ^+ and μ^- in CM after geometrical cut Left:signal MC($\mu\mu$) Right:background MC($\tau\tau$ + uds). Red ellipse is ISR region.

4.4 Improving $\mu\mu(\gamma)$ events selection 1 - Extended cut

Figure 4.7 shows the acolinearitycm between two tracks in CM after the geometrical cut. There is a clear difference between signal and background in the ISR region.

In the Rm vs Remc 2D histogram (figure 4.8) we can divide it into three region: no radiation region, ISR region and FSR region. Each region represents different kinematic properties. If each MC is different for a specific physical quantity, the degree of difference would vary from region to region. For this reason it has been decided to check out the difference in physical quantities between MC for each region of Figure

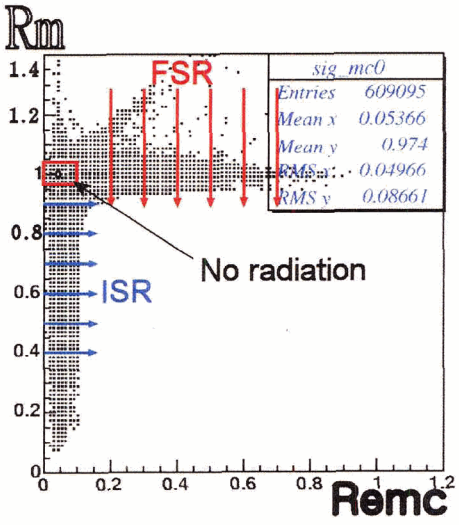

Figure 4.8: Dividing into sub-regions for mu MC. Each region represents different kinematic properties.

4.8.

We begin with the ISR region. Figure 4.9 shows the acolinearitycm between μ^+ and μ^- for sub-region 0.4<Rm<0.5 and 0.5<Rm<0.6. We can see the same quantities for sub-region 0.6<Rm<0.7 and 0.7<Rm<0.8 in Figure 4.10. We conclude that we can use the distribution of acolinearitycm to distinguish signal from background for sub-region 0.4<Rm<0.7 . For sub-region Rm<0.4 there were too few signal events compared to background events and there is too much two-photon event contamination, we simply cut it altogether. Figure 4.11 drawn for sub-region(0.2<Rm<0.3) shows the small energy of each track, small acoplanaritycm between two tracks and small energy of the most energetic photon. These are the properties of two-photon events. But these are also properties of ISR events. Thus, in fact, we don't know whether these are two-photon events which are not modelled in MC, or ISR events which implies that KK2f does not describe ISR events well for sub-region Rm<0.3 or both at the same time. If a significant number of these events are two-photon events, then this sub-region is outside of the scope of my study, because there are no two-photon events MC.

Therefore, the first extended cut

$$\text{acolinearitycm} > -3.75 \times \text{Rm} + 2.94$$

has been applied for sub-region 0.4<Rm<0.8. If we apply this cut, we can find that it does not change much in the 0.7<Rm<0.8 sub-region. It is possible to cut off background contamination in that region but it is not done because bottom figure of 4.10 didn't show clear discrimination between signal and background.

As a next step let us look at the FSR sub-region a little more closely. From Figure 4.5 we can see there is more uds contamination than $\tau\tau$ contamination for FSR region. We can see Bhabha events around Remc≈1 area clearly and there are not many FSR μ events above 0.6 compared to total FSR μ events and uds, $\tau\tau$ contamination. The energy distribution of

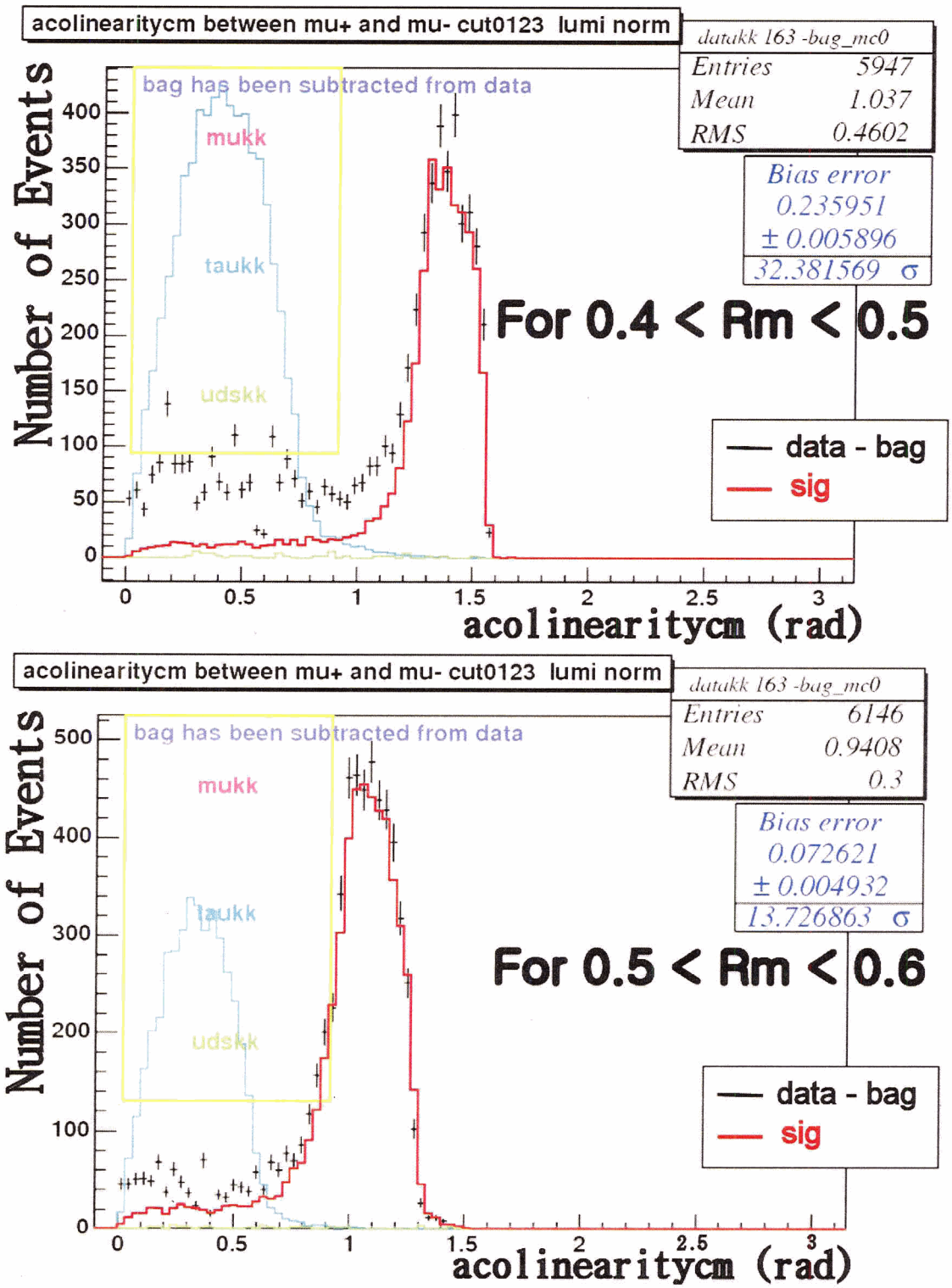

Figure 4.9: Acolinearitycm Upper : for sub-region(0.4<Rm<0.5) Lower : for sub-region(0.5<Rm<0.6)

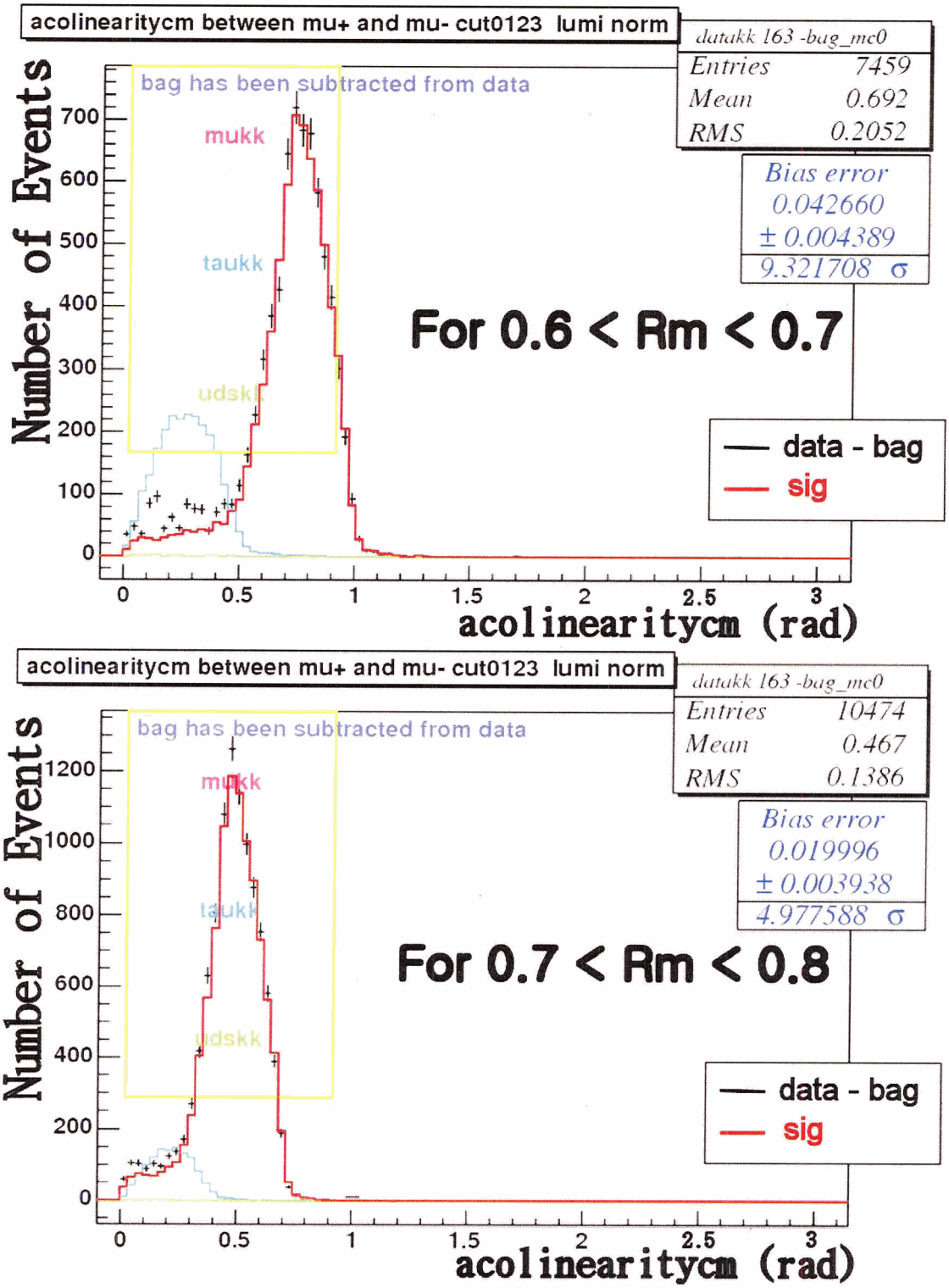

Figure 4.10: Acolinearitycm Upper : for sub-region(0.6<Rm<0.7) Lower : for sub-region(0.7<Rm<0.8)

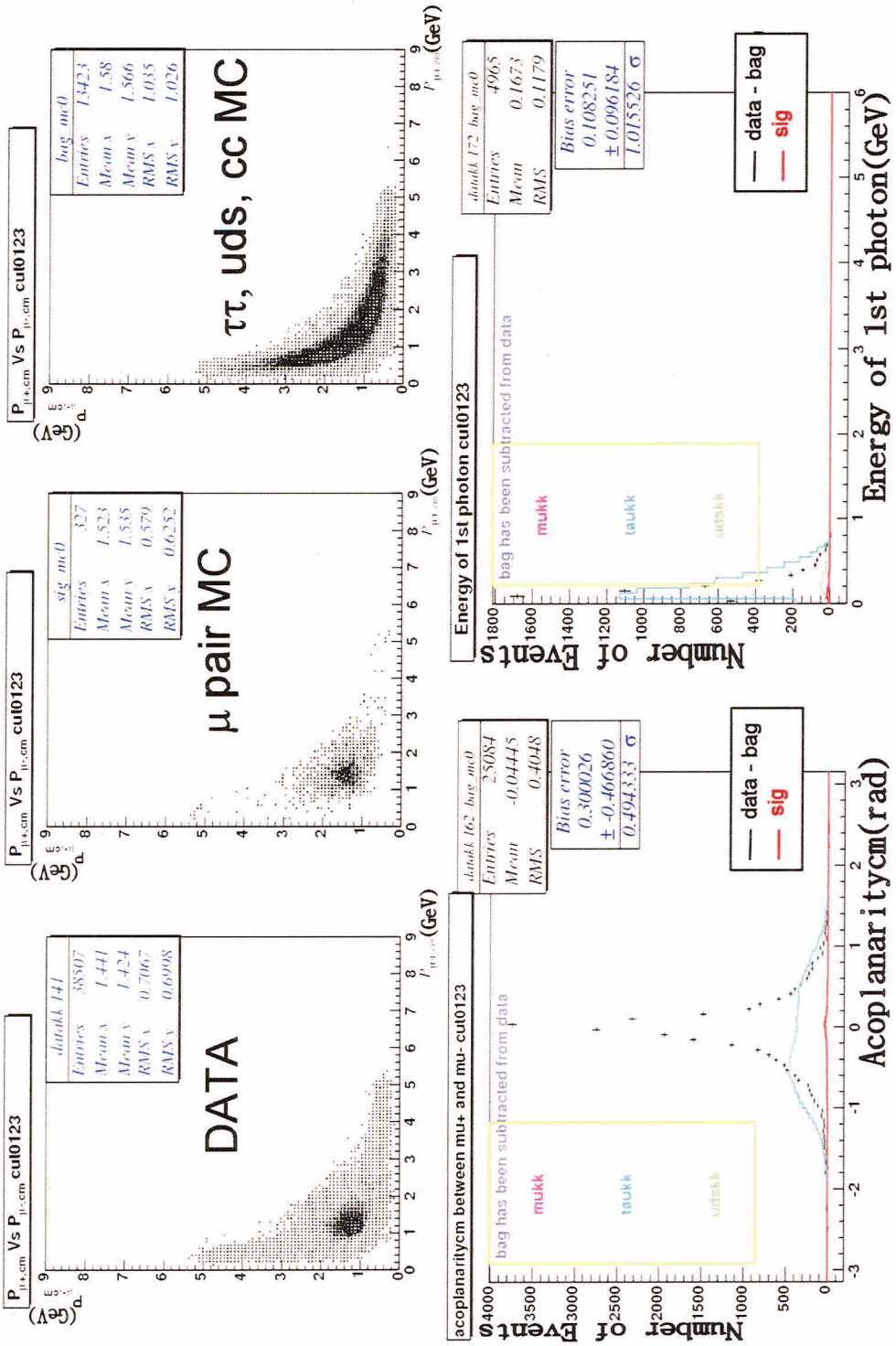

Figure 4.11: For sub-region(0.2<Rm<0.3) Upper : $P_{\mu^-} vs P_{\mu^+}$ Lower-left : acoplanaritycm Lower-right : energy of highest energy photon

the most energetic photon($E_{\gamma 1,CM}$) in CM has been plotted for each sub-region of FSR in Figures 4.12 and 4.13. From these histograms we can get the extended cut to exclude uds and $\tau\tau$ contamination in the FSR region. The second extended cut

$$\text{Energy of the most energetic photon} > 13 \times \text{Remc} - 2.95$$

has been applied for photon events on 0.1<Remc<0.6 FSR region. We can see from the bottom Figure of 4.13 that it is not worth applying this extended cut to the 0.6<Remc sub-region where there are not many FSR μ events and there is a large background contamination from Bhabha.

Before determining the extended cut, I had tried using a simple cut

$$\text{Rm} > 0.4 \text{ and } \text{Remc} < 0.45$$

to eliminate the major $\tau\tau$ and uds contamination. The result of this simple cut and the extended cuts have been compared. Using the simple cut, the efficiency of $\mu\mu$ was 52.16% and purity of $\mu\mu$ was 98.39%. Applying extended cut the efficiency of $\mu\mu$ is 52.41% and purity of $\mu\mu$ is 99.57%. The point is not only the numerical improvement but also the improvement on high radiation region where we are especially interested in testing the MC.

Figure 4.14 shows acolinearitycm versus Rm after the extended cuts. Because the extended cuts are almost not applied to the 0.7<Rm<0.8 sub-region there still exist some disagreement for that region.

Figures 4.15, 4.16 and 4.17 shows the result of extended cuts for Rp+($\equiv P_{\mu^+,CM}/P^{max}_{\mu,CM}$), Rp-($\equiv P_{\mu^-,CM}/P^{max}_{\mu,CM}$), Rp±($\equiv P_{\mu^\pm,CM}/P^{max}_{\mu,CM}$), respectively.

Here $P^{max}_{\mu,CM}$ means $\sqrt{(E_{beam}/2)^2 - m_\mu^2}$. We can see the bias error of $P_{\mu^\pm,CM}/P^{max}_{\mu,CM}$ is 0.0719%.

Figures 4.18 and 4.19 show Remc and Rm, respectively, after applying the extended cuts. Comparing with Figure 4.5 and 4.6 we can see the improvement of reducing $\tau\tau$ and

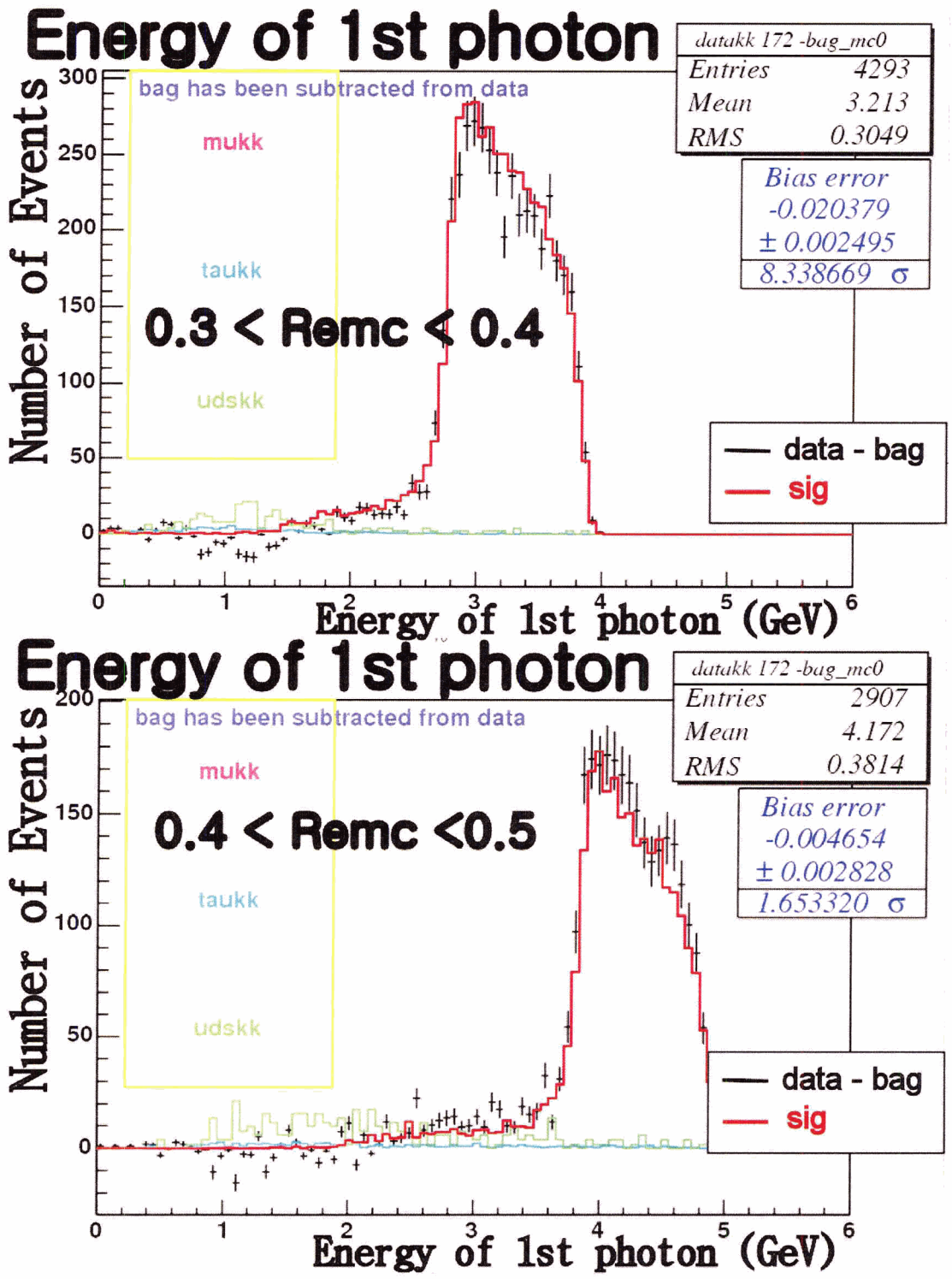

Figure 4.12: $E_{\gamma 1,CM}$ Upper:0.3<Remc<0.4, Lower:0.4<Remc<0.5. We can exclude many uds contamination in the FSR region.

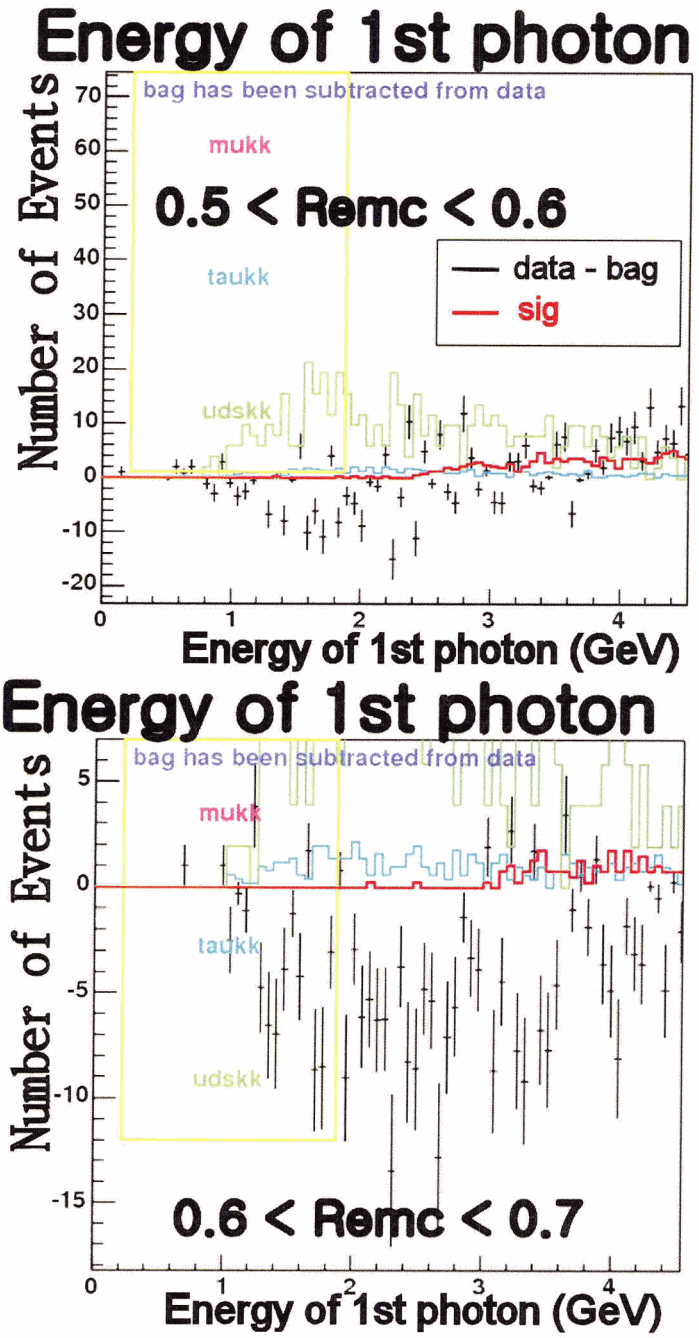

Figure 4.13: $E_{\gamma 1,CM}$Upper:0.5<Remc<0.6, Lower:0.6<Remc<0.7. We can exclude many uds contamination in the FSR region.

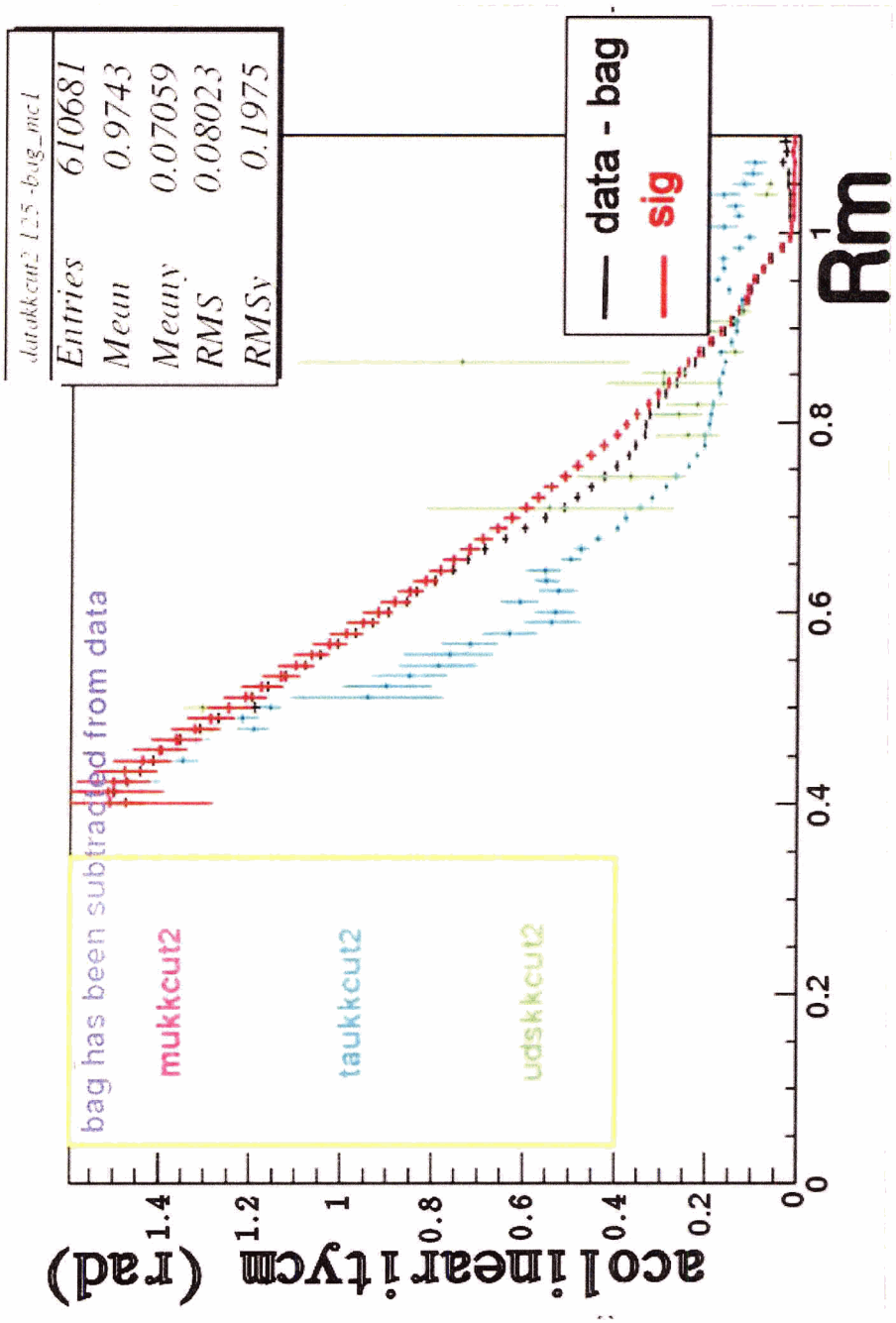

Figure 4.14: Profile of acolinearitycm vs Rm after extended cut

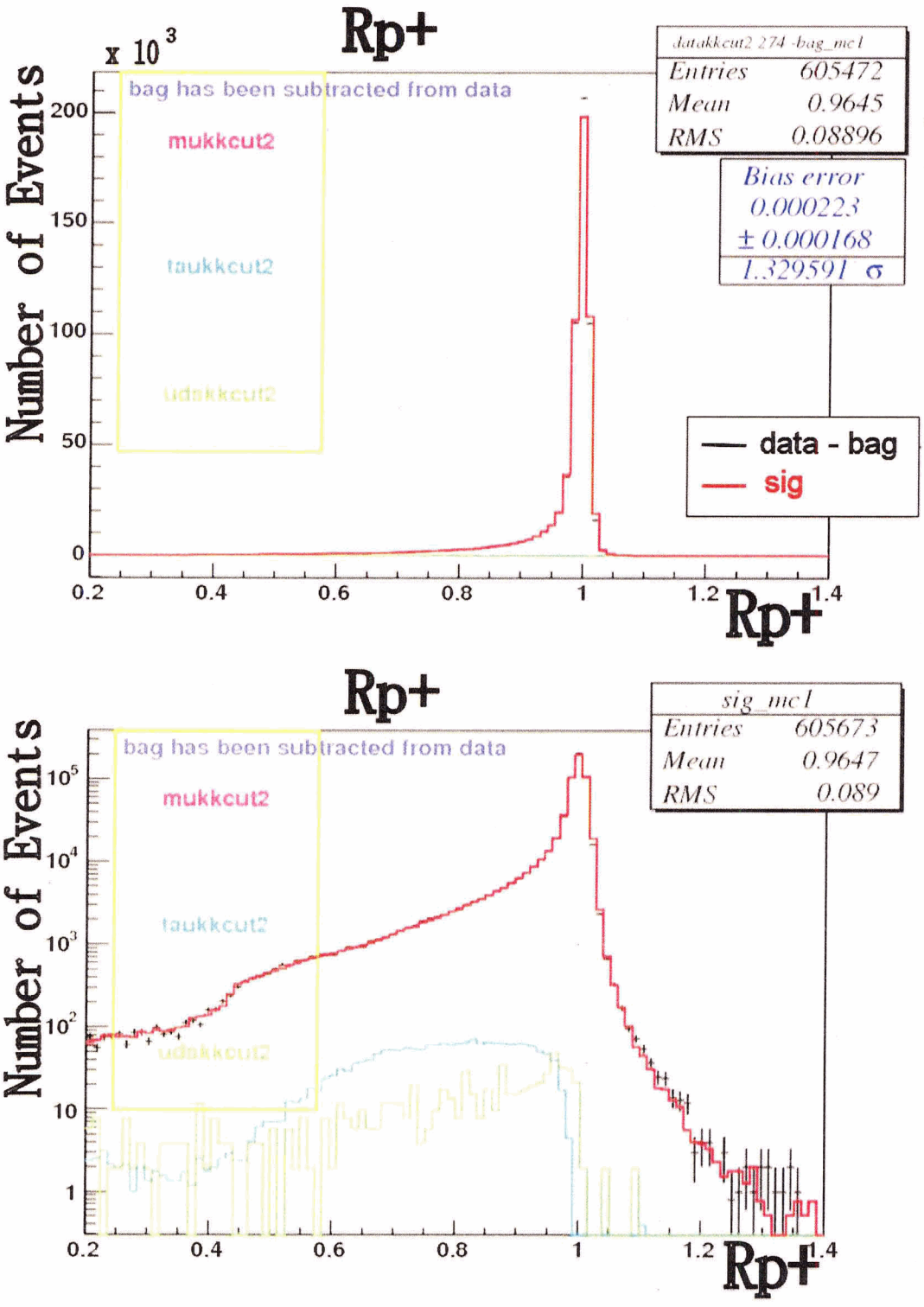

Figure 4.15: $P_{\mu^+,CM}/P^{max}_{\mu,CM}$ after extended cut

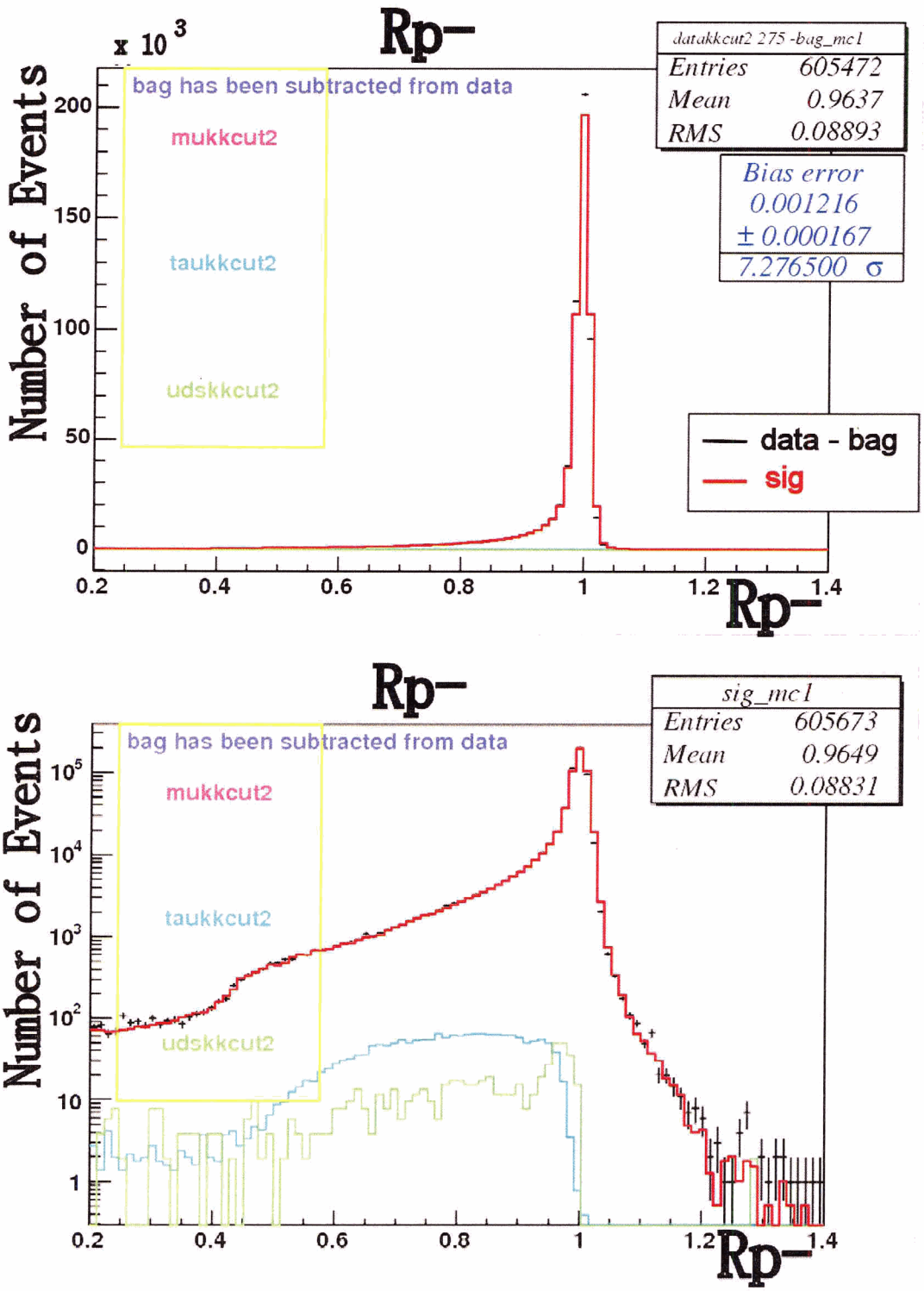

Figure 4.16: $P_{\mu^-,CM}/P^{max}_{\mu,CM}$ after extended cut

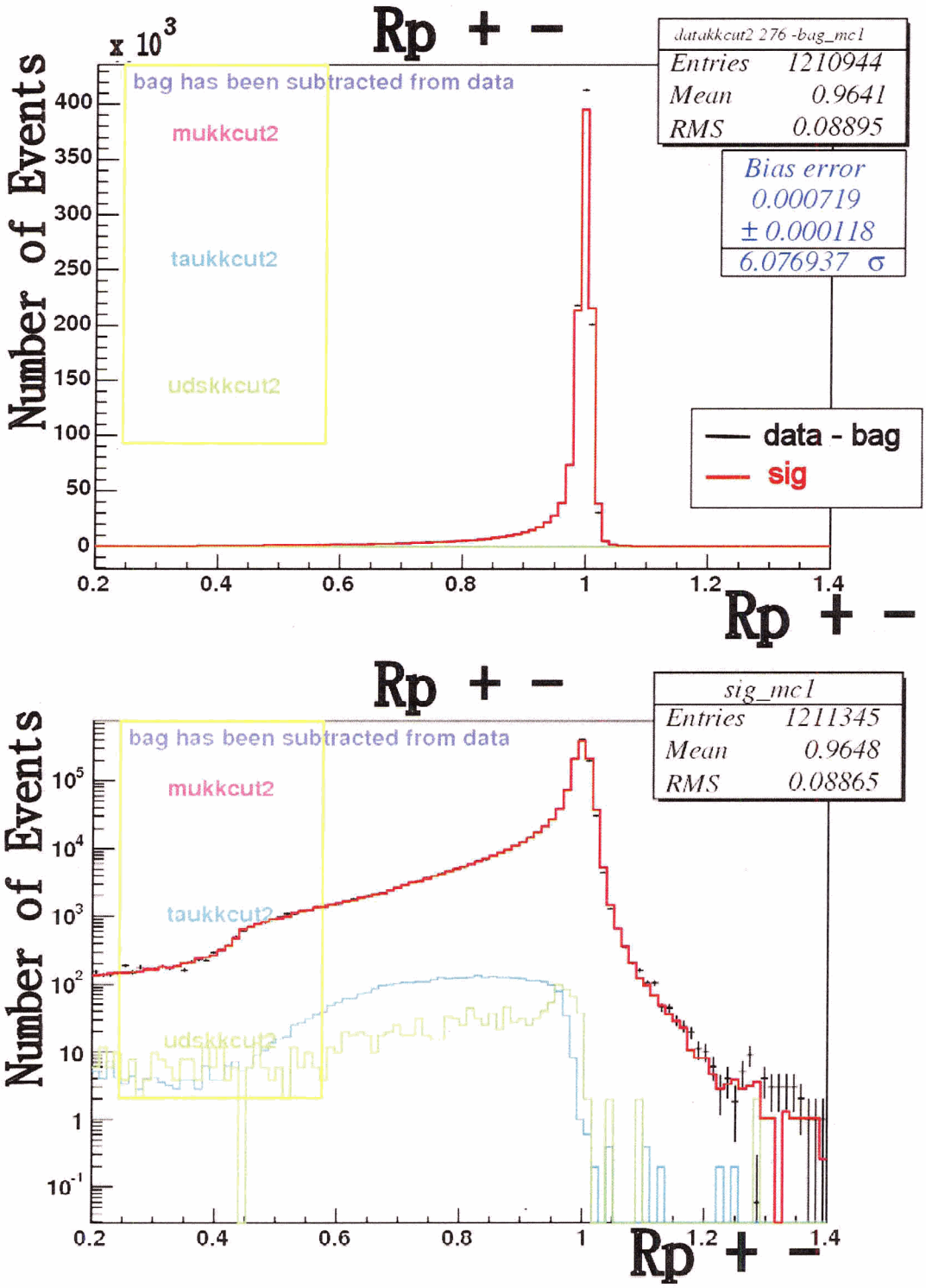

Figure 4.17: $P_{\mu^{\pm},CM}/P^{max}_{\mu,CM}$ after extended cut

uds contamination. We note that there is some disagreement around Remc $\approx$ 0.5. We can see slightly more data events than MC events around $E_\gamma \approx 5$ on Figure 4.20. These extra events of data have been observed even limiting the number of photons to 1. But applying simple cut (Rm>0.4 and Remc<0.45) did not show these extra events. This implies that the disagreement emerged when we added more FSR region. So it must come from the added FSR region. Figure 4.21 shows the distribution of $E_{\mu onEMC}$ (Energy deposition of muon on EMC in Lab) versus $P_{\mu,CM}$ for data. Some events which do not exist in MC emerged for $E_{\mu^- onEMC}$ vs $P_{\mu^-,CM}$ but not many for $E_{\mu^+ onEMC}$ vs $P_{\mu^+,CM}$. The $\mu^+\mu^-$ MC did not show any of these extra events for either μ^+ or μ^-. We can clearly see the effect of these extra events on dashed line of Figure 4.22 which is a plot of average $E_{\mu onEMC}$ vs $P_{\mu,CM}$ Let's look at these extra events more closely.

4.5 Improving $\mu\mu(\gamma)$ events selection 2 - Final cut

Events shown inside dashed line of Figure 4.21 were next selected and studied. The selection of extra events is shown in Figure 4.23 for data. Note that events circled in red correspond to each other.

The upper part of Figure 4.24 shows $E_{\mu^+,CMonEMC} + E_{\mu^-,CMonEMC}$. The left side is after the extended cuts and right side is for only extra events. Comparing these two we can see that the disagreement below the 2 GeV region may come from extra events. But it tells us that the disagreement above 2 GeV does not come from extra events. It will be discussed soon.

Figure 4.25 shows that the energy of the second energetic photon($E_{\gamma 2,CM}$) is negligible compared to the energy of the most energetic photon($E_{\gamma 1,CM}$) for extra events. Comparing the same way in figures 4.24, 4.25, 4.26, 4.27 and 4.28 we can conclude that they imply that the disagreement which emerged after applying the extended cut can be eliminated or at least can be reduced by excluding these extra events. But before we exclude the extra

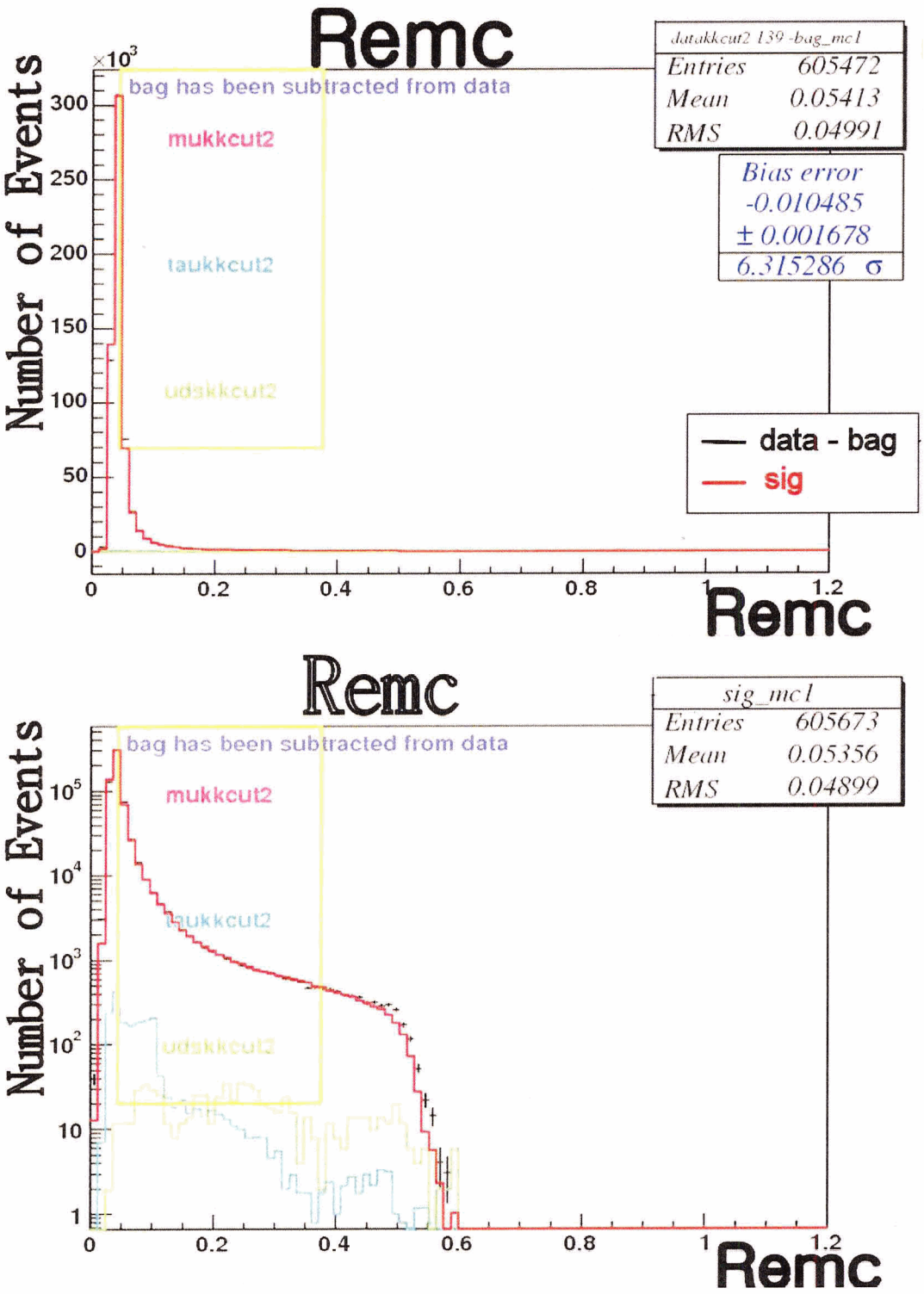

Figure 4.18: Remc after extended cut

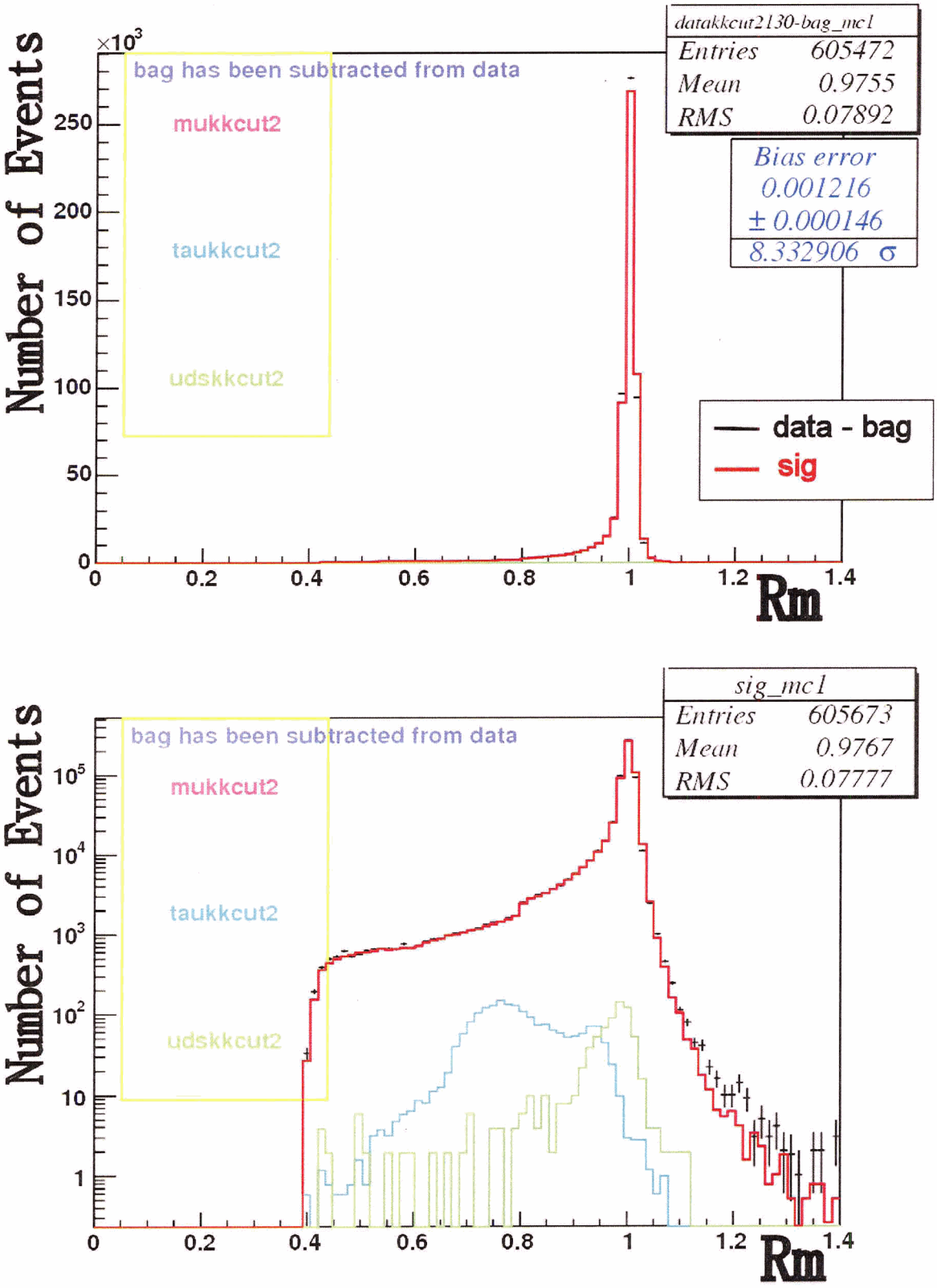

Figure 4.19: Rm after extended cut

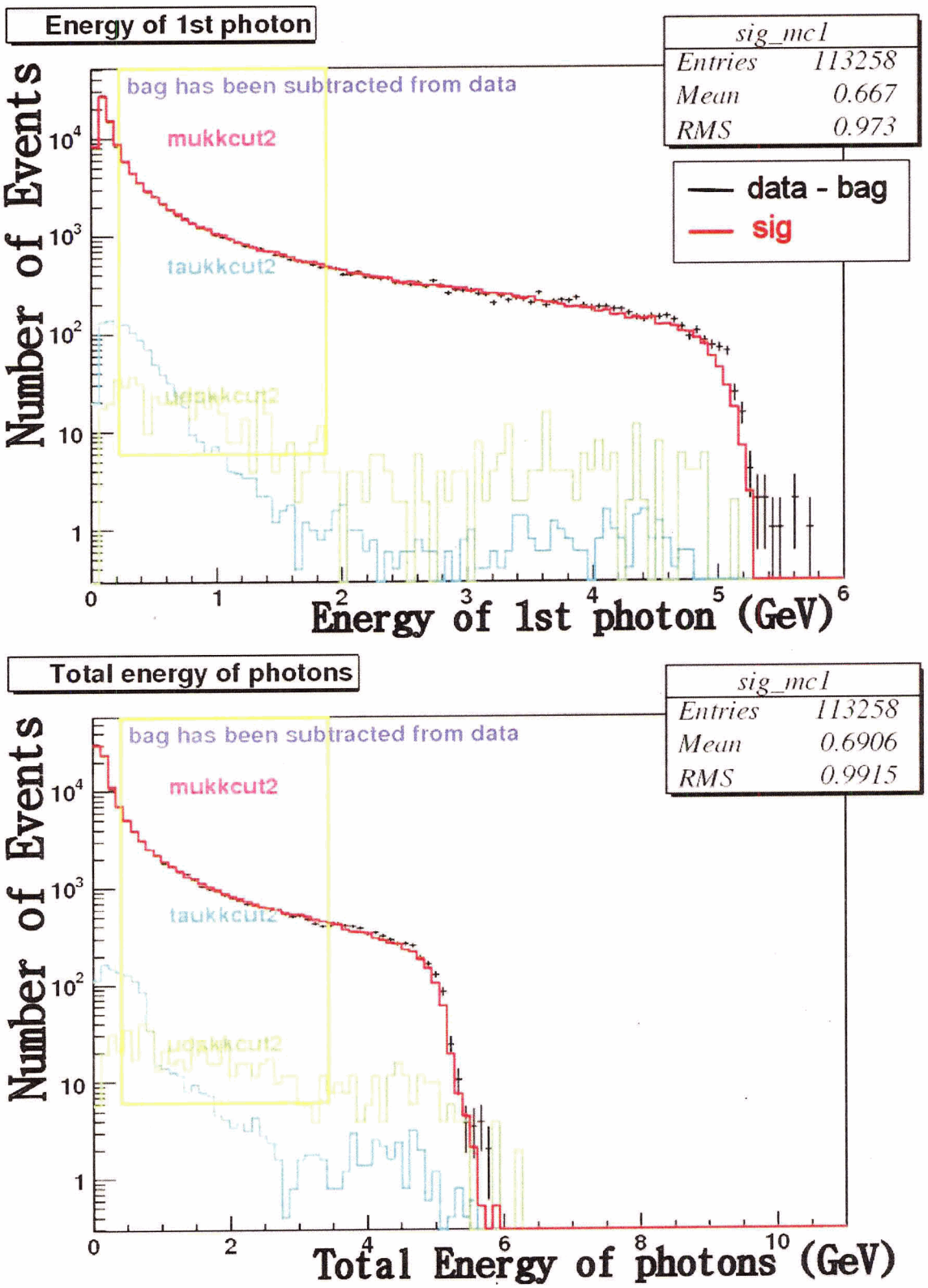

Figure 4.20: Upper:$E_{\gamma 1,CM}$ Lower:$\Sigma E_{\gamma,CM}$ After extended cut

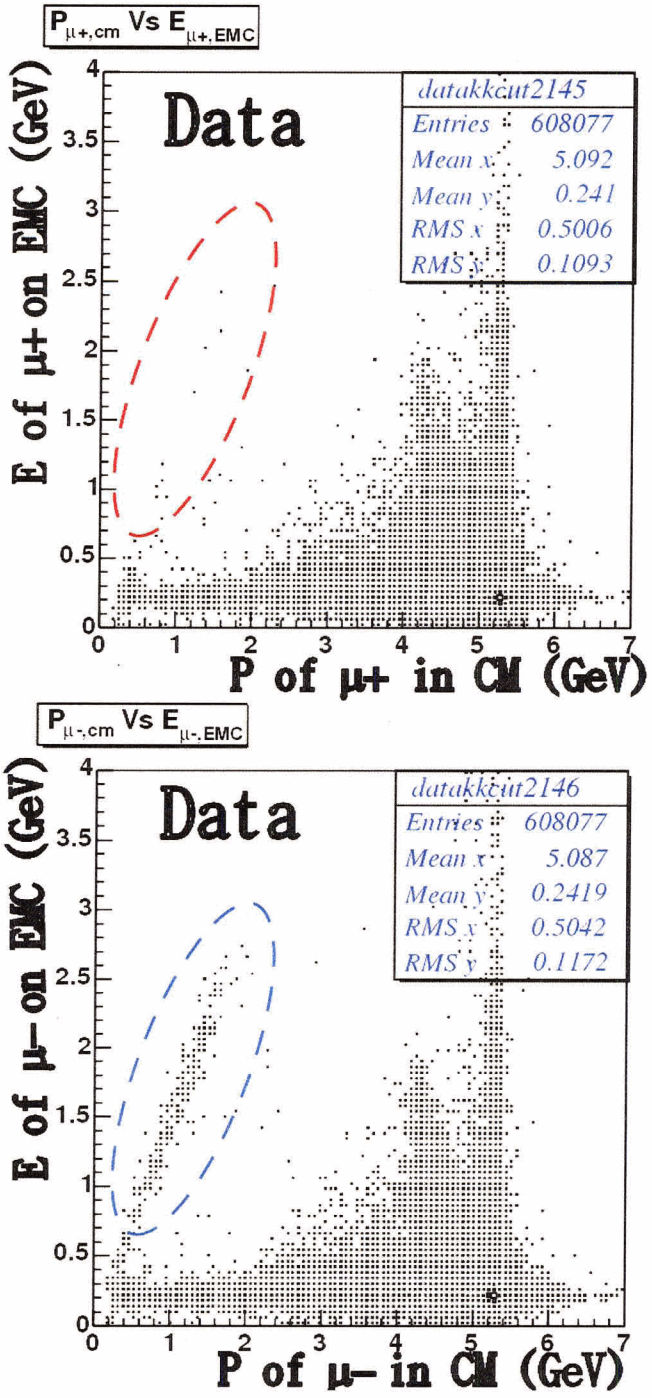

Figure 4.21: Upper:$E_{\mu^+ onEMC}$ vs $P_{\mu^+,CM}$ Lower:$E_{\mu^- onEMC}$ vs $P_{\mu^-,CM}$ After extended cut for data.

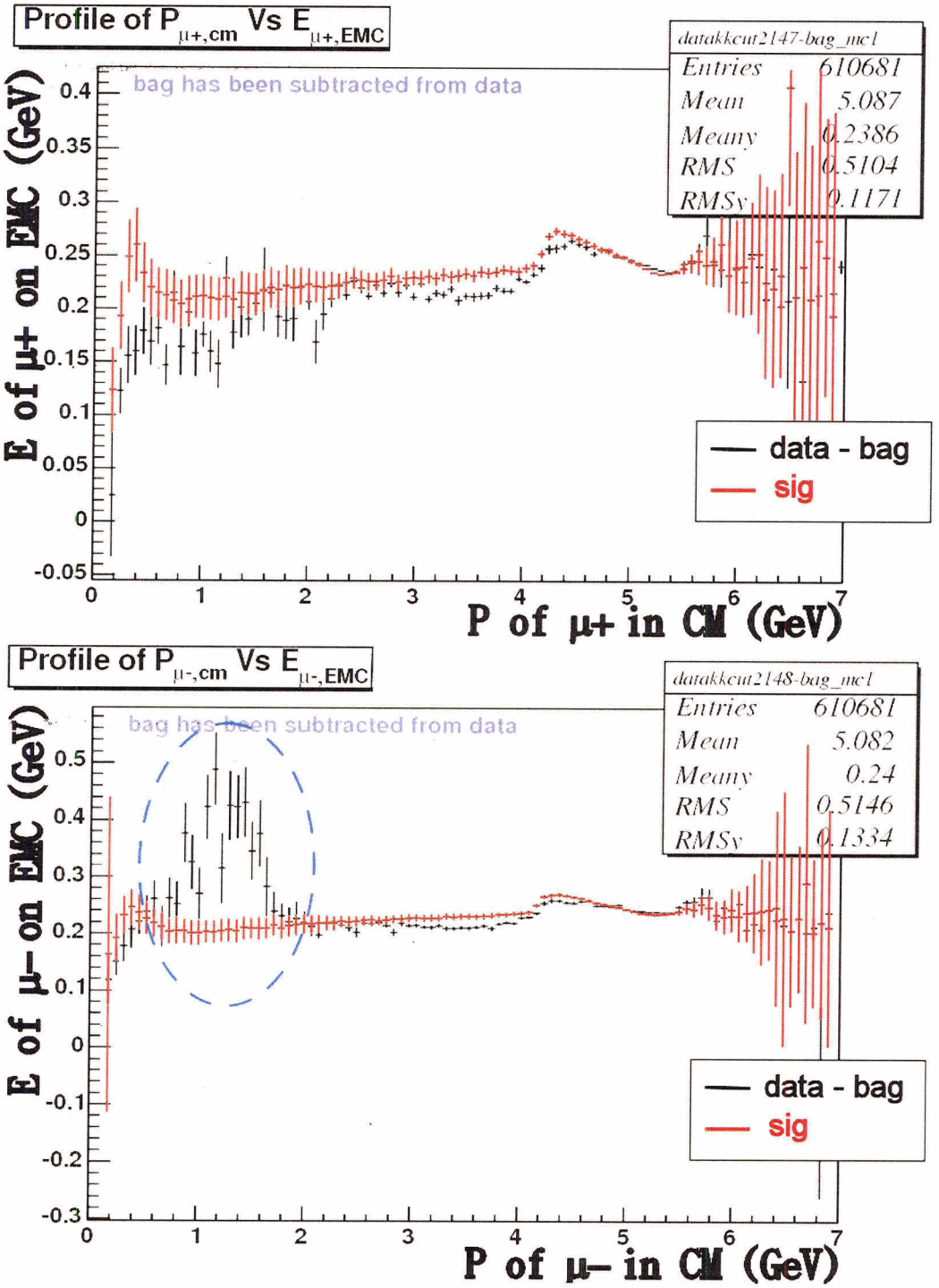

Figure 4.22: Upper:$< E_{\mu^+ onEMC} >$ vs $P_{\mu^+,CM}$ Lower:$< E_{\mu^- onEMC} >$ vs $P_{\mu^-,CM}$ After extended cut. The events inside dashed ellipse correspond to the events inside dashed ellipse in 4.21. The $\mu^+\mu^-$ MC did not show any of these extra events for either μ^+ or μ^-.

events we have to be confident to say that "These extra events are all background events" because it might be the kind of problem with MC we are trying to uncover.

Thus the properties of extra events were examined further in Figures 4.29 and 4.30 in addition to the previous figures. We can check that they are back to back events (Upper-right of Figure 4.29, Upper Figure 4.30), positive particles go in the backward direction and negative particles go in the forward direction(Lower Figure 4.30). Photons go to almost the same direction as negative charged particle (Lower-right of Figure 4.28). These are associated with photons radiated from the negative charged particle and the momentum of the negative charged particle is less than 2GeV (Lower-right of Figure 4.29). These extra events have high energy photons (Lower-left of Figure 4.29) and the measured total energy is consistent with the CM energy (Rm=1 in Upper-left of Figure 4.29). It has also been checked that the total measured momentum of the event is zero. These pieces of evidence indicate that they are leptonic events.

$E_{\mu^- onEMC}$ versus $P_{\mu^-,CM}$ has been plotted for the events with $P_{\mu^-,CM} < 2$ GeV from the ISR region on Figure 4.31 to get the property of a normal muon with momentum less than 2 GeV. It says that a μ^- with $P_{\mu^-,CM} < 2$ GeV deposits energy less than 0.5 GeV. Thus, the negative charged particles in the lower part of Figure 4.23 cannot be muons. They must be electrons as can be seen from E/P$\approx$1 in the lower part of Figure 4.23. Then what are the positive charges? The properties of normal muons and extra events are compared in Figure 4.32. Upper histograms plot the minimum of $E_{\mu^+,LABonEMC}$ and $E_{\mu^-,LABonEMC}$. Extra events show different distribution from usual muon distribution. Lower histograms are $dE/dX_{\mu^+} inDCH$. The mean value of $dE/dX_{\mu^+} inDCH$ for muon is about 610, whereas the right Figure shows that extra events have a mean value of $dE/dX_{\mu^+} inDCH$ of about 670. It has been checked that the mean value of $dE/dX_{\mu^+} inDCH$ for electron is about from 670 to 680. It tells us that positive charges are not muons or at least most of them are not muons. They are also electrons likely where the EMC crystal have been missed by

the track.

If they are Bhabha events why do they show the charge asymmetry as shown in figure 4.23? Only the events inside of red line of Figure 4.23 were selected and plotted in Figure 4.33 and Figure 4.34. In this case, positive charges must be positrons. Figure 4.33 and Figure 4.34 imply that at least most of negative charges are not muons. Let's compare the lower part of Figure 4.30 and Figure 4.34. In Figure 4.30 electrons go in the forward direction and positrons go in the backward direction. In Figure 4.34 electrons go in the backward direction and positrons go in the forward direction. It means that a positron or a electron going in the backward direction has more probability of leaving small energy in the EMC than a forward going particle has. Because in Bhabha events, electrons usually go in the forward direction and positrons usually go in the backward direction, we can understand the charge asymmetry in Figure 4.23.

These extra events were excluded as the final cut to extract $e^+e^- \rightarrow \mu^+\mu^-(\gamma)$. Because the number of extra events is very small(less than 0.01%), there is no change in efficiency and purity compared to the extended cut.

Let's check the events of upper-left part of Figure 4.24 indicated by the arrow, which remain after excluding extra events. In upper-right and lower parts of Figure 4.35 and Figures 4.36 and 4.37 only the region of disagreement in the upper-left Figure 4.24 was selected (Sum of track energy associated with EMC $>$ 2 GeV). From Figure 4.36 both tracks have high momentum. From lower part of Figure 4.35 and from middle part of figure 4.36 representing μ MC we can conclude that one of mu particle leaves small energy($<$0.4 GeV) on EMC and the other mu leaves high energy($>$1.0 GeV) on EMC. The upper part of figure 4.37 shows there are more data at large angle for positive charges and more data in small angle for negative charges. So it is suspected that these are from Bhabha contamination. Therefore the big disagreement of upper-left part of Figure 4.24 is likely to come from Bhabha contamination. But these events were not excluded in the final cut because they may not

be Bhabha events. If we compare the lower-left of Figure 4.37 and upper-left of figure 4.25 (small disagreement around 4 GeV) or lower-right of Figure 4.38 (small disagreement around 4.5 GeV) and upper-left of Figure 4.27 (small disagreement around 6 GeV), we can see that these Bhabha suspected events are not responsible for those disagreements.

Some plots of distribution after the final cut excluding extra events were presented in Figure 4.38 and 4.39. We can see that the disagreements have been reduced compared to the extended cut. The bias error for $P_{\mu^{\pm},CM}/P_{\mu,CM}^{max}$ has been improved from 0.0719% of the extended cut to 0.0646% of the final cut.

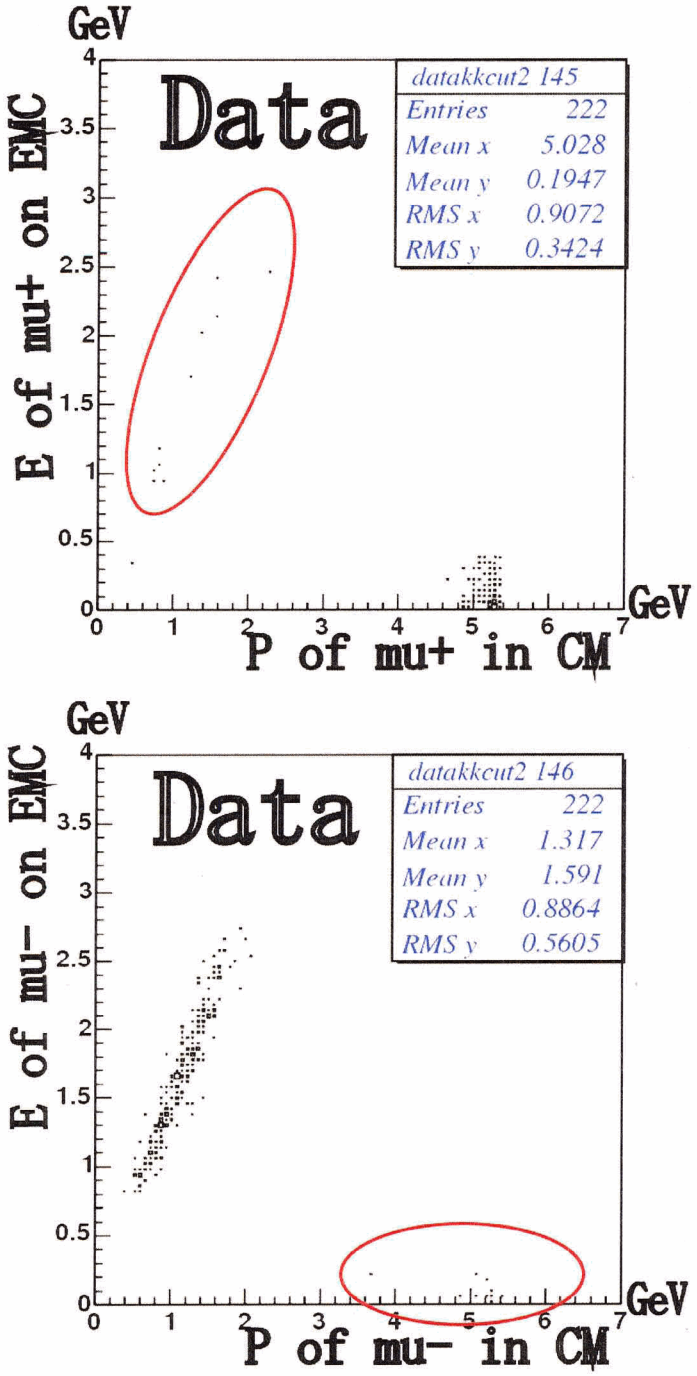

Figure 4.23: Only extra events shown inside dashed line of Figure 4.21 have been selected Upper:$E_{\mu^+,onEMC}$ vs $P_{\mu^+,CM}$ for data Lower:$E_{\mu^-,onEMC}$ vs $P_{\mu^-,CM}$ for data. Note that events circled in red correspond to each other.

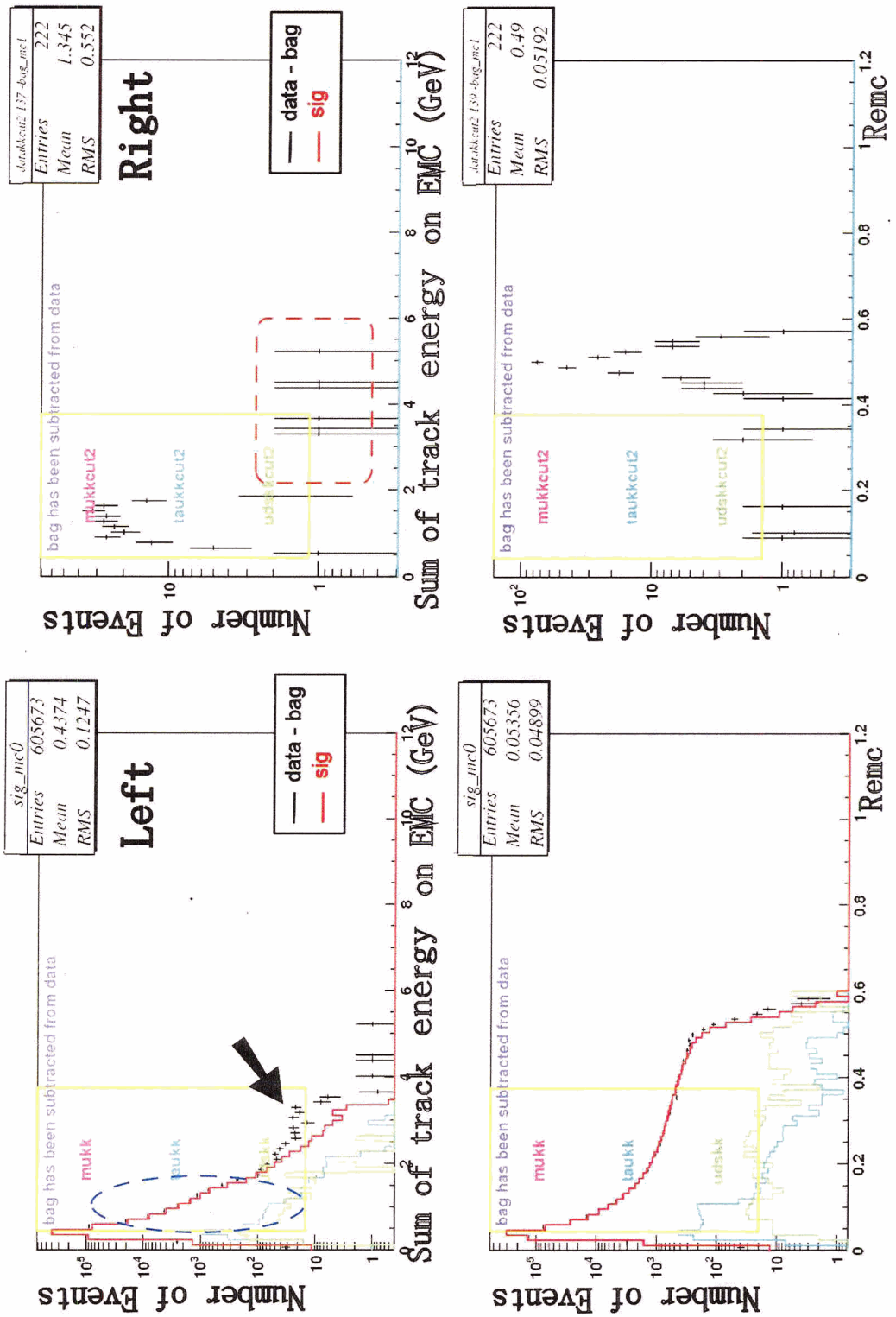

Figure 4.24: Upper:$E_{\mu^+,CMonEMC} + E_{\mu^-,CMonEMC}$ Lower:Remc Left:After extended cut Right:Only extra events selected

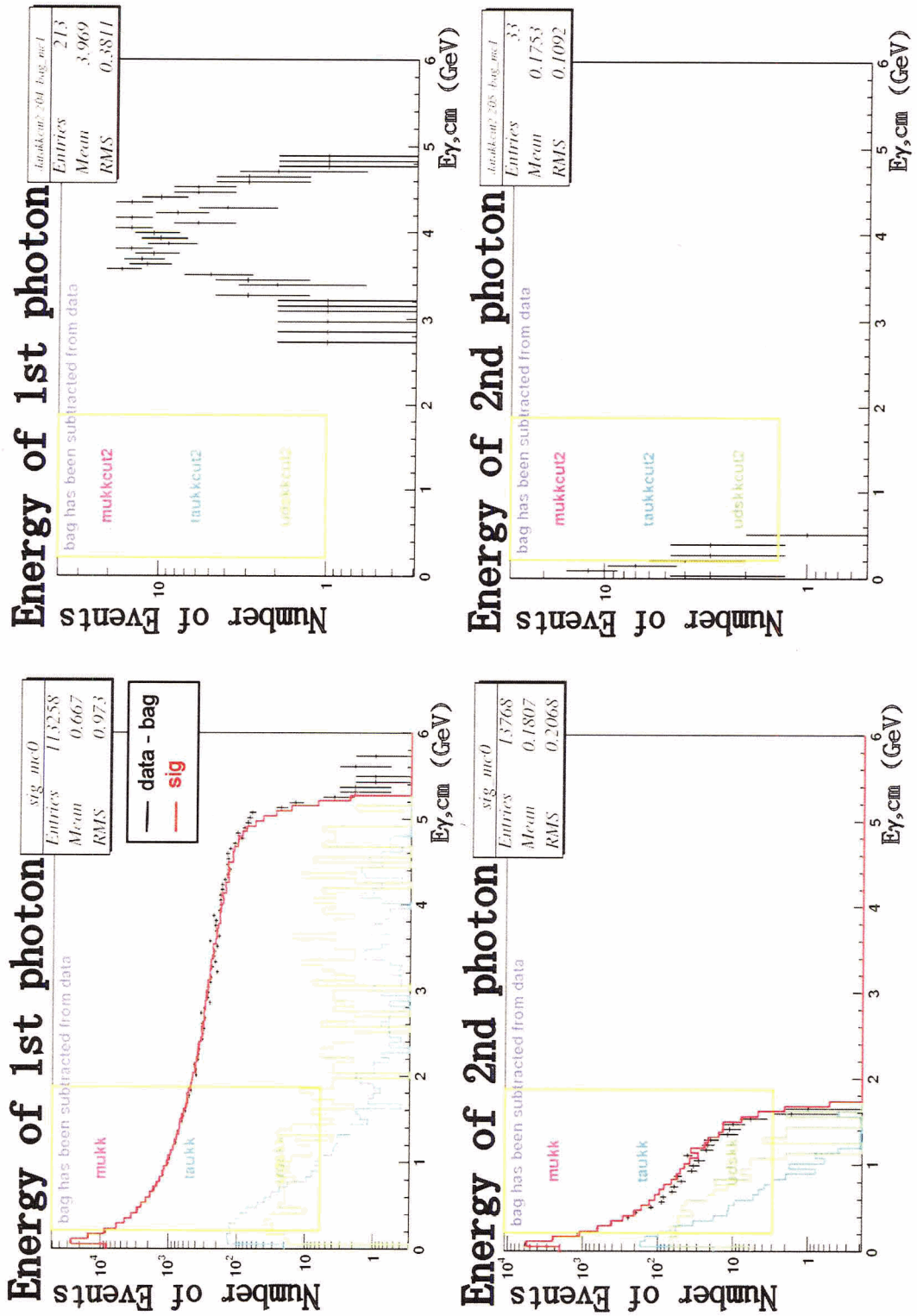

Figure 4.25: Upper:Energy(GeV) of most energetic photon($E_{\gamma 1,CM}$) Lower:Energy(GeV) of second energetic photon($E_{\gamma 2,CM}$) Left:After extended cut Right:Only extra events selected

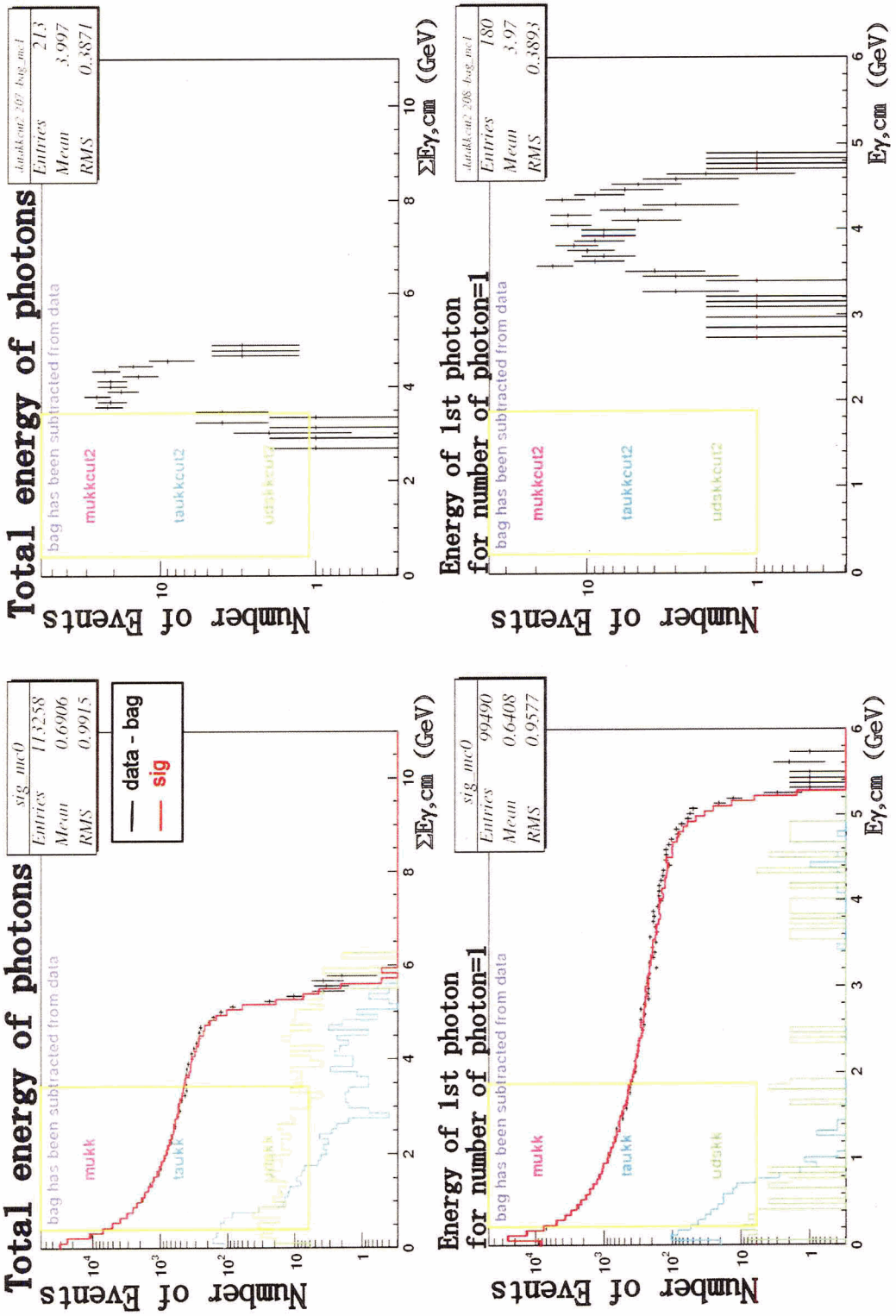

Figure 4.26: Upper:$\Sigma E_{\gamma,CM}$(GeV) Lower:$E_{\gamma 1,CM}$(GeV) for number of photon=1 Left:After extended cut Right:Only extra events selected

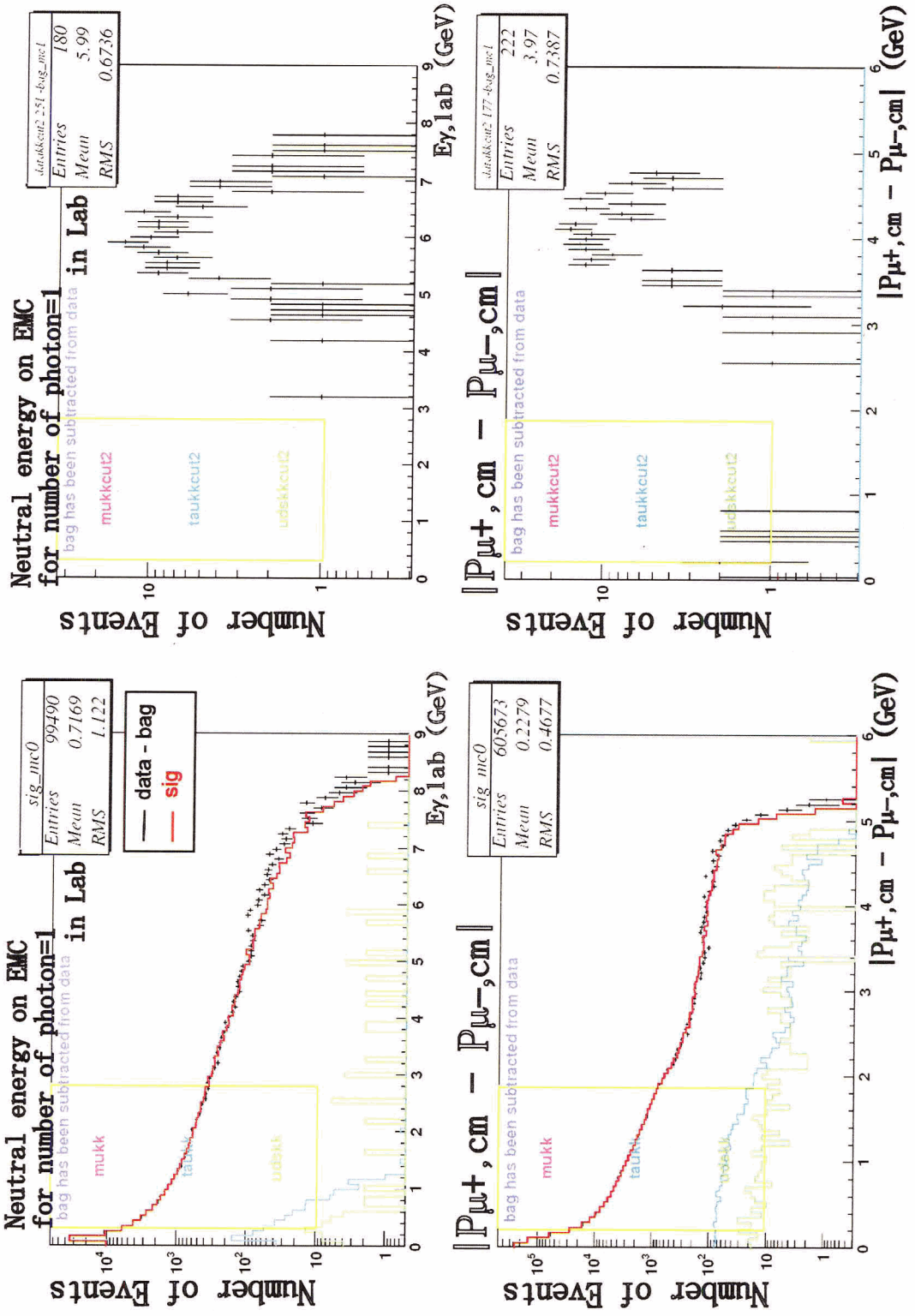

Figure 4.27: Upper:$E_{\gamma 1,lab}$ for number of photon=1 Lower:—$P_{\mu^+,CM} - P_{\mu^-,CM}$— Left:After extended cut Right:Only extra events selected

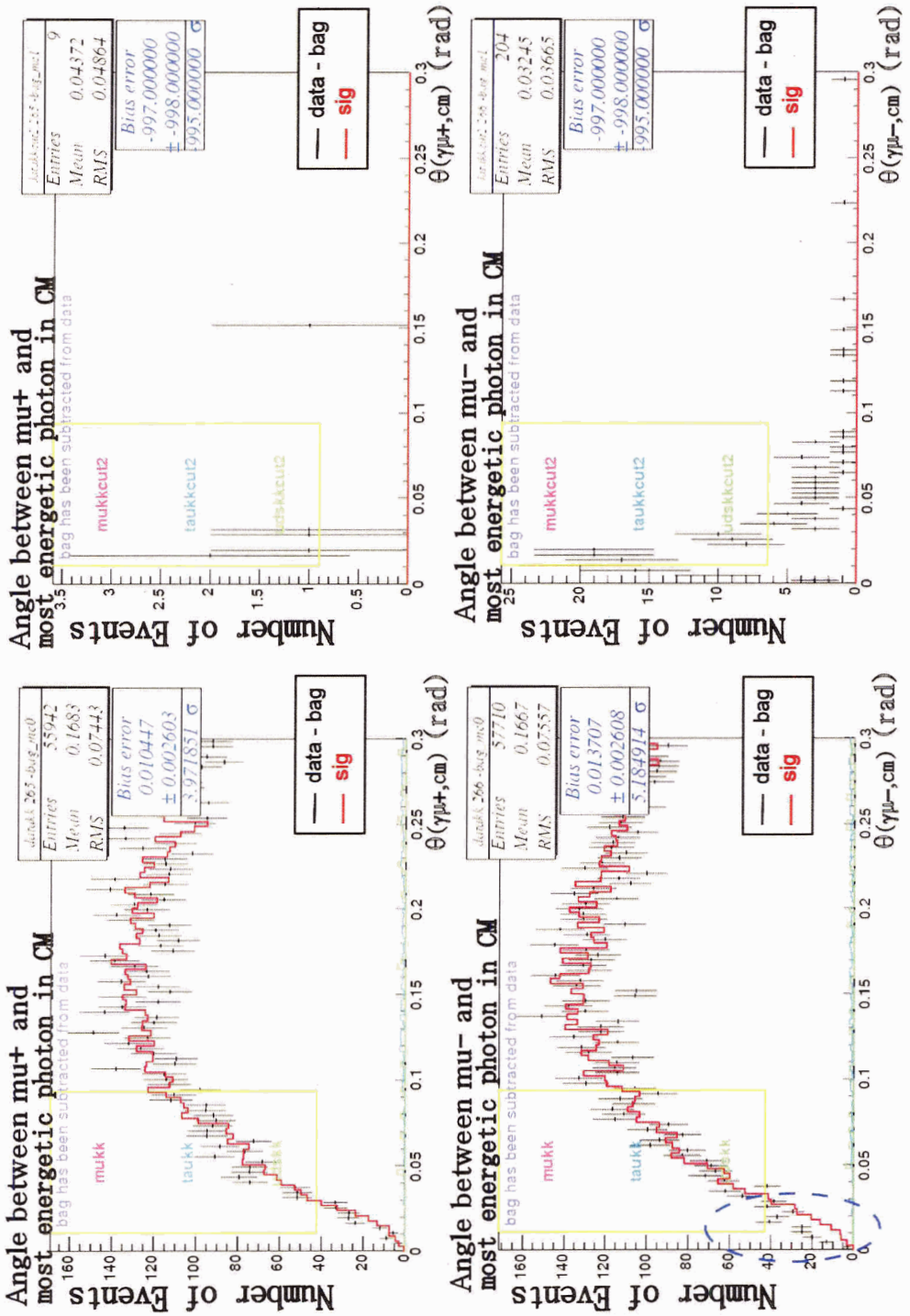

Figure 4.28: Upper:θ between μ^+ and $\gamma 1, CM$ Lower:θ between μ^- and $\gamma 1, CM$ Left:After extended cut Right:Only extra events selected

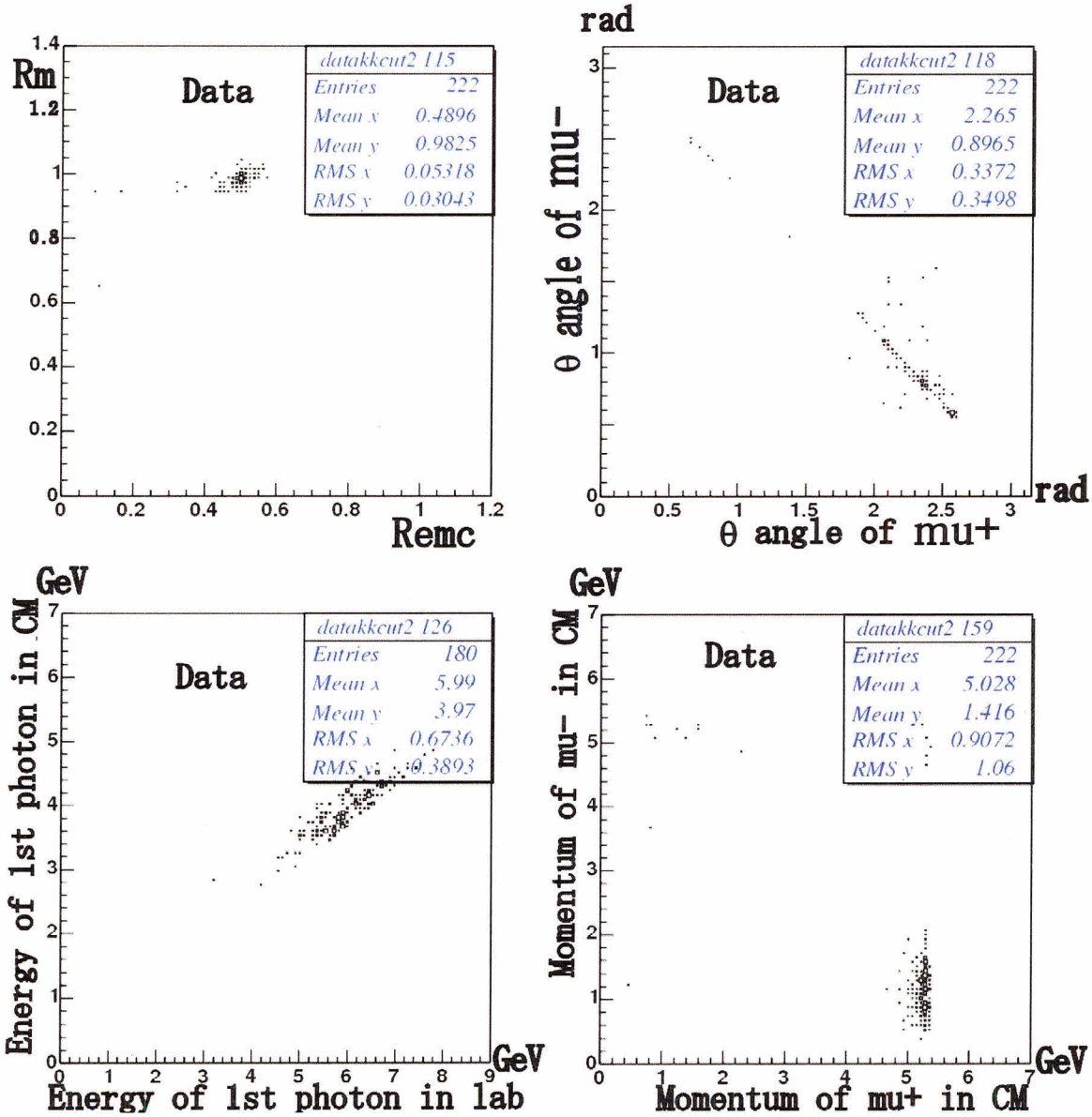

Figure 4.29: Only extra data events selected Upper-left:Rm vs Remc, Upper-right:$\theta_{\mu^-,CM}$ vs $\theta_{\mu^+,CM}$, Lower-left:$E_{\gamma 1,CM}$ vs $E_{\gamma 1,lab}$, Lower-right:$P_{\mu^-,CM}$ vs $P_{\mu^+,CM}$

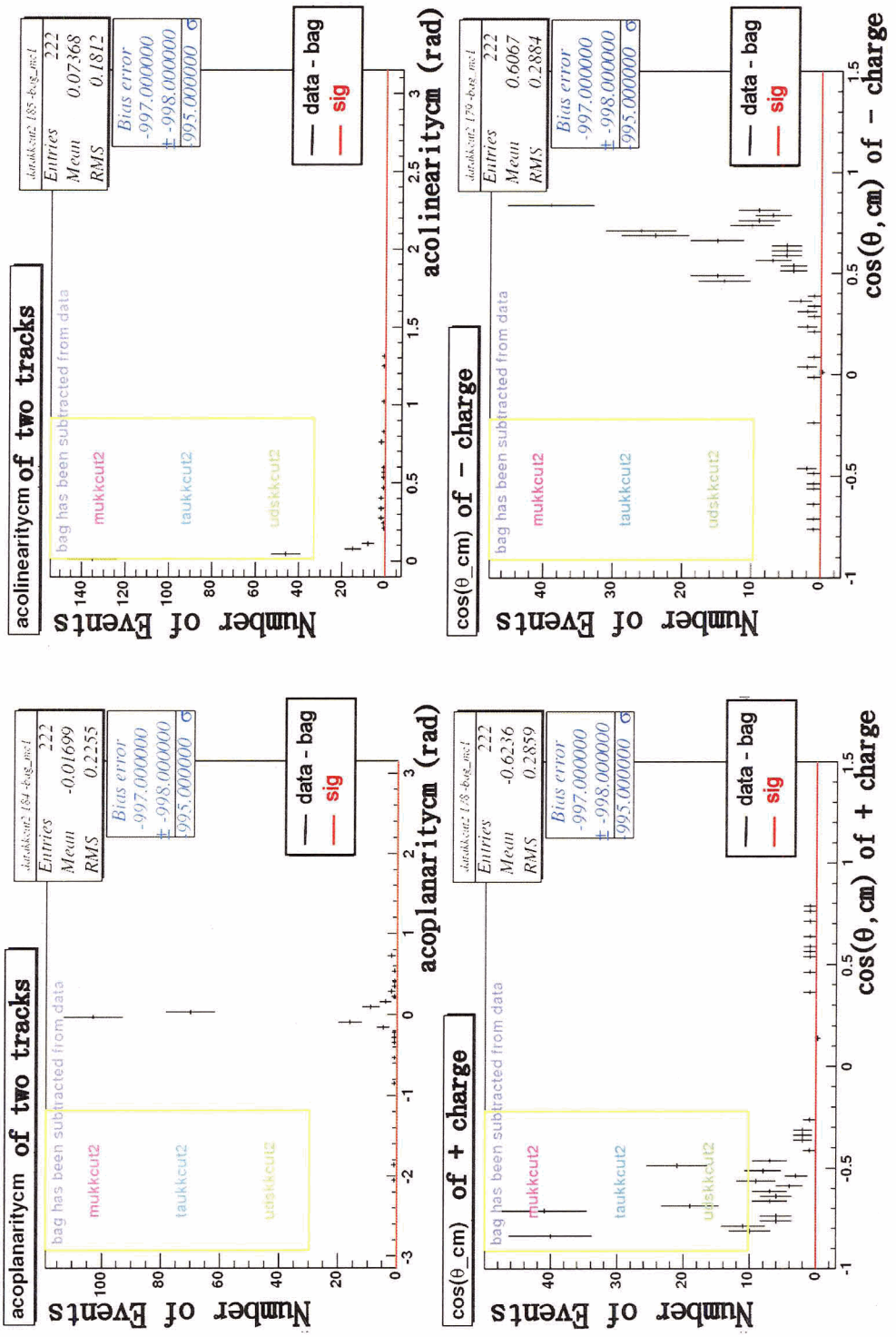

Figure 4.30: Only extra events selected Upper-left:acoplanaritycm Upper-right:acolinearitycm Lower-left:cos(θ,CM, μ^+) Lower-right:cos(θ, CM, μ^-)

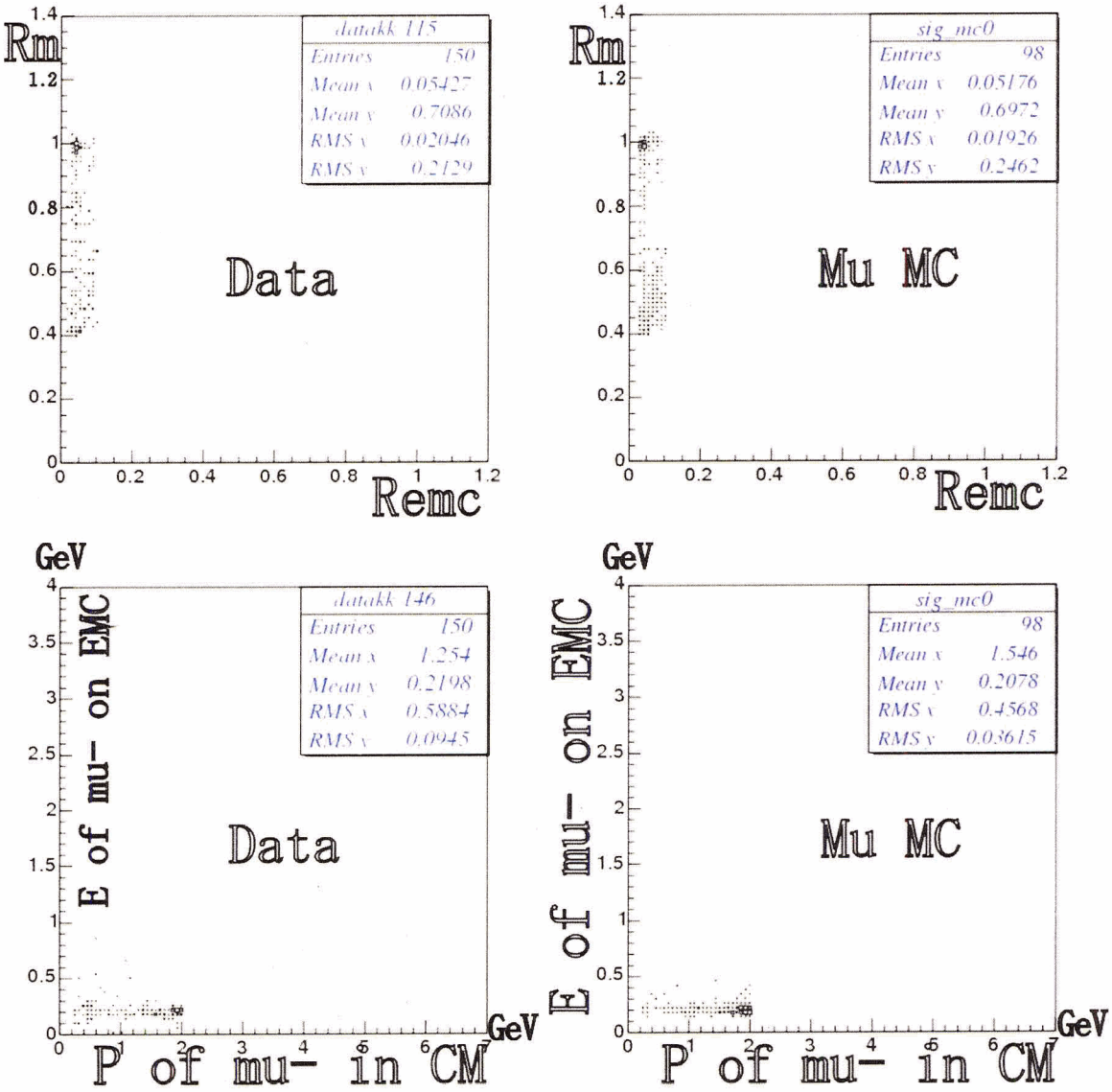

Figure 4.31: Only the events with $P_{\mu^-,CM} < 2$GeV from ISR region have been selected Upper:Rm vs Remc Lower:$E_{\mu^- onEMC}$ vs $P_{\mu^-,CM}$

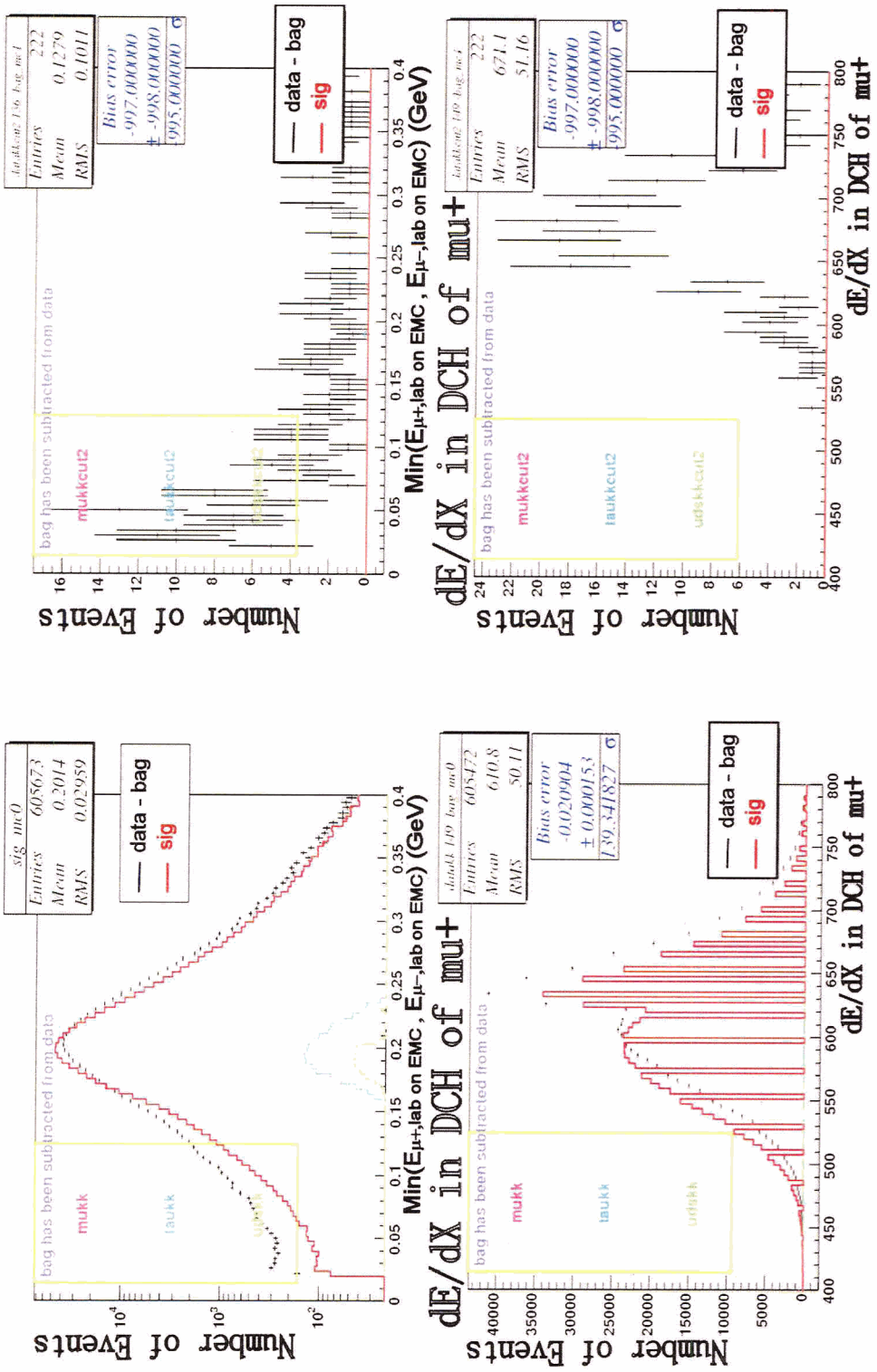

Figure 4.32: Upper: minimum of $E_{\mu^+,CMonEMC}$ and $E_{\mu^-,CMonEMC}$ Lower:$dE/dX_{\mu^+}inDCH$ Left:After extended cut Right:Only extra events selected

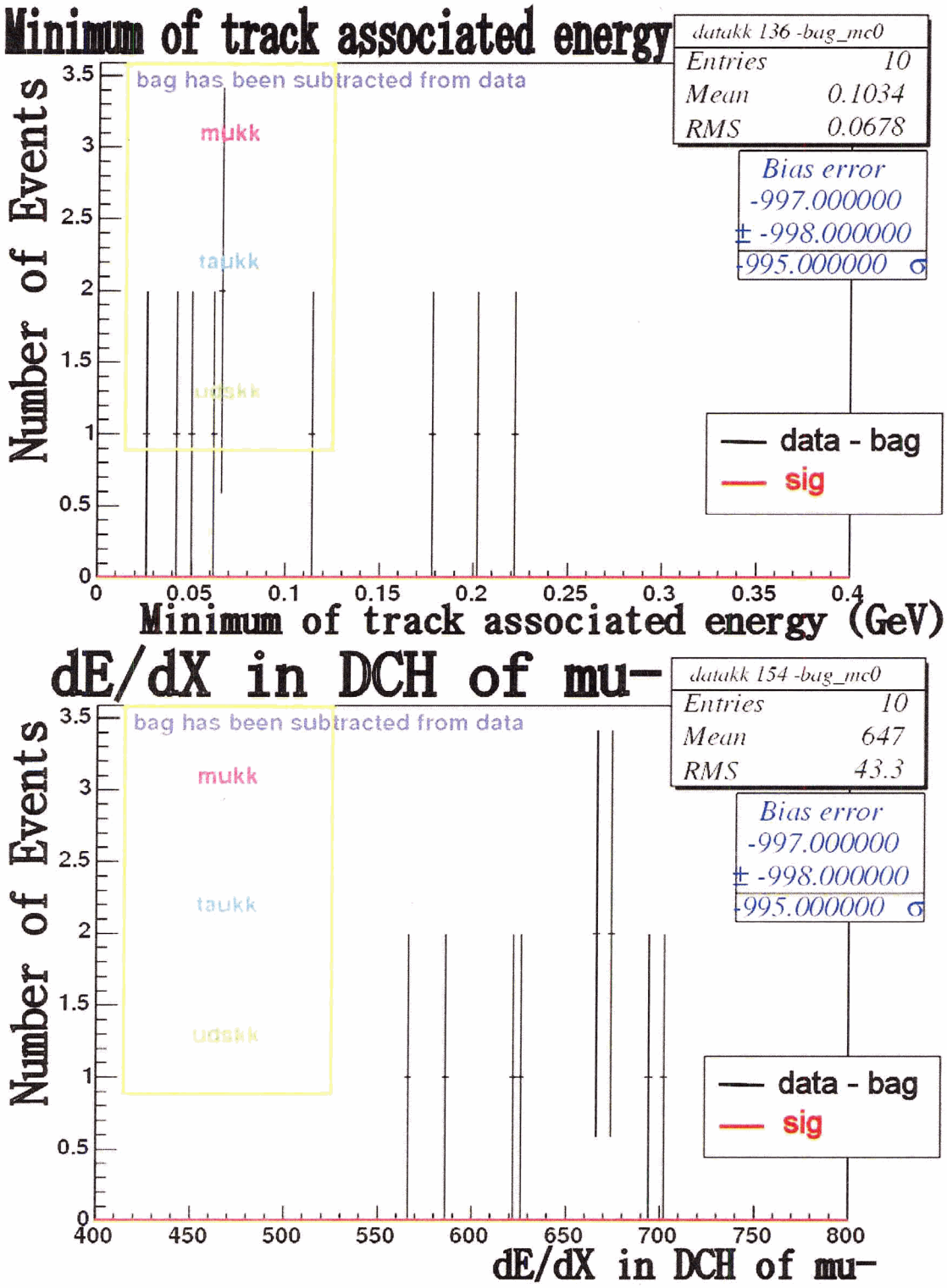

Figure 4.33: Events inside of red line of Figure 4.23 are selected Upper:minimum of $E_{\mu^+,CMonEMC}$ and $E_{\mu^-,CMonEMC}$, Lower:$dE/dX_{\mu^-}inDCH$

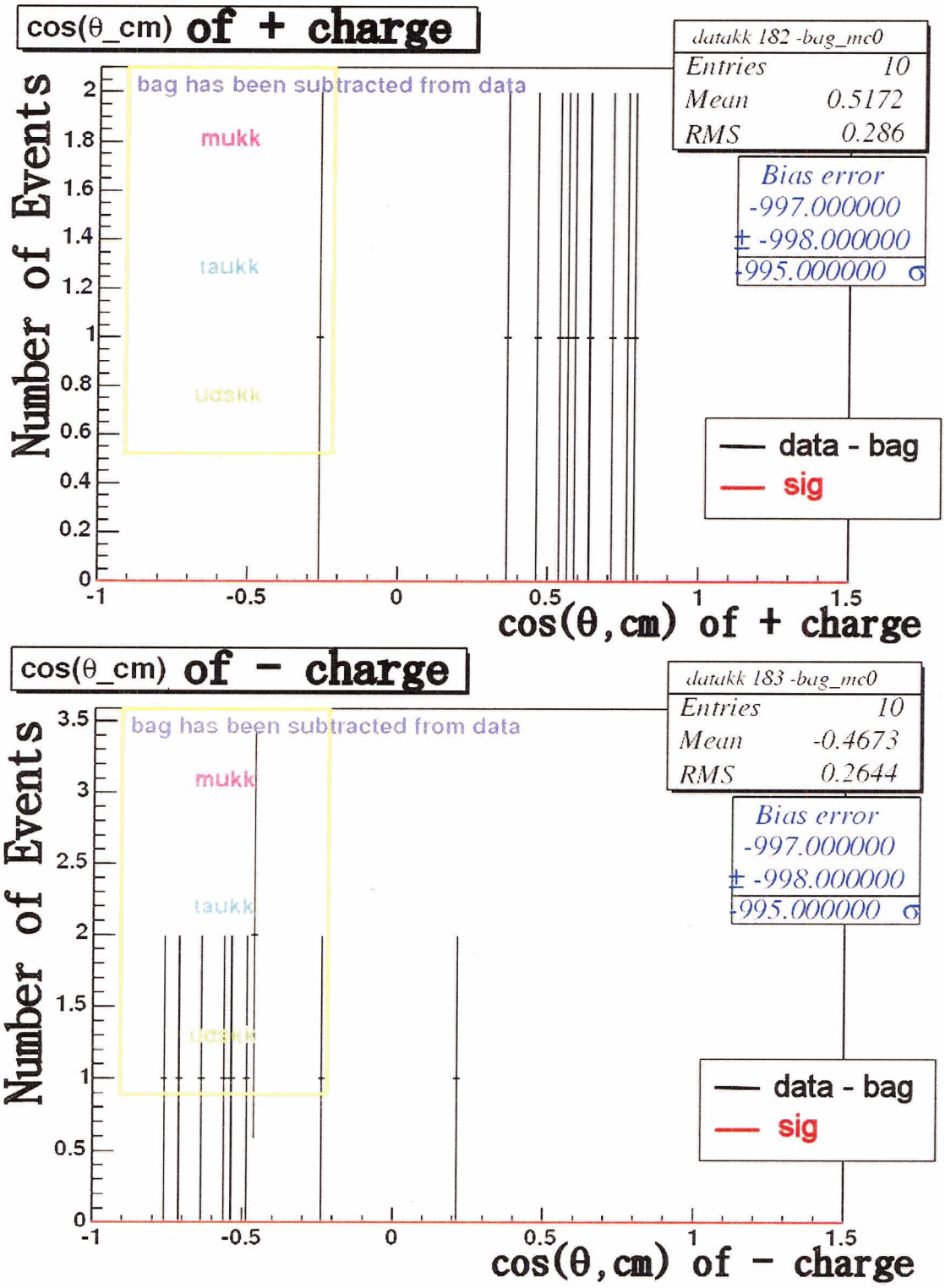

Figure 4.34: Events inside of red line of Figure 4.23 are selected Upper:cos(θ,CM, μ^+) Lower:cos(θ,CM, μ^-)

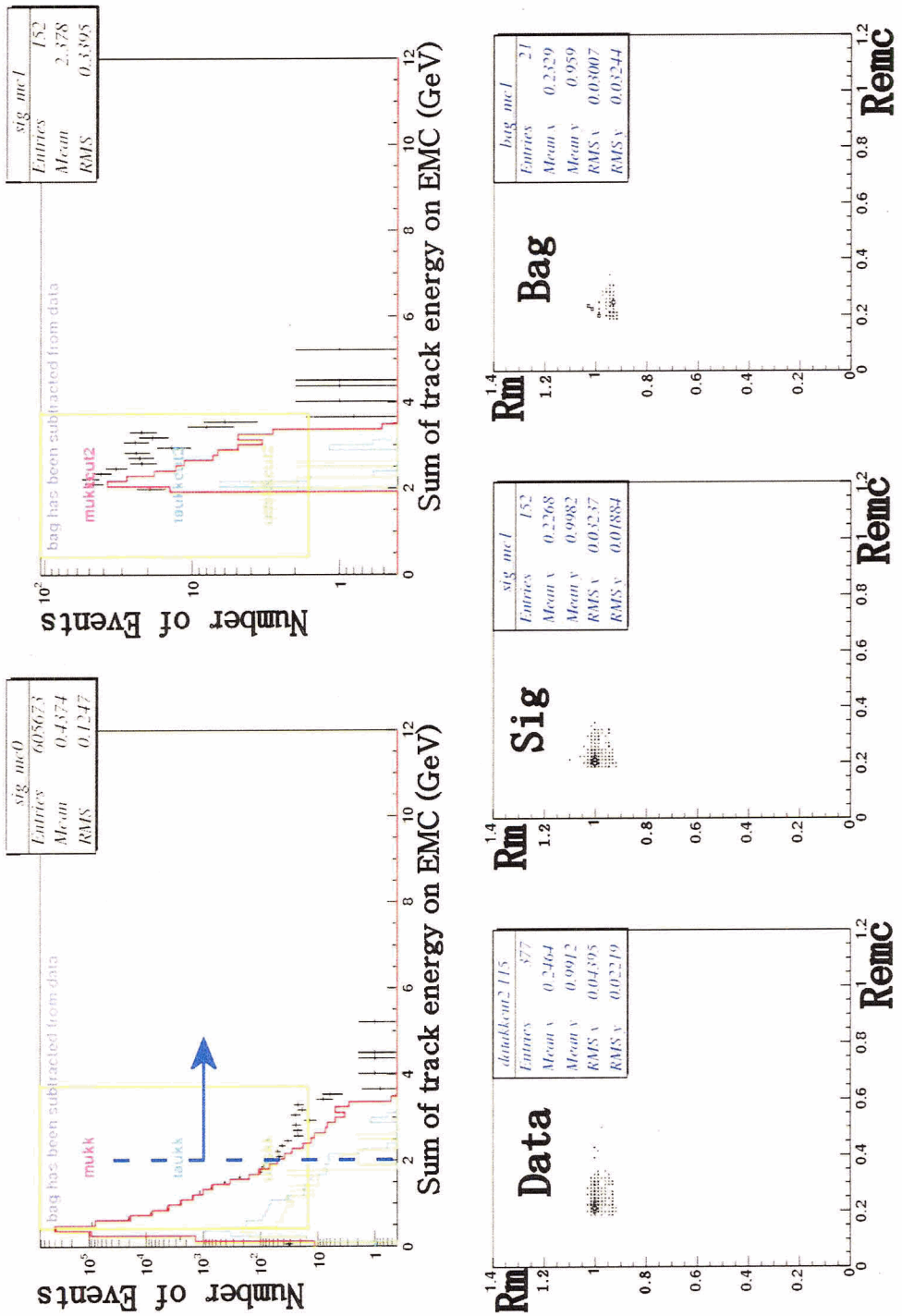

Figure 4.35: Upper-left:$E_{\mu^+,CMonEMC} + E_{\mu^-,CMonEMC}$ for extended cut. Upper-right:$E_{\mu^+,CMonEMC} + E_{\mu^-,CMonEMC}$ for $E_{\mu^+,CMonEMC} + E_{\mu^-,CMonEMC} > 2$ GeV. Lower:Rm vs Remc for $E_{\mu^+,CMonEMC} + E_{\mu^-,CMonEMC} > 2$ GeV

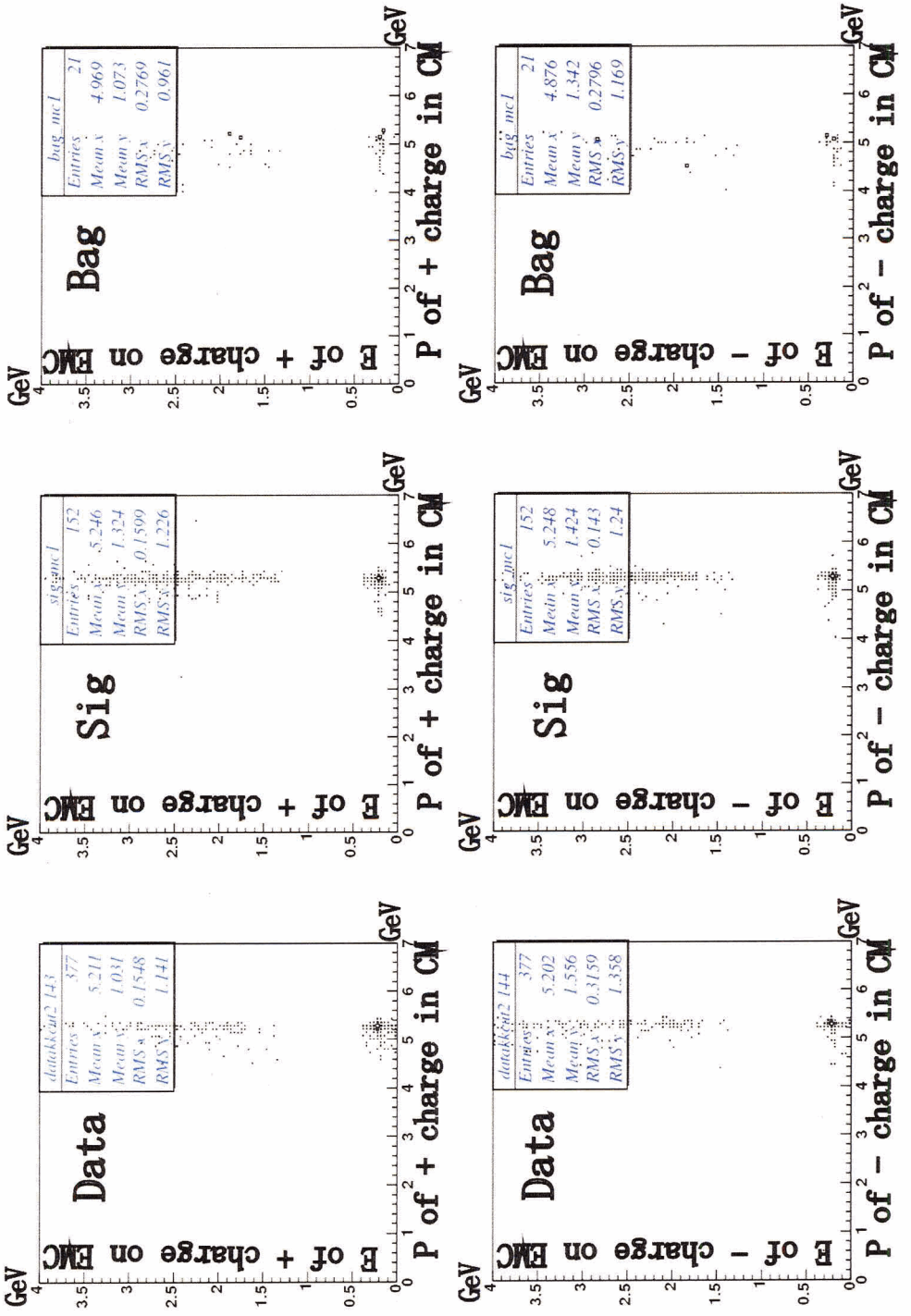

Figure 4.36: Only $E_{\mu^+,CMonEMC} + E_{\mu^-,CMonEMC} > 2$ GeV events are selected Upper:$E_{\mu^+,onEMC}$ vs $P_{\mu^+,CM}$ Lower:$E_{\mu^-,onEMC}$ vs $P_{\mu^-,CM}$

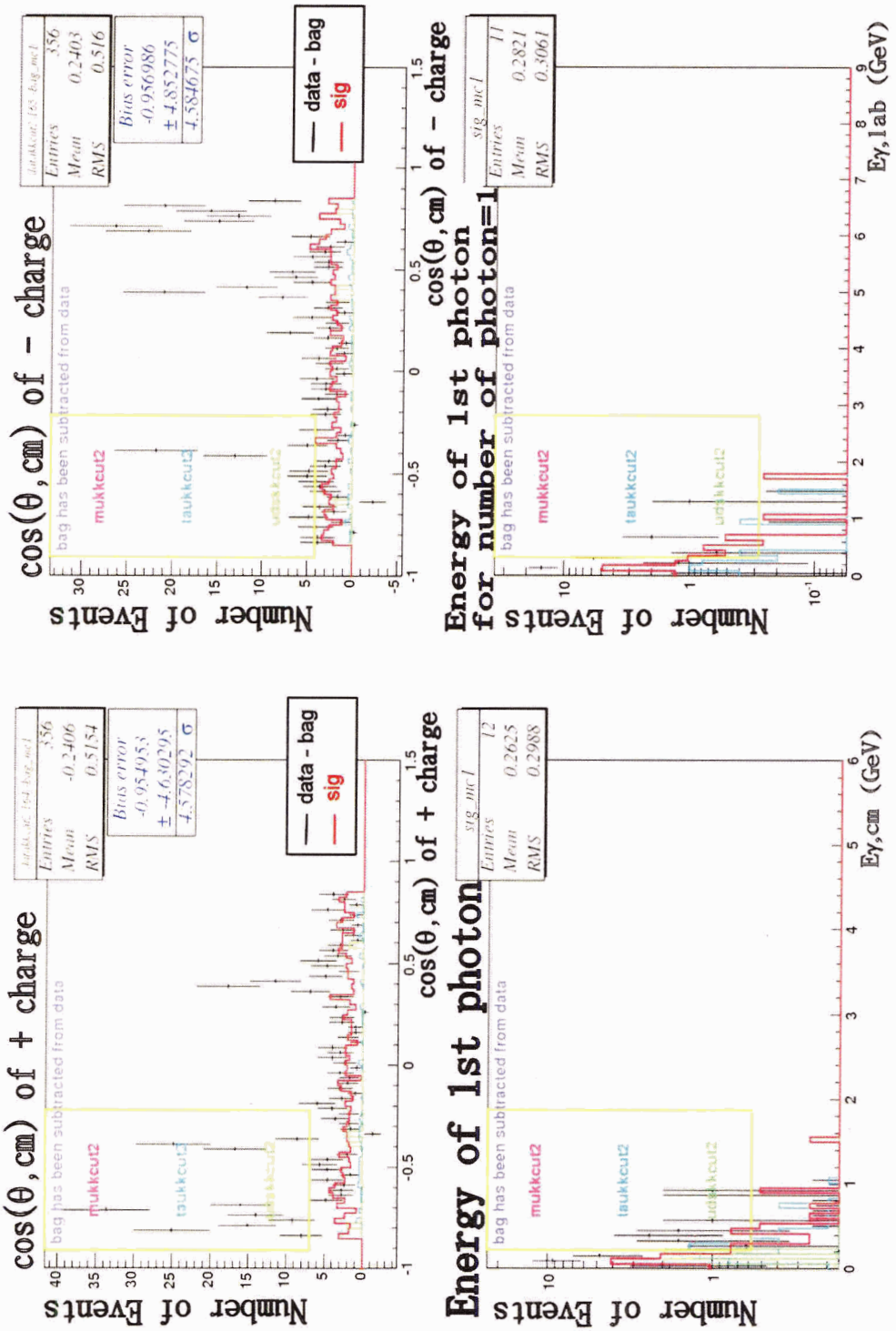

Figure 4.37: Only $E_{\mu^+,CMonEMC} + E_{\mu^-,CMonEMC} > 2$ GeV events are selected Upper-left:cos(θ,CM, μ^+) Upper-right:cos(θ,CM, μ^-) Lower-left:$E_{\gamma 1,CM}$ Lower-right:$E_{\gamma 1,lab}$ for number of photon=1

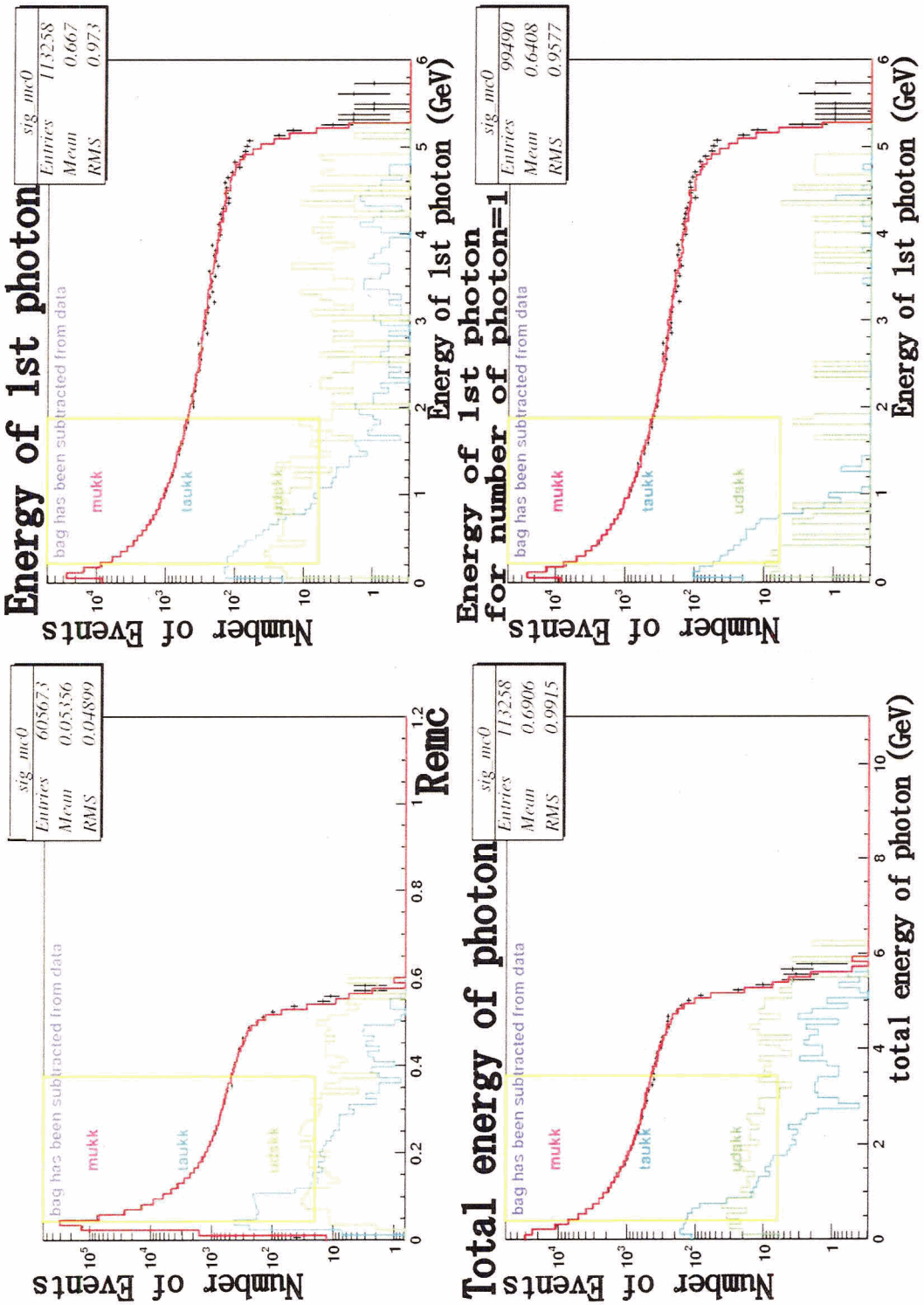

Figure 4.38: Final cut (excluding extra events) Upper-left:Remc Upper-right:$E_{\gamma 1,CM}$ Lower-left:$\Sigma E_{\gamma,CM}$ Lower-right:$E_{\gamma 1,CM}$ for number of photon=1

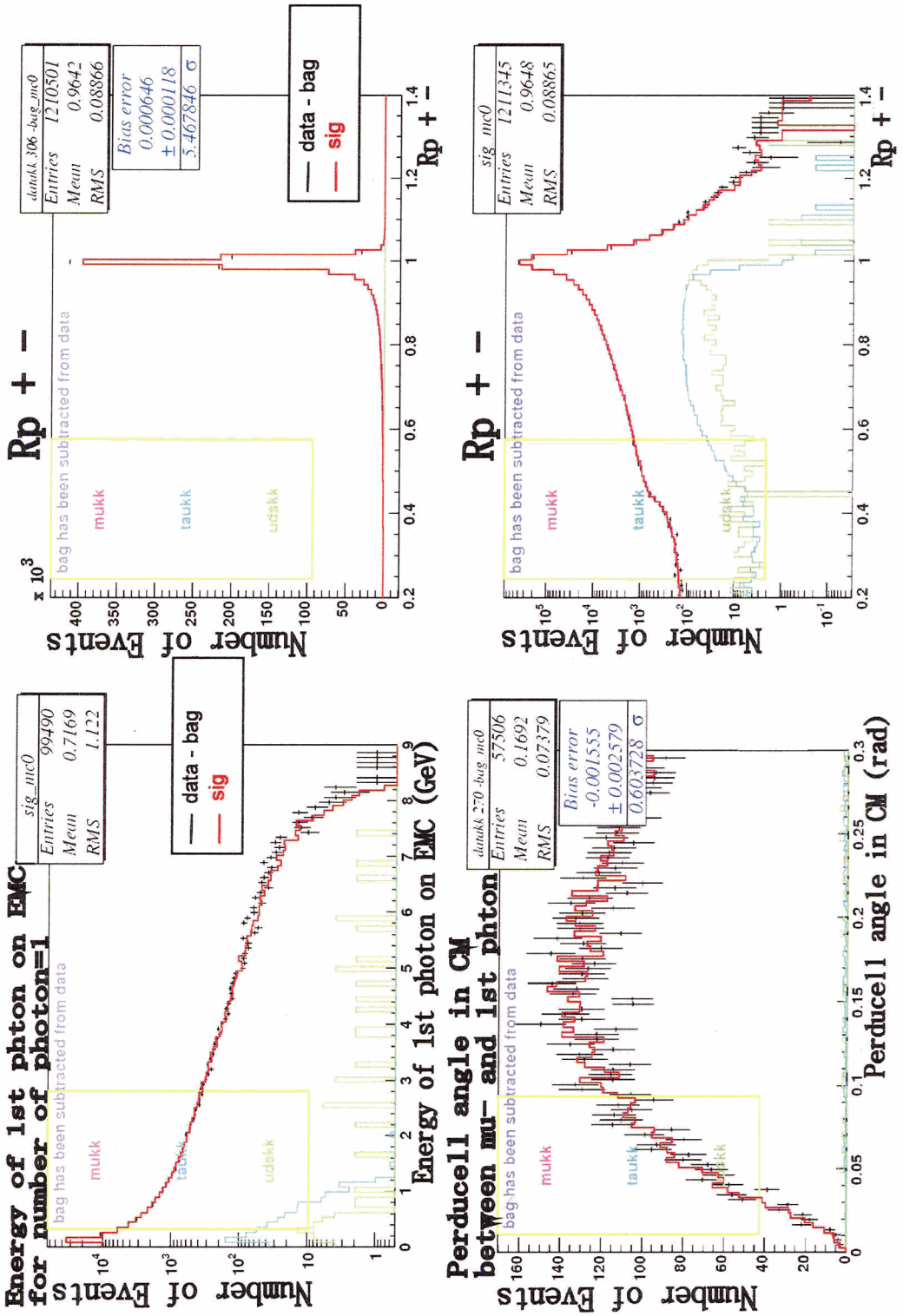

Figure 4.39: Final cut Upper-left:$E_{\gamma 1,lab}$ for number of photon=1 Right:$P_{\mu^{\pm},CM}/P^{max}_{\mu,CM}$ Lower-left:θ between μ^- and $\gamma 1, CM$

4.6 Photon energy cut

In the BaBar experiment, lots of machine-induced background is generated. Thus we need to simulate machine-induced and other background in MC including radiation, beam-gas, beam-wall events, detector noise and other sources. We select "background frames" using a randomly triggered real events to overlay on top of the MC signal event. We apply this snapshot to MC to simulate these machine-induced and other background. Thus it is important to compare the same period data and MC in the analysis. Lots of electronic noise comes from the BaBar detector itself. Thus, many low energy "photons" come from electronic noise, not from e^+e^- interactions. In the mutau preselection[8] we eliminated these noise photons by ignoring photons with energy less than 20 MeV.

Figure 4.40 shows some histograms of this photon energy cut. We can see a clear discrepancy between data and MC. It will be shown that if we apply a photon energy threshold beyond 20 MeV this discrepancy would be reduced. In the analysis presented so far, photons with energy less than 80 MeV in the lab frame have been ignored.

In Figures 4.41, 4.42, 4.43, 4.44 and 4.45 several photon related quantities accepting photons with $E_{\gamma,lab}$ >50MeV, $E_{\gamma,lab}$ >70MeV, $E_{\gamma,lab}$ >80MeV, $E_{\gamma,lab}$ >90MeV are presented. Significant variation in the means of the distributions is seen as the threshold is varied from 20 MeV to 90 MeV.

In addition to these histograms, the histograms of number of photons, energy of second energetic photon, energy of the most energetic photon in CM and in lab for the events of the number of photons satisfying cut=1, the distance between photon and its closest track, energy constrained mass and ΔE have been checked for each photon energy cut even though they are not presented in this paper. From these histograms the mean values of each histogram vary significantly as the photon threshold changes. In most histograms for the $E_{\gamma,lab}$ >50MeV photon threshold, there is reasonable data-MC agreement. But histograms of the energy of the most energetic photon in lab for the events of the number of photons

satisfying cut=1, distance between photon and its closest track and Figure 4.45 force me to compromise between accuracy and efficiency of photon related events. Thus $E_{\gamma,lab}$ >80MeV was chosen as a photon threshold energy.

$P_{\mu^{\pm},CM}/P_{\mu,CM}^{max}$ for each photon energy cut was also checked. Because this is not a photon related quantity, no big difference between each photon energy cut has been observed. Other quantities(not photon related such as acoplanaritycm, acolinearitycm, etc) also have been checked and found that the difference of mean value for each photon energy cut was less than 2%. Therefore the previous analysis applying $E_{\gamma,lab}$ >80MeV photon energy cut is still valid to other photon energy cuts when we study the "no photon" related quantities. Figure 4.46 shows $E_{\gamma 1,lab}$ (upper) and $\cos(\theta_{\gamma 1,CM})$ (lower) for $E_{\gamma,lab}$ >80MeV (left) and for $E_{\gamma,CM}$ >80MeV (right). Histograms for photon energy cut of 50MeV, 70MeV, 90MeV also have been drawn but their distributions show no big difference from photon energy cut 80MeV. From upper part of this histogram we can check the fact that photon energy threshold should be calculated in the lab frame, as expected if the discrepancy is coming from machine background. The lower part of these histograms show the worst agreement between data and MC occurs in the direction of the beams, again suggesting the problem is from machine background. The remaining analysis applies a cut-off 80 MeV to all photons.

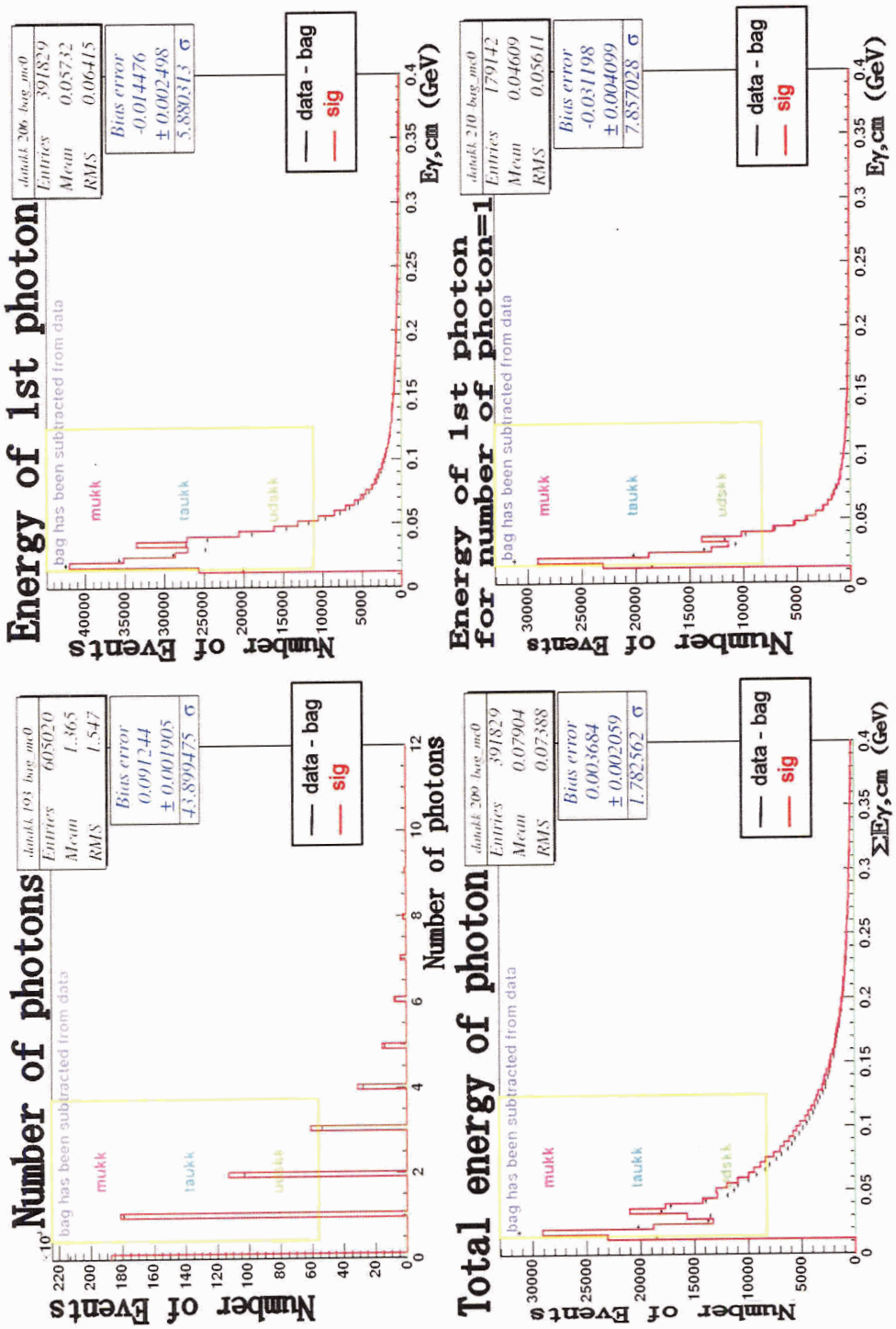

Figure 4.40: No photon energy cut is applied Upper-left:Number of photons Upper-right:Energy of most energetic photon in CM($E_{\gamma 1,CM}$) Lower-left:Total energy of photons in CM($\Sigma E_{\gamma,CM}$) Lower-right:$E_{\gamma 1,CM}$ for number of photon=1

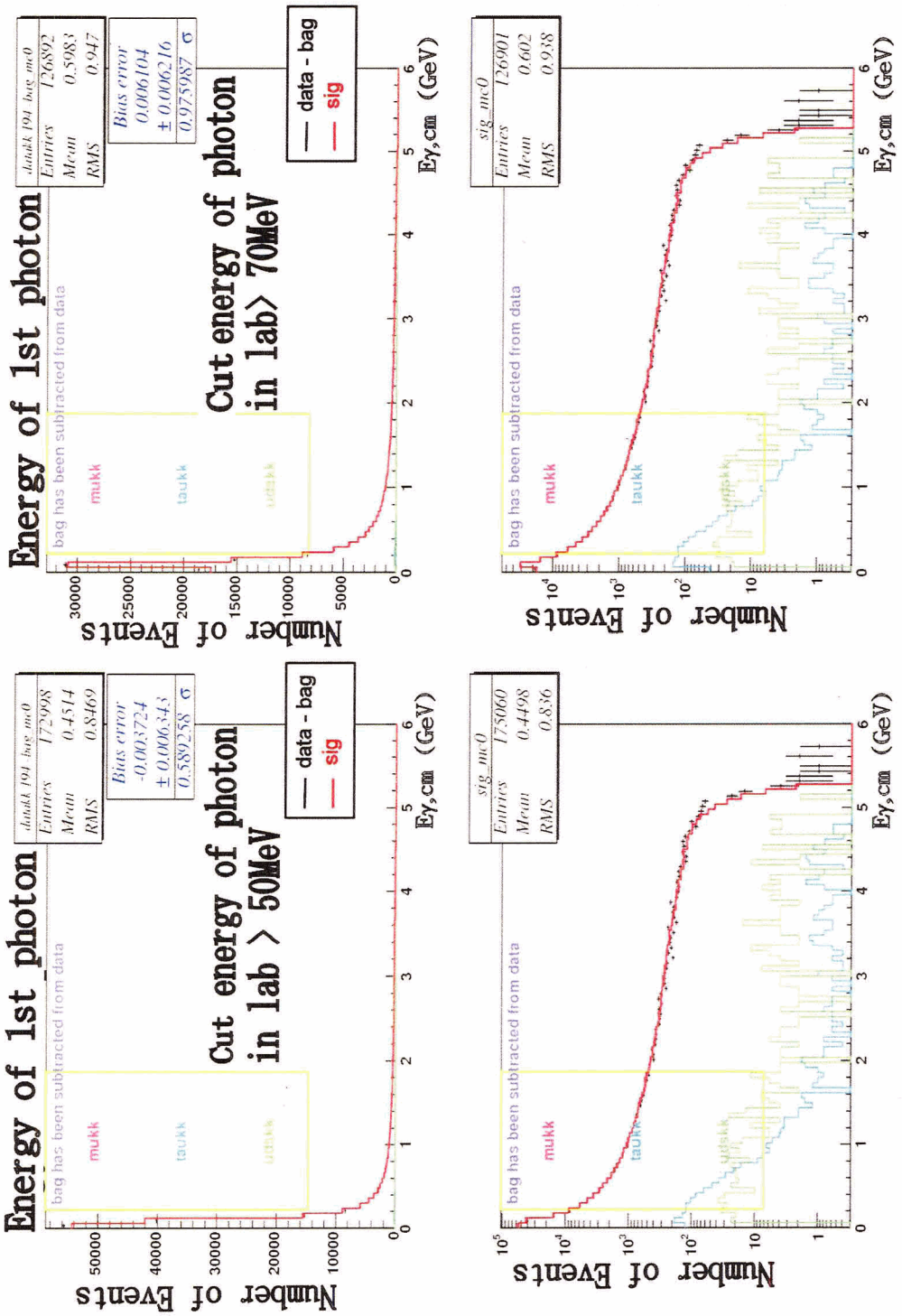

Figure 4.41: Energy of most energetic photon in CM($E_{\gamma 1,CM}$) Left:for $E_{\gamma,lab}$ >50MeV Right:for $E_{\gamma,lab}$ >70MeV. Upper:Linear scale. Lower:Log scale.

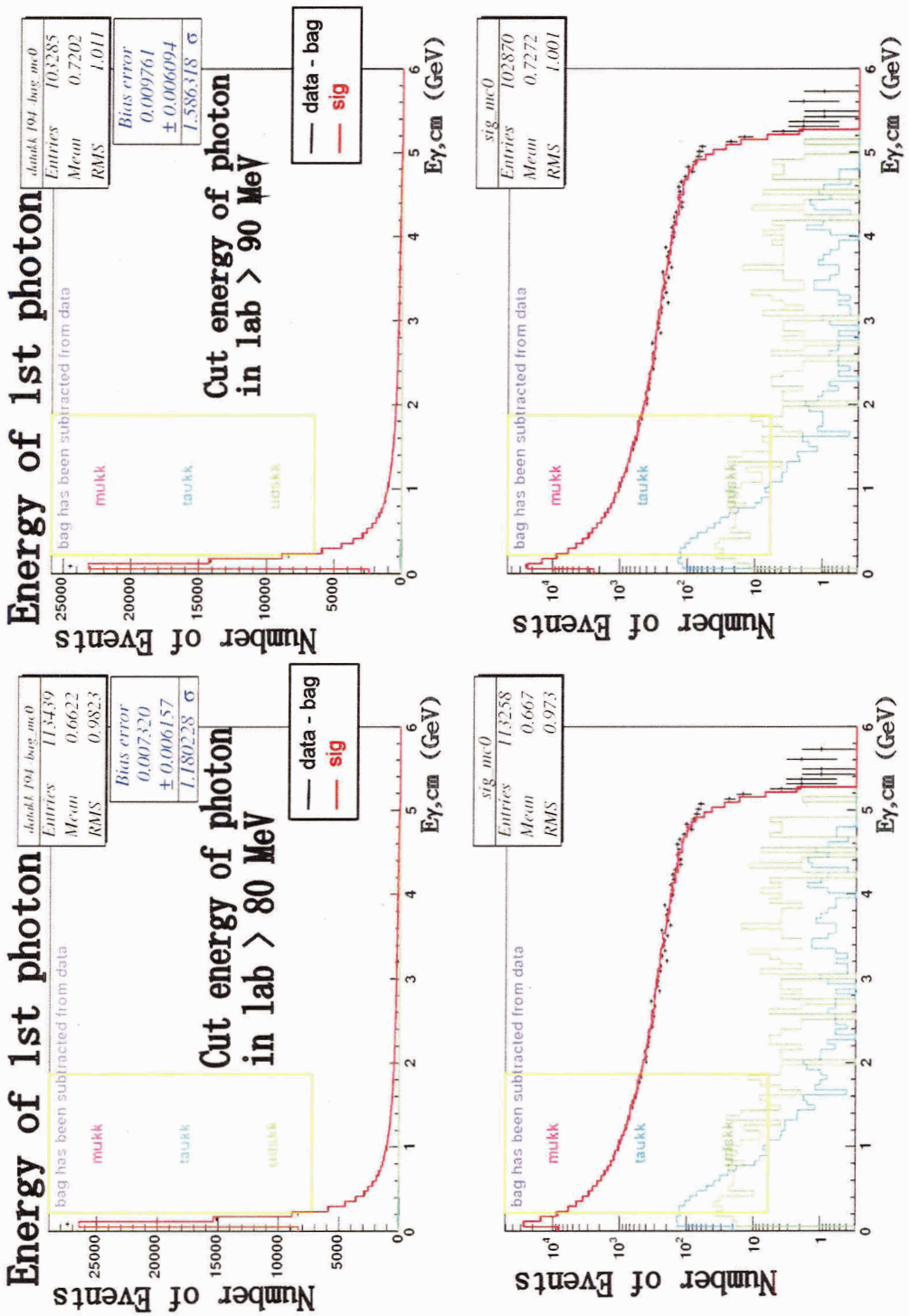

Figure 4.42: Energy of most energetic photon in CM($E_{\gamma 1,CM}$) Left:for $E_{\gamma,lab}$ >80MeV Right:for $E_{\gamma,lab}$ >90MeV. Upper:Linear scale. Lower:Log scale.

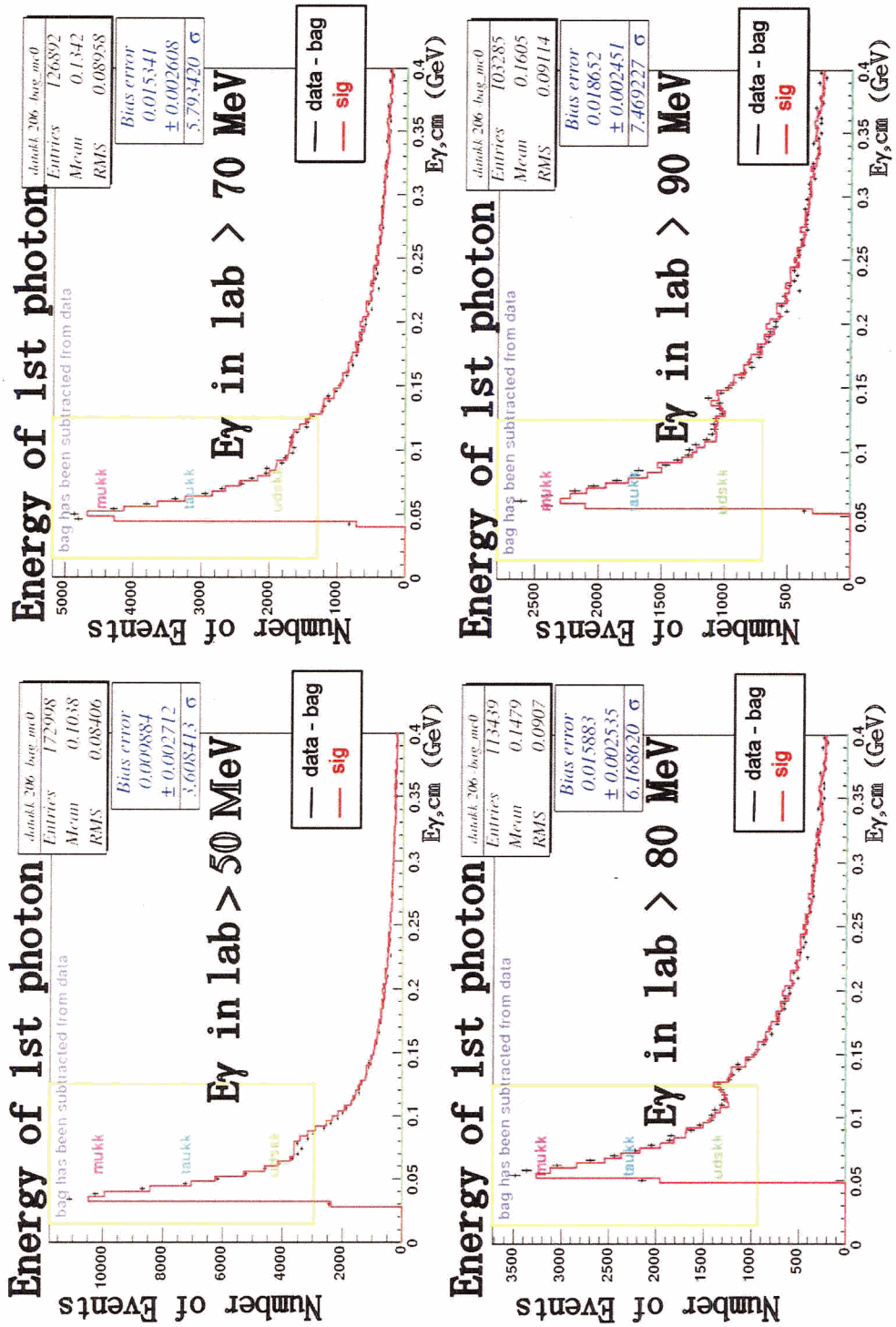

Figure 4.43: $E_{\gamma 1,CM}$ Upper-left:for $E_{\gamma,lab}$ >50MeV Upper-right:for $E_{\gamma,lab}$ >70MeV Lower-left:for $E_{\gamma,lab}$ >80MeV Lower-right:for $E_{\gamma,lab}$ >90MeV

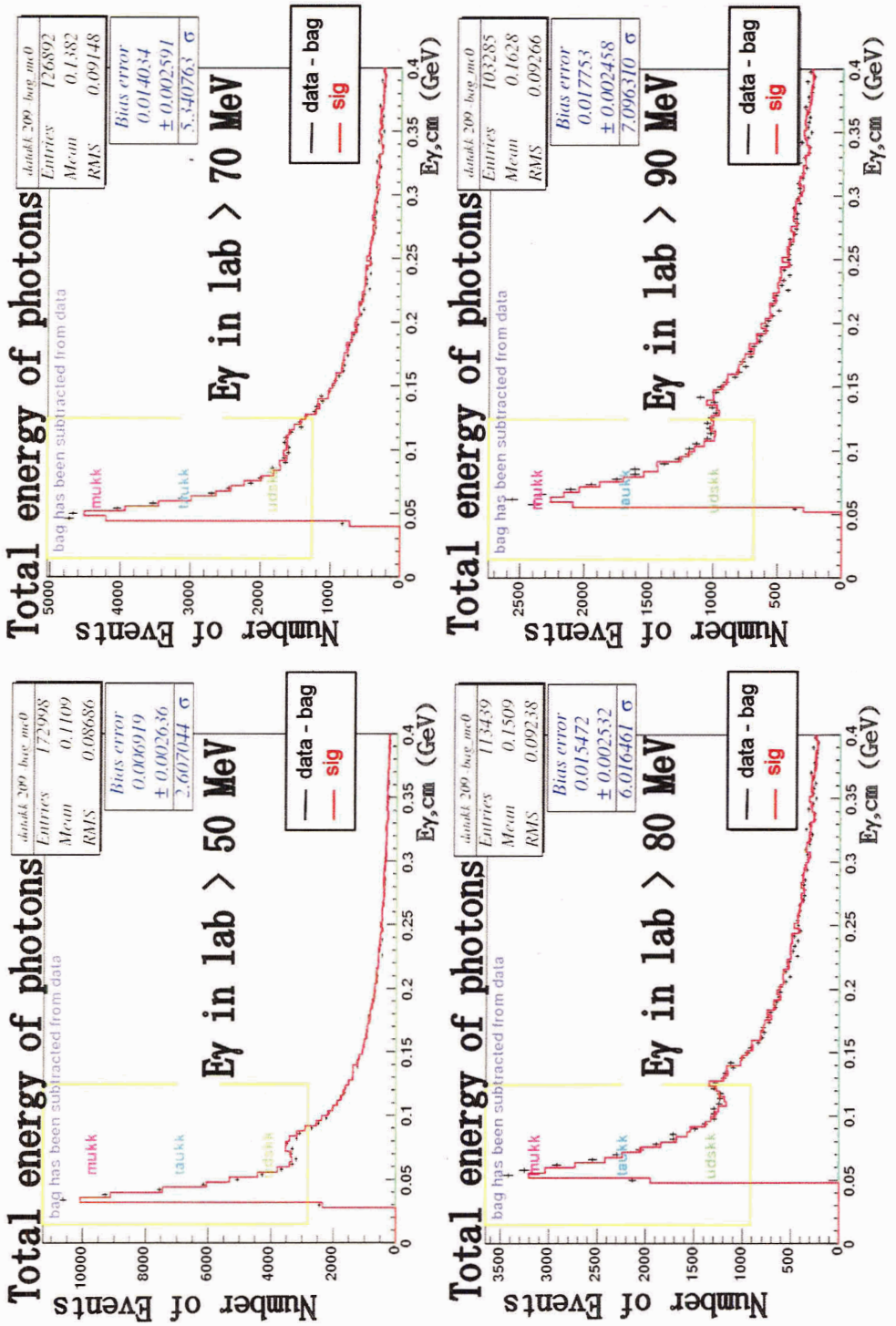

Figure 4.44: Total energy of photons in CM($\Sigma E_{\gamma,CM}$) Upper-left:for $E_{\gamma,lab}$ >50MeV Upper-right:for $E_{\gamma,lab}$ >70MeV Lower-left:for $E_{\gamma,lab}$ >80MeV Lower-right:for $E_{\gamma,lab}$ >90MeV

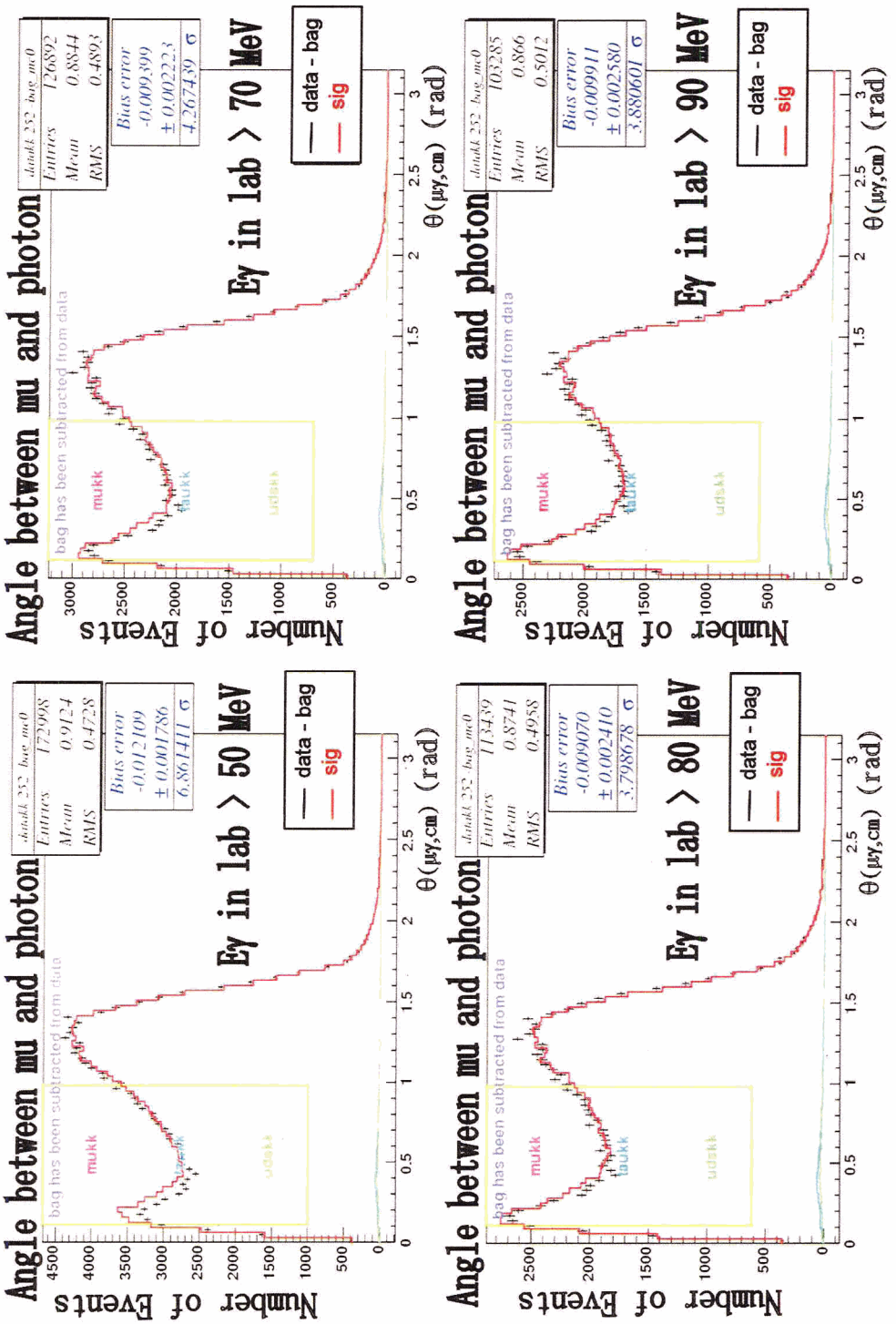

Figure 4.45: $\theta_{\mu\gamma,CM}$ Upper-left:for $E_{\gamma,lab}$ >50MeV Upper-right:for $E_{\gamma,lab}$ >70MeV Lower-left:for $E_{\gamma,lab}$ >80MeV Lower-right:for $E_{\gamma,lab}$ >90MeV

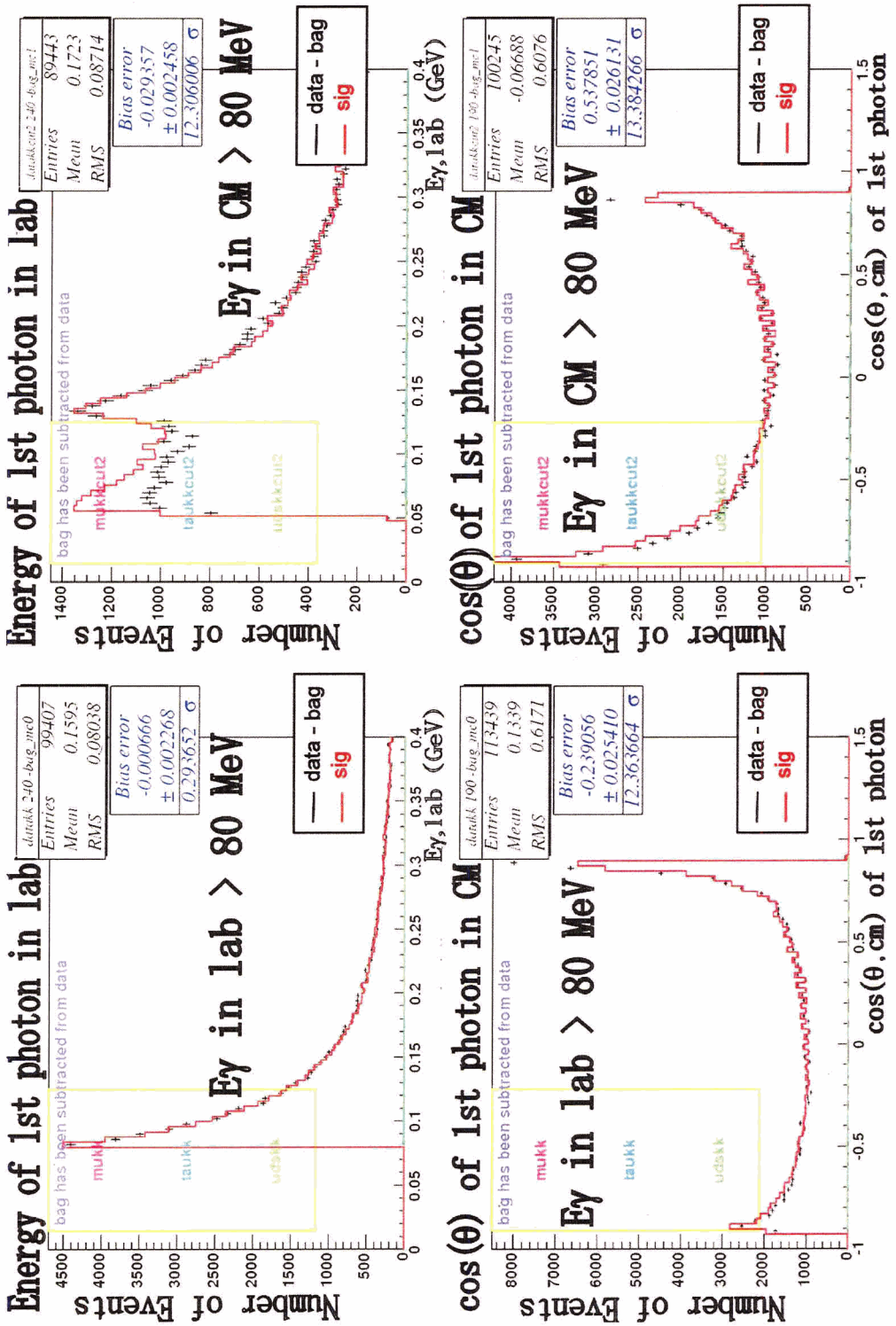

Figure 4.46: Upper:$E_{\gamma 1,lab}$ for number of photon=1, Lower:cos($\theta_{\gamma 1,CM}$), Left:for $E_{\gamma,lab}$ >80MeV, Right:for $E_{\gamma,CM}$ >80MeV

Chapter 5

ANALYSIS

In order to perform the $\tau \rightarrow \mu\gamma$ or τ lifetime analysis, we must be confident that the detector modelling of MC is sufficiently accurate.

5.1 Modelling of the detector response

In this section we explore various aspects of the modelling of the detector response using $e^+e^- \rightarrow \mu^+\mu^-\gamma$ events. In particular we study the response to γ and μ in EMC and the response to μ in DCH. Accurate modelling of the energy deposition of minimum ionization in a scintillator is generally difficult to achieve. Although not perfect, upper Figure 5.1 shows reasonable agreement to the average track energy deposited in the EMC in lab frame. Considering the fact that the resolution of data and MC are about 157 MeV and 136 MeV, the difference of mean values, 10 MeV, is relatively small.

Figures 5.2 and 5.3 show θ and ϕ distributions of muons in the detector in the CM frame. The agreement between MC and data can be quantified by the significance of the difference between the mean of the MC and data distributions. Recall, from Chapter 4, bias error is defined by ($<$ signal MC $>$ - $<$ data - background MC $>$)/$<$ data - background MC $>$ and the bias standard deviation(σ) is the significance of the discrepancy between MC and data. For both $\cos(\theta, CM)$ and ϕ there is good agreement. Averaging over μ^+ and

μ^-, the $\cos(\theta, CM)$ significance is 0.27σ and ϕ significance is 1.2σ. This gives us confidence in both detector response and the modelling of these quantities for the $e^+e^- \rightarrow \mu^+\mu^-(\gamma)$ process by KK2f.

Figure 5.4 and 5.5 show the acoplanarity (which is sensitive to FSR) and acolinearity (which is sensitive to both ISR and FSR) of μ^+, μ^- in CM frame. From the bias, we see the MC describing the data is better than 3×10^{-5} radian for acoplanarity and 9×10^{-4} radian for acolinearity.

The upper part of Figure 5.6 is the azimuthal angle of the most energetic photon in the event where we require the energy of the photon to be more than 80 MeV. The lower plot is for photons having more than 250 MeV. The z-axis of detector is in the e^- beam direction. The x-axis points toward the center of the PEP-II ring and the y-axis is in the vertical direction. Thus the peak in the upper part of Figure 5.6, which is suppressed in the Figure 5.6 lower plot can be understood as lower energy photons from machine background which travel toward the outside of the PEP-II ring and in the plane of the ring. This is consistent with synchrotron radiation from the e^+ and e^-.

We can study the modelling of DCH angle measurement by selecting $e^+e^- \rightarrow \mu^+\mu^-$ events with no measurable radiation. In Figures 5.7, 5.8 and 5.9 a "no-radiation" cut, which is defined as

> mupaircut[0] and mupaircut[1] (See section 4.1) and 0 GeV $< E_{\mu,CMonEMC} <$ 0.4 GeV and 0.03 $<$ Remc $<$ 0.05 and 0.99 $<$ Rm $<$ 1.02 and number of photons $= 0$ and total momentum of tracks in the CM $>$ 9.5 GeV,

has been used to get clean $\mu^+\mu^-$ tracks with no photon radiation. From Figure 5.7, the transverse momentum in the MC has a mean shifted 0.2% down relative to the data. From

the sigma values of fits in Figure 5.8, we see that the resolution of the θ angle between two tracks is well modelled at the 50 μrad level. From Figure 5.9 we see the mean momentum (transverse momentum / sinθ) is modelled at the 0.05% level and the RMS agree at the 0.5% level (Data RMS is 0.09437 GeV for μ^+ and 0.09832 GeV for μ^-. MC RMS is 0.09383 GeV for μ^+ and 0.09788 GeV for μ^-).

5.2 KK2f modelling of QED

5.2.1 Angular distributions

As discussed in Chapter 1, angular distributions are very critical for the $\tau \rightarrow \mu\gamma$. From Figures 5.2(cos$\theta, CM$, bias=0.27$\sigma$), 5.3($\phi$, bias=1.2$\sigma$), 5.4(acoplanarity in CM, bias=0.15σ) and 5.5(acolinearity in CM, bias=2.45σ) we can conclude that the track angle, acoplanarity and acolinearity are reasonably well described by KK2f.

Figure 5.10 is the profile of the $\mu^+ - \mu^-$ acolinearity in the CM versus the total energy of photons. We can verify that bigger total neutral energy in the CM corresponds to bigger acolinearity as expected from QED description of ISR and FSR. Clearly, KK2f is properly describing this.

5.2.2 $P_{\mu^\pm,CM}/P^{max}_{\mu,CM}$ study

In the τ lifetime measurement it is important to know how well the MC momentum describes real τ momentum. As shown in Figure 2.8 this μ momentum study can be used to infer that information. Figures 5.11, 5.12 and 5.13 present Rp($\equiv P_{\mu,CM}/P^{max}_{\mu,CM}$) for μ^+, μ^- and $\mu^\pm$ respectively, where $P^{max}_{\mu,CM}$ means $\sqrt{(E_{beam}/2)^2 - m^2_\mu}$. Bias errors(defined as a relative error between data - background MC and signal MC: (< signal MC > - < data - background MC >)/< data - background MC >) are (0.023±0.017)%, (0.107±0.017)%, (0.065±0.012)% for μ^+, μ^- and $\mu^\pm$.

We can see some data exceeding the MC in Figure 5.11 and 5.12 indicated by blue dashed ellipse. We study this further by plotting the peak regions in Figure 5.14. We see that the

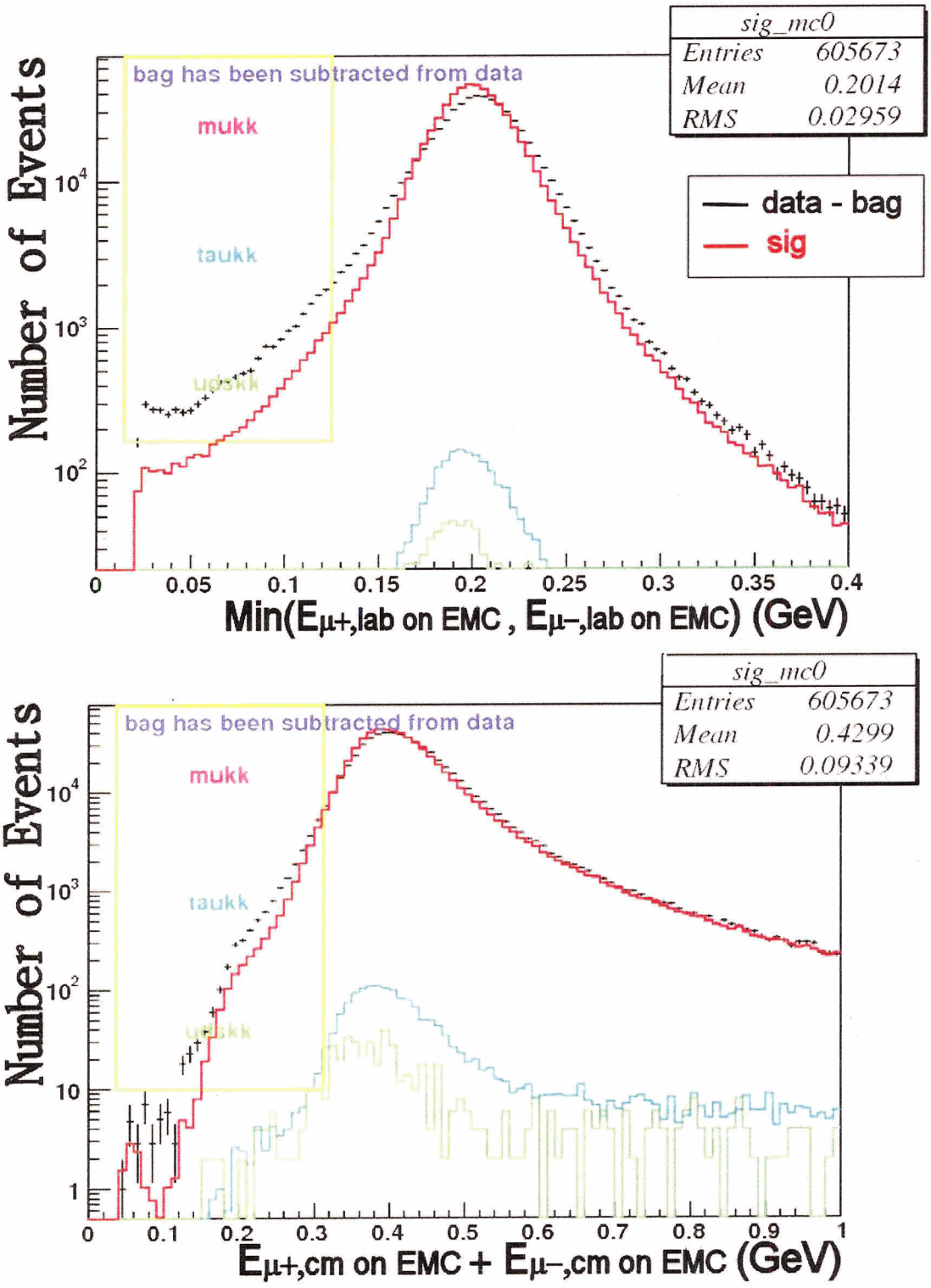

Figure 5.1: Upper:minimum of $E_{\mu^+,LABonEMC}$ and $E_{\mu^-,LABonEMC}$ Lower:$E_{\mu^+,CMonEMC} + E_{\mu^-,CMonEMC}$ Point with error bars represent data minus background. Red line histograms represent KK2f MC for $e^+e^- \to \mu^+\mu^-(\gamma)$

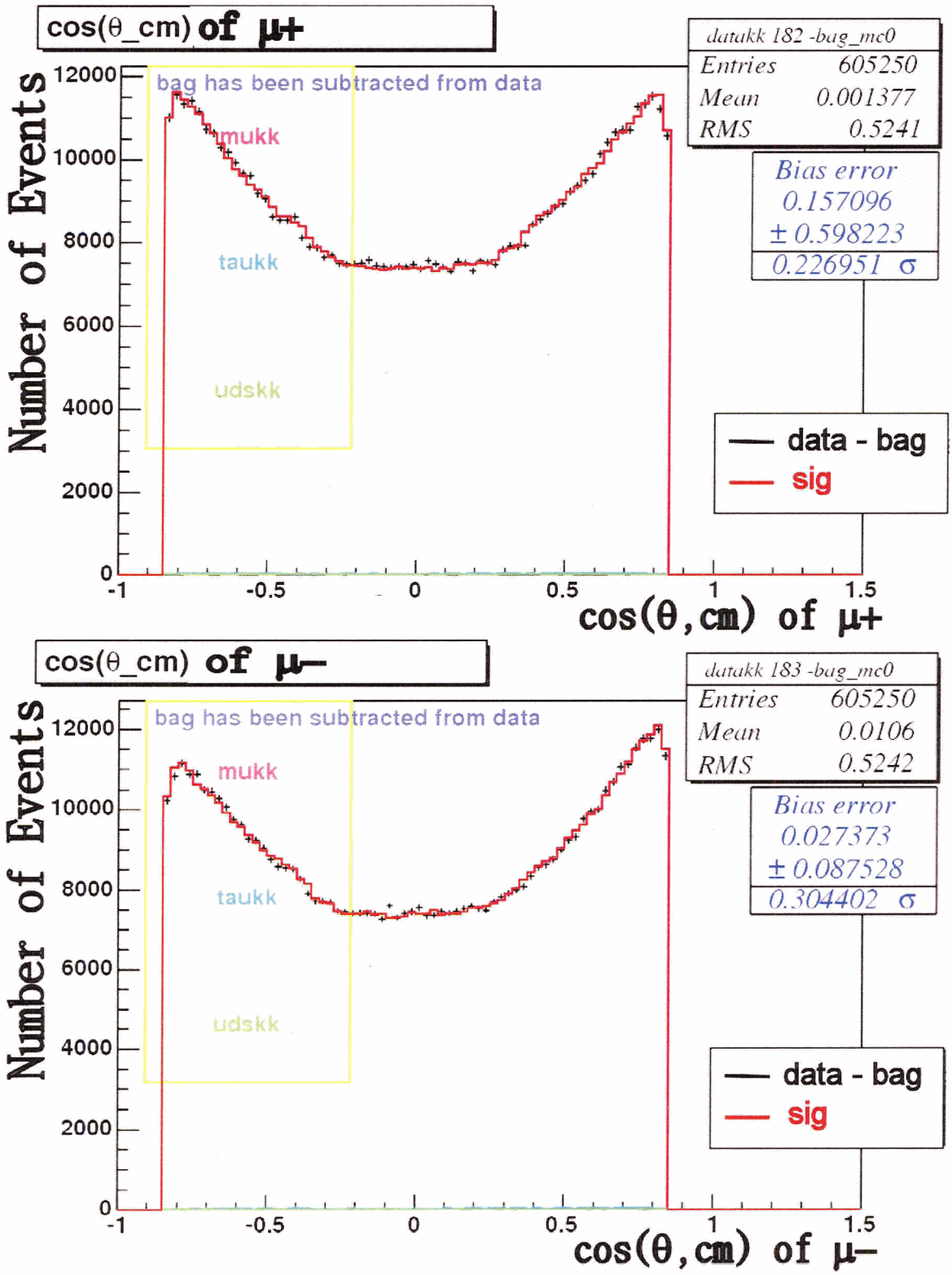

Figure 5.2: Upper:cos(θ,CM, μ^+) Lower:cos(θ,CM, μ^-). Point with error bars represent data minus background. Red line histograms represent KK2f MC for $e^+e^- \to \mu^+\mu^-(\gamma)$

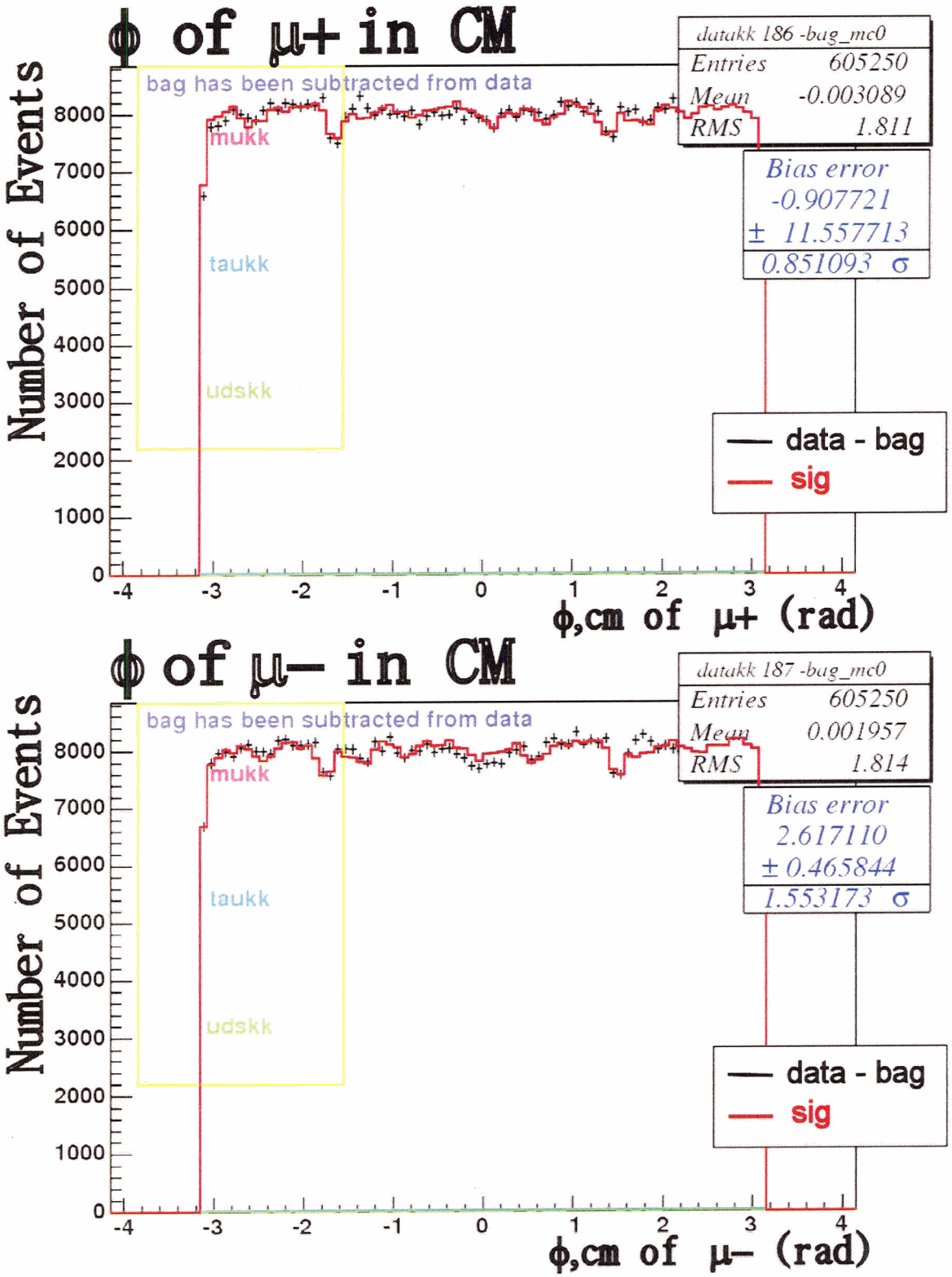

Figure 5.3: Upper:ϕ_{CM,μ^+}Lower:ϕ_{CM,μ^-} Point with error bars represent data minus background. Red line histograms represent KK2f MC for $e^+e^- \to \mu^+\mu^-(\gamma)$

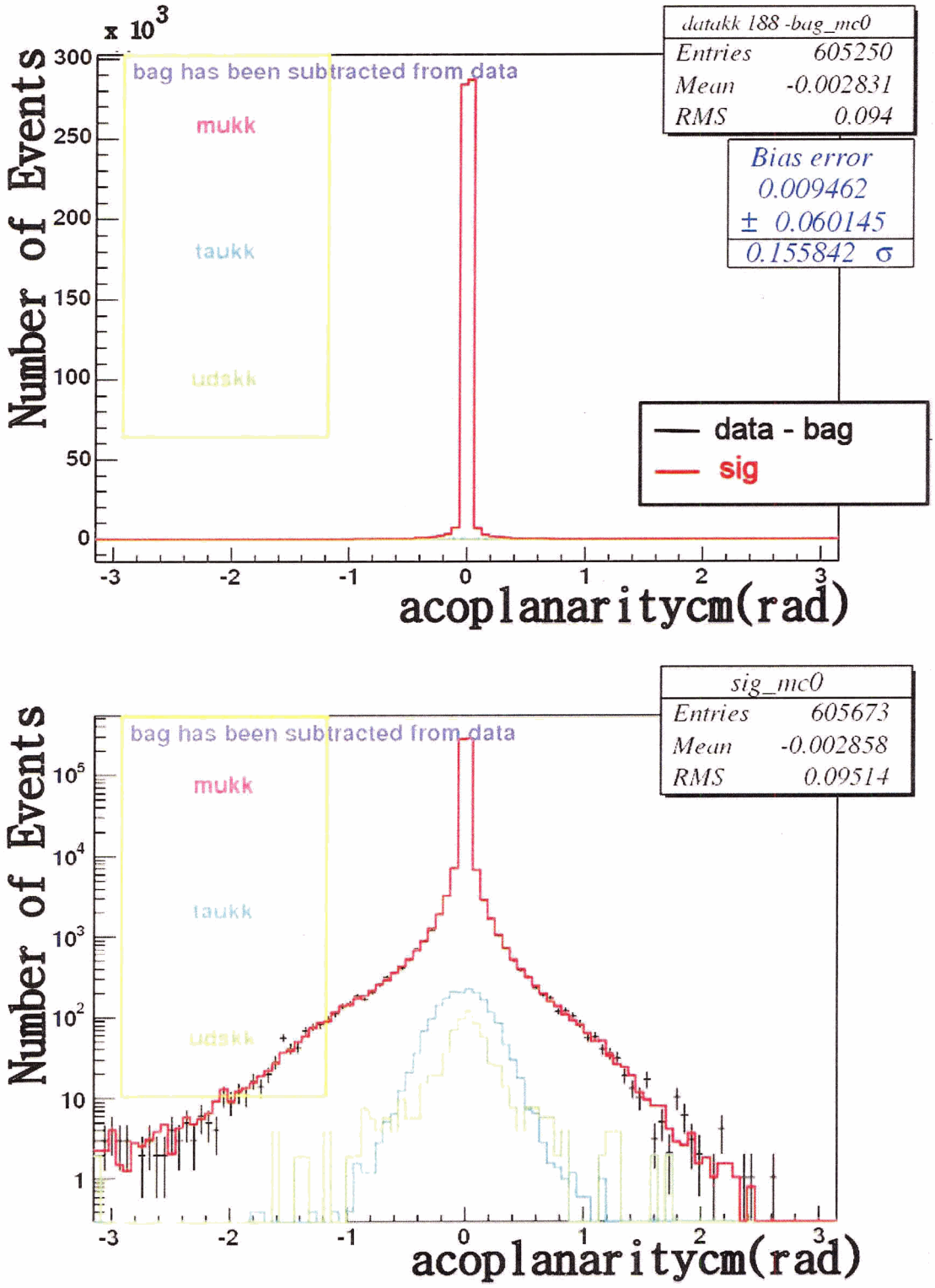

Figure 5.4: acoplanaritycm(in radian) between $\mu^+\mu^-$. Point with error bars represent data minus background. Red line histograms represent KK2f MC for $e^+e^- \rightarrow \mu^+\mu^-(\gamma)$ The error bars are too small to see on this plot.

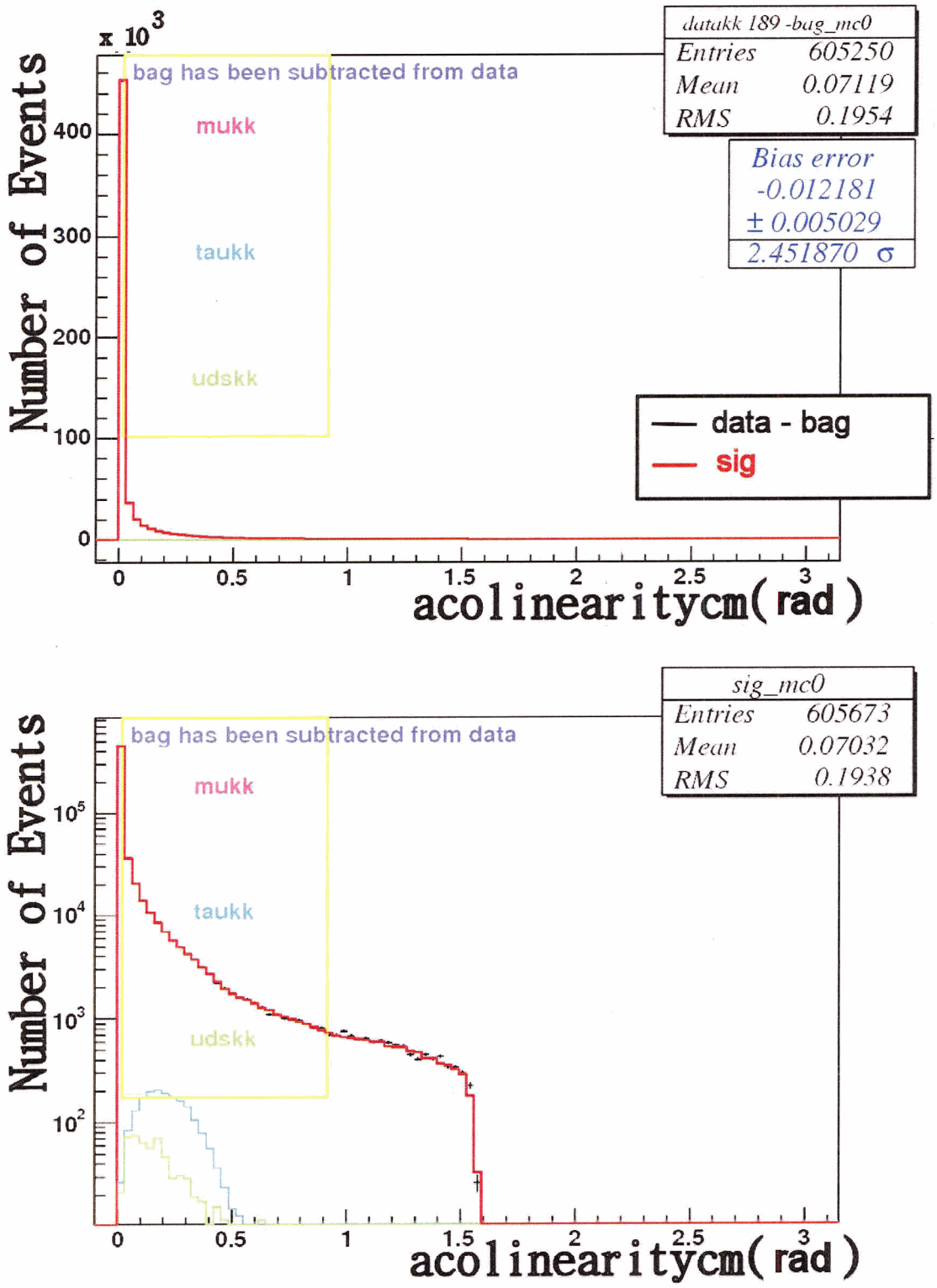

Figure 5.5: acolinearitycm(in radian) between $\mu^+\mu^-$. The error bars are too small to see on this plot. Point with error bars represent data minus background. Red line histograms represent KK2f MC for $e^+e^- \to \mu^+\mu^-(\gamma)$

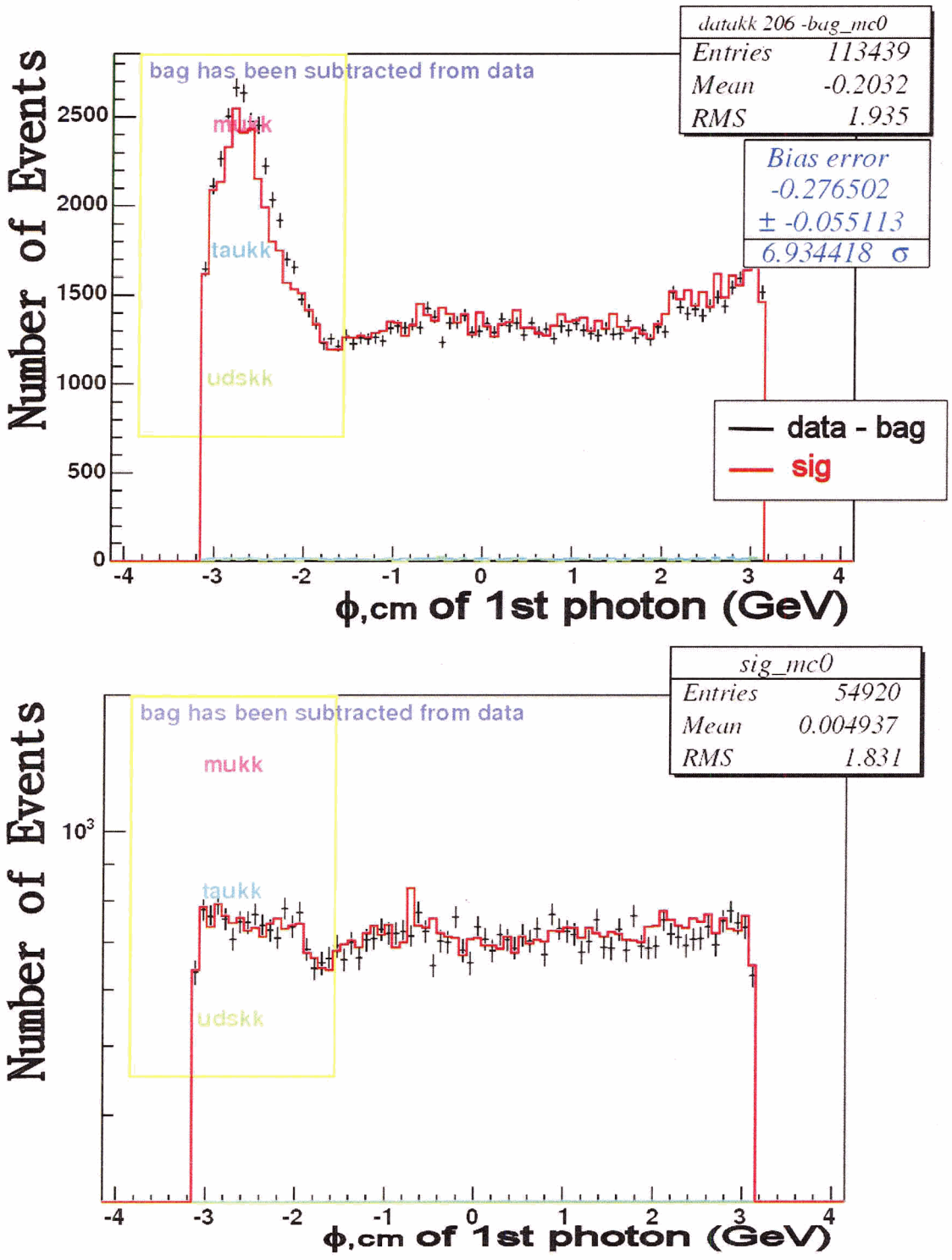

Figure 5.6: $\phi_{\gamma,CM}$ of 1st energy photon Upper:For E_γ >80 MeV Lower:For E_γ >250 MeV. Point with error bars represent data minus background. Red line histograms represent KK2f MC for $e^+e^- \to \mu^+\mu^-(\gamma)$

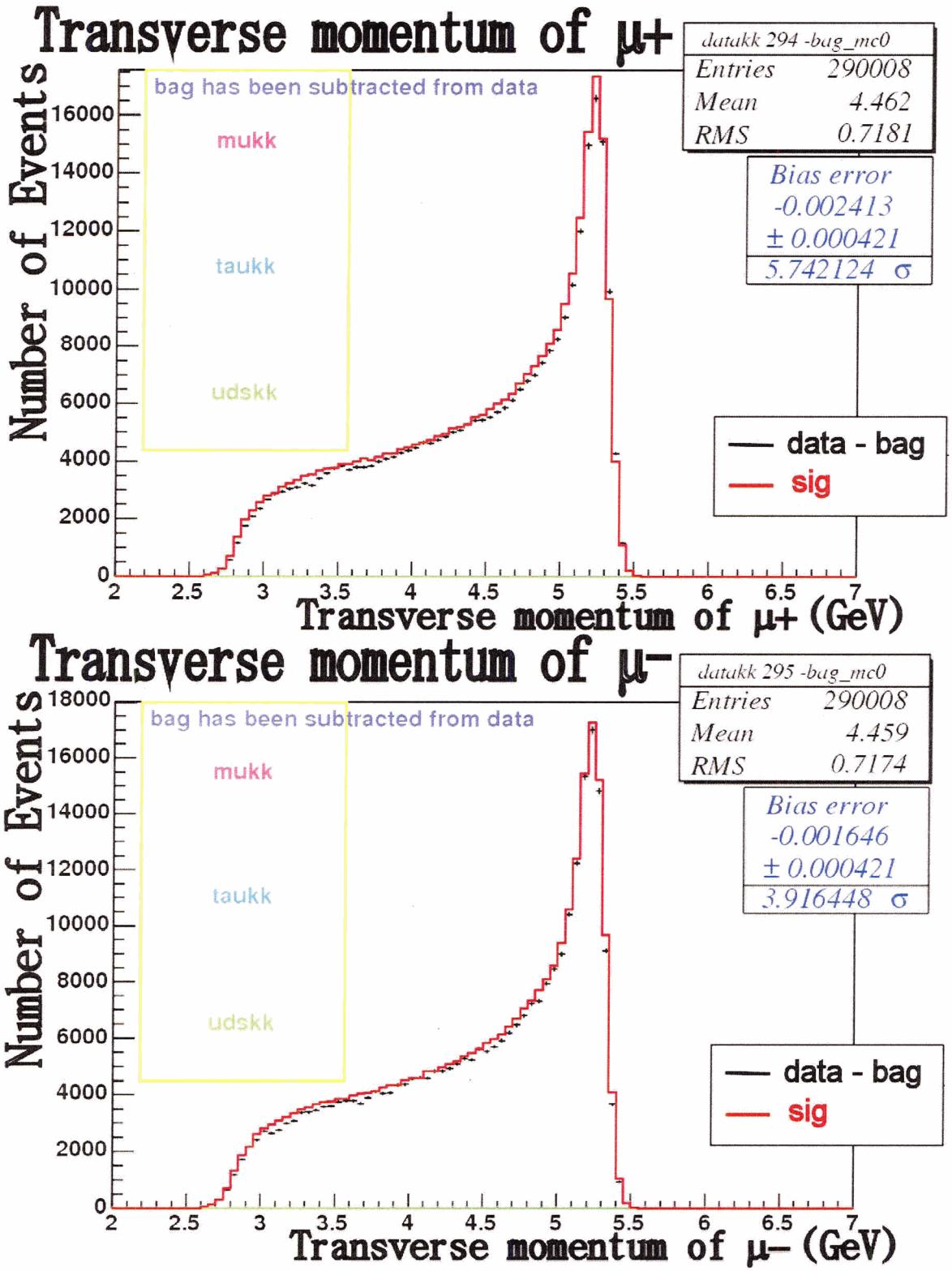

Figure 5.7: No-radiation cut applied Upper:$P_{transverse,\mu^+}$ Lower:$P_{transverse,\mu^-}$. Point with error bars represent data minus background. Red line histograms represent KK2f MC for $e^+e^- \to \mu^+\mu^-(\gamma)$

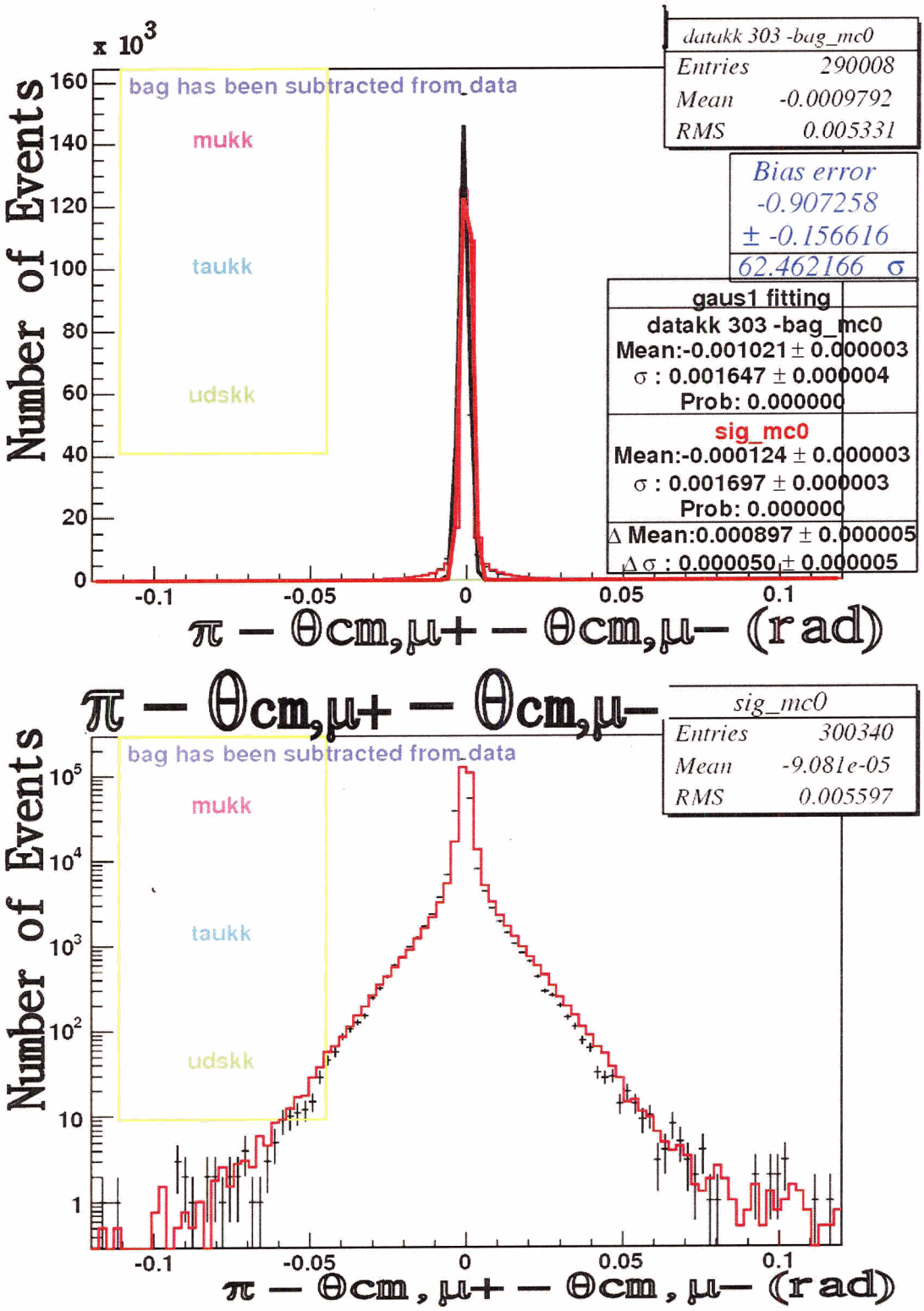

Figure 5.8: No-radiation cut applied $\pi - \theta_{CM,\mu^+} - \theta_{CM,\mu^-}$. Point with error bars represent data minus background. Red line histograms represent KK2f MC for $e^+e^- \to \mu^+\mu^-(\gamma)$

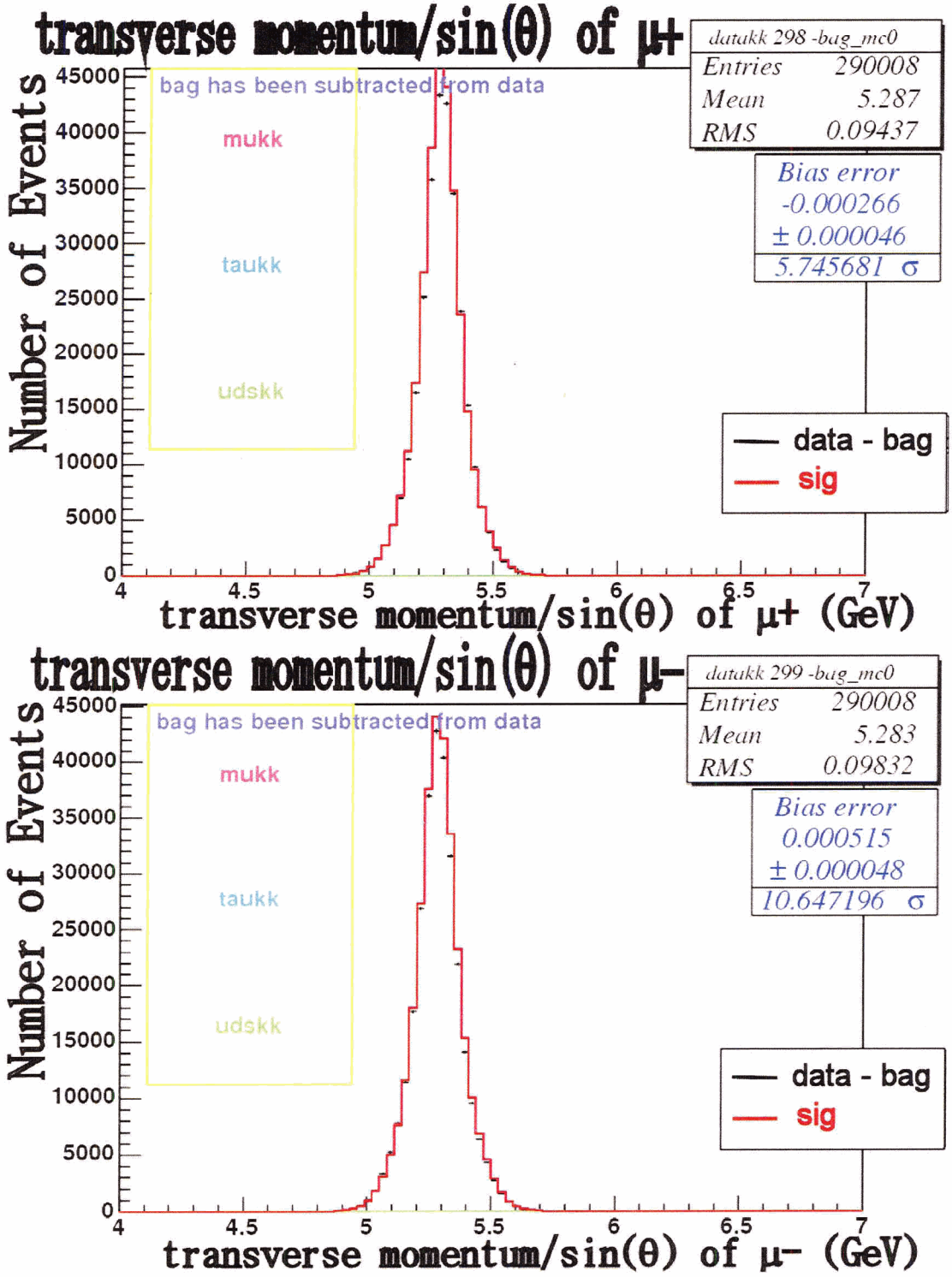

Figure 5.9: No-radiation cut applied Upper:$P_{transverse,\mu^+}/sin(\theta_{\mu^+})$ Lower:$P_{transverse,\mu^-}/sin(\theta_{\mu^-})$. Point with error bars represent data minus background. Red line histograms represent KK2f MC for $e^+e^- \rightarrow \mu^+\mu^-(\gamma)$

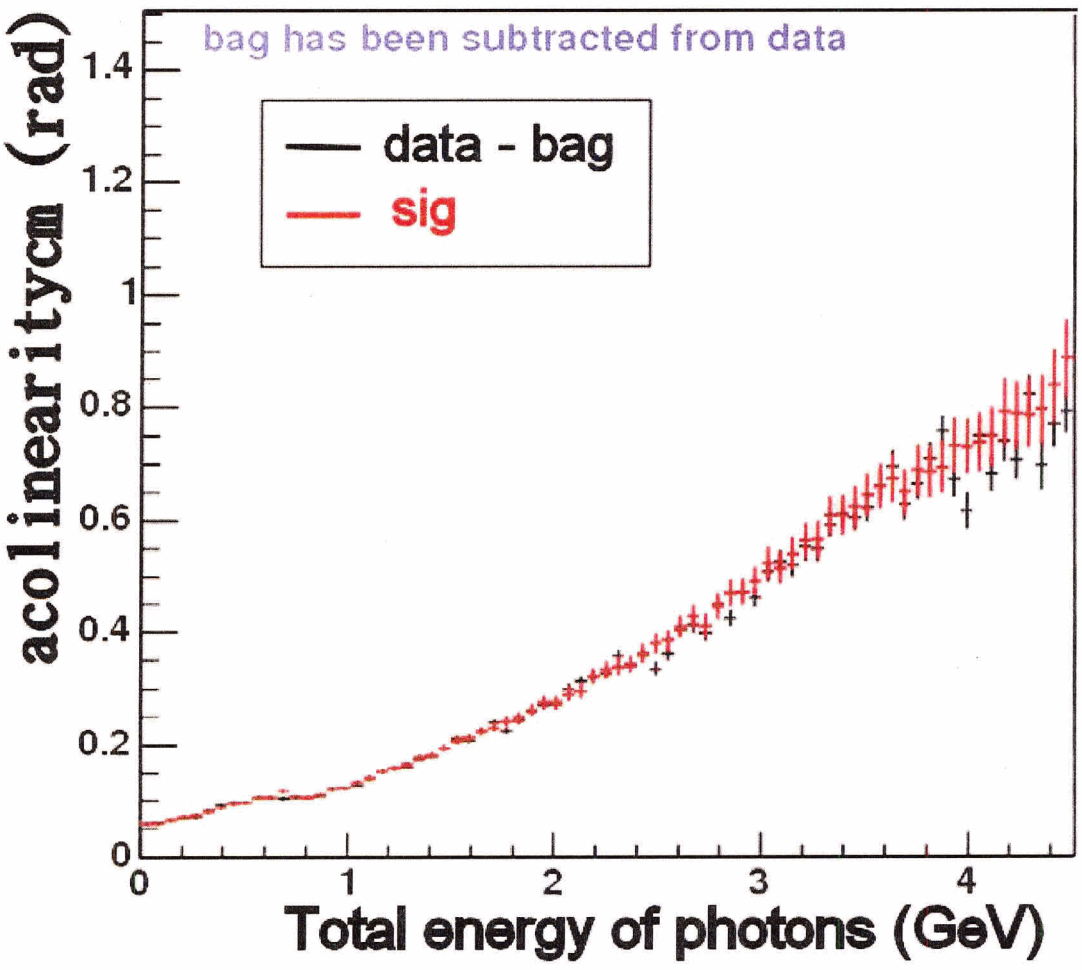

Figure 5.10: Profile of acolinearitycm vs $\Sigma E_{\gamma,CM}$

RMS and σ values of a Gaussian fit to the peak region are different between data(actually data - background) and MC(sig). For data they are RMS=2.222%, (σ=0.954±0.002)% for μ^+ and RMS=2.217%, (σ=0.957±0.002)% for μ^-. For MC they are RMS=2.238%, (σ=1.006±0.002)% for μ^+ and RMS=2.246%, (σ1.015±0.003)% for μ^-. The MC resolution is 5% larger than in the data. We can correct the MC for this: Let's define

$$\Delta^{MC} \equiv P^{MC}_{reco} - P^{MC}_{true}$$

$$P^{MC}_{reco} = P^{MC}_{true} + \Delta^{MC} \tag{5.1}$$

where P^{MC}_{true} is the true momentum of μ as calculated by KK2f and P^{MC}_{reco} is the reconstructed momentum via the GEANT4[5] detector simulator [1] and reconstruction software. So if we draw a histogram of Δ^{MC} we will get the approximately Gaussian distribution. The resolution of this Gaussian distribution must be the momentum resolution of detector. It means if the resolution of the detector for μ momentum is not well modelled by GEANT4 then the resolutions for data and MC in Figure 5.14 will show a disagreement. Thus we can think the resolution difference between data and MC in Figure 5.14 as a problem of GEANT4 detector simulator not of KK2f physics theory simulator. If we force the MC reconstructed resolution to be the resolution of the detector measured in the data, we expect better agreement for resolution in Figure 5.14. We can do it by defining

$$\Delta^{MC}_{corr} = \frac{\sigma^{data}_{Rp}}{\sigma^{MC}_{Rp}} \Delta^{MC}$$

here σ^{data}_{Rp} and σ^{MC}_{Rp} mean the σ value of Gaussian fit in Figure 5.14. Thus, if we substitute this Δ^{MC}_{corr} instead of Δ^{MC} in equation 5.1 we can improve the momentum resolution problem of GEANT4:

$$P^{MC}_{reco} = P^{MC}_{true} + \Delta^{MC}_{corr}$$

[1]The GEANT program describes the passage of elementary particles through the matter.The principal applications of GEANT in High Energy Physics are: 1. the tracking of particles through an experimental setup for simulation of detector response. 2. the graphical representation of the setup and of the particle trajectories.

$$P_{reco}^{MC} = P_{true}^{MC} + \frac{\sigma_{Rp}^{data}}{\sigma_{Rp}^{MC}} \Delta^{MC}$$

$$P_{reco}^{MC} = P_{true}^{MC} + \frac{\sigma_{Rp}^{data}}{\sigma_{Rp}^{MC}} (P_{reco}^{MC} - P_{true}^{MC}) \tag{5.2}$$

From Figure 5.15 we can see another detector problem. It shows the charge asymmetry in the high momentum region for data but not for μ MC. (Good agreement between μ^+ and μ^- in low momentum region has been observed for both data and MC). It may come from other kinds of contamination such as Bhabha. But we do not expect many Bhabha events in this selection as seen in Chapter 4. In conclusion we can fix this detector modelling problem by correcting P_{reco}^{MC}

$$P_{reco,corr}^{MC}(= Rpc) = \left(P_{true}^{MC} + \frac{\sigma_{Rp}^{data}}{\sigma_{Rp}^{MC}} (P_{reco}^{MC} - P_{true}^{MC}) \right) \frac{< P^{data} >}{< P^{MC} >} \tag{5.3}$$

here $< P^{data} >$ and $< P^{MC} >$ are the mean values of Gaussian fit in Figure 5.14. This $P_{reco,corr}^{MC}$ was calculated using equation 5.3 and it was used instead of P_{reco}^{MC} in equation 5.1 to correct detector problems. This correction was applied and the corrected distributions are shown in Figures 5.16, 5.17, 5.18, 5.19 and 5.20. In Figure 5.16 we can see the charge asymmetry on both data and MC by this manipulation. In Figure 5.17 the agreement between data and MC for resolution has been improved. The agreement of mean value between data and MC also improved, but not enough because ΔMean values(0.0054% for μ^+ and 0.0086% for μ^-) are beyond their error range (0.0032% for μ^+ and 0.0034% for μ^-). But compared with Figure 5.14 we can say it is a clear improvement on resolution and on the mean value of momentum. From Figures 5.18 and 5.19 we can see the improvement on the bias error of $P_{\mu,CM,corr}/P_{\mu,CM}^{max}$ from (0.023±0.017)% to (0.017±0.017)% for μ^+ and from (0.107±0.017)% to (0.035±0.017)% for μ^-. From Figure 5.20 we can see the improvement on bias error of $P_{\mu^\pm,CM,corr}/P_{\mu,CM}^{max}$ from (0.065±0.012)% to (0.026±0.012)%.

The cumulative result of different cuts is presented in Table 5.1 for the corrected MC.

Applied cut(cumulative)	Efficiency(%)	Purity(%)	Before	correction	After	correction
No cut	100.00	28.02	-0.74237	±0.00357	-0.74241	±0.00357
mutau preselection	67.82	22.77	-0.51060	±0.00109	-0.51074	±0.00109
Number of tracks=2	63.54	65.50	0.15066	±0.00022	0.15028	±0.00022
Each track is a prime track	61.27	68.35	0.11435	±0.00020	0.11398	±0.00020
TrackCharge$\neq$0 ΣTrackCharge=0	61.27	68.45	0.11455	±0.00020	0.11418	±0.00020
$\lvert cos(\theta_{tracks,cm})\rvert < 0.85$	55.69	68.81	0.09979	±0.00020	0.09936	±0.00020
$E_{EMC,\text{two tracks}} \neq$-1 and $E_{EMC,\text{one of track}} < 0.4$GeV	53.31	72.34	0.05244	±0.00019	0.05203	±0.00019
Exclude extra Bhabha events	53.23	75.77	0.04889	±0.00018	0.04848	±0.00018
Geometrical cut. Figure 4.8 region	52.70	92.18	0.05144	±0.00018	0.05103	±0.00018
Rm>0.4 and Remc<0.6	52.60	97.19	0.00283	±0.00012	0.00244	±0.00012
Extended cut on ISR, IFR region	52.41	99.57	0.00065	±0.00012	0.00026	±0.00012

Table 5.1: Muon Efficiency, purity, bias error of $P_{\mu,cm}/P^{max}_{\mu,cm}$ before and after correction for KK2f(Second numbers are the statistical error of bias error). They are cumulative result as applying more cuts

		$P_{\mu+}$		$P_{\mu-}$		$P_{\mu\pm}$	
KK		0.00022	±0.00016	0.00106	±0.00016	0.00065	±0.00012
		0.00016	±0.00016	0.00034	±0.00016	0.00026	±0.00012
	Rp(c)>0.3	0.00025	±0.00016	0.00109	±0.00016	0.00067	±0.00011
		0.00018	±0.00016	0.00037	±0.00016	0.00028	±0.00011
	Rp(c)>0.4	0.00029	±0.00015	0.00111	±0.00015	0.00070	±0.00011
		0.00023	±0.00015	0.00040	±0.00015	0.00031	±0.00011
	Rp(c)>0.5	0.00033	±0.00014	0.00109	±0.00014	0.00071	±0.00010
		0.00027	±0.00014	0.00038	±0.00014	0.00033	±0.00010
KKbag10%		0.00096	±0.00016	0.00180	±0.00016	0.00138	±0.00011
		0.00090	±0.00016	0.00109	±0.00016	0.00100	±0.00011
	Rp(c)>0.3	0.00093	±0.00016	0.00179	±0.00016	0.00136	±0.00011
		0.00087	±0.00016	0.00107	±0.00016	0.00097	±0.00011
	Rp(c)>0.4	0.00095	±0.00015	0.00177	±0.00015	0.00136	±0.00011
		0.00089	±0.00015	0.00106	±0.00015	0.00097	±0.00011
	Rp(c)>0.5	0.00095	±0.00014	0.00171	±0.00014	0.00133	±0.00010
		0.00089	±0.00014	0.00101	±0.00014	0.00095	±0.00010
KKbag50%		0.00063	±0.00016	0.00147	±0.00016	0.00105	±0.00011
		0.00057	±0.00016	0.00076	±0.00016	0.00067	±0.00011
	Rp(c)>0.3	0.00063	±0.00016	0.00148	±0.00016	0.00105	±0.00011
		0.00057	±0.00016	0.00076	±0.00016	0.00066	±0.00011
	Rp(c)>0.4	0.00066	±0.00015	0.00148	±0.00015	0.00107	±0.00011
		0.00060	±0.00015	0.00076	±0.00015	0.00068	±0.00011
	Rp(c)>0.5	0.00068	±0.00014	0.00144	±0.00014	0.00106	±0.00010
		0.00062	±0.00014	0.00073	±0.00014	0.00067	±0.00010
KKbag90%		0.00030	±0.00016	0.00114	±0.00016	0.00072	±0.00011
		0.00024	±0.00016	0.00043	±0.00016	0.00033	±0.00011
	Rp(c)>0.3	0.00032	±0.00016	0.00117	±0.00016	0.00074	±0.00011
		0.00026	±0.00016	0.00045	±0.00016	0.00036	±0.00011
	Rp(c)>0.4	0.00037	±0.00015	0.00119	±0.00015	0.00078	±0.00011
		0.00030	±0.00015	0.00047	±0.00015	0.00039	±0.00011
	Rp(c)>0.5	0.00040	±0.00014	0.00116	±0.00014	0.00078	±0.00010
		0.00034	±0.00014	0.00045	±0.00014	0.00040	±0.00010

Table 5.2: Bias error of $P_{\mu,cm}/P^{max}_{\mu,cm}$ for KK2f. Second numbers are the statistical error of bias error. Upper numbers are the ones before correction and lower numbers are the ones after correction.

		$P_{\mu+}$		$P_{\mu-}$		$P_{\mu\pm}$	
KKbag110%		0.00014	±0.00016	0.00098	±0.00016	0.00056	±0.00011
		0.00008	±0.00016	0.00026	±0.00016	0.00017	±0.00011
	Rp(c)>0.3	0.00017	±0.00016	0.00101	±0.00016	0.00059	±0.00011
		0.00011	±0.00016	0.00029	±0.00016	0.00020	±0.00011
	Rp(c)>0.4	0.00022	±0.00015	0.00104	±0.00015	0.00063	±0.00011
		0.00016	±0.00015	0.00032	±0.00015	0.00024	±0.00011
	Rp(c)>0.5	0.00027	±0.00014	0.00102	±0.00014	0.00064	±0.00010
		0.00021	±0.00014	0.00031	±0.00014	0.00026	±0.00010
KKbag150%		-0.00018	±0.00016	0.00065	±0.00016	0.00023	±0.00011
		-0.00024	±0.00016	-0.00006	±0.00016	-0.00015	±0.00011
	Rp(c)>0.3	-0.00013	±0.00016	0.00070	±0.00016	0.00028	±0.00011
		-0.00019	±0.00016	-0.00001	±0.00016	-0.00010	±0.00011
	Rp(c)>0.4	-0.00006	±0.00015	0.00074	±0.00015	0.00034	±0.00010
		-0.00012	±0.00015	0.00003	±0.00015	-0.00004	±0.00010
	Rp(c)>0.5	-0.00000	±0.00014	0.00074	±0.00014	0.00037	±0.00010
		-0.00006	±0.00014	0.00004	±0.00014	-0.00001	±0.00010
KKbag200%		-0.00060	±0.00016	0.00023	±0.00016	-0.00018	±0.00011
		-0.00066	±0.00016	-0.00048	±0.00016	-0.00057	±0.00011
	Rp(c)>0.3	-0.00051	±0.00016	0.00031	±0.00016	-0.00010	±0.00011
		-0.00058	±0.00016	-0.00040	±0.00016	-0.00049	±0.00011
	Rp(c)>0.4	-0.00043	±0.00015	0.00037	±0.00015	-0.00002	±0.00010
		-0.00049	±0.00015	-0.00033	±0.00015	-0.00041	±0.00010
	Rp(c)>0.5	-0.00035	±0.00014	0.00040	±0.00014	0.00002	±0.00010
		-0.00041	±0.00014	-0.00030	±0.00014	-0.00036	±0.00010

Table 5.3: Bias error of $P_{\mu,cm}/P^{max}_{\mu,cm}$ for KK2f. Second numbers are the statistical error of bias error. Upper numbers are the ones before correction and lower numbers are the ones after correction.

		$P_{\mu+}$		$P_{\mu-}$		$P_{\mu\pm}$	
KB		-0.00118	±0.00020	-0.00059	±0.00020	-0.00089	±0.00015
		-0.00110	±0.00020	-0.00129	±0.00020	-0.00120	±0.00015
	Rp(c)>0.3	-0.00115	±0.00020	-0.00045	±0.00020	-0.00080	±0.00014
		-0.00107	±0.00020	-0.00115	±0.00020	-0.00111	±0.00014
	Rp(c)>0.4	-0.00102	±0.00019	-0.00041	±0.00019	-0.00071	±0.00013
		-0.00094	±0.00019	-0.00111	±0.00019	-0.00102	±0.00013
	Rp(c)>0.5	-0.00100	±0.00017	-0.00031	±0.00017	-0.00066	±0.00012
		-0.00092	±0.00017	-0.00100	±0.00017	-0.00096	±0.00012
KBbag10%		-0.00064	±0.00020	-0.00004	±0.00020	-0.00034	±0.00014
		-0.00056	±0.00020	-0.00074	±0.00020	-0.00065	±0.00014
	Rp(c)>0.3	-0.00063	±0.00020	0.00007	±0.00020	-0.00027	±0.00014
		-0.00054	±0.00020	-0.00062	±0.00020	-0.00058	±0.00014
	Rp(c)>0.4	-0.00050	±0.00019	0.00010	±0.00019	-0.00020	±0.00013
		-0.00042	±0.00019	-0.00059	±0.00019	-0.00051	±0.00013
	Rp(c)>0.5	-0.00051	±0.00017	0.00017	±0.00017	-0.00016	±0.00012
		-0.00042	±0.00017	-0.00050	±0.00017	-0.00046	±0.00012
KBbag50%		-0.00088	±0.00020	-0.00028	±0.00020	-0.00058	±0.00014
		-0.00080	±0.00020	-0.00098	±0.00020	-0.00089	±0.00014
	Rp(c)>0.3	-0.00086	±0.00020	-0.00016	±0.00020	-0.00051	±0.00014
		-0.00078	±0.00020	-0.00086	±0.00020	-0.00082	±0.00014
	Rp(c)>0.4	-0.00073	±0.00019	-0.00012	±0.00019	-0.00043	±0.00013
		-0.00065	±0.00019	-0.00082	±0.00019	-0.00074	±0.00013
	Rp(c)>0.5	-0.00073	±0.00017	-0.00004	±0.00017	-0.00038	±0.00012
		-0.00064	±0.00017	-0.00072	±0.00017	-0.00068	±0.00012
KBbag90%		-0.00112	±0.00020	-0.00052	±0.00020	-0.00082	±0.00014
		-0.00104	±0.00020	-0.00123	±0.00020	-0.00113	±0.00014
	Rp(c)>0.3	-0.00109	±0.00020	-0.00039	±0.00020	-0.00074	±0.00014
		-0.00101	±0.00020	-0.00109	±0.00020	-0.00105	±0.00014
	Rp(c)>0.4	-0.00096	±0.00019	-0.00035	±0.00019	-0.00066	±0.00013
		-0.00088	±0.00019	-0.00105	±0.00019	-0.00097	±0.00013
	Rp(c)>0.5	-0.00095	±0.00017	-0.00026	±0.00017	-0.00060	±0.00012
		-0.00087	±0.00017	-0.00094	±0.00017	-0.00090	±0.00012

Table 5.4: Bias error of $P_{\mu,cm}/P^{max}_{\mu,cm}$ for KORALB. Second numbers are the statistical error of bias error. Upper numbers are the ones before correction and lower numbers are the ones after correction.

		$P_{\mu+}$		$P_{\mu-}$		$P_{\mu\pm}$	
KBbag110%		-0.00124	±0.00020	-0.00065	±0.00020	-0.00095	±0.00014
		-0.00116	±0.00020	-0.00135	±0.00020	-0.00126	±0.00014
	Rp(c)>0.3	-0.00121	±0.00020	-0.00051	±0.00020	-0.00086	±0.00014
		-0.00113	±0.00020	-0.00121	±0.00020	-0.00117	±0.00014
	Rp(c)>0.4	-0.00108	±0.00019	-0.00047	±0.00019	-0.00077	±0.00013
		-0.00100	±0.00019	-0.00117	±0.00019	-0.00108	±0.00013
	Rp(c)>0.5	-0.00106	±0.00017	-0.00037	±0.00017	-0.00071	±0.00012
		-0.00098	±0.00017	-0.00105	±0.00017	-0.00102	±0.00012
KBbag150%		-0.00149	±0.00020	-0.00089	±0.00020	-0.00119	±0.00014
		-0.00141	±0.00020	-0.00159	±0.00020	-0.00150	±0.00014
	Rp(c)>0.3	-0.00145	±0.00020	-0.00075	±0.00020	-0.00110	±0.00014
		-0.00137	±0.00020	-0.00145	±0.00020	-0.00141	±0.00014
	Rp(c)>0.4	-0.00131	±0.00019	-0.00070	±0.00019	-0.00100	±0.00013
		-0.00123	±0.00019	-0.00140	±0.00019	-0.00131	±0.00013
	Rp(c)>0.5	-0.00128	±0.00017	-0.00059	±0.00017	-0.00094	±0.00012
		-0.00120	±0.00017	-0.00127	±0.00017	-0.00124	±0.00012
KBbag200%		-0.00179	±0.00020	-0.00119	±0.00020	-0.00149	±0.00014
		-0.00171	±0.00020	-0.00190	±0.00020	-0.00180	±0.00014
	Rp(c)>0.3	-0.00174	±0.00020	-0.00105	±0.00020	-0.00139	±0.00014
		-0.00166	±0.00020	-0.00175	±0.00020	-0.00170	±0.00014
	Rp(c)>0.4	-0.00160	±0.00019	-0.00099	±0.00019	-0.00129	±0.00013
		-0.00151	±0.00019	-0.00169	±0.00019	-0.00160	±0.00013
	Rp(c)>0.5	-0.00156	±0.00017	-0.00086	±0.00017	-0.00121	±0.00012
		-0.00148	±0.00017	-0.00155	±0.00017	-0.00151	±0.00012

Table 5.5: Bias error of $P_{\mu,cm}/P^{max}_{\mu,cm}$ for KORALB. Second numbers are the statistical error of bias error. Upper numbers are the ones before correction and lower numbers are the ones after correction.

We now systematically study the MC, data bias as a function of the lower cut on P_μ and on the amount of background subtracted. In Table 5.3 the bias error of $P_{\mu,CM}/P^{max}_{\mu,CM}$ was presented for Rp(c) >0.3, >0.4, >0.5, respectively, and for background subtraction of 0%, 10%, 50%, 90%, 110%, 150%, 200% of the original expected level of background. The upper numbers are the ones before correction and lower numbers are the ones after correction. As we increase lower momentum cut, the bias error becomes worse. It implies that the bias error is more serious in the higher momentum region than the lower momentum regions. From this table we can also check the effect of changing the background by ±10%. Since the mean value of the MC is bigger than the mean value of the data, we can understand that subtracting more background, which populates the lower momentum region, makes the bias error smaller. From differences between $P_{\mu^+,CM,corr}/P^{max}_{\mu,CM}$ and $P_{\mu^-,CM,corr}/P^{max}_{\mu,CM}$, changing the lower momentum cut and changing the background efficiency by ±10% we can calculate systematic error for KK2f before and after the correction:

$$\begin{aligned} \text{Bias error of } P_{\mu^\pm,CM}/P^{max}_{\mu,CM} &= (0.065 \pm 0.012(stat) \pm 0.043(syst))\% \\ \text{Bias error of } P_{\mu^\pm,CM,corr}/P^{max}_{\mu,CM} &= (0.026 \pm 0.012(stat) \pm 0.015(syst))\%. \end{aligned}$$

The tau lifetime study being performed until now uses KORALB MC[20]. Therefore, the systematic error for KORALB also has been calculated before and after correction:

$$\begin{aligned} \text{Bias error of } P_{\mu^\pm,CM}/P^{max}_{\mu,CM} &= (-0.089 \pm 0.015(stat) \pm 0.038(syst))\%. \\ \text{Bias error of } P_{\mu^\pm,CM,corr}/P^{max}_{\mu,CM} &= (-0.120 \pm 0.015(stat) \pm 0.026(syst))\% \end{aligned}$$

The mean values of $P_{\mu^-,CM}/P^{max}_{\mu,CM}$ in the overall range were observed to be 0.9637 for data(data - background) and 0.9631 for MC(μ MC). The mean values of Gaussian fit between $0.985 < P_{\mu^-,CM}/P^{max}_{\mu,CM} < 1.02$ were observed to be 0.99760 for data and 0.998301 for MC. Thus $< P^{data} > / < P^{MC} >$ in equation 5.3 is less than 1. This makes a worse bias error after correction. $< P^{data} > / < P^{MC} >$ of $P_{\mu^+,CM}/P^{max}_{\mu,CM}$ is almost unity. Thus it didn't affect the correction as much correction to μ^- do. Note that the software used to

model the detector and reconstruct tracks was not identical for the KORALB (for production SP5) and KK2f (for production SP5) MC.

In Table 5.5 the systematic study table is presented for KORALB. In contrast to KK2f, KORALB shows a bigger mean value of data than of MC for $P_{\mu^\pm,CM,corr}/P^{max}_{\mu,CM}$. Subtracting less background makes the bias error smaller. We can check that subtracting -10% of background results in a bias error -0.113±0.014%. Subtracting +10% of background results in a bias error -0.126±0.014%. Comparing the bias error $P_{\mu^\pm,CM,corr}/P^{max}_{\mu,CM} = -0.1199 \pm 0.0148$ without subtracting we can see the fact that subtracting less background makes the bias error smaller. This is because mean value of $P_{\mu^\pm,CM,corr}/P^{max}_{\mu,CM}$ for data(0.9641) is bigger than that for MC(0.9632).

From these studies the τ lifetime measurement assigns a systematic error on the τ momentum predicted by KORALB to be 0.1%. Next time when someone studies the tau lifetime using KK2f, he can reduce the systematic error using an error of 0.026% for this.

5.3 Systematic study of ΔE and $M_{EC,\mu\gamma}$

Figures 5.21 and 5.22 present M_{EC}(Beam-energy constrained mass of $\mu\gamma$[2]) and $\Delta E(E_{CM}/2 - E^{CM}_{\mu\gamma})$, respectively. Here the μ and photon are chosen by selecting the highest momentum track in either hemisphere of detector combined with the most energetic photon in the same hemisphere and the origin for the γ is selected as the point of closest approach of the μ track from beam spot.

When we search for the lepton flavor violating decay, $\tau \rightarrow \mu\gamma$, one of the criteria in selecting those events uses $\Delta E(=E_{CM}/2 - E^{CM}_{\mu\gamma})$ and the $\mu\gamma$ invariant mass, $M_{EC,\mu\gamma} \approx m_\tau = 1.777 GeV/c^2$. For signal events the μ and γ have a half of the CM energy in the CM frame and $\Delta E \approx 0$. Thus, the uncertainties on ΔE and $M_{EC,\mu\gamma}$ affects the systematic errors associated with the $\tau \rightarrow \mu\gamma$ signal efficiency. So we study the uncertainty on ΔE and $M_{EC,\mu\gamma}$

[2] $M_{EC} = \sqrt{E^{*2} - P^{*2}}$, where E^{*2} and P^{*2} are center-of-mass frame quantities obtained by performing a kinematic fit with the constraint that the $\mu\gamma$ system has an energy equal to the half of the CM energy.

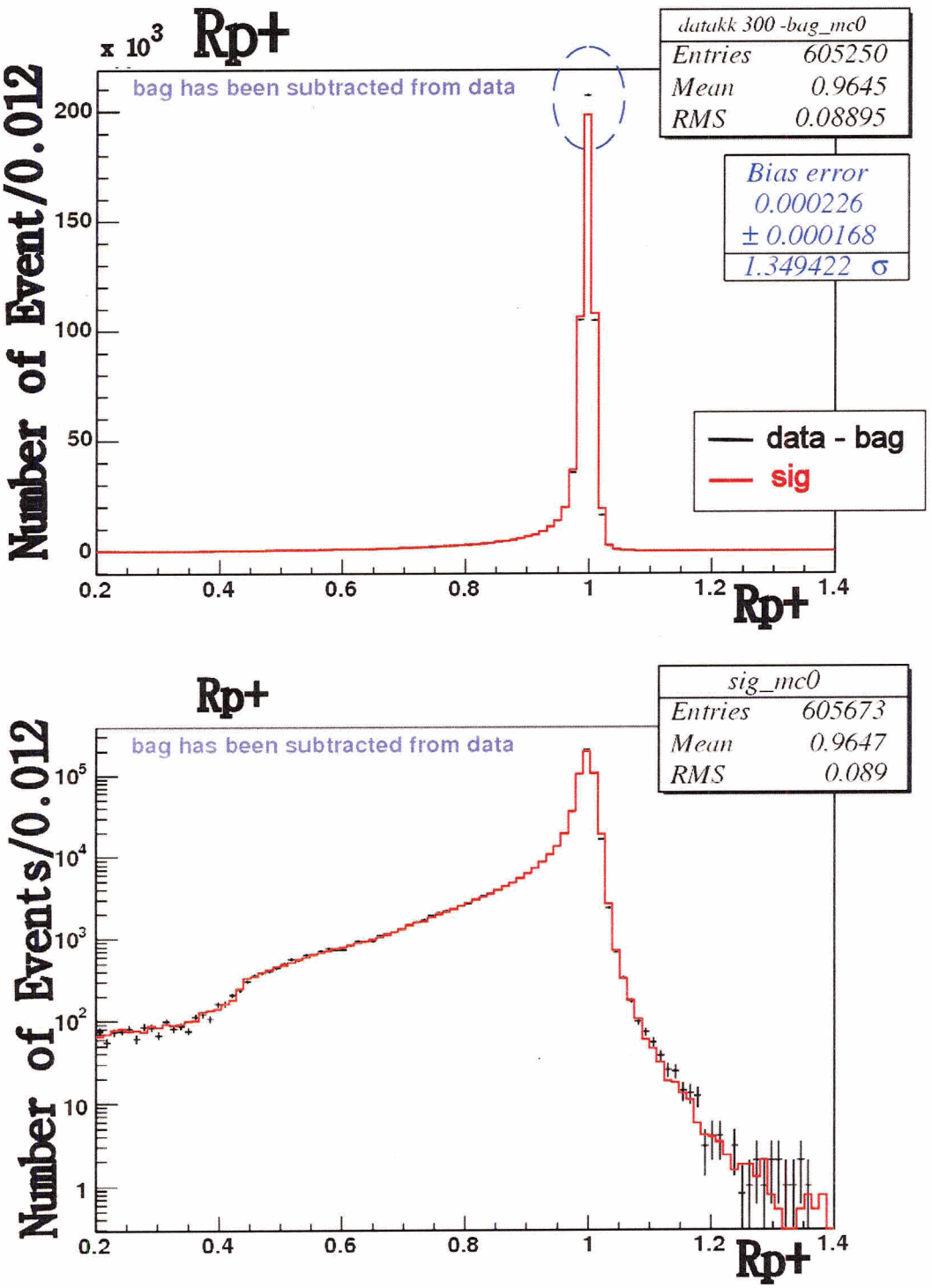

Figure 5.11: $P_{\mu^+,CM}/P^{max}_{\mu,CM}$; Bias error means ($< sig > - < data - background >)/ < data - background >$. Point with error bars represent data minus background. Red line histograms represent KK2f MC for $e^+e^- \rightarrow \mu^+\mu^-(\gamma)$

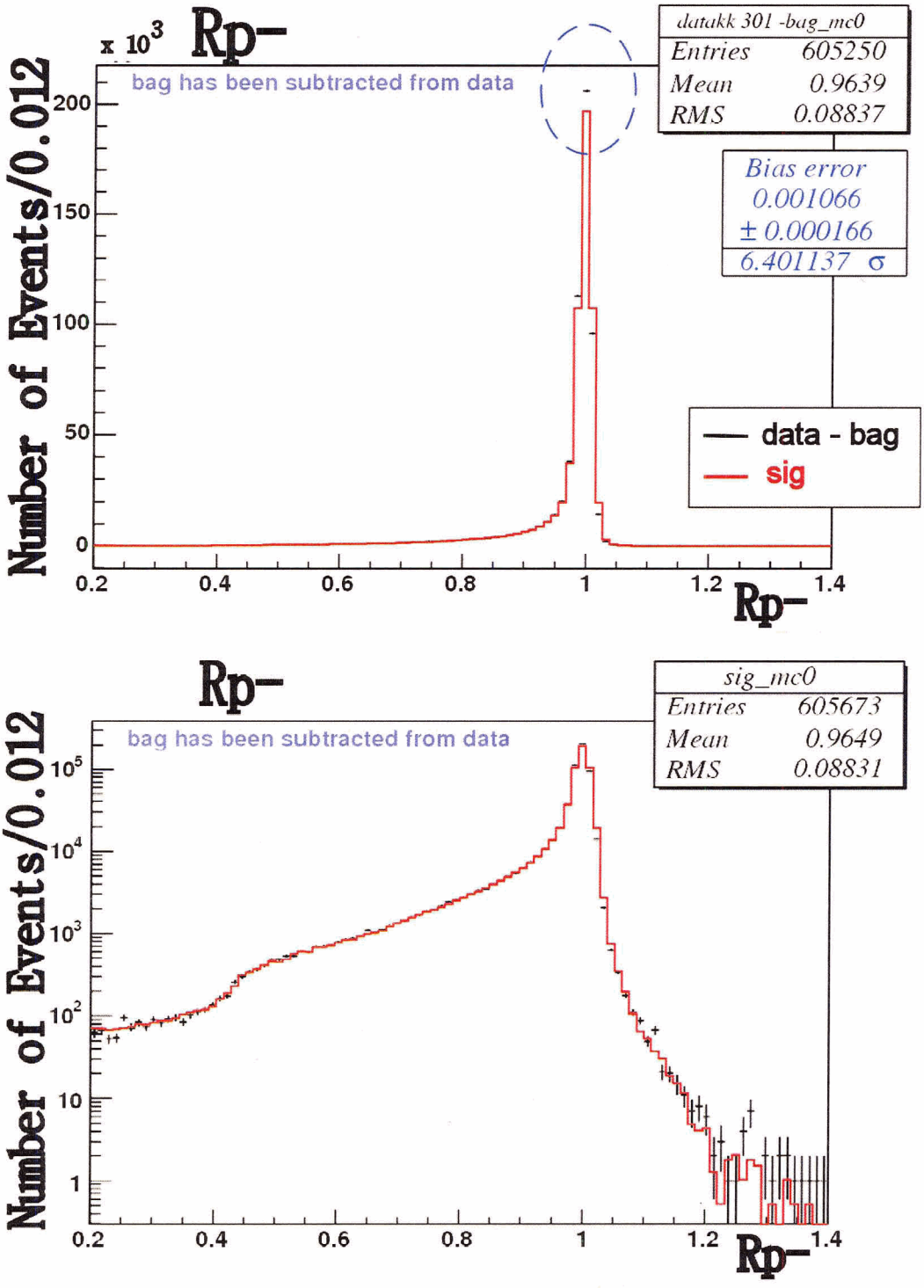

Figure 5.12: $P_{\mu^-,CM}/P^{max}_{\mu,CM}$

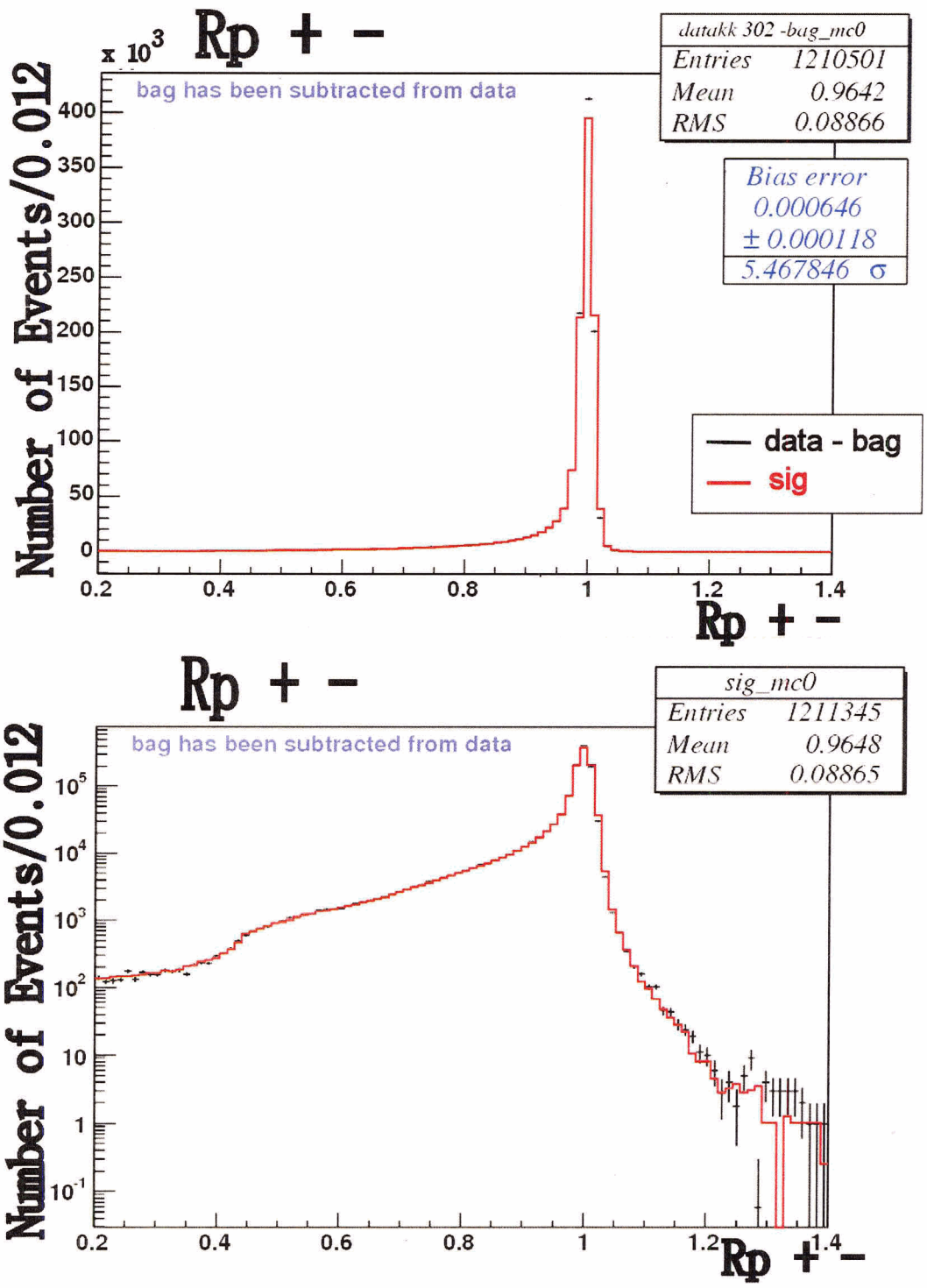

Figure 5.13: $P_{\mu^{\pm},CM}/P^{max}_{\mu,CM}$

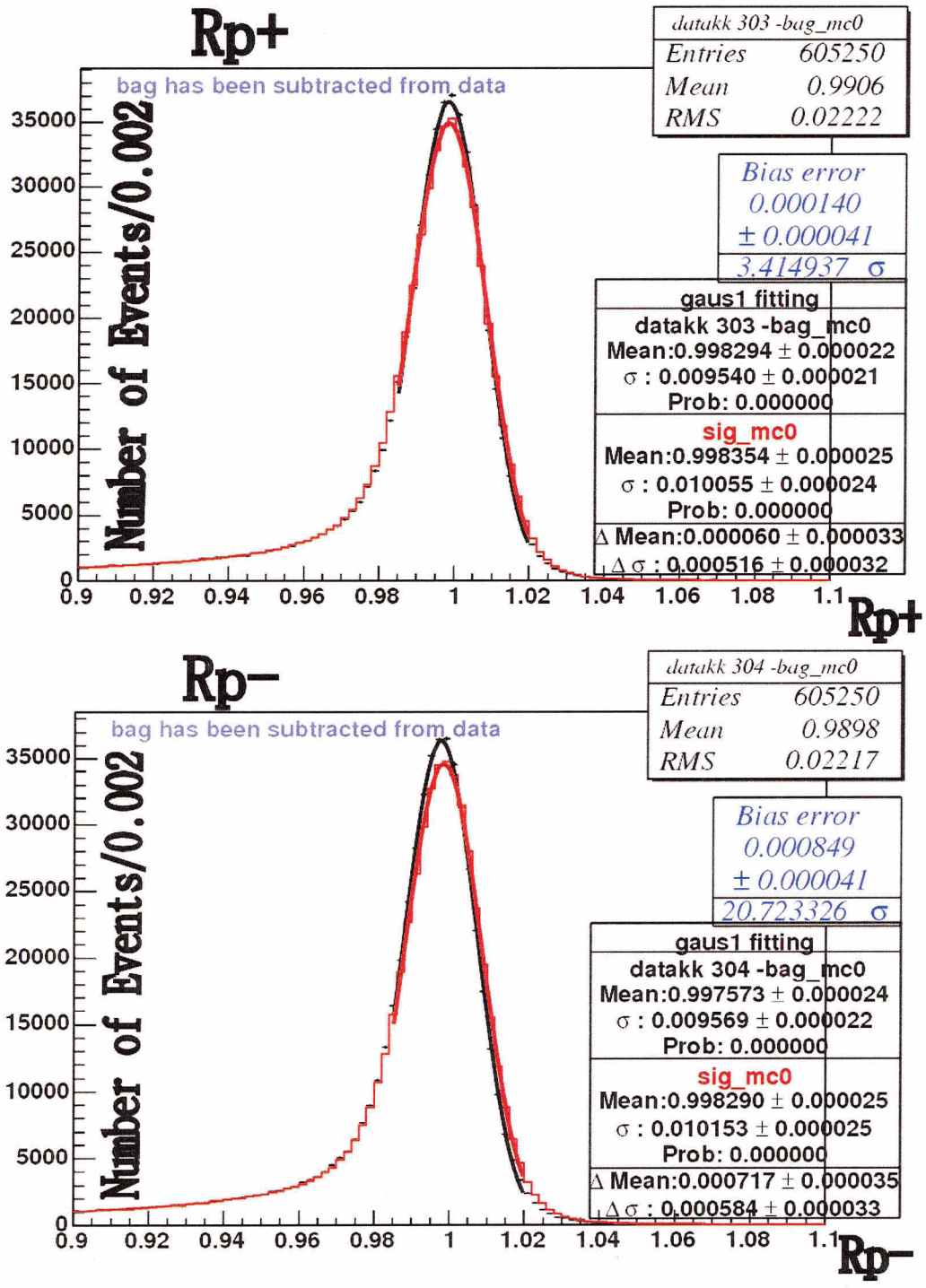

Figure 5.14: Upper:$P_{\mu^+,CM}/P^{max}_{\mu,CM}$ Lower:$P_{\mu^-,CM}/P^{max}_{\mu,CM}$ ΔMean means $Mean_{Gaussian fit,sig} - Mean_{Gaussian fit,data-background}$

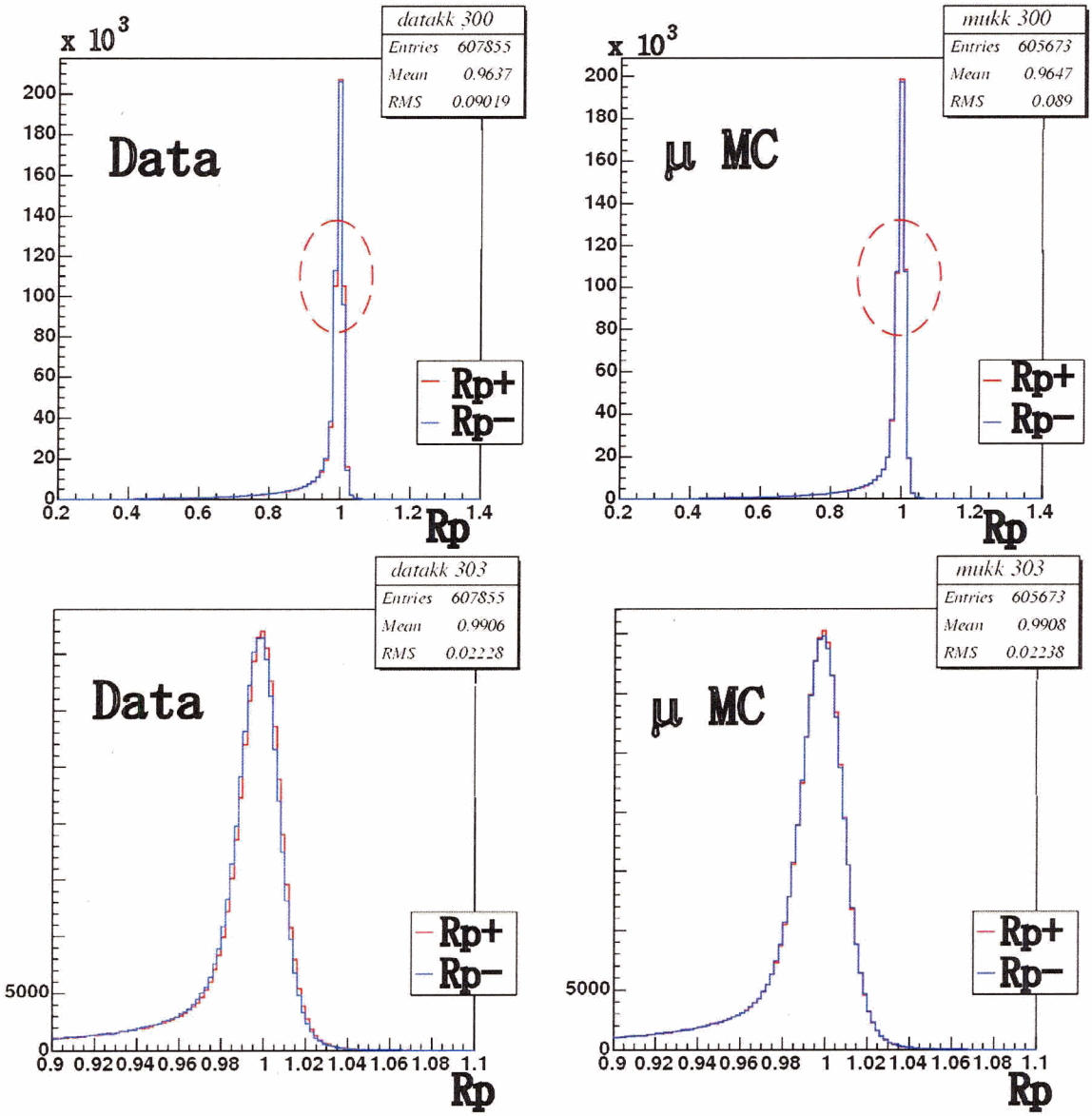

Figure 5.15: $P_{\mu,CM}/P^{max}_{\mu,CM}$ Red line is +charge Blue line is -charge Bias error means ($< P_{\mu^-} > - < P_{\mu^+} > / < P_{\mu^+} >$ Left:data Right:μ MC. Lower plots are in the high momentum region.

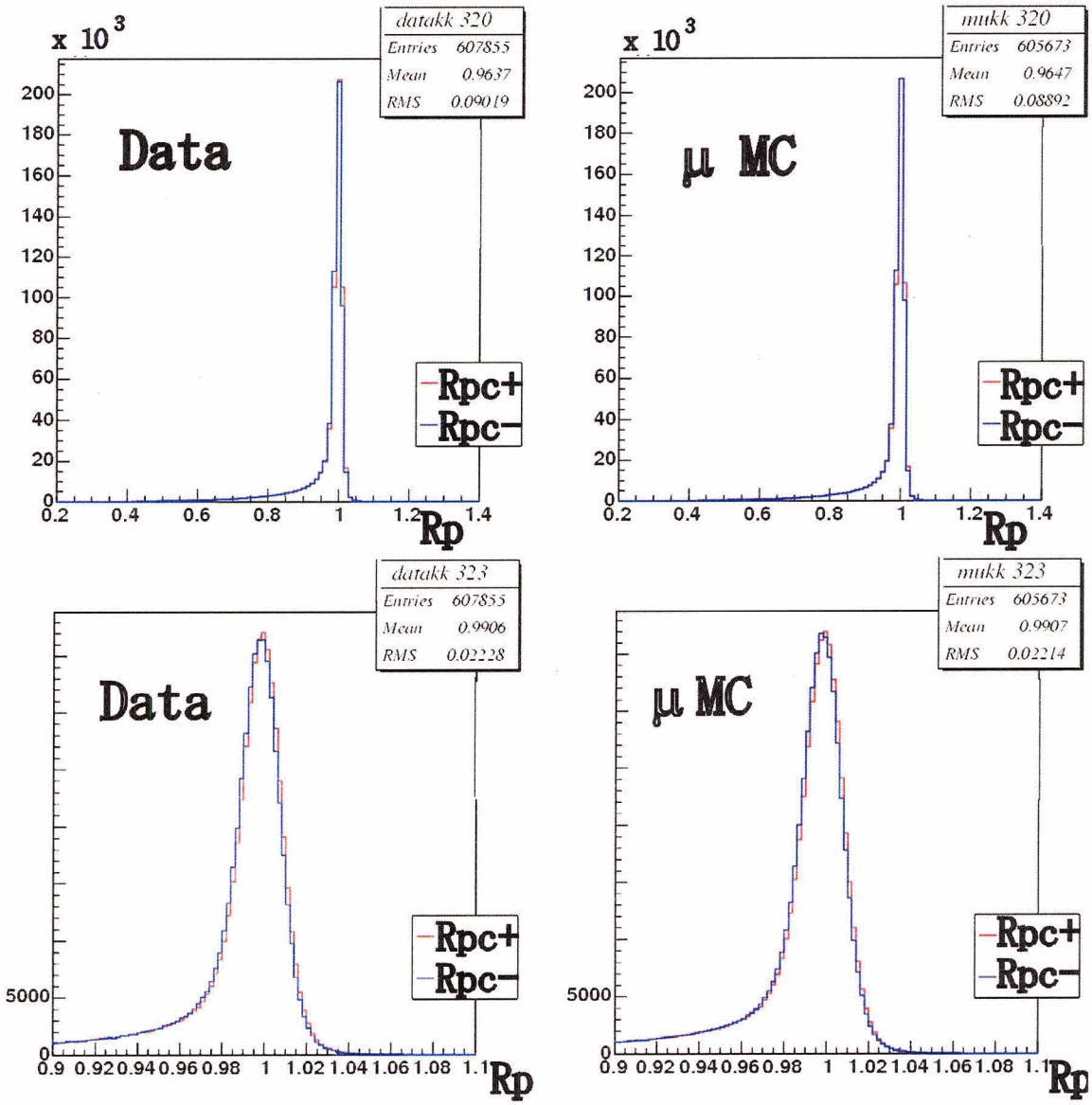

Figure 5.16: $P_{\mu,CM,corr}/P^{max}_{\mu,CM}$ Red line is +charge Blue line is -charge Bias error means $(< P_{\mu^-} > - < P_{\mu^+} >)/ < P_{\mu^+} >$ Left:data Right:μ MC. Lower plots are in the high momentum region.

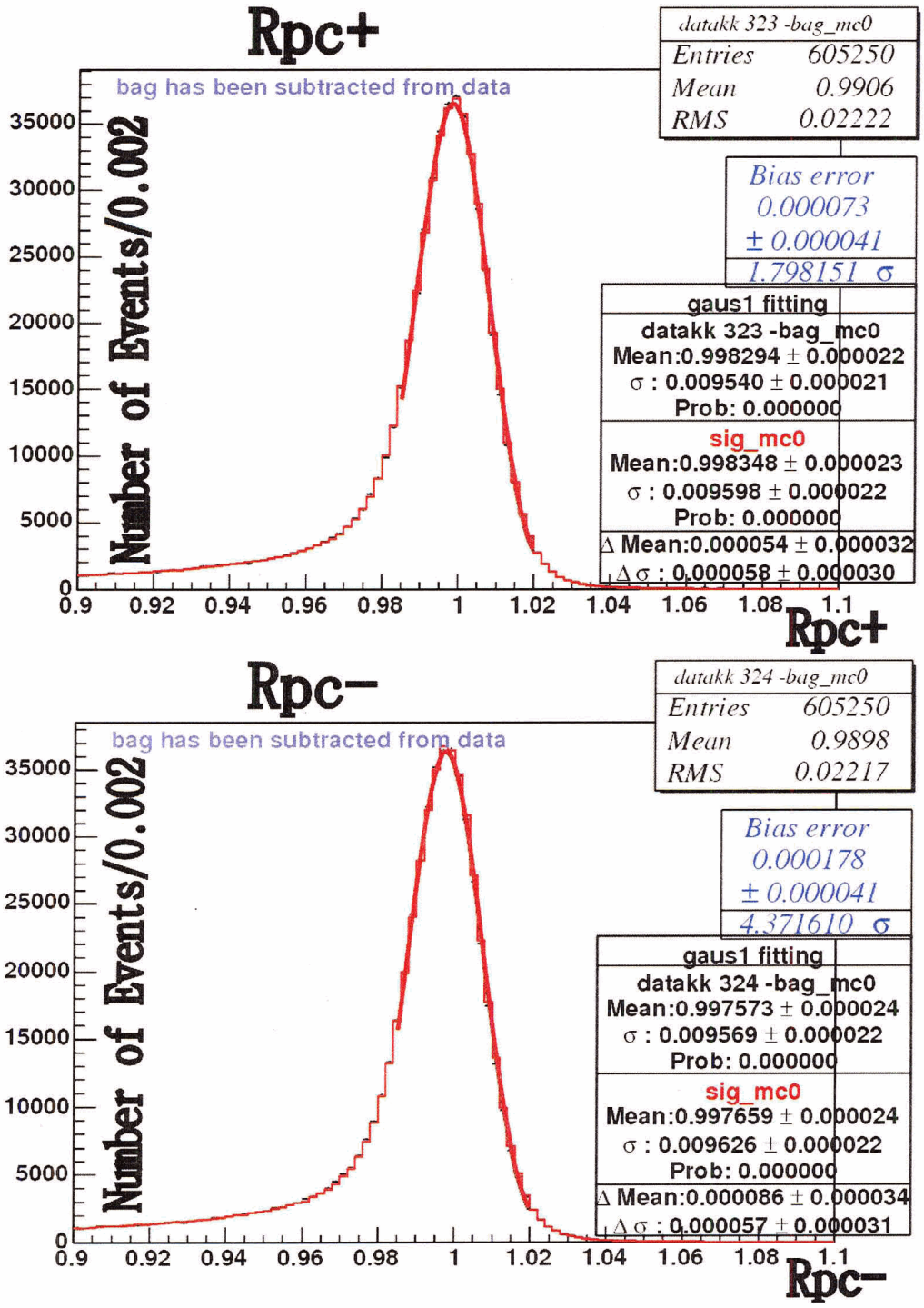

Figure 5.17: Upper:$P_{\mu^+,CM,corr}/P^{max}_{\mu,CM}$ Lower:$P_{\mu^-,CM,corr}/P^{max}_{\mu,CM}$

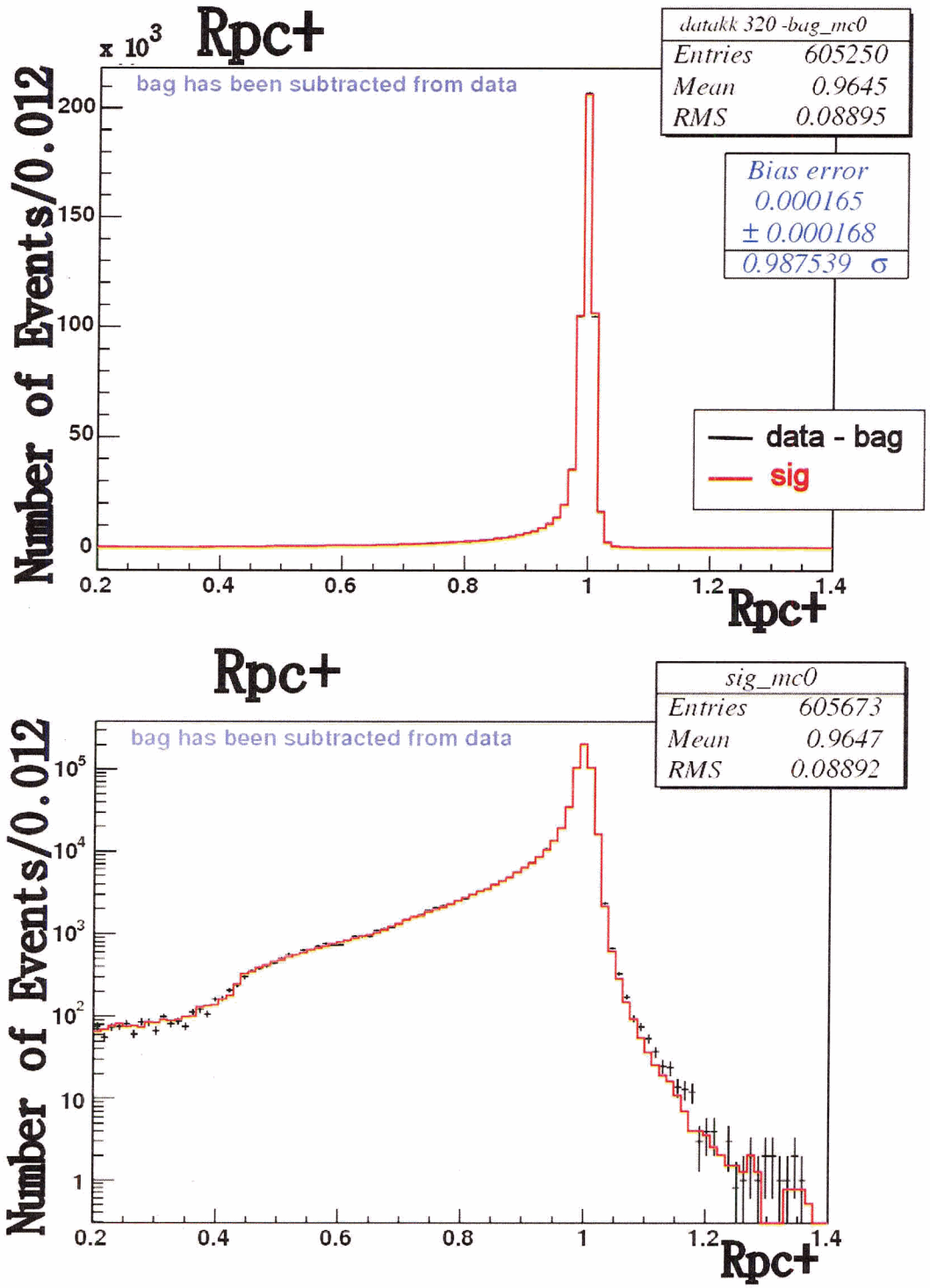

Figure 5.18: $P_{\mu^+,CM,corr}/P^{max}_{\mu,CM}$

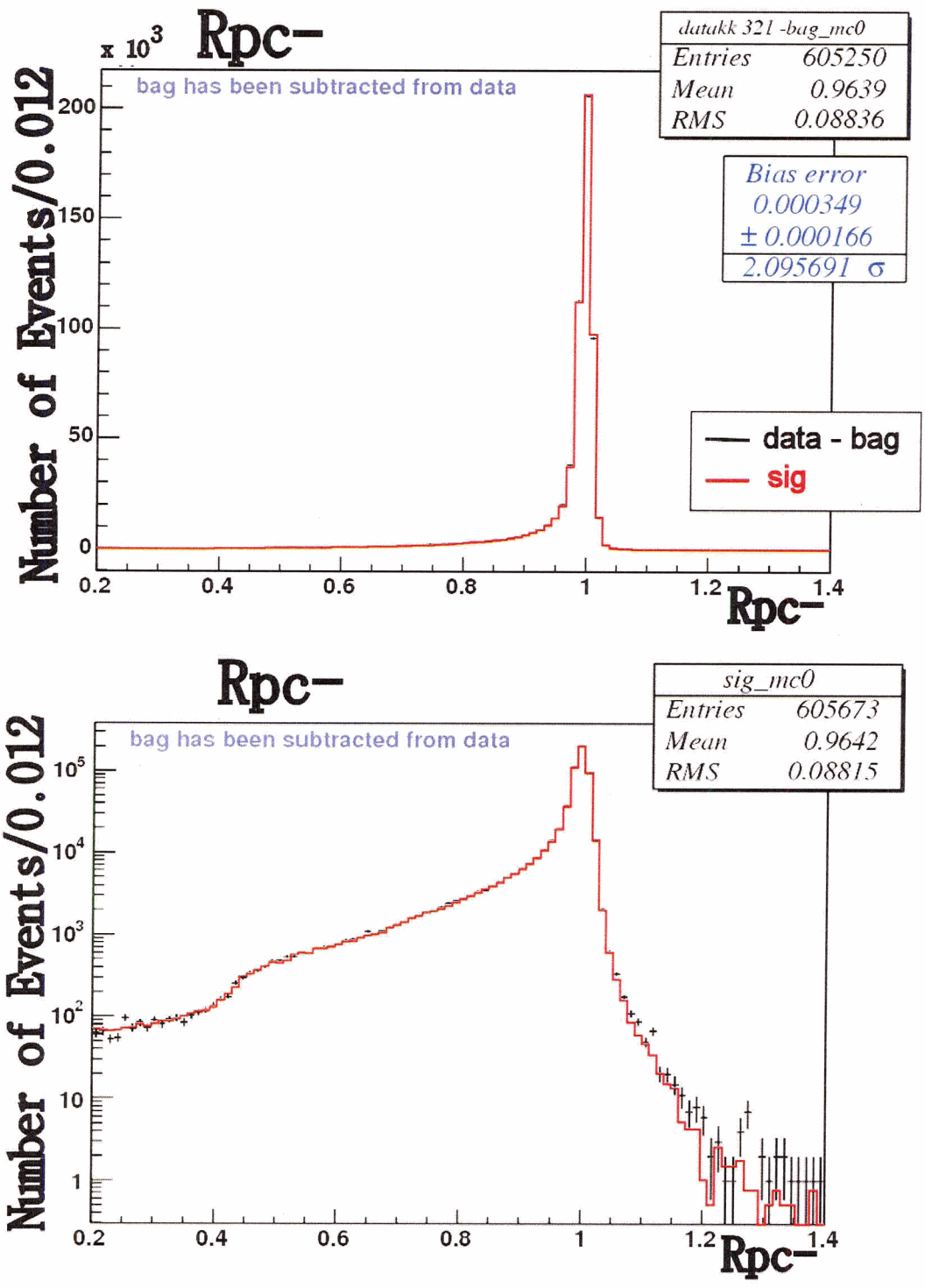

Figure 5.19: $P_{\mu^-,CM,corr}/P^{max}_{\mu,CM}$

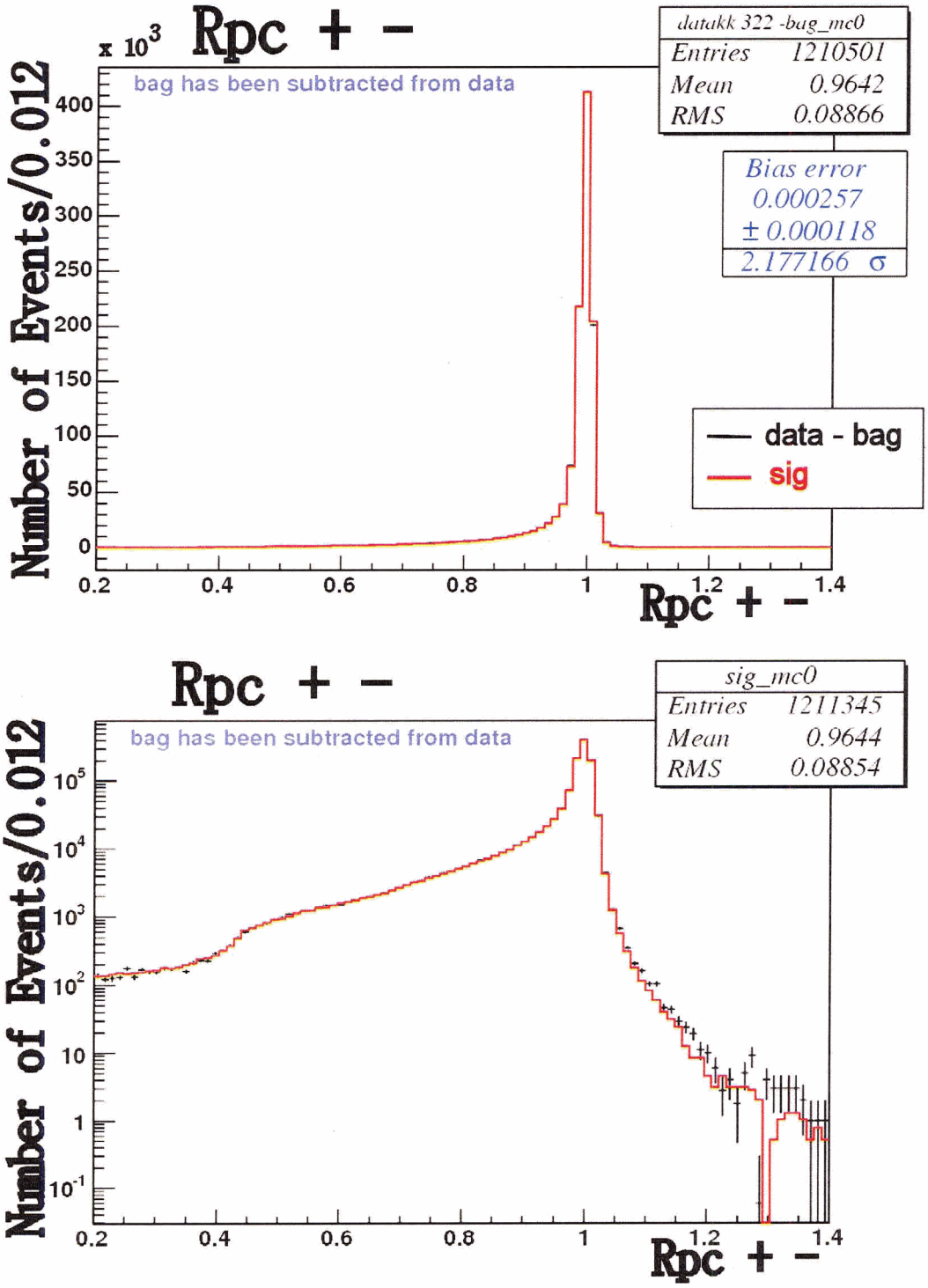

Figure 5.20: $P_{\mu^{\pm},CM,corr}/P^{max}_{\mu,CM}$

using $e^+e^- \to \mu^+\mu^-\gamma$ events to determine the systematic errors associated with the signal efficiency. We expect that the uncertainty on ΔE of $\tau \to \mu\gamma$ in $e^+e^- \to \tau^+\tau^-$ events would be the same as that on ΔE for $e^+e^- \to \mu^+\mu^-\gamma$ events.

Figure 5.23 presents the distributions of ΔE for $e^+e^- \to \mu^+\mu^-\gamma$ events. Those events which have only one photon with energy more than 400 MeV were selected. To get the right $\mu\gamma$ pair, the $|\Delta E|$ region was restricted to $|\Delta E| < 0.2GeV$ and Rm>0.98. The top histogram shows the comparison of data - background and μ MC. The middle and bottom histograms show the data - background and μ MC. We can see that the mean value of ΔE for MC is deviated from that of data - background by amount of 3.55 MeV and the RMS of ΔE for MC is bigger than that of data by 0.64 MeV.

We also fit the data and MC using the function:

Number of events

$$= Ae^{-(\Delta E - <\Delta E>)^2/(2\sigma^2)} + (t_1 + t_3\Delta E)(tan^{-1}(t_0\Delta E - t_2) + \pi/2) + c_3\Delta E^3 + c_2\Delta E^2 + c_1\Delta E + c_0$$

A total of 11 fitting parameters were found to be needed to describe the shape of the distribution. After fitting the Gaussian term gives:

$$< \Delta E_{data} > - < \Delta E_{MC} >= -0.002 \pm 0.0031 GeV,$$

where the error is statistical. From this we have a 3 MeV estimate of the systematic error on $< \Delta E >_{MC}$. Thus the mean values of ΔE for data and μ MC are consistent with each other within an uncertainty of 3 MeV. We can also check that two σ (resolution) values are consistent with each other and find there exist about a 14% error between data and μ MC:

$$\frac{\sigma_{\Delta E}^{data}}{\sigma_{\Delta E}^{MC}} = \frac{0.0281 \pm 0.002}{0.0297 \pm 0.004} = 0.945 \pm 0.142.$$

Note that

$$|\sigma_{\Delta E}^{data} - \sigma_{\Delta E}^{MC}| = 0.002 \pm 0.005 GeV$$

The σ value of $M_{EC,\mu\gamma}$ for $\tau \to \mu\gamma$ MC has been studied and the result was about 9.1 MeV. The resolution of ΔE is dominated by the resolution of E_γ and we can roughly say that the uncertainty from the MC modelling of E_γ on the resolution of $M_{EC,\mu\gamma}$ is about 1.3 MeV (14% of 9.1 MeV). From Figure 5.21, we can get the bias error of $M_{EC,\mu^+\gamma}$ and $M_{EC,\mu^-\gamma}$ between data and MC. For data and μ MC respectively.

$$< M_{EC,\mu^+\gamma} >_{MC} - < M_{EC,\mu^+\gamma} >_{data} = (-0.0103 \pm 0.0052) \times 0.9818 GeV = -0.010 \pm 0.0048 GeV$$

$$< M_{EC,\mu^-\gamma} >_{MC} - < M_{EC,\mu^-\gamma} >_{data} = (-0.0003 \pm 0.0051) \times 0.9723 GeV = 0.000 \pm 0.0050 GeV$$

Thus we get the uncertainty for the mean value of $M_{EC,\mu\gamma}$ of about 4 MeV by

$$< M_{EC,\mu\gamma} >_{data} - < M_{EC,\mu\gamma} >_{MC} = 0.005 \pm 0.004 GeV.$$

Figure 5.24 shows the $M^2_{EC} - M^2_{recoil}$ distribution for data - background and μ MC. The same cut and fitting as ΔE case have been applied. Here M_{recoil} (recoil means the track which is not associated with photon) is defined as

$$M_{recoil} \equiv \sqrt{(E_{beam} - E_{recoil})^2 - P^2_{recoil}}$$

Again we can calculate ratio of two σ (resolution) values

$$\frac{\sigma^{data}_{M^2_{EC} - M^2_{recoil}}}{\sigma^{MC}_{M^2_{EC} - M^2_{recoil}}} = 1.045 \pm 0.020$$

This means the error on the resolution of the MC modelling of the recoil mass is at most 4.5%. Since the M_{recoil} uncertainty is dominated by the uncertainty on recoil momentum P_{recoil}, 4.5% is roughly the uncertainty on P_{recoil}. We apply this as a crude estimate of the uncertainty for resolution of $M_{EC,\mu\gamma}$ (σ_{MEC}), and deduce a systematic uncertainty on resolution of $M_{EC,\mu\gamma}$ from the momentum uncertainty of around 1 MeV.

These systematic uncertainties of ΔE and $M_{EC,\mu\gamma}$ can be used to study the systematic error associated with the $\tau \to \mu\gamma$ signal efficiency due to the uncertainty of ΔE and $M_{EC,\mu\gamma}$ of $e^+e^- \to \tau^+\tau^-$ events. By manipulating mean and RMS of ΔE and $M_{EC,\mu\gamma}$ for $\tau \to \mu\gamma$ of $e^+e^- \to \tau^+\tau^-$ events by these amounts, we can estimate the systematic errors associated with the signal efficiency due to the uncertainty on ΔE and $M_{EC,\mu\gamma}$ of $e^+e^- \to \tau^+\tau^-$ events. These resolution studies provide the ΔE and $M_{EC,\mu\gamma}$ modeling uncertainty on the efficiency for selecting $\tau \to \mu\gamma$ signal events. The scale and resolution uncertainties contribute 6.3% to the systematic error on the efficiency.[22]

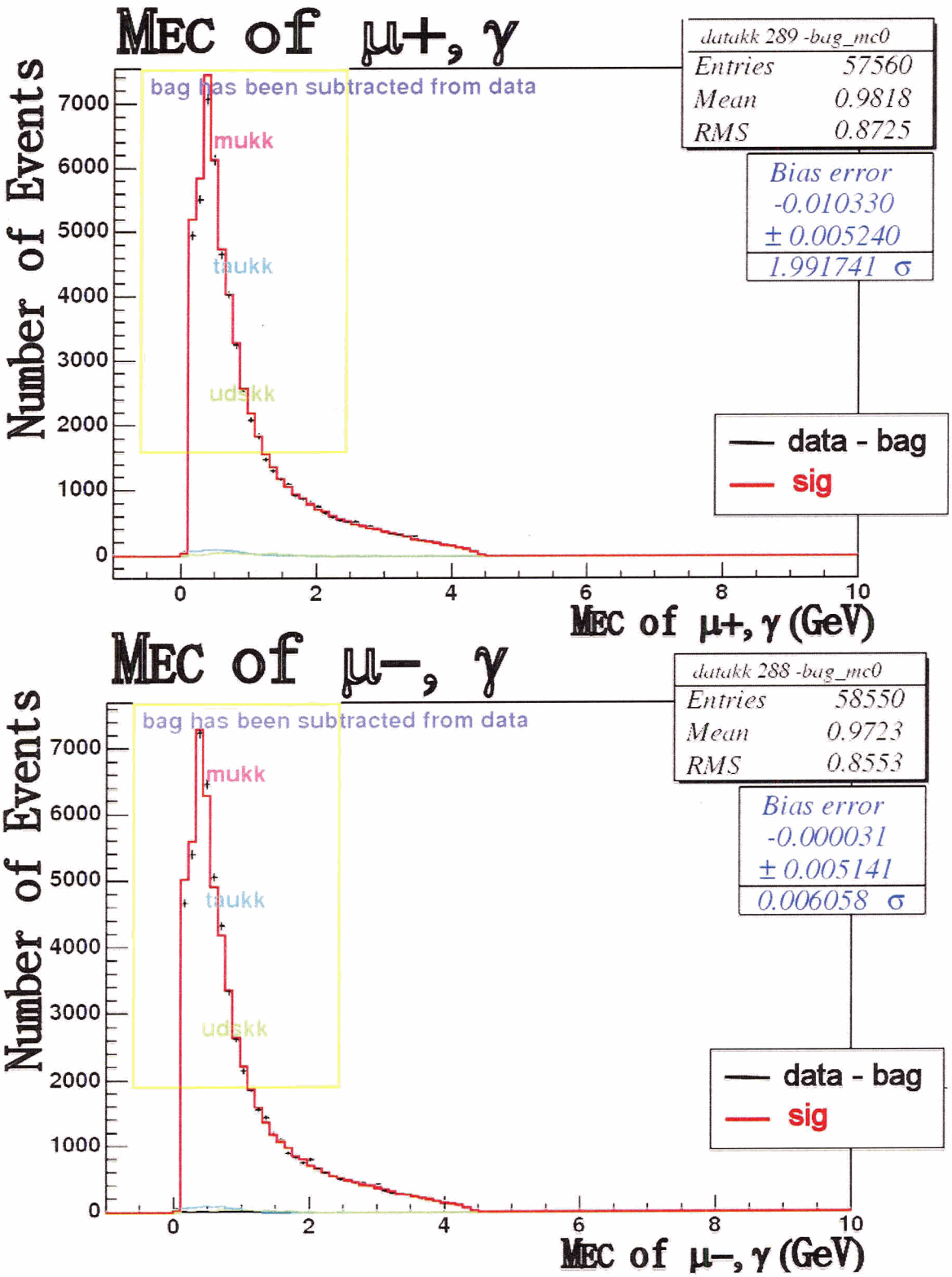

Figure 5.21: Upper:M_{EC} of $\mu^+\gamma$, Lower:M_{EC} of $\mu^-\gamma$

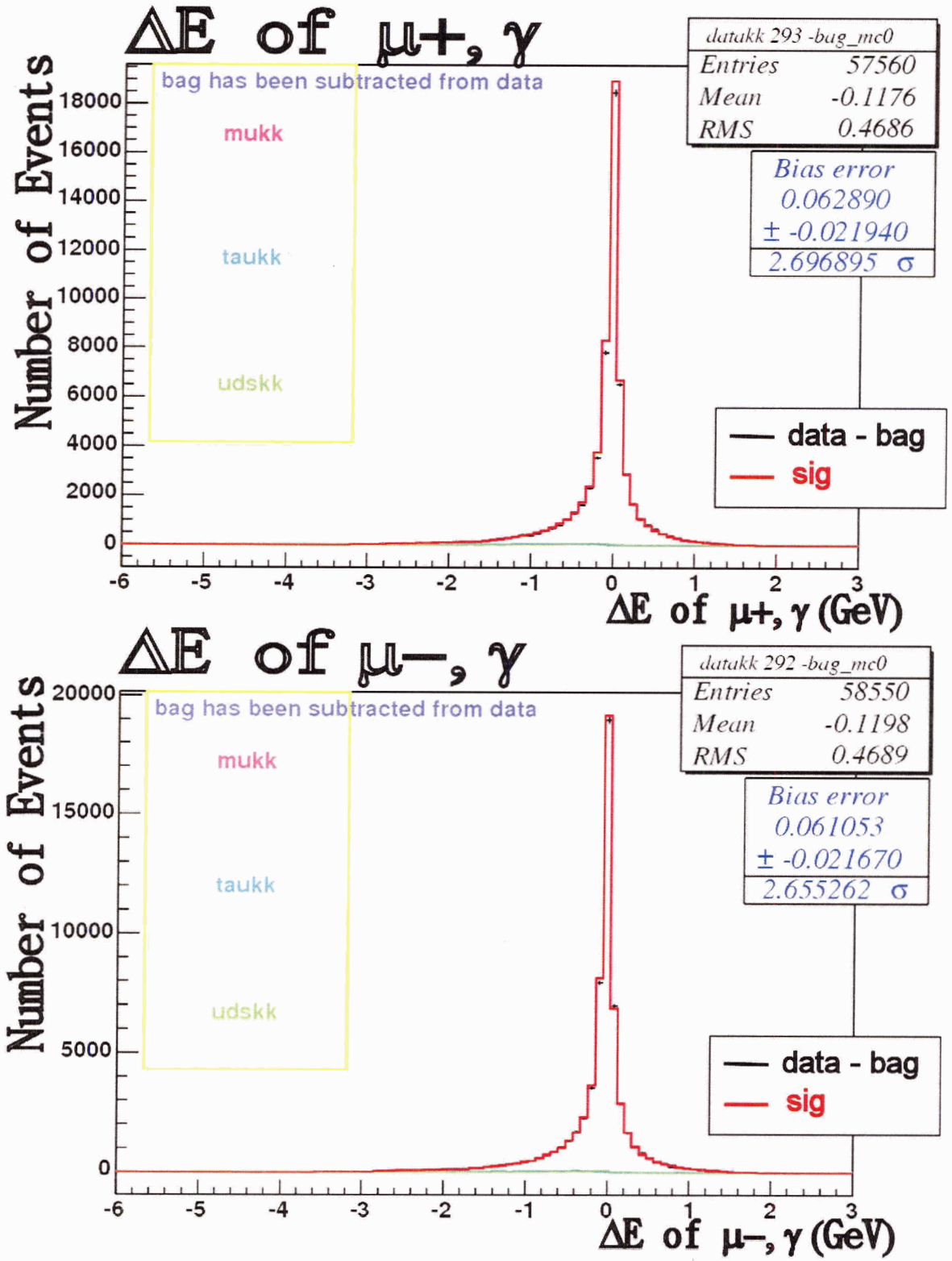

Figure 5.22: Upper:$\Delta E(=E_{CM}/2 - E^{CM}_{\mu\gamma})$ of $\mu^+\gamma$, Lower:$\Delta E(=E_{CM}/2 - E^{CM}_{\mu\gamma})$ of $\mu^-\gamma$

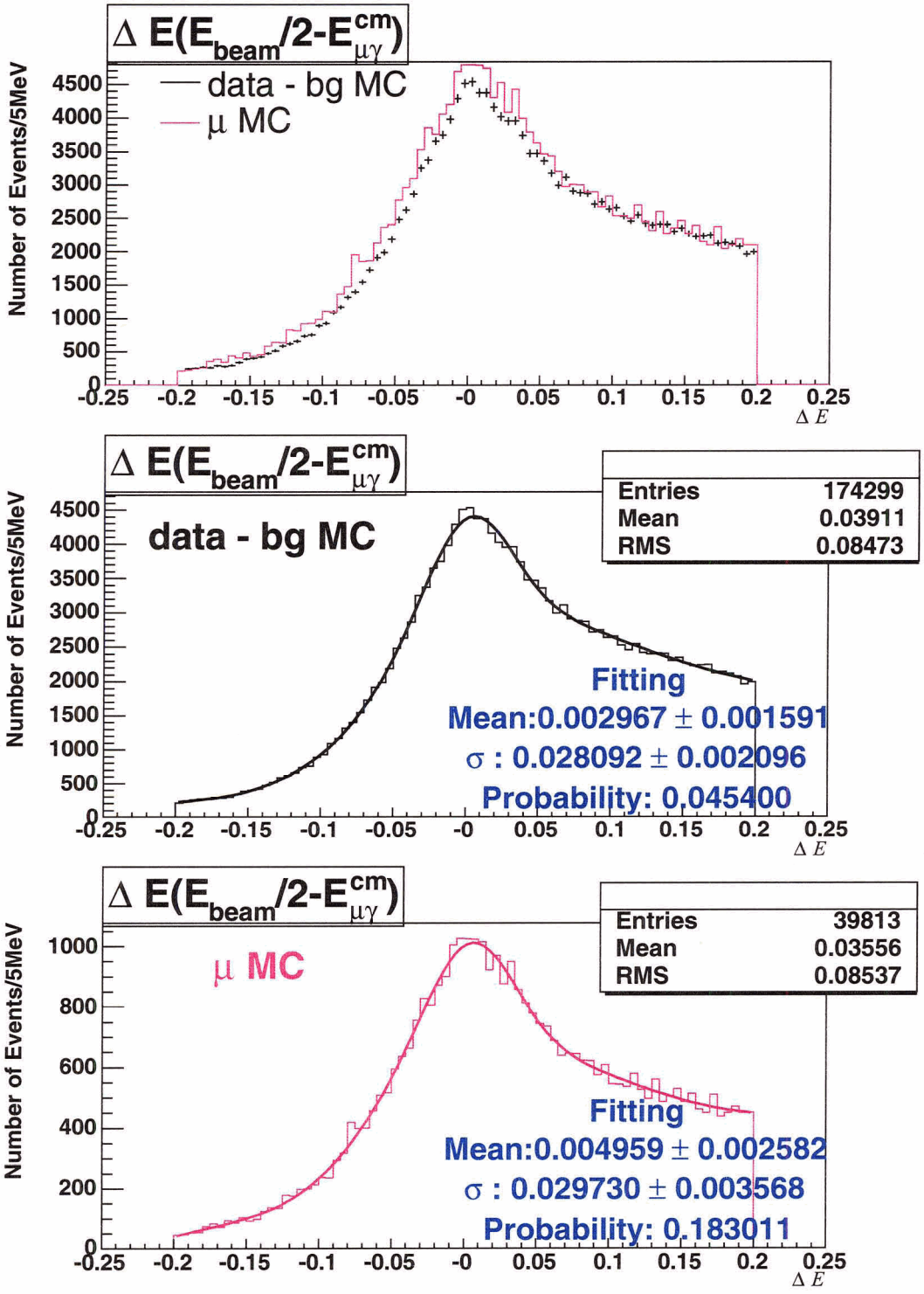

Figure 5.23: $\Delta E(E_{CM}/2 - E^{CM}_{\mu\gamma})$ after extended cut and Rm>0.98 and number of photon=1 and $E_\gamma > 0.4$GeV;Top:comparison of data - background and mu MC, Middle:data - background with Gaussian fit + background fit, Bottom:mu MC with Gaussian fit + background fit

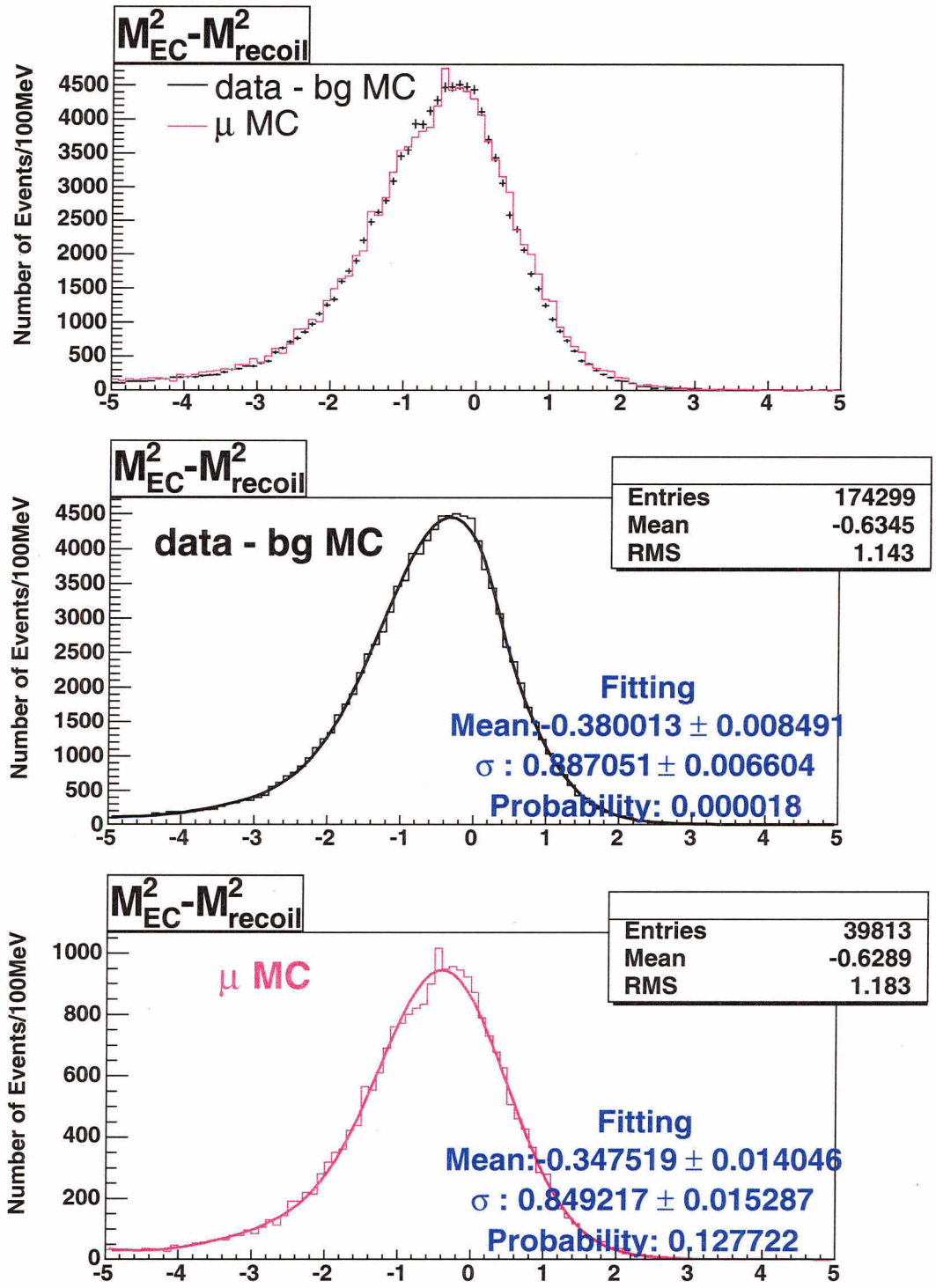

Figure 5.24: $M^2_{EC} - M^2_{recoil}$ after extended cut and Rm>0.98 and number of photon=1 and $E_\gamma > 0.4$GeV;Top:comparison of data - background and mu MC, Middle:data - background with Gaussian fit + background fit, Bottom:mu MC with Gaussian fit + background fit

Chapter 6

CONCLUSION

In order to get $e^+e^- \to \mu^+\mu^-(\gamma)$ with high purity and efficiency the mutau preselection[8] and cuts developed in this analysis were applied to data and MC. Applying all cuts, an efficiency of 52.41% and purity of 99.57% were achieved while preserving most of the ISR and FSR events of mutau preselection. Various photon minimum energy cuts also have been investigated: the results were insensitive for minimum photon energies ranging from 50 MeV to at least 90 MeV in the LAB frame.

The validation of the MC for other interesting detector quantities was also checked. We can see good agreements(below 3σ) in the means of the distributions between data and KK2f for cos(θ,CM, μ), $\phi_{CM,\mu}$, acoplanaritycm and acolinearitycm between $\mu^+\mu^-$ while KORALB shows worse agreement. For cos($\theta_{\gamma 1,CM}$), $\phi_{\gamma 1,CM}$, the energy of most energetic photon in CM($E_{\gamma 1,CM}$), total energy of photons in CM($\Sigma E_{\gamma,CM}$), energy constrained mass of $\mu\gamma(M_{EC,\mu\gamma})$, $\Delta E_{\mu\gamma}$ KK2f shows better agreement between data and MC than KORALB.

From the $\Delta E(=E_{CM}/2 - E^{CM}_{\mu\gamma})$ and $M_{EC,\mu\gamma}$ studies we obtained 3 MeV systematic error on the mean value of ΔE, 1.3 MeV on the resolution of the MC modelling of the ΔE, 4 MeV of the uncertainty for mean value of $M_{EC,\mu\gamma}$ and roughly 1 MeV of the systematic uncertainty on resolution of $M_{EC,\mu\gamma}$. These are used in reference [21].

For the τ lifetime measurement study, the momentum distributions of muons for data and MC have been studied. There was a charge asymmetry which is suspected as the result of a detector effect in the data but not modelled in the MC. The bias errors of $P_{\mu^{\pm},CM}/P^{max}_{\mu,CM}$ for KK2f before and after correcting this charge asymmetry and disagreement of resolution were obtained.

$$\begin{aligned} \text{Bias error of } P_{\mu^{\pm},CM}/P^{max}_{\mu,CM} &= (0.065 \pm 0.012(stat) \pm 0.043(syst))\% \\ \text{Bias error of } P_{\mu^{\pm},CM,corr}/P^{max}_{\mu,CM} &= (0.026 \pm 0.012(stat) \pm 0.015(syst))\% \end{aligned}$$

For KORALB,

$$\begin{aligned} \text{Bias error of } P_{\mu^{\pm},CM}/P^{max}_{\mu,CM} &= (-0.089 \pm 0.015(stat) \pm 0.038(syst))\% \\ \text{Bias error of } P_{\mu^{\pm},CM,corr}/P^{max}_{\mu,CM} &= (-0.120 \pm 0.015(stat) \pm 0.026(syst))\% \end{aligned}$$

These studies indicated that a 0.1% error on P_τ should be assigned in the tau lifetime measurement[20].

Bibliography

[1] D. F. Carvalho, Charged lepton Flavor Violation in Supersymmetry with Bilinear R-Parity Violation, Phys.Rev. D65 (2002) 093013

[2] Lowell S. Brown, Quantum Field Theory(Cambridge University Press, 1992, ISBN 0 521 46946 5)

[3] B. F. Ward, S. Jadach, Z. Was, Nucl. Phys. Proc. Suppl. (2003)

[4] T. Sjostrand, Comp. Phys. Comm. 82, 74 (1994)

[5] S. Agostineli *et al,* [GEANT4 Collab.], Nucl. Istr. (2003)

[6] B. Aubert *et al,* The BABAR Collaboration, "The BABAR detector", Nuclear Instruments and Methods in Physics Research A 479, 1-116 (2002)

[7] http://www.slac.stanford.edu/BFROOT/ [Last visited on February 22, 2005]

[8] S. Banerjee, M. Hodgkinson, M. Roney, BABAR Analysis Document #739, "Nano and Micro Level Preselection for $e^-e^+ \to \mu^-\mu^+$ and $e^-e^+ \to \tau^-\tau^+$ events"

[9] R. Rudolf, Particle Accelerators(1967)

[10] K. Kleinknecht, Detectors for particle radiation 2nd ed. (New York: Cambridge University Press, 1998, ISBN 0 521 64032 6)

[11] M. Livingston, J. Blewett, Particle Accelerators(Mcgraw-hill book Company, INC, 1962, 38140)

[12] J. Livingood, Principles of cyclic particle accelerators(D. Van Nostrand Company, INC, 1961)

[13] A. Das, T. Ferbel, Introduction to nuclear and Particle physics(John Wiley & Sons, INC, 1994, ISBN 0 471 57132 6)

[14] E. Segre, Nuclei and Particles, An Introduction to nuclear and sub nuclear physics Second edition (W. A. Benjamin, INC, 1977)

[15] A. O Weissenberg, Muons(North-Holland Publishing Company, Amsterdam, 1967)

[16] T. Hoyd, Electronic Devices(Bell & Howell Company, 1984)

[17] R. Bruno, High-energy particles(Prentice-Hall, INC, 1952)

[18] http://rd11.web.cern.ch/RD11/rkb/PH14pp/PH14pp.html [Last visited on February 22, 2005]

[19] M. Hodgkinson, "Comparison of Tau Lepton Monte Carlo Event Generators in BaBar"

[20] A. Lusiani, Proceeding of the 8th international workshops on tau lepton physics, Nara, Japan, September, 2004. Measurement of the tau life time with BaBar.

[21] J.M Roney, Proceeding of the 8th international workshops on tau lepton physics, Nara, Japan, September, 2004. Search for $\tau \to \mu\gamma$.

[22] S. Banerjee, BABAR Analysis Document #1079, "Search for Lepton Flavor Violation in the Decay $\tau^{\pm} \to \mu^{\pm}\gamma$"

Publications:

- Z. Yun, *Basic postulate of Quantum Mechanics* , Inha University. (1999) .